# 2D-3D Registration of Cardiac Images

Truong, Michael Vi Nguyen

*Awarding institution:*
King's College London

KING'S COLLEGE LONDON, UNIVERSITY OF LONDON

# 2D–3D Registration of Cardiac Images

## PhD Thesis

**Michael Vi Nguyen Truong**

**Division of Imaging Sciences & Biomedical Engineering**
**School of Medicine**
**King's College London**
**University of London**

**28/02/2014**

A thesis submitted in partial fulfilment of the requirements for the degree of Doctor of Philosophy of King's College London, University of London

# Abstract

This thesis describes two novel catheter-based 2D-3D cardiac image registration algorithms for overlaying preoperative 3D MR or CT data onto intraoperative fluoroscopy, and fusing electroanatomical data onto clinical images. The work is intended for use in cardiac catheterisation procedures. To fulfil this objective, the algorithms must be accurate, robust and minimally disruptive to the clinical workflow.

The first algorithm relies on the catheterisation of vessels of the heart and registers by minimising a vessel-radius-weighted distance between the catheters and corresponding vessel centrelines. A novelty here is a global-fit search strategy that considers all vessel branches during registration, adding robustness and avoiding manual branch selection.

Another contribution to knowledge is an analysis of catheter configurations for registration. Results show that accuracy is highly dependent on the catheter configuration, and that using a coronary vessel (CV) with the aorta (Ao) was most accurate, yielding mean 3D target registration errors (TRE) between 0.55 and 7.0 mm with phantom data. Using two large-diameter vessels was least accurate, with TRE between 10 and 43 mm, and should be avoided. When applied to clinical data, registrations with the CV/Ao configuration resulted an estimated mean 2D-TRE of 5.9 mm, on average.

The second 2D-3D registration algorithm extends the novelty of exploring catheter configurations by registering using catheters looped inside chambers of the heart. In phantom experiments, two-view registration yielded an average accuracy of 4.0 mm 3D-TRE (7.8-mm capture range). Using a single view, average reprojection distance was 2.7 mm (6.0-mm capture range). Application of the algorithm to a clinical dataset resulted in an estimated average 2D-TRE of 10 mm. Single view registrations are ideal when biplane X-ray acquisition is undesirable and for correcting bulk patient motion.

In current practice, registration is performed manually. The algorithms in this thesis can register with comparable accuracy to manual registration, but are automated and can therefore fit better with the clinical workflow.

# Acknowledgements

Firstly, I would like to express my deepest gratitude to my supervisors, Dr Kawal Rhode and Dr Graeme Penney, for their patience, knowledge and continuous support throughout my doctoral journey. I am very glad to have had such a privilege.

My gratitude extends to Ying Liang who has been a big help during my PhD, to James for going through this thesis with such a fine-toothed comb, and to the rest of our team, Maria, Cata, Rashed and Zhi Quing for all their help. I would also like to thank my students, Thomas, Abdullah, Sid, Nina and Asha for their dedication and hard work. My thanks also go to the rest of the colleagues from the lab, especially those with whom I have become good friends: David, Mick, Max, Harry, Mazen, Markus, Giulio, Yolanda, Sally, Peter, Alexis and Elaine.

My funding throughout my PhD was provided by EuHeart, for which I am very grateful. I am also grateful to Matt, Aldo, Anoop, Kalpa, and Tarique from the clinical team for providing me with the patient data used in my research.

Outside of my studies, I would like to say thank you to Gary and Mihaela who have always been like mentors to me and have never hesitated to impart their wisdom and guidance. I would also like to make a special mention to people from King's Kung Fu club at the KCLSU: my instructors Sifu Leppard, Kevan and Hauke, and my peers (past and present) in training, particularly Leo, Jan, David, Phil, Laura, Marta, Li Hong, Alicia and Alison, with whom I have become good friends. They have been an integral part of my life in London while I pursued my PhD and a source of focus and recentering. I would especially like to thank Leo who has always been there when I needed her, and Alicia for opening the door for me to her family and home.

A huge thank you goes to Alison for the countless hours of her time helping me with my work, proof reading this thesis and providing the nice illustrations used throughout. Your help couldn't have come at a better time.

Finally, I would like to say thank you to my family, to whom I dedicate this thesis: Mom, Dad, Linh, Vi, Kiet, Angel, Jade and Juliana. Your endless love and support has always been felt from across the pond.

# Contents

# List of Tables

# List of Figures

# List of Abbreviations

**Cardiac Anatomy**

| | |
|---|---|
| CS | Coronary Sinus |
| CA | Coronary Artery |
| RCA | Right Coronary Artery |
| LCA | Left Coronary Artery |
| LAD | Left Anterior Descending |
| LCx | Left Circumflex |
| VC | Vena Cava |
| IVC | Inferior Vena Cava |
| SVC | Superior Vena Cava |
| PV | Pulmonary Vein |
| LUPV | Left Upper Pulmonary Vein |
| LLPV | Left Lower Pulmonary Vein |
| RUPV | Right Upper Pulmonary Vein |
| RLPV | Right Lower Pulmonary Vein |
| PA | Pulmonary Artery |
| Ao | Aorta |
| AAo | Ascending Aorta |
| TAo | Aortic Arch (Transverse Aorta) |
| DAo | Descending Aorta |
| LA | Left Atrium |
| LV | Left Ventricle |
| RA | Right Atrium |
| RV | Right Ventricle |
| LRV | Left and Right Ventricle |
| WH | Whole Heart |

**Geometry**

| | |
|---|---|
| 2D | Two-Dimensional, Projective Two-Dimensional |
| 3D | Three-Dimensional |
| RMS | Root-mean-square |
| DOF | Degree-of-Freedom |
| FRE | Fiducial Registration Error |
| TRE | Target Registration Error |

**Imaging**

| | |
|---|---|
| CT | (X-ray) Computed Tomography |
| 3DRx | 3D Rotational X-ray |
| MR | Magnetic Resonance |
| PET | Positron Electron Tomography |
| SPECT | Single Proton Emission Computed Tomography |
| OCT | Optical Coherence Tomography |

**Heart Disease**

| | |
|---|---|
| AF | Atrial Fibrillation |
| AFL | Atrial Flutter |
| EP | Electrophysiology, -logical, -logically |
| CABG | Coronary Artery Bypass Graft |
| CRT | Cardiac Resynchronisation Therapy |
| RFA | Radiofrequency Ablation |
| PCI | Percutaneous Coronary Intervention |

# List of Notations and Conventions

| **Notations** | | **Conventions** | |
|---|---|---|---|
| vector | $\vec{v} = (v_x, v_y, \dots)$ | position | $\vec{r}, \vec{p}$ |
| pseudovector | $\tilde{v} = [v_x \quad v_y \quad \cdots]$ | 3D positions | $\vec{r}$ |
| vector length, norm | $\|\vec{v}\|$ | 2D positions | $\vec{p}, \vec{q}$ |
| | | coordinates | $(x, y, \dots)$ |
| set | $S = \{S_i\}$ | image coordinates | $(u, v, \dots)$ |
| count, cardinality | $\|S\| = \|\{S_i\}\|$ | indices | $i, j, k$ |
| matrices | $M$ | radius | $\rho$ |
| transformation matrices | $\mathcal{M}$ | area | $A$ |
| pseudoinverse | $M^+, \mathcal{M}^+$ | line | $\ell = \vec{m}\lambda + \vec{b}$ |
| identity | $I_n$ | | |
| image | $I = I_i(\vec{r}_i) = I_i(u_i, v_i, \dots)$ | | |

| | | | |
|---|---|---|---|
| rotation matrix | $\mathcal{R} = \begin{bmatrix} R & \vec{0} \\ \tilde{0} & 1 \end{bmatrix}$ | projection matrix | $\mathcal{P} = [P \quad \vec{0}]$ |
| translation matrix | $T = \begin{bmatrix} I_3 & \vec{\delta} \\ \tilde{0} & 1 \end{bmatrix}$ | camera matrix | $\mathcal{C} = [C \quad \vec{c}]$ |
| rigid body matrix | $\mathcal{M} = \begin{bmatrix} R & \vec{\delta} \\ \tilde{0} & 1 \end{bmatrix}$ | | |

# Chapter 1

## 1. Introduction and Overview

The main focus of this thesis is the algorithmic registration of high-contrast 3D images of the heart, acquired from imaging modalities such as magnetic resonance (MR) imaging (MRI) and X-ray computed tomography (CT) onto 2D shadowgrams of the chest taken from X-ray fluoroscopy. This type of algorithm is often referred to as 2D-3D image registration. This translational research draws motivation from the clinical requirements in image-guided cardiac catheterisation procedures to overlay preoperatively acquired 3D anatomical data onto intraoperative X-ray. A second application for this work is the fusion of electroanatomical mapping (EAM) data acquired using electrophysiological (EP) mapping and navigation systems such as EnSite™ (St. Jude Medical, St. Paul, MN, US) and Carto™ (Biosense Webster, Diamond Bar, CA, US) with preoperative data for biophysical modelling, using X-ray as an intermediary.

The work will be presented in this thesis in eight chapters. The remainder of this chapter is dedicated to providing a short introduction and overview for each of the chapters that follow, starting with the clinical and technical background and motivation, the theory and framework behind 2D-3D registration, two 2D-3D image registration algorithms designed for cardiac catheterisations, and a 3D-3D image registration algorithm to further augment EAM data to an already co-registered 2D-3D space. The final chapter, Chapter 8, ends with concluding remarks, a general discussion of what has been presented and suggested future work.

### 1.1. Image-Guided Cardiac Catheterisations

Cardiovascular disease is the leading cause of death in the western world for both men and women. Throughout the European Union (EU), this disease claims the lives of 1.9 million each year, accounting for two-fifths of the EU's annual death rate and with an associated cost of €196 billion to its economy per year [1].

Cardiac catheterisation is a minimally-invasive and cost effective approach to treat conduction abnormalities and other pathophysiologies of the heart [2] [3] [4] [5] [6] [7] [8] [9]. Patients admitted for these procedures often undergo, or would have already undergone, preoperative CT or MR imaging for diagnosis and treatment planning [10]. These modalities are suitable for

this purpose due to their excellent soft-tissue contrast and 3D imaging capabilities. Intraoperatively, these procedures are guided using X-ray fluoroscopy due to its real-time imaging capabilities, high-device visibility, low-cost, and widespread availability. However this projective modality offers no depth information and poorly visualises the heart itself.

In catheter-based cardiac procedures, such as electrophysiology (EP) studies, percutaneous coronary intervention (PCI) [4], cardiac resynchronisation therapy (CRT) [11], and radio frequency ablation (RFA) for atrial fibrillation (AF) and flutter (AFL) [8] [9] [12], the cardiologist must accurately and remotely position catheters into the heart. The limited visibility of the heart offered by fluoroscopy makes catheter navigation difficult, time-consuming and potentially dangerous since there is a chance that the catheter may puncture through the vessel wall. These result in significant X-ray exposure to the patient and staff, repeat toxic radio-opaque contrast agent injections, and often suboptimal success rates [10] [13] [14]. It would be beneficial for the cardiologist if the 3D soft tissue information taken preoperatively could be overlaid onto the X-ray automatically and in real-time [15] [16] [17]. Generating overlays requires finding the relationship between coordinate systems of the 3D imaging system and 2D fluoroscopy, a problem known as 2D-3D image registration. Electroanatomical mapping information acquired intraprocedurally, with EnSite™ or Carto™, can also be overlaid onto the X-ray, or fused with the overlaid preoperative 3D data. This provides the interventionist with further diagnostic information to guide and assess the treatment, and has further applications in offline biophysical modelling [18] [19].

Chapter 2 of this thesis provides an in-depth description of cardiac catheterisation procedures, their typical clinical workflow and the imaging modalities involved, supported by clinical literature to provide the motivation for the research presented in this thesis.

Recently, there has been much research to augment X-ray fluoroscopy by overlaying high-quality soft-tissue-contrast 3D information of the heart using 2D-3D image registration. This research is systematically organised according to well-established classification schemes [20] [21] and is comparatively reviewed in Chapter 3. The methods are classified according to their imaging modality, image dimensionality, feature-space, search-space, search-strategy and similarity metric. While it will be evident in Chapter 3 that numerous approaches are available to perform 2D-3D image registration, it will also be clear that there is not yet a single approach in which 2D-3D registration is fully automatic, accurate, robust and extensively tested while also fitting with the cardiac catheterisation workflow. Therefore, the purpose of Chapter 3 is to not only summarise the state-of-the-art, but to also provide heuristic justification for two novel automatic 2D-3D cardiac image registration algorithms, designed with the clinical flow in mind. The two algorithms are valid for complimentary scenarios in cardiac catheterisations and aim to

be accurate and robust. The rigorous development and validation of these algorithms is the principle aim of this thesis.

## 1.2. 2D-3D Image Registration Definition and Framework

2D-3D image registration has been previously defined as "*the determination of a projection mapping, from a 3D to a 2D coordinate system such that points in each space which correspond to the same anatomical point are mapped to each other*" [22]. This definition is valid where the 2D coordinate system coincides with the projective plane belonging to any modality that follows the pin-hole camera model, such as an X-ray fluoroscope (Figure 1.1a, b). The projective nature of fluoroscopy results in an almost total loss of depth information, evident in Figure 1.1b, and presents an ill-conditioned problem where an anatomical 2D point can be mapped to an infinite number of 3D points belonging to the projection line segment between the X-ray source and the 2D point (Figure 1.1a). The 2D and 3D points can be brought into spatial correspondence with one another by forward projection, back-projection, or epipolar reconstruction. These three techniques are described in Chapter 3 to help classify the 2D-3D registration algorithms found in the literature.

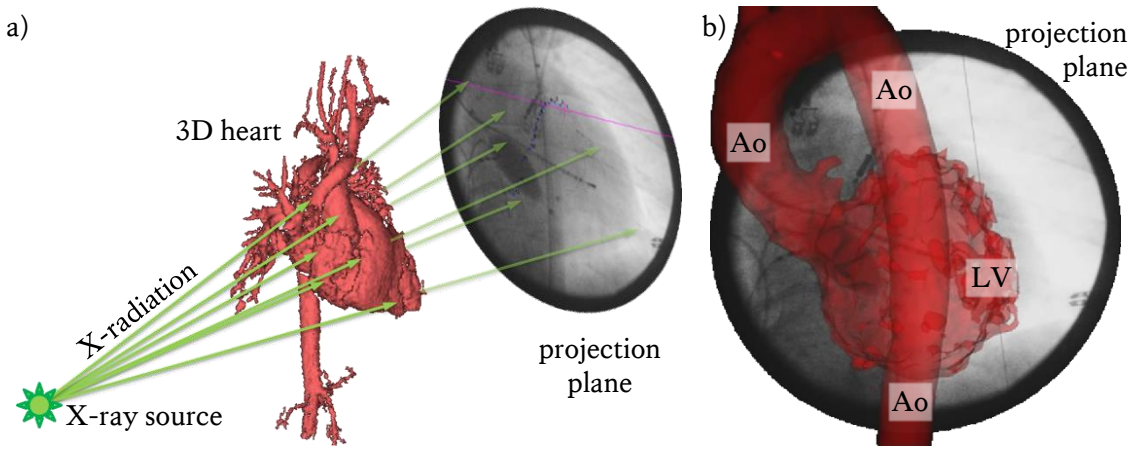


Figure 1.1 a) Surface rendering of the heart (*red, opaque*) and projection lines (*green, opaque before the heart, translucent afterwards*) representing X-radiation emanating from an X-ray point source and producing a shadowgram of the heart onto the projection plane (*greyscale, circular disk*). This perspective projection assumes that the X-ray device follows the pin-hole camera model. b) Overlay of aorta (Ao) and left ventricle (LV) surface rendering (*red, translucent*) onto the shadowgram.

Chapter 4 aims to provide a framework for geometric techniques used throughout this thesis. It starts with a mathematical description of the 2D-3D registration problem and three techniques to establish spatial correspondence. It then describes some tools to extract 2D and 3D geometry information necessary for registration. The use of extracted features for the purposes of aligning the 2D and 3D images is a defining characteristic of the class of *feature-based image registration* methods, to which the two algorithms presented in this thesis belong. Chapter 4 concludes with

a description of fiducial and manual methods of registrations to provide standards against which the accuracy and robustness of the registration methods developed in this thesis are measured.

## 1.3. Catheter-Vessel-Based Registration Algorithm

Chapters 5 and 6 of this thesis are dedicated to the first novel 2D-3D image registration method proposed. The method is a feature-based biplane reconstruction approach, and requires the catheterisation of one or two vessels during the cardiac catheterisation procedure. This is a realistic and achievable requirement since it is common practice to insert one catheter to perform the treatment, such as RF ablation, and a second decapolar catheter to gather vital electrical data inside the coronary sinus (Figure 1.2). The algorithm globally matches between the catheters reconstructed from X-ray, using epipolar geometry, and corresponding vessel centreline. The vessel radii are also used to provide further constraints.

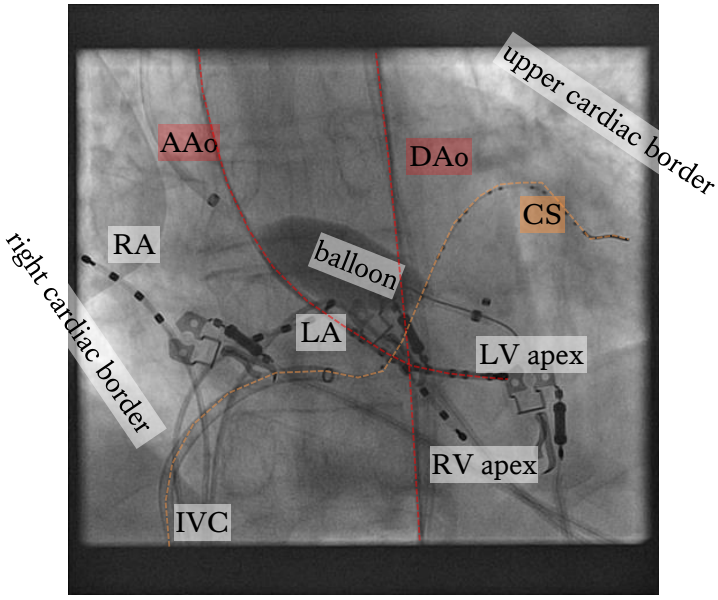


Figure 1.2) This shows a posterior-anterior view of the heart, with catheters entering the coronary sinus (CS, *orange dashed*), left atrium (LA), right atrium (RA), left ventricle (LV), and right ventricle (RV) via the inferior vena cava (IVC) and EnSite™ balloon, roving catheter and pressure catheter inserted in the LV via the descending and ascending aorta (DAo, AAo, *red dashed*). The devices can be seen with excellent visibility in the X-ray, but there is poor visibility of the heart itself with only some regions of its epicardial border that can be delineated. The CS and aorta catheter can be used for registration.

A key advantage of this algorithm is the minimal disruption of the clinical work flow since the images and devices used for registration are the same ones used for treatment. The full description of the algorithm is presented in Chapter 5 which provides the results and an in-depth discussion of the algorithm's application in two phantom experiments designed to simulate the clinical workflow. In Chapter 6, the algorithm is adapted to deal with the additional difficulties when registering with data taken from live catheterisation procedures, such a more complex anatomy and cardiorespiratory gating errors. Registration is then applied to three clinical cases

postoperatively. These cases include an RFA to treat AF, a CRT, and a PCI. Both anatomical information from MR images, and electroanatomical mappings acquired using EnSite™, are overlaid onto intraoperatively acquired X-rays with accuracy compared against clinically standard manual methods of registration described in Chapter 4.

## 1.4. Looped-Catheter-Based Registration Algorithm

During catheterisations, in scenarios where two vessels cannot be catheterised simultaneously or where sequential biplane cannot be acquired to perform catheter reconstruction, the catheter-vessel-based method of the previous section would not be able to produce an accurate or reliable registration. This necessitates a second 2D-3D cardiac image registration approach which does not rely on catheterisation of vessels and can register using a single view.

In current clinical settings, a common technique is for the interventionalist to insert a catheter into a chamber of the heart depending on which side of the heart is receiving treatment and looping it around the interior wall of the chamber (Figure 1.3) where it can remain for a long duration of the procedure. This allows the interventionist to quickly localise the chamber as reference while remotely navigating other catheters and intracardiac devices. These catheter loops have been demonstrated to also provide a good visual constraint for manual 2D-3D overlays using multiple X-ray views (EP navigator, Philips Healthcare, Best, Netherlands) [23].

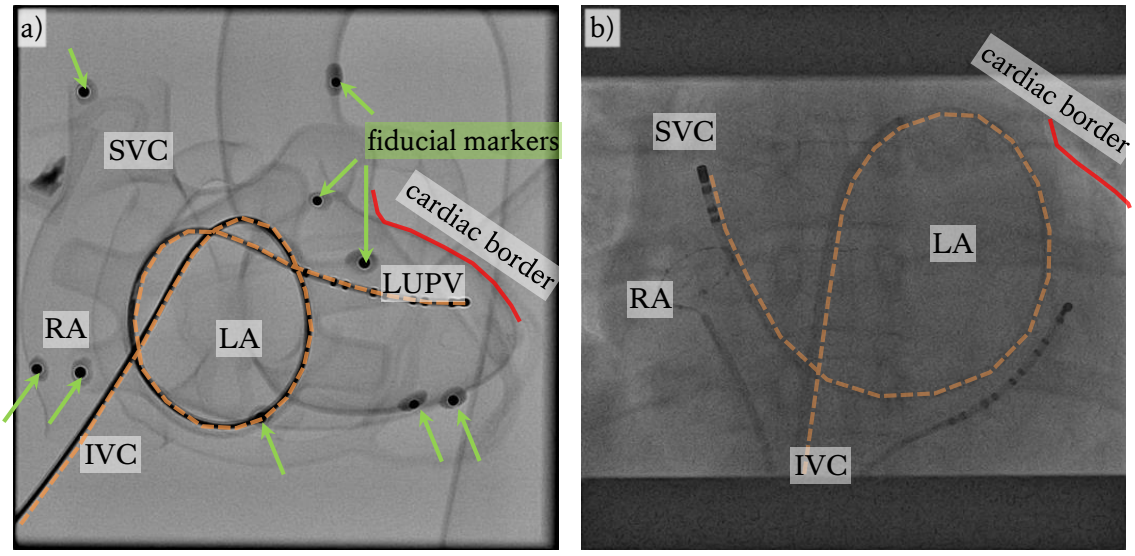


Figure 1.3) Posterior-anterior X-ray image of a a) plastic heart and b) clinical patient's heart with loop (*orange curve, dashed*) formed by inserting a catheter through the inferior vena cava (IVC) passing through the right atrium (RA) and inter-atrial septum and into the left atrium (LA) where it follows the chamber's inner wall with the loop exiting via a) the left upper pulmonary vein (LUPV) and in b) the superior vena cava (SVC). Upper cardiac border (*red curve, solid*) is highlighted and in a) radio-opaque fiducial markers used to obtain a gold-standard registration are identified (*tip of green arrows*).

A second novel and automatic registration algorithm takes advantage of the looping technique to provide 2D-3D image registration of cardiac images. This feature-based algorithm uses a projection strategy which first projects the 3D information onto the 2D image, and then corrects for the pose of the overlaid information in 2D, using a catheter looped within a chamber and the upper border of the cardiac shadow as constraints. Results from applying this algorithm to a heart phantom experiment, an *ex vivo* porcine heart, and a clinical atrial flutter ablation case, are presented in Chapter 7.

## 1.5. Validation of Registration Algorithms

In both 2D-3D registration algorithms presented, the heart is assumed to return to the same shape, size and pose when at similar cardiac and respiratory phases. However, the heart is a highly deformable structure that undergoes significant deformations and motions through the cardiorespiratory cycle, presenting the main cause of error in current rigid registration methods. Such errors can reduce registration accuracy and potentially lead to misregistration.

For biplane registrations, accuracy is measured in terms of a 3D target registration error (3D-TRE) [24] [25], which is a root-mean-squared (RMS) distance measure between corresponding landmarks of the target and taken from co-registered images. For cardiac catheterisations, accuracy requirements vary depending on the location and purpose of the navigating catheter [14]. In RF ablation procedures, the tip of the catheters are usually 4-mm or 8-mm in diameter, with a mean lesion diameter of 8 mm in the papillary muscles, and 6 mm elsewhere [26]. To ensure the lesion covers the intended target, the centre of the catheter tip should be within half the lesion diameter, and therefore, the clinical tolerance for RF ablation procedures is defined as 4 mm for ventricular ablations, and 3 mm for atrial ablations. In procedures where a vessel needs to be catheterised, a suitable clinical tolerance would be defined as half the size of the vessel ostium. PCIs require catheter navigation into either the left or right coronary arteries whose ostia have a mean diameter of 4.5 and 3.9 mm respectively [27], and therefore would require an accuracy of around 2.5 mm. CRTs requires a lead placed inside the coronary sinus, which has a mean ostium diameter between 10 and 12 mm [28], and therefore accuracy between 5 and 6 mm would be suitable for these procedures. Furthermore, accuracy requirements depend on the target site to where the catheter needs to navigate. In PCI and CRT, navigation is needed in the coronaries that mostly wrap around the LV, while in ablation, the optimal site is determined prior to the procedure. While each procedure has different accuracy requirements, 5-mm has been used in this thesis as a general guideline and is consistent with the literature [14] [29] [30]. Therefore, throughout this thesis, the 5-mm target will be used as a general guideline for cardiac catheterisations, and then the more specific accuracy requirements will be discussed when applicable to each case.

Accuracy assessment is dependent on the realism of the data used in the study. In the phantom experiments of Chapter 5 and 7, multi-modal fiducial markers were placed directly on the heart to provide a very accurate registration. This acts as a gold standard to which the 2D-3D algorithms developed in this thesis can be compared for a reliable measure of TRE. Fiducial markers were also placed around an *ex vivo* porcine heart used in Chapter 7. However, in the clinical case studies of Chapter 6 and 7, the clinical issues of placing fiducial markers on the heart make this approach impractical. Therefore, accuracy was scored by expert clinicians by viewing the registration and approximating a value for TRE. These results are compared to manual registration (Chapter 4) performed by clinical experts, which was also visually assessed for accuracy by independent expert observers.

## 1.6. Objectives

In image-guided cardiac catheterisations, there is a clinical requirement to overlay preoperative 3D anatomical data onto the live X-ray, and to fuse intraoperative 3D EAM data to the preoperative 3D anatomical data using X-ray as an intermediate modality. The work in this thesis is directed towards the development algorithmic solutions to these 2D-3D cardiac image registration problems. As a form of translational research, the proposed algorithms must be suitable for deployment in cardiac catheterisation procedures and therefore must provide minimal disruption to the already existent clinical workflow.

Disruption to the clinical workflow can be avoided if the registration algorithm makes use of images and interventional techniques that are already part of the clinical protocol, and therefore no additional imaging or training is required. The algorithm must also register images within a reasonable amount of time to avoid the clinical staff waiting for the overlays. In current clinical practice, manual 2D-3D registration using a commercially available software platform (EP navigator, [23]) is typically performed within five to ten minutes, according to clinical experts, providing a suitable target time-window for the algorithmic approach.

High degrees of accuracy and robustness are two additional criteria that the registration algorithm must have for suitable deployment in the clinical environment, as any inaccurate information provided to the interventionalist may result in a fatal mistake in the procedure. The algorithm should have a degree of accuracy sufficient for the procedure in which it will be applied, and should be able to achieve these accuracies within this tolerance at least 95% of the time, using the capture range definition in [31].

The development and validation of algorithms to perform 2D-3D image registration of cardiac images that:

1) minimally disrupt the clinical workflow,
2) has a sufficient degree of accuracy for the intended procedure, and
3) has a high degree of robustness,

define the objectives of this thesis.

# Chapter 2

## 2. Clinical Background

The introduction of imaging sciences to medicine has resulted in a number of devices that provide surgeons with the ability to view internal images of the body without the need to incise the patient and expose target organs. This development has induced a growing trend in the clinical community to move towards a minimally-invasive approach to surgery [3] [4] [5] [6] [7] [8] [32] by providing the surgeon with non-invasively-obtained live images of the patient allowing the subcutaneous delivery of the treatment using intracardiac devices. In these image-guided surgeries, two or more complementary imaging modalities can provide a better picture to complete the procedure in a relatively safe and successful way, due to the complementary information provided by each image [20] [21] [22] [33]. For cases involving heart disease, imaging of the heart is difficult due to its rapid change in shape and size while pumping blood throughout the body, and its continuous change of position throughout the respiratory cycle. The real-time imaging capability, excellent device visibility, low-cost and widespread availability of X-ray fluoroscopy makes it a suitable modality for these procedures (Figure 1.2). However this projective modality provides no depth information and suffers from poor soft-tissue contrast. In catheter-based cardiac procedures, such as percutaneous coronary intervention (PCI), cardiac resynchronisation therapy (CRT), and ablation for atrial fibrillation (AF), the cardiologist needs to rely on nephrotoxic contrast agent injections in order to accurately position catheters.

Using multi-modality image-guided approaches, there is scope to reduce procedure time, decrease X-ray exposure, and improve success rates. According to clinical experts, presenting the surgeon with the images from multiple modalities combined as a single spatially aligned fused image (Figure 1.1b) can provide confidence and ease of visibility for the clinician, as opposed to viewing separate images and requiring the surgeon to mentally combine them.

The aim of this chapter is to provide in detail the motivation and background of the work behind this thesis. It starts with a general description of the heart and its functioning role as an organ within the body. Pathologies of the heart are then described which may compromise the heart's function, and then non-image-based methods of treatment are discussed. The chapter then goes through the imaging modalities currently available in the clinical setting that can image the

heart's anatomy and function, and describes their unique advantages and disadvantages in terms of cardiac imaging. Finally, the primary objectives of 2D-3D and 3D-3D image registration algorithms to co-register complementary information obtained from two or more imaging modalities are discussed.

## 2.1. Anatomy and Function of the Heart and its Pathologies

The heart is a vital organ and together with a system of connected blood vessels make up the cardiovascular system responsible for blood circulation throughout the body. The heart itself is made up of four chambers, the left atrium (LA) and left ventricle (LV) make up the left side of the heart, and the right atrium (RA) and right ventricle (RV) make up the right side of the heart, with the septum dividing the two sides (Figure 2.1a). The blood pool of the chambers can often be modelled using spheroids [34]. The walls of the chambers are made up of cardiomyocytes that help facilitate the pumping of blood. Cardiomyocytes are conductive muscle cells that contract upon reception of an electrical signal and eventually relax after conducting the signal to neighbouring cells.

A repetitive time-coordinated sequence of contraction and expansion of the four chambers is called the *cardiac cycle* (Figure 2.2b, top). The electric signal is initiated by the heart at the sinoatrial node (SAN) which propagates across the walls of the atria and gathers at the atrioventricular (AV) node (AVN) (Figure 2.1b). The electric propagation across the RA wall results in its contraction which pushes deoxygenated blood, drained from the body via the superior and inferior venae cavae (SVC and IVC), into the RV with the tricuspid valve preventing any backward flow. Meanwhile, the contraction of the LA pushes oxygenated blood, drained from the lungs via the four pulmonary veins (PV), into the LV with backflow prevented by the mitral valve.

From the AVN, the electric signal travels to the apex of the ventricles via the AV bundle of His, a set of conducting fibres embedded within the interventricular septum. The Purkinje fibres buried inside the ventricular myocardium then carry the signal up the ventricular walls and cause them to contract. Contraction of the RV pushes the deoxygenated blood though the pulmonary arteries and into the lungs for re-oxygenation with the pulmonary valve preventing blood backflow. Meanwhile contraction of the LV pushes the oxygenated blood to the rest of the body via the aorta, with the aortic valve preventing backward blood flow. This contraction phase of the cardiac cycle is called ventricular *systole*. After contraction, the heart muscles relax to allow the blood from the body to reflow back into the atria. This period of relaxation is known as *diastole*. Once the atria are filled with blood, the cardiac cycle repeats itself.

While the heart supplies blood to the rest of the body, a small amount of oxygenated blood is needed to supply the muscles of the heart itself. Circulation of blood to the heart is known as *coronary circulation* and is delivered through the coronary vessels (CV) which include the coronary arteries (CA), and the coronary sinus (CS). The CAs branch out from the base of the aorta (Ao) and take a small portion of the oxygenated blood to supply the heart. Most patients have two CAs, a left CA (LCA) and right CA (RCA) serving their respective sides of the heart. Deoxygenated blood is transported back to the heart via cardiac veins, first collecting into the coronary sinus (CS) and then drained into the RA during RA expansion. The ostium of the CS is located on the interarterial septum between the IVC and tricuspid valve.

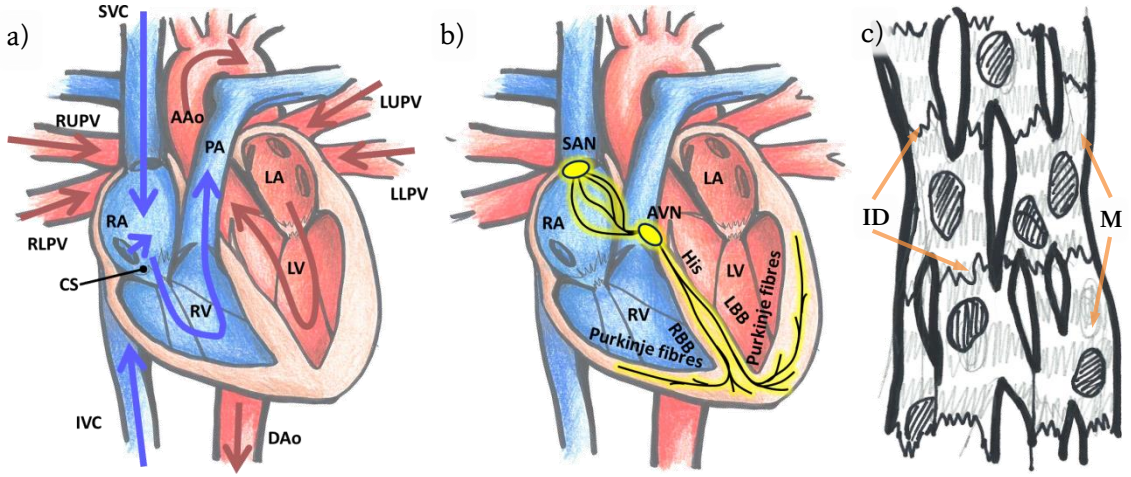


Drawings by Alison Liu, with permission.

Figure 2.1 a) Cross-sectional diagram of the heart showing the circulation of deoxygenated (*blue*) and oxygenated (*red*) blood to and from the rest of the body via the great vessels, and throughout the four chambers. b) Cross-sectional diagram of the heart showing the conduction system starting from the SAN to the Purkinje fibres via the AVN, bundle of His (*His*), and left (*LBB*) and right bundle branches (*RBB*). c) Illustration of cardiomyocytes (*M*) joined together by intercalated disks (*ID*).

### 2.1.1. Electrical Activity of the Heart

Cardiomyocytes of the heart are connected to one another by bridges called intercalated discs (Figure 2.2c). These discs allow the cells to rapidly propagate the electric signal to their neighbouring cells, thereby permitting the time-coordinated contraction of the myocardium as a whole. Electric signals are generated in the membrane of the cell by an exchange of sodium ($Na^+$), potassium ($K^+$), chloride ($Cl^-$) and calcium ($Ca^{2+}$) ions between the intracellular and extracellular space. These ions are regulated by channels that help shape the electrical event known as a cardiac action potential (Figure 2.2b, bottom). Action potentials occur once per heartbeat in a normal, healthy heart, which can be divided into five phases. Phase 0 begins upon reception of an electric stimulation, usually from an adjacent cell, causing contraction and an influx of $Na^+$ into the cell, depolarizing it. Once the cell reaches maximum depolarisation, phase 1 starts with an efflux of $K^+$, causing slight repolarisation. Phase 2 is known as the plateau phase

with the muscle contraction sustained by an electrical balance between influxing $Ca^{2+}$ and effluxing $K^+$. The cell begins to relax at phase 3 with a close in calcium channels but still effluxing $K^+$. Once fully at rest, the cell is in phase 4. In this phase the cell's electrochemical gradients are returned to their original state by ion pumps in the cardiac myocyte membrane. During this period, the myocyte is in a refractory state, and cannot contract again. This phase is therefore associated with the diastolic phase of the heart while the other phases correspond to systole.

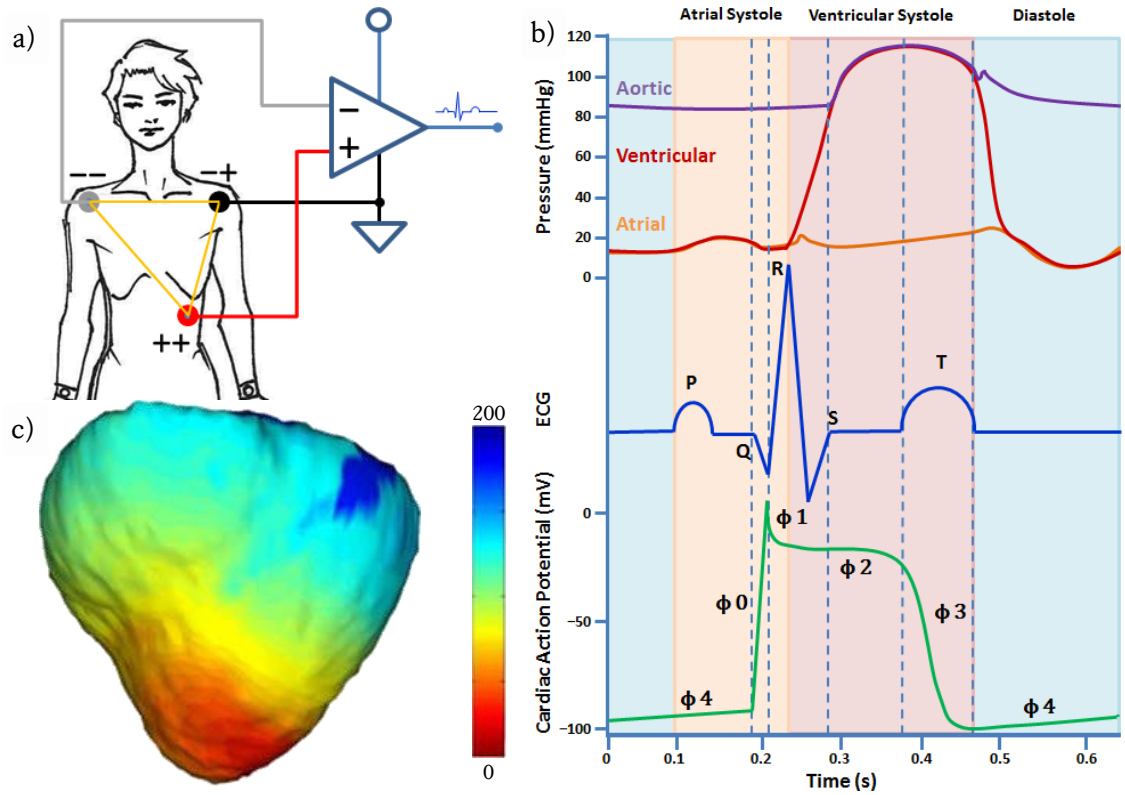


a) Drawing by Alison Liu, with permission.
c) Taken from [35], with permission.

Figure 2.2 a) 3-lead ECG lead placement on the body forming an Einthoven triangle pattern (*yellow*) connected to a circuit diagram whose output produces an ECG trace. b) Aortic (*top, purple*), left ventricular (*top, red*) and left atrial (*top*, orange) pressure over one heartbeat with corresponding ECG trace (*middle, blue*) and action potential of a ventricular cardiomyocytes (*bottom, green*). Regions of the cycle are divided by the action potential phases (ϕ). c) Depolarisation isochronal lines (ms) colour mapped onto the epicardial surface of an *ex vivo* porcine heart.

Most cardiomyocytes require some sort of electrical stimulation before they can enter the cardiac action potential cycle. However, there are a small number of cells which can spontaneously generate a signal and fire a new cardiac action potential without such stimulation, a property known as automaticity. These cardiomyocytes are found in the SAN, and are called pacemaker cells, and the regular timing of their depolarisations is responsible for the regular rhythm of the beating of the heart. A normal depolarisation wave propagating across a porcine model of the heart is shown in Figure 2.2c.

The heart's electrical activity can be monitored with an electrocardiograph (ECG) machine, which measures the overall flux of ions in the heart, across electrically conductive leads placed on the body. The most basic ECG setup involves three leads, one placed on the right arm or shoulder, one placed on the left arm or shoulder, and one placed on the left leg or lower abdomen, forming *Einthoven's triangle* (Figure 2.2a). To obtain the classical ECG trace, the left arm lead acts as ground and the voltage is usually measured along the plane across the right arm and left leg leads, which is parallel to the long axis of the heart. A normal ECG trace over a normal heartbeat is shown in (Figure 2.2b, middle) and a consistent normal heartbeat is known as *normal sinus rhythm*.

### 2.1.2. Pathologies of the Heart

Many complications can develop within the heart that compromises its ability to deliver oxygen and essential nutrients, carried in the blood stream, to the cells of the body. Limited blood circulation to the body is known as *heart failure* and can result in symptoms such as fatigue, shortness of breath, swelling in the legs and chest pains (angina). These are usually caused by morphological defects of the heart (Figure 2.3a), deterioration of its muscles (cardiomyopathy; Figure 2.3b) and valves (valvular heart disease), or conduction abnormalities [36].

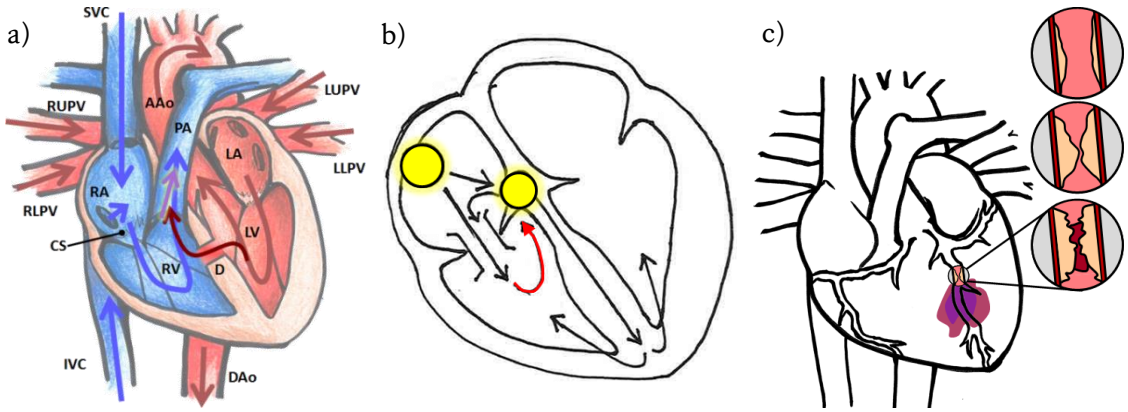


Drawings by Alison Liu, with permission.

Figure 2.3 a) Illustration showing congenital heart defect where a ventricular septal defect (D) allows the oxygenated blood (red) to mix with the deoxygenated blood (blue) into the pulmonary arteries (purples). b) A heart with cardiomyopathy where the left ventricle myocardium is abnormally thick, reducing its ability to contract. c) Coronary heart disease showing the progressive build-up of plaque within the inner wall of the left coronary artery (LCA) with purple region represents ischemic cardiomyocytes with oxygenated blood shortage due to the occlusion.

*Coronary heart disease* (CHD) is another circulation problem that can arise when blood flow is restricted to the heart itself due to the stiffening or narrowing of the CAs (Figure 2.3c). This is a potentially more serious cardiovascular disease because it affects the heart acutely, with symptoms ranging from angina and a general intolerance to exercise, to a potentially fatal myocardial infarction (MI), also known as a heart attack (Figure 2.4a) [36]. In most cases of MI,

permanent damage to the heart occurs, due to the prolonged restricted blood flow to the cardiomyocytes, causing death from oxygen starvation. The ischaemic conditions and release of chemicals from dying cells creates a toxic environment where cardiomyocytes may start contracting without electrical stimulation from neighbouring cells, triggering abnormal conduction pathways and uncoordinated contraction of the ventricles. The contraction of ventricular cardiomyocytes may be so rapid and uncoordinated that little to no blood is pumped by the heart at all, and this is known as *ventricular fibrillation* (VF) (Figure 2.4b, c). VF is potentially fatal, as the ability of the heart to supply blood to the rest of the body is compromised, causing cardiac arrest, and eventually leading to death [37].

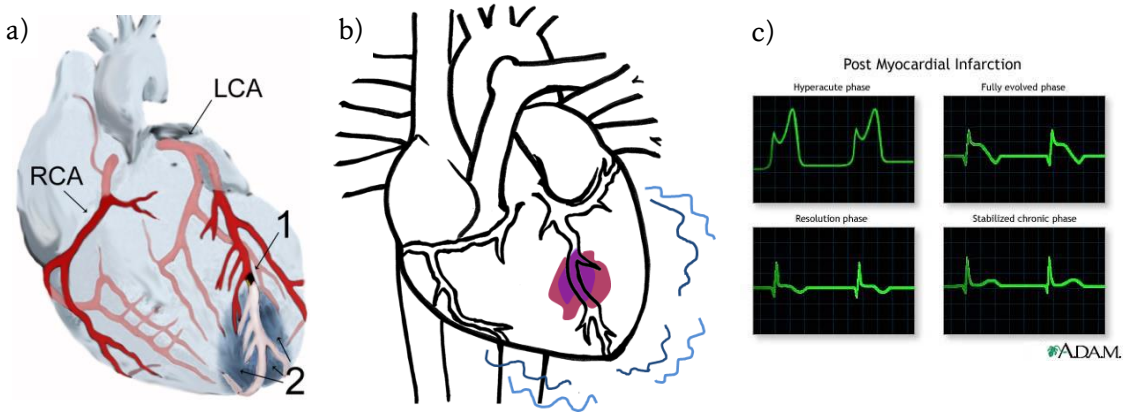


a) Taken from: http://en.wikipedia.org/wiki/Myocardial_infarction
b) Drawing by Alison Liu, with permission.
c) Taken from: http://www.umm.edu/imagepages/18030.htm

Figure 2.4 a) Illustrations showing myocardial infarction leading to scar and b) ventricular fibrillation due to heart attack. Blue squiggly lines represent a quivering heart instead of a pumping one. c) ECG trace of a post myocardial-infarcted heart.

Cardiopulmonary resuscitation (CPR) and defibrillation [38] are methods that can be applied by another person that can help reset conduction pathways of the heart and prevent death if applied quickly after the attack. The electrical reset of the heart is known as *cardioversion*.

However, even if death is successfully prevented, the damage to the heart is permanent, and areas of scarring are left behind, placing the person at risk of heart failure and possibly another heart attack. This is because the scarring can lead to ventricular arrhythmias due to the creation of abnormal conduction pathways in and around the scarred areas. This can affect the co-ordination of ventricular contraction, reducing the efficiency with which blood is pumped out of the heart and causing heart failure. The uncoordinated propagation of electrical signals along these pathways may also trigger another onset of VF and cardiac arrest [37].

Conduction abnormalities are a class of electrophysiological (EP) problems of the heart that affects the time-coordinated beating of the heart as it deviates from normal sinus rhythm.

Arrhythmias can be caused by any of the non-EP diseases described earlier in this section, or by other external factors such as stress, drugs, diabetes, physical trauma and electric shock [37].

Tachycardias are arrhythmias that speed up the beating of a chamber of the heart relative to the rest and can result in uncoordinated heartbeats. Atrial flutter (AFL) is a type of supraventricular tachycardia, tachycardia of the atria, where one or both of the atria beat at a rate between 240 and 360 bpm [39] with the ventricles usually beating at a rate of approximately 150 bmp [36]. This usually lasts for a short period of time and may not cause symptoms, but may deteriorate into atrial fibrillation (AF). AF is a more serious form of supraventricular tachycardia that is characterised by a fast and irregular beating of the atria at rates between 300 and 600 bpm [39]. The rapid beating of the atria causes the AVN (Figure 2.1b) to trigger additional electrical signals to the ventricles, raising the ventricular beating to rates between 120 and 180 bpm [36]. This disrupts the LV function, so instead of producing a strong, single contraction of the chamber to push the blood out, the chaotic electric signal causes the walls of the chamber to quiver. Both AFL and AF may cause symptoms of heart failure, and can place the patient at risk of stroke, since the blood in the ventricles can remain stationary and form clots, which may then travel through the blood stream and block the carotid arteries. It can also place them at risk of VF and cardiac arrest as described earlier in this section [39].

There are three mechanisms by which conduction abnormalities of the heart can degenerate into tachycardia. These are *reentry*, *abnormal automaticity* and *triggered automaticity* [37]. The most common mechanism for tachycardia is reentry which usually occurs around scar or lesions that cause slow conduction of the action potential. During a heartbeat, scar or slow conduction regions can cause a division of the action potential depolarisation wave. The divided waves may either circle around the damaged region, called a reentrant circuit, or join in a disruptive way forming reentrant spirals [40]. Reentrant circuits which have a small diameter, usually contained within one chamber, are called *micro-reentrant* circuits, while those spanning more than one chamber are called *macro-reentrant*. The second mechanism for tachycardia is abnormal automaticity, which occurs when damaged non-pacemaker tissue begins the process of automaticity independent of normal cardiac rhythm and causing a second, *ectopic*, beat. The last mechanism for tachycardia is triggered automaticity. This occurs when heart cells exhibit abnormal action potentials that results in the triggering of a second action potential called an afterpotential which in turn, causes another beat.

### 2.1.3. Open Heart Surgery

Prior to the invention of X-ray fluoroscopy [41] and the Seldinger technique [32] in the 1950's, enabling technologies of cardiac catheterisation, open heart surgery was the only option for treating disease of the heart and great vessels. These are very invasive procedures where the

surgeons cut through the sternum or ribs in order to gain open access to the heart and operate. This allows the surgeon to treat pathologies such as congenital heart disease, valvular disease, and coronary heart disease (CHD) [36].

Coronary artery bypass grafts (CABG) are open heart procedures to treat CHD. In these procedures, occlusions in the coronary arteries are bypassed. This is done by sewing vessels taken from elsewhere in the body onto the coronary artery on either side of the occlusion, restoring circulation to the disease-affected parts of the heart distal to the blockage. During the procedure, the patient is under general anaesthesia and heart and lung functions are managed by a heart–lung machine to reduce heart motion. Once the bypass is complete, the chest is closed and wiring is used to hold together the cut sternum, and the chest tissue is stitched together with sutures. Recovery from open heart surgery can requires up to 12 weeks before patients are able to take up activities such as swimming and low-impact sports [42].

### 2.1.4. Medical Management

Depending on the severity of the heart disease, the clinical team may opt for non-surgical and non-catheterization methods. This can include recommending a healthier diet, moderate exercise and limiting smoking and alcohol. This may also involve taking anti-arrhythmic medication to reduce the probability of tachycardia, or for CHD and morphological defects, medication to lower blood pressure, lower cholesterol or thin the blood [43]. Medication does not usually cure the disease but can lessen its symptoms and minimise risk of fatality.

## 2.2. Cardiac Imaging and Mapping

Since the discovery of X-rays, a type of electromagnetic (EM) radiation, in 1895 [41], it was realised that images of internal organs of the body could be acquired non-invasively. Since then, a number of imaging modalities have become available that make use of the penetrating properties of various types of energy. These energies include X-radiation for X-ray fluoroscopy, 3D Rotational X-ray (3DRx) and X-ray computed tomography (CT); radiofrequency (RF) for magnetic resonance (MR); ultrasound; EM fields for electroanatomical mapping (EAM); visible light for optical mapping and optical coherence tomography (OCT); and gamma radiation for single photon emission computed tomography (SPECT) and positron emission tomography (PET). The unique physics of each form of energy results in very different and complimentary images produced by each modality.

The ability to image the inside of a patient provides the medical team with an invaluable tool for diagnostics and treatment planning. Cardiac imaging is the branch of medical imaging that deals with acquiring images of the heart and its diseases. The heart is a particularly difficult organ to image as it undergoes rapid changes in shape and size throughout the cardiac cycle.

Additionally, the motion of the diaphragm causes the heart to undergo complex motions throughout the respiratory cycle. As a quantitative example, cardiac motion can cause local displacements in the LV of up to 13.1 mm at a speeds of 140 ± 40 mm/s, while respiratory motion can displace the LV as much as 22.5 ± 4.2 mm, with the diaphragm moving at speeds of up to 13.3 ± 5.3 mm/s [44]. This non-rigid and non-stationary nature of the heart can result in blurring or distortion within the cardiac image. Therefore, the ability to image the heart quickly is a beneficial factor when determining the appropriate modality to deploy. Other factors include the cost associated with the scan, the availability of the imaging equipment, whether the radiation is ionising or non-ionising, the image quality produced in terms of visibility, the type of data represented by the image and the image dimensionality. Most of these factors are self-explanatory, except for the latter two which will be described in the following subsections.

### 2.2.1. Type of Cardiac Image Data

Cardiac imaging can produce images of two types: either anatomical or functional. Anatomical images reveal insight into the geometry and composition of the heart, with different imaging intensities usually corresponding to different types of cells or materials. For example, in a MR image of the torso, the blood pools that fill up the chambers of the heart can appear bright grey, while the heart muscle appears dark grey, the spine and ribcage appear light grey and the air inside the chest cavity appears black (Figure 2.5a). The geometry of the heart is accurately preserved in the image, except where there is blurring or distortion.

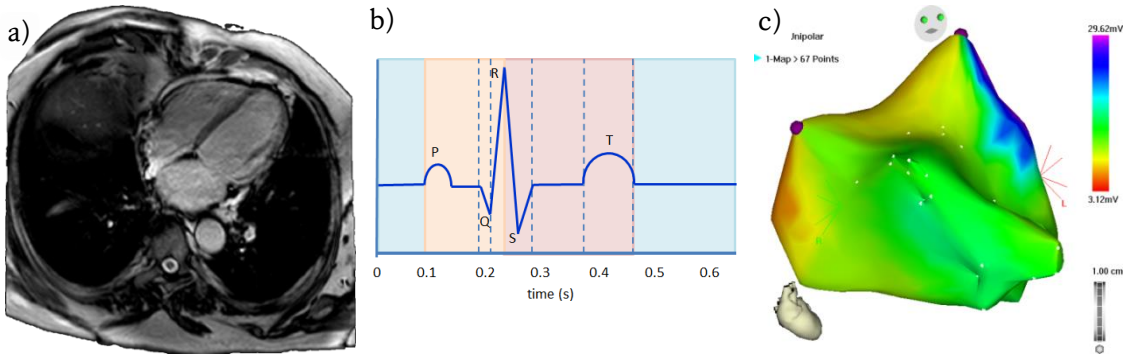


Figure 2.5 a) An anatomical image of the heart, long-axis view, acquired using an MR scanner. b) ECG trace over one heart cycle. This is an example where functional information of the heart is not mapped to any specific geometry. c) Unipolar voltage information mapped onto a geometric shell of the right ventricle provided by an electroanatomical mapping (EAM) system (Carto™ XP).

Functional images on the other hand reveal physiological activities of the heart such as electrical conduction, blood flow, chamber pressure and scarring. It is sometimes possible to infer how the functional image spatially relates to the underlying anatomy and this may be enough for the medical team to make a diagnosis, as in an ECG (Figure 2.5b). In most other scenarios however, additional structural information of the underlying anatomy is obtained, providing a geometry

on which the functional information can be mapped. The combined function and geometry information is known as a mapping (Figure 2.5c).

### 2.2.2. Imaging Dimensionality

The dimensionality refers to the components of space and time preserved in the image, and how it discards the others. There are three mutually orthogonal spatial coordinates and one time coordinate in the real world. In cardiac imaging, the three coordinate axes are commonly chosen to align with the scanning device (Figure 2.6a) or with the heart (Figure 2.6b).

Imaging devices that capture and preserve all three spatial dimensions of the imaging target are called *tomographs* and produce volumetric 3D images known as *tomograms* or 2D *tomographic slices*. Examples of tomographic modalities are MR, CT, ultrasound, PET, SPECT and OCT. On the other hand, projective imaging modalities capture only a projection of the target, discarding depth information in the process. Two examples of such modalities are X-ray imaging and photography, both of which produce projective 2D images. Both these modalities follow a pin-hole projection model (Figure 1.1; §4.2.1).

Due to the loss of depth information in projective images, the dimensionality of a 2D image produced by a projective modality is not the same as the dimensionality of a 2D tomographic slice. Therefore, in this thesis, the term 3D in the context of imaging will refer explicitly to images produced by a tomograph while the term 2D will be reserved to mean projective 2D, unless otherwise stated.

A 2D image can be obtained by performing a projection of a tomogram. Conversely, a number of 2D images can produce a tomogram with a tomographic reconstruction algorithm provided that the projection geometry and pose of the camera is known at each acquisition of the 2D images. When only two images are used, a 3D texture-mapped surface can be created, called a stereogram [35].

In terms of temporal coordinates there is only one, as consistent with the real world. However, in cardiac imaging, the imaging equipment can make use of the assumption that the heart returns to the same shape and pose when at the same cardiac and respiratory phase, and therefore should have the same image,

$$\begin{aligned} I(u,v,w;\theta,\phi) &= I(u,v,w;\theta+\Delta\theta,\phi) \\ I(u,v,w;\theta,\phi) &= I(u,v,w;\theta,\phi+\Delta\phi) \end{aligned} \quad , \qquad (2.1)$$

where $(u,v,w)$ are the three orthogonal spatial coordinates of the image. This allows time to be divided into two independent temporal coordinates $(\theta,\phi)$ corresponding to the cardiac and respiratory phases respectively (Figure 2.6c). $\Delta\theta$ is the period of the cardiac cycle and $\Delta\phi$ is the period of the respiratory cycle.

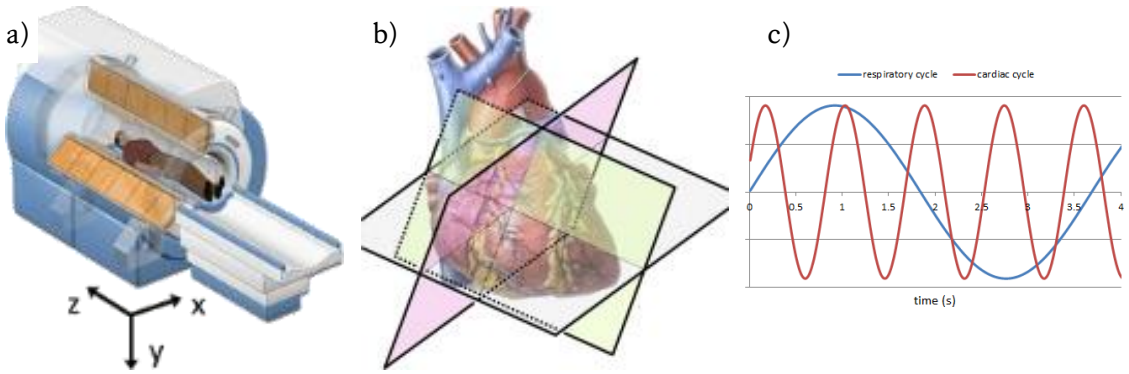


a) Taken from: http://www.slicer.org/slicerWiki/index.php/Coordinate_systems
b) Taken from: http://www.sciencedirect.com/science/article/pii/S1064968907000918

Figure 2.6 a) Spatial coordinate axes aligned with the scanner, b) spatial coordinate axes aligned with the long and short axes of the heart, c) time coordinate broken into two independent cardiac and respiratory time coordinates which are periodic.

A still cardiac image captures the heart at a particular moment, discarding the time components. Fast imaging modalities, such as X-ray fluoroscopy and ultrasound, have sufficient temporal resolution to acquire a still image with minimal blurring or distortion due to cardiac motion. Slower modalities, sometimes due to the acquisition of tomograms, may need minutes to acquire the image. In order to avoid capturing motion from hundreds of cardiac and respiratory cycles during the scan time, the scanner can choose to acquire images during a particular cardiac and respiratory phase of the cycle by using assumption (2.1). This prolongs the scan even more, but ensures that motion blurring and distortion is minimised. This technique is known as *cardiorespiratory gating*.

Instead of waiting for the respiratory cycle to return to the same phase in order to image, the patients could be asked to hold their breath during the acquisition. These scans are known as *breath-held* scans, while *free-breathing* scans allow the patient to breath during the scan.

Videos of the heart acquired during breath-holding record only the motion of the heart during the cardiac cycle are called *cine* images.

### 2.2.3. Imaging Modalities

While there is a multitude of imaging modalities capable of imaging the heart, anatomically and functionally, not all of them are routinely used in the cardiac catheterisation procedures which defines the scope of this thesis. In current clinical practice, the modalities routinely used in catheterisations include X-ray fluoroscopy and EAM intraoperatively, and CT and MR preoperatively. In this section, these four modalities will be described in greater detail, particularly for the advantages they offer to the catheterisations, while the remaining cardiac imaging modalities will be mentioned only briefly.

### 2.2.3.1. X-Ray Imaging

The first non-invasive image taken of the body was performed by Röntgen at the end of the 19th century using X-rays [41]. This form of radiation can be generated by passing electricity through a modified vacuum tube known as an X-ray tube [45] (Figure 2.7).

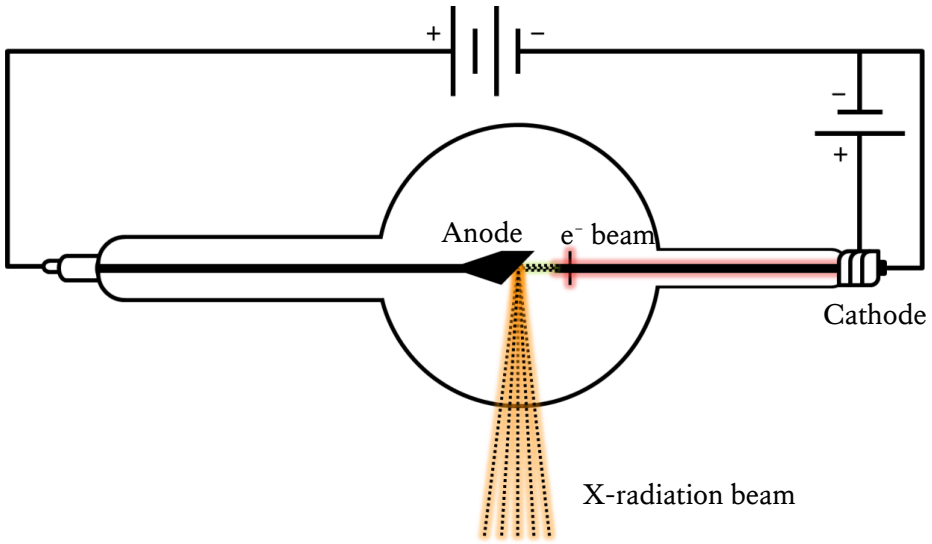


Figure 2.7) A cartoon of a Coolidge X-ray tube invented in the early 20th century [46], with electronic schematic representation of external components. When a high voltage is applied across the vacuum tube, thermionic electrons are accelerated from the cathode towards the anode. As the electrons bombard the anode, X-rays are produced.

An X-ray tube is a glass tube fitted with a cathode on one end containing a metal filament and an anode usually made of Tungsten on the other. The air inside the glass is pumped out to protect the filament from oxidation, creating a vacuum within the tube. A high voltage is applied across the filament and between the electrodes (Figure 2.7). The voltage across the filament causes it to heat up and produce thermionic emissions of electrons. These electrons are accelerated towards the anode due to the voltage potential across the electrodes. The electron bombardment of the anode produces X-radiation via X-ray fluorescence and deceleration. *Fluorescence* occurs when a bombarding electron collides with an inner orbital electron of an anode atom and knocks it out of orbit. This compels an outer orbital electron to fill in the electron hole, giving off excess energy in the form of an X-ray photon. Bombarding electrons that do not cause fluorescence get attracted to the positively charged nuclei of the anode atoms. This deflects and decelerates the electrons resulting in their loss of kinetic energy in the form of an X-ray photon called *Bremsstrahlung*. The X-rays due to fluorescence, together with the Bremsstrahlung radiation make up the X-ray beam [45]. The maximum energy of the X-ray beam is directly proportional to the voltage across the electrodes.

In an X-ray imaging system, an X-ray tube is used to generate a radiation beam that is directed towards a target. The beam is attenuated by the target before it reaches a detector positioned

behind it (Figure 1.1), forming a projective image on the detector, also referred to as a shadowgram.

The amount of attenuation is dependent on a number of factors, such as the beam energy and the material composition of the target, with the largest factor being the density of the material. When imaging a patient, denser materials of the body, such as bone, attenuate the beam more than less dense material such as soft tissue. This forms an image on the detector that represents a patient's anatomy. A range of detectors can be used for this purpose. In traditional radiography, photographic film is used for this purpose to capture still images.

#### 2.2.3.1.1. C-arm Fluoroscopy

In modern fluoroscopy, the detector is an X-ray image intensifier, which converts X-ray energy into visible light and captures the light image with a digital video camera at real-time frame rates, up to 30 frames per second (fps). This has the advantage of capturing X-ray video sequences that can be displayed on computer monitors and/or electronically stored for offline reviewing. The tube and detector are usually housed in a 'C'-shaped gantry (C-arm) with a patient table placed between the ends of the 'C' (Figure 2.8).

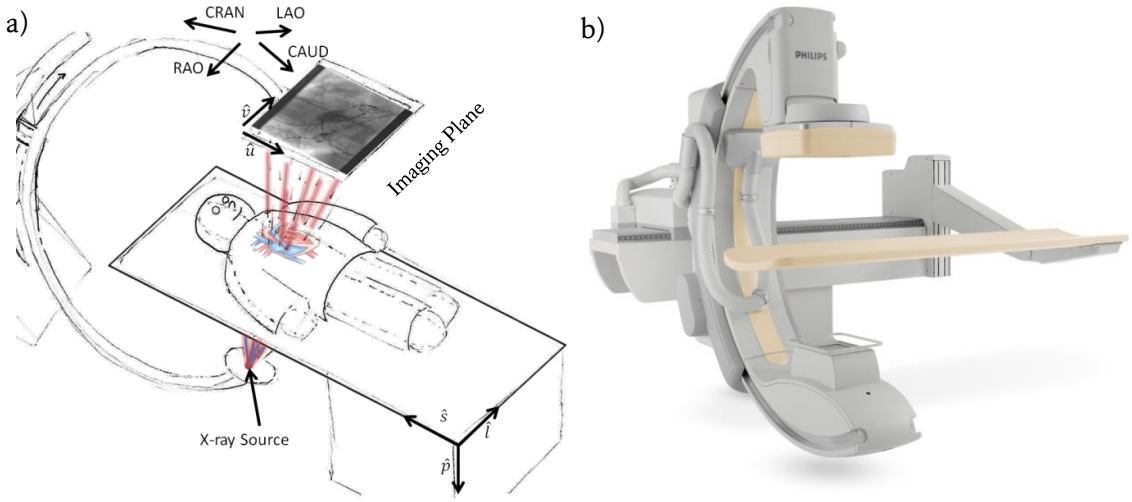


b) Image taken from: http://www.newscenter.philips.com/main/standard/about/news/press/20081121_xray_business_backgrounder.wpd

Figure 2.8 a) A cartoon of C-arm X-ray fluoroscopy unit with patient lying on the bed. The C-arm can rotate towards the left (LAO) and right (RAO), or towards the head (CRAN) and foot (CAUD). Vectors $\hat{u}$ and $\hat{v}$ define the image coordinate system and vectors $\hat{l}$ (left), $\hat{p}$ (posterior) and $\hat{s}$ (superior) define a patient-oriented coordinate system. b) Photograph on a C-arm fluoroscopy unit with patient bed.

The systems allow rotational movement of the C-arm so that different views of the patient can be acquired without having to move either the patient or the table. The ability to take videos of the beating heart is essential for real-time cardiac imaging, and makes fluoroscopy suitable for guiding cardiac catheterisation procedures.

Typical X-ray images acquired during these procedures are usually matrices of $512^2$ pixels with an isotropic resolution of 0.24 mm at the isocentre, covering a field of 12 cm field of view (Figure 2.9a). These images are usually acquired at rates of 7.5 to 15 fps for the duration of one or more heartbeats, or of a complete contrast agent injection.

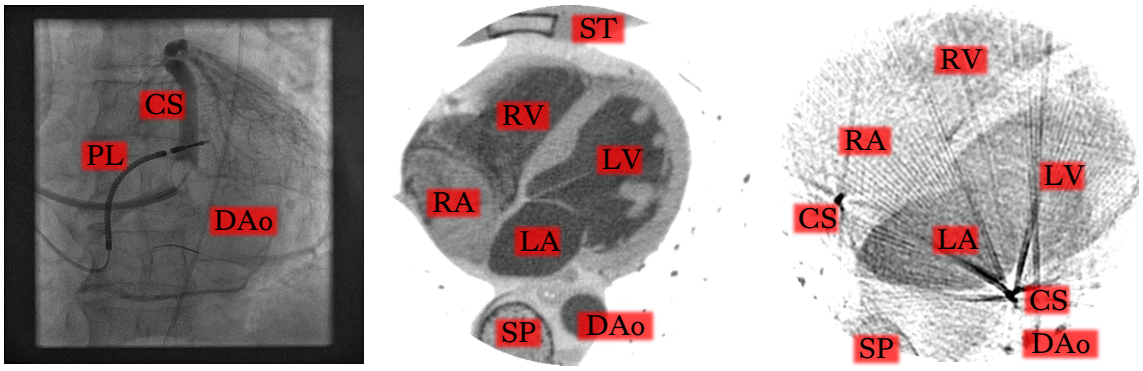


Figure 2.9 a) A contrast enhanced coronary angiogram taken with a flat panel X-ray fluoroscope in PA view. Catheters are inserted into the DAo and CS and a pacing lead (PL) is inserted into the RV. b) Four-chamber axial cross sectional tomographic slice of a heart from a CT scan and c) from a 3DRx tomographic reconstruction. A catheter inserted into the CS of the patient during the 3DRx scan produces large streaking artefacts. The cardiac chambers, DAo, spine (SP) and sternum (ST) locations are labelled.

#### 2.2.3.1.2. X-ray Computed Tomography and 3D Rotational X-ray

X-ray Computed Tomography (CT) and 3D Rotational X-ray (3DRx) are imaging modalities that produce a volumetric image of the patient's anatomy by taking many X-ray projections of the patient from different views around a single axis of rotation, and applying a tomographic reconstruction.

CT is a standalone imaging modality with a dedicated scanner that houses a motorised X-ray gantry. The gantry is constrained to rotate axially around a patient lying on a bed. The special housing allows the motor to rotate at high speeds which, combined with quick frame acquisitions, allows a complete 3D scan with good spatial resolution to be acquired within a matter of seconds. Acquisition of a CT image is a relatively straight forward procedure for a radiographer since most of the motor rotation, projection acquisition, and tomographic reconstruction are performed by the hardware, leaving very few options available. This provides the advantage of being very easy to acquire images compared to tomographs such as MR, which will be discussed in the next section.

3DRx generate 3D images in a similar way to CT, but uses the rotating C-arm of an X-ray fluoroscope. The 3D image quality of 3DRx is not as good as those generated by CT, but has the advantage of being able to be performed intraoperatively.

Spatial resolution of CT scans tend to be lower than 3DRx, but have a higher contrast resolution. A typical CT scan of a patient's heart would be a $512^2 \times 256$ image matrix with a voxel size of $0.6^2 \times 1.0$ mm$^3$, while a typical 3DRx can would be a $256^3$ image matrix with a voxel size of $0.43^3$ mm$^3$. A side-by-side comparison of CT and 3DRx of a heart is shown in Figure 2.9b, c.

#### 2.2.3.2. Magnetic Resonance Imaging

MR is an imaging modality based on the principles of nuclear magnetic resonance [45]. The nuclei of atoms that carry an odd number of nucleons have a magnetic dipole moment which preferentially aligns to an external magnetic field, corresponding to the lowest energy state. The dipole of the particles can be forced to align in a direction opposite to the magnetic field, and corresponding to a higher energy state, by adding quanta of RF energy whose frequency matches the Larmor frequency of the particles. The Larmor frequency is dependent on which atom is being considered, and the strength of the external magnetic field. In MR scanners, the RF energy matches the Larmor frequency of hydrogen, since it is the dominant constituent atom of the human body.

The RF energy is usually applied as a pulse and at the end of the pulse the high-energy state atoms will decay back to the lower-energy states. When this happens, quanta of RF energy of the Larmor frequency are released, which can be recorded by coils positioned close to the atoms. The decay rate is dependent upon a number of factors such as temperature, strength of the field and, most importantly, structural characteristics of the tissue containing the Hydrogen. For example, atoms in the blood are relatively freer to move around than in fatty tissue, and consequently demagnetisation will occur much faster in blood than in fat. In medicine, the demagnetisation rates of each tissue type are characterised by two numbers, $T_1$ and $T_2$, which quantify the longitudinal and transverse demagnetisation rates respectively. By reading the RF output of the demagnetising tissue, an anatomical image can be produced with different tissue types having different signal intensities. The tissues' signal intensities can be manipulated depending on the time interval in which the RF pulses are applied, $T_R$, and the time difference between the application of the pulse and the time the magnetisation is measured, $T_E$. Consequently, there are a multitude of images that can be produced and the operator needs to know which pulse sequence will generate the image that yields the best signal- and contrast-to-noise ratios for the regions of interest. This makes MR a highly versatile modality, although a set of parameters inappropriately chosen for the patient may fail to produce a good quality image, translating to longer training requirements to operate.

In some cases during diagnosis and treatment planning of catheterisations, MR may not be a suitable modality, for example when devices such as a pacemaker or an implantable cardioverter-defibrillator have been implanted into the patient's heart. These devices may

contain ferrous metal components and might be affected by the magnetic field, or cause heating in the pacing wires. Even with MR-compatible devices, other metals may cause large artefacts in the images. In these cases, CT provides a suitable alternative.

The resolution of an MR image is dependent on the pulse sequence applied. When imaging the heart, a typical 3D, cardio-respiratory gated scan takes approximately 10 minutes to acquire a $400^2 \times 160$ image matrix with an isotropic voxel resolution of 0.75 mm (Figure 2.5a), while a cine sequence can capture a $256^2$ matrix with a typical frame rate of 7.5 fps.

#### 2.2.3.2.1. Imaging of Function using MRI

Aside from anatomical imaging, MR can be used to acquire functional images of the heart. Two examples of this usage are late-gadolinium enhanced cardiac MR (LGE-CMR) [47] for detection of cardiac scars and tagged MR to measure mechanical heart function [48]. Both techniques are relatively simple but are useful for detecting diseases of the heart.

LGE-CMR involves the injection of gadolinium contrast agent into the heart which dissipates from the blood pool and permeates into the myocardium. After around 20 min, the gadolinium will have dissipated from healthy myocardium, but remains in regions where there is scarring of the heart. A 3D whole heart scan is acquired at this time providing a 3D anatomical image of the heart with the scar in the myocardium highlighted.

Tagged MRI is another method of measuring functional cardiac information using MR using anatomical scans. This is achieved by applying a plane sine-wave magnetisation across the heart (myocardial tag) and acquiring single-slice cine images, resulting in stripes across the heart of dark and light bands. As the heart beats, the stripes are distorted and the amount of distortion is used to calculate the mechanical strain in the heart. From the measurement of strain, diseases such as heart failure can be detected, for example in regions where the strain is low compared to a normal heart.

### *2.2.3.3. Ultrasonography*

Ultrasonography, also known as echo, is an imaging modality capable of 3D video image acquisition. This modality is based on the generation and reception of high frequency ultrasound waves, typically using piezoelectric crystals. In ultrasound, electricity is applied to the crystal housed within a probe, which emits an ultrasonic wave towards an imaging target and capture an image based on the *acoustic impedance* of the target. The impedance is a measure of changes in mass density and tissue compressibility in the target, usually occurring between layers of different tissue types, which cause reflections of the ultrasound waves. Reflected waves are recorded at specific time intervals by the same crystal. By assuming that the speed of sound is constant as it travels from the transducer to the target and back, each recorded waves records

an element in the image of the target, with later signals corresponding to deeper depths within the target [45]. By rotating the transducer along an arc, tomographic slices of the target can be acquired and combined to produce a 3D image of the target.

However, a disadvantage with ultrasound is its low signal-to-noise ratio and restricted field of view compared to other modalities such as CT and MR. Another disadvantage to ultrasound when imaging the human body is that sound travels through different tissue types at different speeds based on their acoustic impedance properties, which results in distortions in the image, especially in the regions furthest away from the probe where the ultrasound would have travelled through a number of different tissue layers. A third issue is that sound waves travel poorly through air and other low mass-density media. In the case of cardiac imaging, this is an issue when the patient is lying supine and the probe is placed on the chest as there is air within the part of the lungs that rests between the ribs and the heart. This is usually avoided by having the patients lay on their left side so gravity can pull the heart closer to the chest and minimising the layer of air. However, in moving patients to their side, the relationship between the heart and the rest of the body changes compared to when lying in a supine position as in most other imaging modalities – this may be an issue for multimodality image registration.

#### *2.2.3.4. Electrical-Activity Acquisition*

The ability to view the electrical activity of the heart enables cardiac electrophysiologists to infer conduction abnormalities of the heart and recommend treatment. ECGs can provide integrated electrical information of the heart over time. However, this signal has no spatial correspondence to regions of the heart, other than an approximate axis of measurement based on lead placement (Figure 2.1b). The ability to localise electrical information onto the surface of the heart is known as *mapping*, forming a type of image called a *map*, and can help provide more insight into the nature of pathologies than ECG alone. Three examples of this functional modality include body surface potential (BSP) mapping (BSPM), electroanatomical mapping (EAM), and optical fluorescence mapping. To improve spatial resolution, the functional data acquired is usually projected onto a geometric surface of the heart.

##### 2.2.3.4.1. Body Surface Potential Mapping (BSPM)

This mapping modality requires the patient to wear a BSPM jacket consisting of a high number, usually between 64 and 256, of ECG leads that surround the body [49] [50]. The lead electrodes are fashioned on the jacket so that when worn, half the leads lie against the patients back, and half the leads lie on the patient's chest (Figure 2.10a). Leads on the front and back are fixed in a grid formation so that the relative positioning of leads to one another can be approximated. The electrical activity simultaneously acquired from all the ECG leads can be localised in space by interpolating measurements across the electrodes [51], creating a BSP map (Figure 2.10b).

Due to the inexact localisation of the electrodes, BSP maps typically have poor spatial resolution. Spatial resolution can be improved by imaging the patient under a 3D imaging modality, typically CT, since most BSPM jackets are not MR compatible. The CT can provide an accurate location of the electrodes, allowing the BSP map to be more accurately reconstructed (Figure 2.10c). Furthermore, structural information of the heart can be segmented from the CT image, providing an accurate geometry of the heart onto which the BSP map can be projected (Figure 2.10d). The augmentation of BSPM onto 3D geometry in this way is known as electrocardiographic imaging (ECGI). The spatial resolution of the 3D geometry is typically 3 mm, with the electrodes sampled at 1 ms intervals [52].

While the high temporal resolution of BSPM and ECGI are suitable for monitoring electrical activity spatially distributed over the heart in real-time, there are limits when mapping arrhythmias in the atria for treatment of AF and AFL. This is due low signal-to-noise ratio of the atrial BSP signal due to the relatively small mass of the atria compared to the ventricles due to its smaller size and thinner walls. Furthermore, the inverse problem for the atria is not well understood compared to the ventricles.

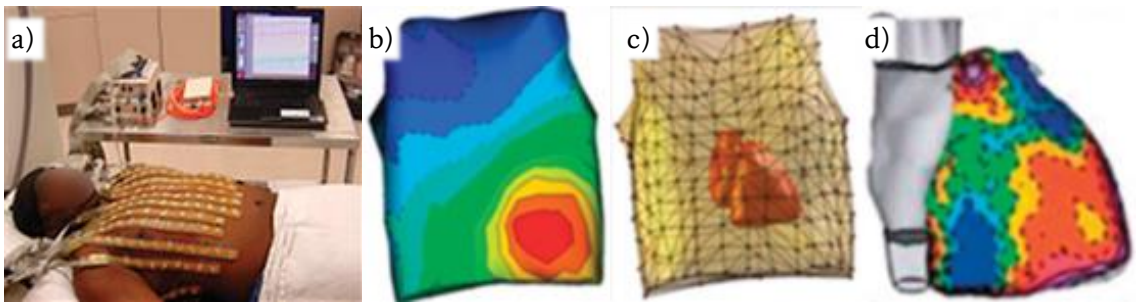

Images taken from [52].

Figure 2.10 a) Photo of a BSPM electrode strips covering a patient's torso. b) BSP map showing electrical activity along the surface of the torso in AP view. c) Surface rendering of a CT scan of the patient's heart (*red*) surrounded by a mesh representing the BSPM jacket. d) Electrical activity on the epicardial surface of the heart computed by inverse mapping the BSP data.

#### 2.2.3.4.2. Electroanatomical Mapping (EAM)

Electroanatomical (EA) mapping (EAM) involves the insertion of catheters into the heart, performed under X-ray fluoroscopy guidance and usually part of a cardiac electrophysiological study prior to, or after, catheterisation but while the patient is still on the operating table (§2.3). EnSite™ and Carto™ XP EP Navigation systems are commonly used in the clinical setting to generate EA maps [53].

EnSite™ system can be used to collect single electrograms from a roving catheter, or it can be used with an EnSite Array™ (Figure 2.11a), usually inserted into the LV which collects unipolar electrical data of single heartbeats at 64 independent electrodes fashioned in an 8×8 grid formation. The balloon is also capable of generating an electromagnetic field used to triangulate

the position of the tip of a separate roving catheter also inserted into the ventricle. After sweeping the roving catheter's tip along the endocardial wall of the ventricle while tracking the tip's location, a geometric surface of the endocardium is generated by taking the convex hull of all points collected. The hull is resampled at a regularly spaced unstructured grid of 2048 points. Finally, the unipolar electrical information collected from the multi-electrode balloon catheter is converted to a bipolar voltage and projected onto the tessellated surface. The convex hull nature of the collected geometry reflects the geometry of the heart at end-diastole, where the heart is at maximum expansion.

The Carto XP system also collects electroanatomical data of the heart using a roving catheter inserted into the LV chamber, but uses a location pad placed under the X-ray patient table (Figure 2.11b) that produces a magnetic field (Figure 2.11c). The magnetic field is used to triangulate the location of the catheter tip. Once the tip is positioned against the endocardial wall, bipolar voltage signals for an entire heartbeat are recorded along with the catheter tip location. The catheter is then repositioned at another spot on the wall and the recording is repeated until the entire interior wall has been sampled with a sufficient density, typically between 200 and 300 individual measurements. The endocardial surface is then generated from the convex hull of the points with points not on the hull discarded. This again reflects the geometry of the heart at end-diastole.


a) Photo taken from www.sjmprofessional.com.
b, c) Photos taken from www.biosensewebster.com.

Figure 2.11 a) EnSite Array™ Catheter collects electrical signals of an entire heartbeat at 64 electrode points. The balloon catheter can be inserted into any chamber of the heart. b) Typical setup of a catheterisation laboratory equipped with a Carto™ System. The location pad is placed under the patient table at location 3. Position of catheters and electrical data captured by the Carto™ system is at location 4. c) The Carto™ location pad In relation to the heart within the body. The heart should be placed within the magnetic field (*blue, translucent column*) so that catheters placed in this region can be geometrically tracked.

Since geometry is collected with the voltage data, no separate anatomical imaging is needed. However, between catheter tip localisations, there is usually a large amount of motion of the heart, resulting in geometric distortions. With EnSite™, the roving catheter location is measured relative to the balloon catheter and therefore the motion is predominantly due to the beating

heart alone, while with the Carto™ system, localisation is measured relative to the location pad placed outside the body, introducing both cardiac and respiratory motion distortions.

#### 2.2.3.4.3. Optical Fluorescence Imaging

Optical fluorescence imaging is an *ex vivo* procedure and therefore has limited application in clinical procedures. However, this method can provide rich and accurate electrical data of the heart useful for biophysical modelling purposes [54] [55]. The technique involves the perfusion of an animal heart removed from its body using the Langendorff technique [56]. Electromechanical uncoupler is added to the blood supply, removing the contractile properties of the cardiomyocytes and therefore preventing cardiac motion, while still allowing the action potentials to propagate. Fluorescent dye is also added to the blood supply that produces luminescence when electrically activated by cellular action potentials. High speed cameras, filtered to only capture the luminescence, are positioned around the heart and simultaneously record the cellular action potentials across the epicardium over time. Using the same cameras, without the filters, photographic images of the heart can be taken. The photographic images can be used to perform stereoscopic surface reconstruction of the epicardium [54], providing a geometry on which to project the functional information.

### 2.2.3.5. Imaging with Gamma Rays

Gamma rays (γ) are another form of penetrating EM radiation similar to X-ray but with higher energy levels, and can be detected by a *gamma camera*. These cameras consist of a plate made of scintillating crystal which absorbs the gamma radiation and re-emits a visible light by a luminescence process called scintillation. The light emitted from the plate is a projective image of the gamma creating activity, and can be captured by photographic devices such as a digital video camera [45].

Unlike X-rays generated by electrons (§2.2.3.1), gamma rays require heavier particles, usually involving the decay processes of the nucleus of an atom. Gamma photons can be created as a direct product of the decay as with single photon emission computed tomography (SPECT), or the reaction can produce antimatter which annihilates with normal matter to form gamma ray photons as with positron emission tomography (PET).

### 2.2.3.6. Single-Photon Emission Computed Tomography (SPECT)

SPECT is a functional cardiac imaging modality that uses gamma radiation to monitor myocardial perfusion. This involves the injection of a radiotracer into the heart. In cardiac imaging technetium-99m is used for this purpose; a nuclear isomer with a nucleon in an excited state and a half-life of 6 hours. As the nucleon returns to the unexcited ground state, a gamma photon is released:

$$^{99m}\mathrm{Tc} \rightarrow {}^{99}\mathrm{Tc} + \gamma \quad . \quad (2.2)$$

The gamma photons generated are detected by a rotating gamma camera which captures projection images as it rotates around the body. The projections are used to create a 3D image by tomographic reconstruction. During the scan, the radiotracers move with the blood flow, and so the 3D image presents the amount of perfusion within the myocardium. This is useful in diagnostic imaging to detect coronary heart disease and heart failure.

#### 2.2.3.7. Positron Emission Tomography (PET)

This functional imaging technique involves the production of a positron ($e^+$) which inevitably finds an electron ($e^-$) to annihilate with, producing a pair of gamma photons travelling at the speed of light in directions opposite to one another. Instead of a rotating gantry as in SPECT, a PET scanner consists of a ring of gamma cameras that are placed around the patient. Since gamma photons are generated in pairs travelling in opposite directions, the location of the positron-electron annihilation event can be approximated. In cardiac imaging, positrons are generated by the decay of fluorine-18 (18-F) into oxygen (18-O), a positron and an electron-neutrino ($\nu_e$),

$$^{18}\mathrm{F} \rightarrow {}^{18}\mathrm{O} + e^+ + \nu_e \qquad e^+ + e^- \rightarrow \gamma + \gamma \quad . \quad (2.3)$$

In order to spatially distribute the 18-F into regions of interest, the atoms are carried as fluorodeoxyglucose (FDG) which is taken up by the heart during metabolic activities. This is known as FDG-PET, and is useful for detecting and localizing scar and coronary heart disease.

## 2.3. Cardiac Catheterisation Procedures

In open heart surgery (§2.1.3), a large vertical incision is made across the chest to gain direct access to the heart where pathologies may be treated. However, the incision, long recovery time and permanent stitches can be very traumatic to the patient. Cardiac catheterisation procedures are a minimally invasive alternative treatment for heart disease. These involve only a small incision, usually in the groin, and a catheter can be inserted through the femoral or radial artery, being remotely guided to the heart, where diagnostics and interventional treatment may be performed [6] [8].

Access to the heart in this way was first performed in 1929 by Werner Forßmann [57], on himself, under X-ray fluoroscopy guidance (§2.2.3.1). The method was later improved by the Seldinger technique in 1953 [32] [58], which first involves the insertion of a thin guidewire through the artery to get access to the heart followed by a plastic sheath passed over the wire. The guidewire is then removed, leaving the empty plastic sheath to control bleeding and act as a passage duct for the easy insertion of interventional catheters and devices. The improved technique is also performed under fluoroscopy. This modality is suitable for this purpose, due to

its real-time imaging capabilities and excellent device visibility. These advantages, combined with the low cost and widespread availability of fluoroscopes in most hospitals, make it the routine imaging modality of choice in current clinical settings. Prior to undergoing these kinds of operations, patients with heart disease, or suspected of having it, usually underwent a diagnostic CT or MR scan of their heart to confirm the presence of the disease and to plan treatment [59].

There are many types of cardiac catheterisation procedures that aim to treat the various pathologies of the heart. The most common of these procedures are percutaneous coronary intervention (PCI) to treat coronary heart disease [4] [5], and cardiac radiofrequency ablation (RFA) to treat conduction abnormalities such as atrial fibrillation (AF) and flutter (AFL) [8].

A procedure closely related to catheterisations is cardiac resynchronisation therapy (CRT) to treat heart failure [11]. In these procedures, a pacemaker is implanted into the patient containing leads inserted into the heart in the same way as catheters would be. In this thesis, for the purpose of simplicity the definition of a catheter will be used to cover the broader sense of any long, thin device inserted through the blood vessels like a catheter, including guidewires, sheaths and electrical leads used in CRT, unless explicitly stated. With this more general definition, the term cardiac catheterisations cover procedures such as CRT.

Cardiac catheterisations are usually performed in conjunction to an electrophysiological (EP) study, where several catheters are inserted into the heart under X-ray guidance and remain there throughout the procedure to collect essential EP information, while another catheter with an electrode tip is used to stimulate regions of the heart. Disturbances to the EP information caused by stimulation are interpreted by an electrophysiologist who can infer the type of abnormality. As part of the EP study, electroanatomical mapping information using EnSite™ or Carto™ systems can also be acquired (§2.2.3.4.2) to provide more insight into complex arrhythmias [53].

A summary of the clinical workflow for the diagnosis and treatment of heart disease is provided as a flowchart in Figure 2.12. The three common cardiac catheterisation procedures, PCI, CRT and RFA, are detailed in the following three subsections.

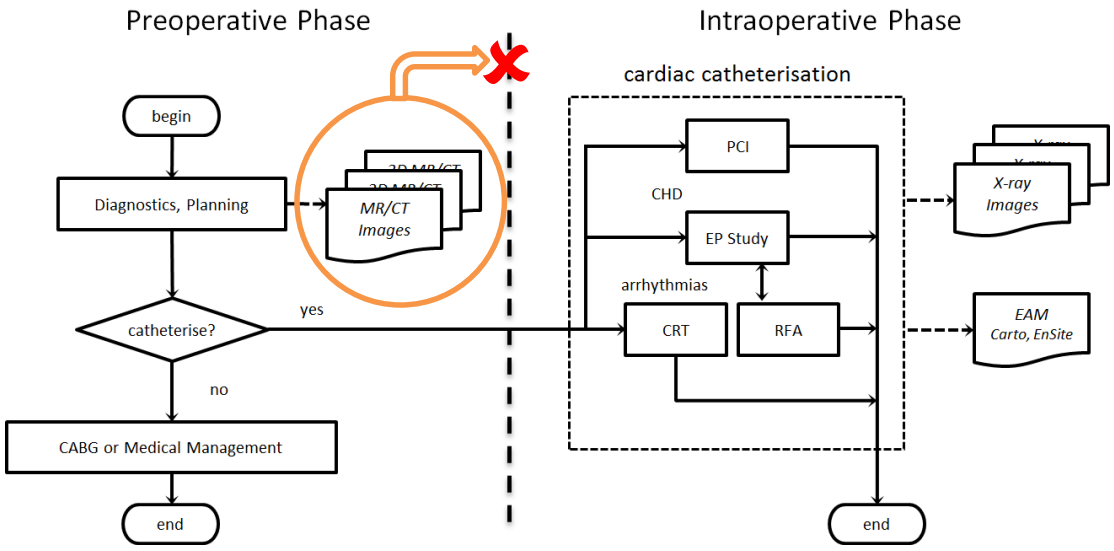


Figure 2.12) Flowchart of the clinical workflow when diagnosing and treating heart disease. A patient will usually undergo 3D imaging for diagnosis and treatment planning purposes. Those suitable can be referred for a minimally invasive EP study and possibly a cardiac catheterisation procedure. Patients not suitable, or whose catheterisation treatment fails, are referred for open heart surgery. Although 3D images (*orange, circle*) are acquired and are available during the preoperative phase, they are not (*red, cross*) yet routinely used during the catheterisation.

### 2.3.1. Percutaneous Coronary Intervention (PCI)

Coronary heart disease is the most common pathology of the heart where coronary arteries are narrowed or stiffened, restricting blood flow to regions of the heart (§2.1.2) [4] [5]. Left untreated, this may lead to a fatal heart attack or cause permanent scarring of the heart. Narrowing, or stenosis, of the arteries is the result of a build-up of plaque along the arterial walls, a condition known as atherosclerosis. Plaque is a mixture of fatty tissue, cholesterol and calcification trapped within a thin layer of muscle tissue (Figure 2.13a). In addition to narrowing of arteries, there is a chance that plaque can rupture and introduce thrombus (blood clots) into the blood stream that can lodge in the brain and cause a stroke.

Coronary CT angiography is usually performed during diagnosis in order to visualise the luminal stenosis and plaque. This involves the injection of a small bolus of iodine-based contrast agent into the heart followed by a 3D CT scan. The field of view (FOV) of the scan is usually limited, between 18 and 20 cm, to encompass only the heart. The required resolution of the image needs to be sub-millimetre, with voxel sizes around $0.4^3$ $mm^3$ in order to effectively detect stenosis and to determine its severity and characteristics [60]. Diagnostics can also be performed using MR angiography [61], using Gadolinium-based contrast agents instead.

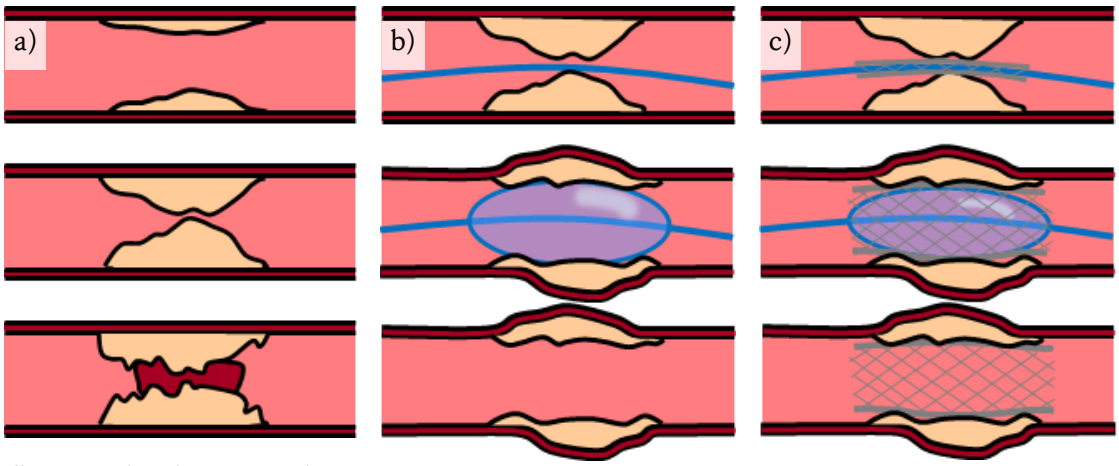


Illustrations by Alison Liu, with permission.

Figure 2.13 a) Illustrations showing build-up of plaque within the arterial walls and possible formation of blood clots that can dislodge and lead to stroke. b) Insertion and inflation of a balloon can cause the plaque to compress, widening the artery and restoring blood flow. c) A stent can be placed on the balloon which expands when the balloon is inflated. The stent remains there to prevent restenosis.

PCI treats this pathology by inserting a balloon at the site of the stenosis and inflating it (Figure 2.13b). This compresses the plaque, widens the artery and restores blood flow. A metal scaffolding called a stent can be introduced with the balloon which expands when the balloon is inflated (Figure 2.13c), and remains as a permanent fixture in the artery to help prevent restenosis [62]. Manoeuvring the guidewire, plastic sheath and catheters to the stenotic vessel is performed under X-ray fluoroscopy guidance (Figure 2.14a). Radio-opaque contrast agent injection into the bloodstream can help the interventionist locate the stenosis (Figure 2.14b).

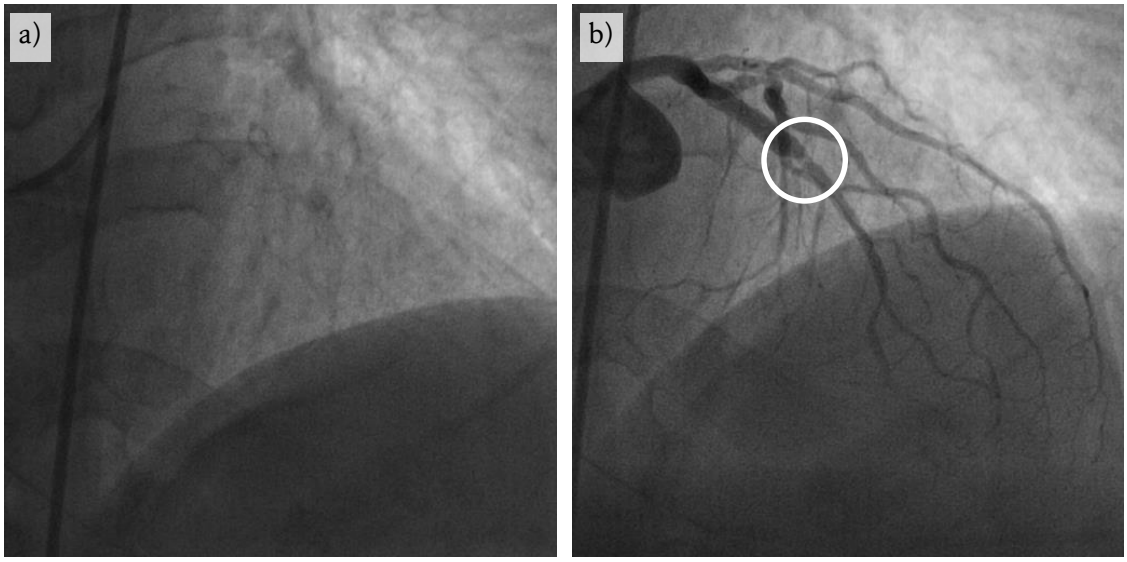


Figure 2.14 a) X-ray fluoroscopic image of the heart from PA view. Poor soft-tissue contrast of the heart is evident, showing only the upper cardiac border of the heart. b) Injection of a radio-opaque contrast agent into the bloodstream reveals a complex coronary vessel structure and helps reveal the location of the stenosis in the X-ray image (*circled in white*).

### 2.3.2. Cardiac Resynchronisation Therapy (CRT)

In some cases of heart failure, the reduced heart functionality is caused by electrical conduction problems of the heart, resulting in bradycardia where the heart cannot pump fast enough, or dyssynchrony where the poor time coordination limits the amount of blood pumped at each heartbeat. In either case, there is usually insufficient blood circulation around the body when needed, leading to a general intolerance to exercise. CRT is another minimally invasive treatment which involves the installation of a biventricular pacemaker into the body (Figure 2.15a) [11]. This device is a battery-operated electric pulse generator with three insulated leads protruding from it. The device is typically inserted into the body via an incision in the left shoulder just below the collar bone where it is permanently affixed (Figure 2.15b).

The three leads from the pacemaker enter the heart via the subclavian vein and through the superior vena cava where they are planted into the high right atrium (atrial lead), apex of the right ventricle (right ventricular lead) and into the coronary sinus, which wraps around the left ventricle (left ventricular lead). The atrial lead helps regulate the contraction of the atria while the ventricular leads aid the simultaneous contraction of the ventricles.

Some pacing systems have an implantable cardioverter-defibrillator (ICD), usually as part of the pacemaker device and sharing the atrial and right ventricular leads. ICDs help detect the onset of ventricular tachycardia or fibrillation and apply cardioversion to reset the cardiac cycle and restore normal sinus rhythm.

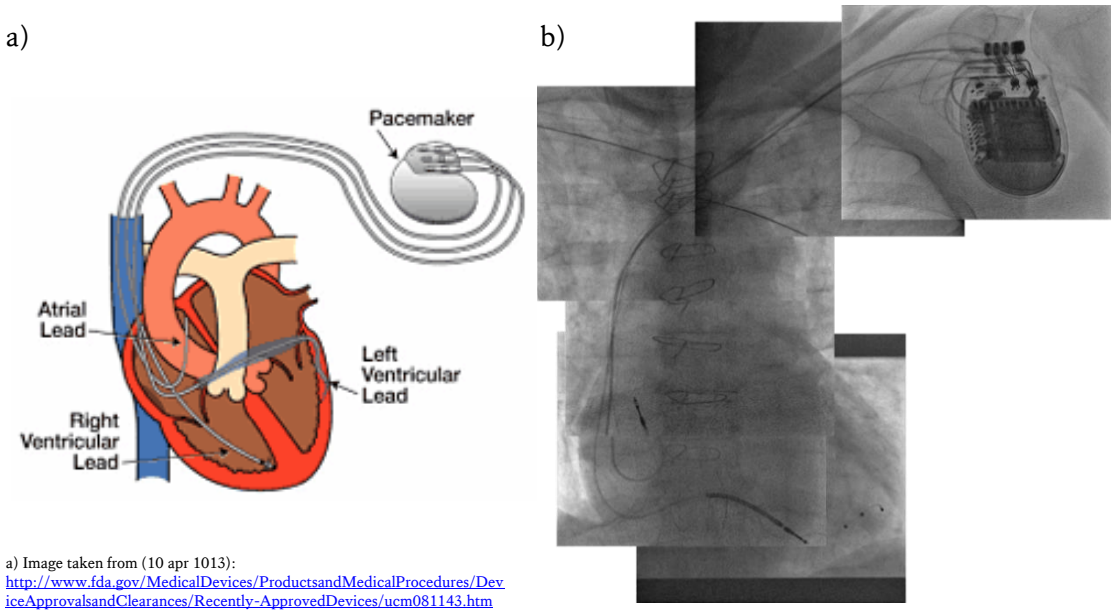


a) Image taken from (10 apr 1013): http://www.fda.gov/MedicalDevices/ProductsandMedicalProcedures/DeviceApprovalsandClearances/Recently-ApprovedDevices/ucm081143.htm

Figure 2.15 a) A diagram of pacemaker and lead placements in the heart. b) Manual stitching of X-ray views to provide a full view of an implantable pacemaker inserted into a patient.

Until recently, these procedures were performed using 2D X-ray angiography with success rates between 85% and 92%, but up to 30% of the patients being non-respondents to the treatment [63]. Preoperative 3D imaging could potentially help identify which patients would respond to treatment, and also determine the optimal lead trajectory and placement. Imaging can be performed using multislice CT, with pixel resolution of the slices around $0.4^2$ $mm^2$, and with around 1-mm spacing between each slice without contrast agent injections. This resolution can identify the CS structure where a lead is usually inserted. More recently, MR can provide a non-radiation alternative to CT, unless the patient had open heart surgery where metal wiring was used close the sternum (Figure 2.15).

### 2.3.3. RF Ablation (RFA) for Atrial Fibrillation (AF) and Flutter (AFL)

Radiofrequency ablations are commonly carried out to treat conduction abnormalities of the heart caused by myocardial scarring or congenital heart defects [8]. This is done by destroying tissue within the endocardium at strategic locations using an ablation catheter. These catheters are designed with a special tip that can heat up on application of radiofrequency (RF) energy, to temperatures high enough to destroy healthy tissue. Locations chosen for ablation are usually determined by an electrophysiology (EP) study performed prior to, or in conjunction with, the ablation procedure. Locations of ablation are usually regions where abnormal automaticity, triggered automaticity or micro-reentry occurs. For macro-reentrant circuits, ablation patterns are usually more complex.

In AF and AFL cases, the four PVs are usually found to be the foci of ectopic beats with the cardiomyocytes of the LA extending a short distance into them [64]. To remove these foci, a ring of points is ablated, typically using lasso catheter, around the PV ostia to isolate the LA myocardium from the cardiomyocytes that have extended into the PV. This procedure is known as a PV isolation. There are typically four PVs that extend from the LA. However, in about 30% of the cases there is an anatomical variation or anomaly [64]. To determine the existence and characteristics of these variation and anomalies, a preoperative CT or MR scan of the patient's heart can be acquired. An isotropic spatial resolution of between 0.5 and 1.0 mm is usually sufficient for this purpose. By being able to visualise the anatomy of the heart in 3D, complex regions of the heart can be avoided while manoeuvring the ablation catheter into position, potentially reducing the overall procedure time while also reducing risk.

## 2.4. Cardiac Image Registration

Throughout a typical clinical workflow (Figure 2.12) there are a number of additional images acquired of the heart. It would be beneficial for the cardiologist if these images with complementary information could be fused together. The augmentation of the 3D preoperative images onto the X-ray fluoroscopy to improve visualisation for the catheterisation procedure

lends itself to a 2D-3D image registration solution for cardiac images. 3D-3D image registration can then be used to further include the EAM data for treatment guidance, validation or biophysical modelling (Figure 2.16).

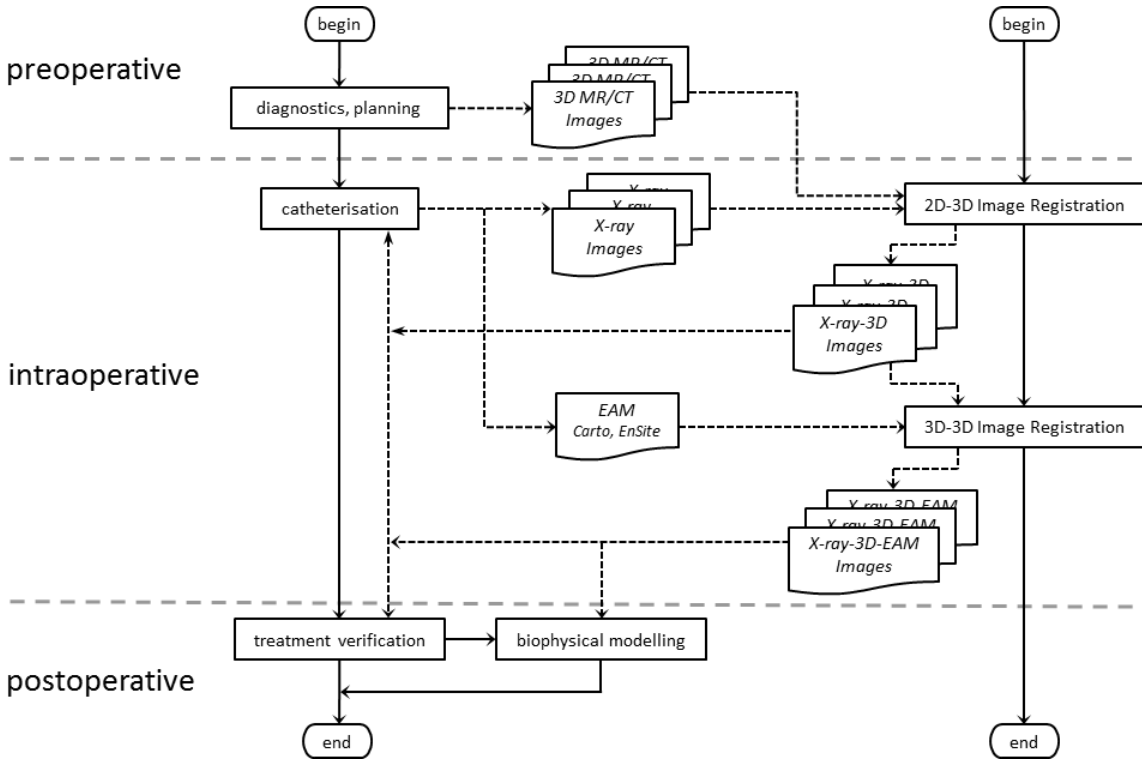


Figure 2.16) Registration workflow running in parallel with the clinical workflow of a typical cardiac catheterisation procedure. Solid lines indicate the flow of processes, while dashed lines indicate the flow of data.

### 2.4.1. 2D-3D Image Registration of Cardiac Images for Catheterisation Procedures

Cardiac catheterisation procedures are routinely guided by X-ray fluoroscopy. However, fluoroscopy has poor soft-tissue contrast and cardiologists rely on a high number of fluoroscopy images and nephrotoxic contrast agent injections to accurately position the catheters. These procedures are often prolonged due to the need for accurate positioning of catheters, resulting in significant radiation exposure to the patient and staff, and an often suboptimal success rate.

It is therefore highly desirable to overlay the X-rays with improved soft-tissue 3D information acquired preoperatively during the diagnostic and treatment planning phase of the procedure. Recently, there has been considerable research on registration of pre-procedural three-dimensional (3D) anatomical information to live two-dimensional (2D) X-ray fluoroscopy. The 3D imaging is done with either computerised tomography (CT) or magnetic resonance (MR) images, and the overlay can help guide the EP procedures.

There are a number of methods to perform an overlay, and which are used in current clinical settings. These methods include the use of a pre-calibrated hybrid X-ray/MR (XMR) imaging

system [15] [30], fiducial skin markers [16] [65], anatomical landmarks from the heart itself for registration, such as vessel bifurcation points and ostia [66], the cardiac shadow [67] or contrast-filled angiograms [68] [69] and intracardiac catheters [17] [23] [70] [71].

In the next chapter, the most relevant of these approaches will reviewed as part of a technical review of 2D-3D image registration of cardiac images. Based on the review, the design choice for the work in this thesis will be decided.

# Chapter 3

## 3. Literature Review of 2D-3D Image Registration in Medicine

Recently, there has been much research done aiming to augment X-ray fluoroscopy by overlaying better soft-tissue-contrast 3D information using 2D-3D image registration. A number of publications have been made, which survey and review the general field of image registration [20] [72] and the applied field of medical image registration [73] [74] [75]. In medical applications involving X-ray imaging, registration is difficult due to the loss of depth information inherent in the projective modality (Figure 1.1, Figure 4.1). This requires the projection geometry to be taken into account as part of the registration algorithm. Publications on medical image registration that address the 2D-3D problem include [21] and [22]. Catheterisation cases, routinely guided under X-ray fluoroscopy, can involve the heart, which is one of the most challenging organs to image and register due to its rapid change in size, shape and pose throughout the cardiorespiratory cycle. Survey and review papers related to cardiac image registration, but not necessarily 2D-3D, include [15] [18] [70] [76] [77] and [78].

In this chapter, the aim is to provide a review of the most relevant 2D-3D image registration algorithms available in the state-of-the-art. The review will focus mainly on the heart as the target organ for registration, however some algorithms are included that do not target the heart. The advantages and disadvantages of each method are then discussed in order to justify the design choices behind the work in this thesis.

### 3.1. Classification of Algorithms

This review uses a classification scheme similar to the ones presented in [21] and [75], but with some slight modifications due to the narrowed focus on cardiac imaging and the 2D-3D challenge. According to [75], a registration algorithm can be uniquely divided into three parts: a problem statement, a paradigm and an optimization procedure. These three parts are described in each algorithm according to the following criteria: study type, target of registration, imaging modality, registration basis, registration constraint, constraining metric and image dimensionality. The classification scheme is summarised in Table 3.1, with each entry in the table explained in the following subsections. For each algorithm, the accuracy in terms of a 3D-TRE, robustness in terms of a success rate and capture range, and computational time cost are

also listed for a quantitative comparison. The typical structure of a 2D-3D registration algorithm is illustrated in Figure 3.1.

| Problem Statement | |
|---|---|
| Procedure | Percutaneous Coronary Intervention<br>RF ablation for Atrial Fibrillation<br>Cardiac Resynchronisation Therapy |
| Target of Registration | Heart |
| Study Type | Simulation<br>Phantom<br>Animal<br>Clinical |
| 3D Imaging modality | Preoperative MR<br>Preoperative CT<br>Perioperative ultrasound<br>Perioperative 3DRx<br>Perioperative Electroanatomical Mapping |
| 2D Imaging modality | X-ray fluoroscopy |

| Paradigm | |
|---|---|
| Registration Basis | Feature-based<br>Intensity-based<br>Hybrid feature/intensity-based<br>Calibration-based |
| Constraint and Metric | Minimum distance between markers<br>Best fit of one feature inside another<br>Similarity between intensities<br>Similarity between intensity derivatives<br>Similarity between intensity functions |
| Image dimensionality | Projection<br>Back-projection<br>Reconstruction |

| Optimization Procedure | |
|---|---|
| Search Space | Rigid Body<br>Rigid Body Perspective Projection<br>Non-Rigid Affine |
| Search Strategy | Manual<br>Analytic<br>Local (Iterative)<br>Global (Iterative) |

Table 3.1 – Classification of 2D-3D image registration for cardiac catheterisation procedures.

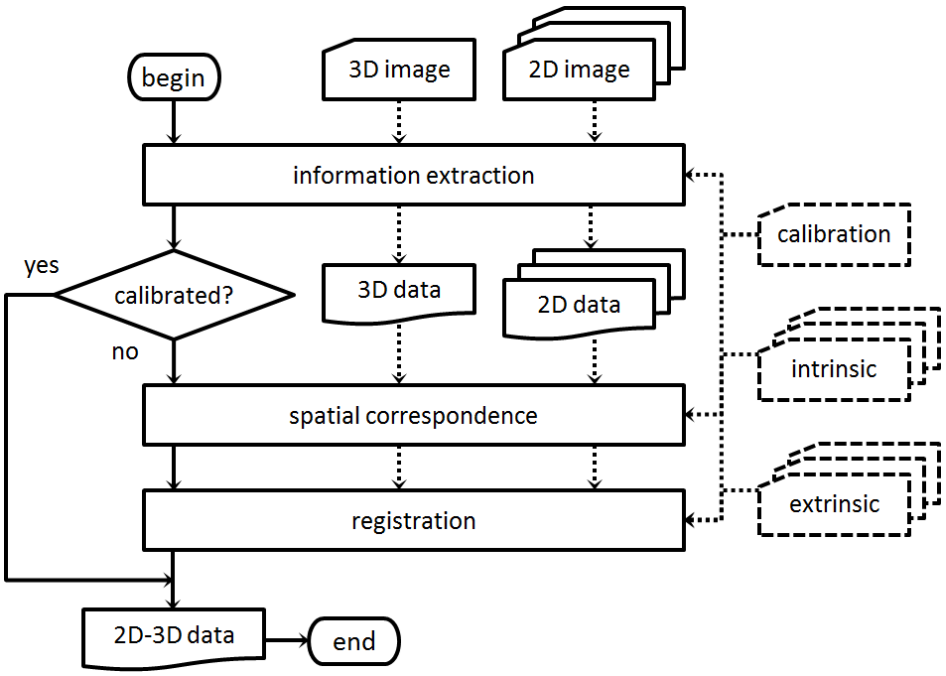


Figure 3.1) This flowchart illustrates the typical 2D-3D image registration algorithm which determines the relationship between the 2D and 3D images. Solid lined arrows represent the flow of the algorithm while dashed lines indicate the flow of data and information. Input data in dashed lines are optional. Data is first extracted from the images. In calibration-based approaches, the 2D-3D relationship make used of a predetermined calibration and bypasses the entire pipeline. Otherwise, the extracted data are brought into spatial correspondence using the any necessary intrinsic and extrinsic parameters of the 2D imaging system and registration can be performed in 2D or 3D space. The final result is the co-registered 2D-3D data.

### 3.1.1. Problem statement: Study Type and Imaging Modality

The problem statement of the registration algorithm is defined by the type of study that the algorithm is intended for, the target of registration, and the imaging modalities involved. In medicine, a registration algorithm is only useful if it can be applied to patient data from clinical cases. However, rigorous development of these algorithms is easier on geometrically realistic *phantom* or *computer* simulated models of the target organ, since a ground-truth registration can be obtained. Additionally, models can often afford a higher degree of control, flexibility and validation as no lives are at risk and there are no imaging restrictions, such as X-radiation dosage limits. However, these studies do not provide the full realism of live *clinical* case studies. Animal co-registration experiments fall in the middle of the spectrum, simulating many sources of error of typical clinical cases, such as the deformability of the heart during the cardiorespiratory cycle, while lifting some of the imaging restrictions as long as it is justifiable and ethical. The study type indicates the level of animacy of the target being registered in ascending order: computer models, phantom models, animals or clinical patient data.

For cardiac catheterisations, the only 2D imaging modality is X-ray. The 3D imaging modalities available to register to the fluoroscopy are preoperative MR, CT, SPECT and PET, or

perioperative 3DRx, ultrasound and EAM. However, in this thesis, only MR, CT and EAM data are available and therefore will be the focus of this review.

### 3.1.2. Paradigm: Registration Basis, Constraint, Metric and Dimensionality

The paradigm of an algorithm is its underlying concept and methodology. For 2D-3D registration algorithms it is broken down into its nature of registration basis, the constraints used for registration, the constraining metric, and image dimensionality used to achieve spatial correspondence between the 2D projective and 3D volumetric modalities.

The nature of the registration basis indicates what kind of information is taken from the image to perform the registration [75] [22]. The information can be geometric features segmented from the images used in a *feature-based approach*. Alternatively the intensities, or a function of the intensities, can be used directly in an *intensity-based approach*. Thirdly, the registration can be based entirely on a pre-calibration of the imaging systems in a *calibration-based* approach. The information is extracted during the information extraction step in Figure 3.1 in feature- and intensity-based approaches.

#### *3.1.2.1. Feature-based Approaches*

In feature-based approaches, corresponding features are extracted from the raw perioperative images during the information extraction step and used to constrain the registration, and sometimes used for validation. The features can be either *intrinsic* if they belong to the patient, such as chambers and vessels of the heart, or *extrinsic* if they have been introduced into the image, such as fiducial markers. Pairs of corresponding features, one from the 3D image and one from the 2D image, are used as *constraints* to align the images together. The alignment stage can be a single *analytic* step, for example aligning principal axes, or can be iterative using an estimate-check-and-refine strategy. This involves first making an initial estimate of the pose necessary to make the images line up, and then measuring how well they line-up based on a measurement between the two constraining features, known as a *metric*. The metric is usually some measure of how far apart the constraining features are. The estimated pose that optimises the metric is the pose used for registration. Estimating the pose during the process is dictated by the algorithms optimisation strategy, which is discussed in the section 3.1.3.

Measurements can be taken in either the X-ray's projection plane or in the volumetric space of the 3D image. This property of the algorithm is known as its *image dimensionality* and comes in three forms. *Projection* algorithms compute their metric by first projecting the 3D features onto the X-ray images, and then taking measurements between each projected feature and its corresponding feature extracted from the X-rays (Figure 3.2a). Methods that behave in the opposite way are called *back-projection* algorithms. They start by taking the features extracted

from X-ray, then back-project their shape back to the X-ray's source position in 3D space and measurements are taken between the feature extracted from the 3D image and the extrusion (Figure 3.2b).

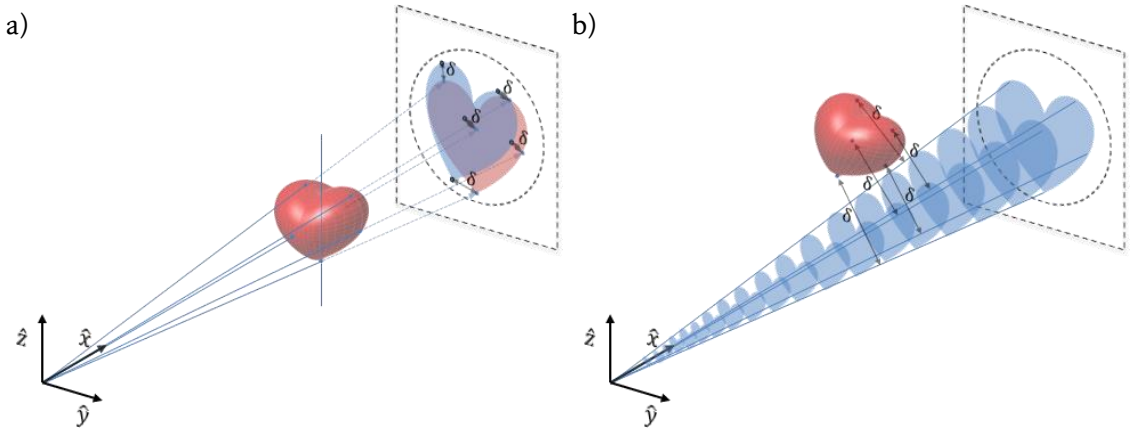


Figure 3.2 a) The forward projection is the mapping of 3D points (*red volumetric heart*) onto the 2D projective plane using the system's projection parameters. There is a significant loss of depth information due to the many-to-one nature of this technique. If the points are coupled with intensity information, their forward projection can form an image. Registration is based on the forward projection match on projections of the 3D data (*red flat heart*) with data from the 2D image (*blue flat heart*), usually minimising some distance measure ($\delta$) between them. b) The back-projection can be visualised as the extrusion of a shape from a projective modality (*blue flat hearts*) back to the source of projection. The back-projection of a point forms a projection line (*blue lines*). Algorithms that match using this technique usually minimum some distance measure ($\delta$) between the 3D data (*red volumetric heart*) and corresponding projection lines.

In projective geometry, there is a significant loss of depth information where points on the X-ray projective plane extrude a *projection line segment* back towards the X-ray source. Any out-of-plane translations, i.e. translations of the target 3D object along these lines, make very little change to the X-ray image captured (Figure 4.2). For projection algorithms, this leads to an ill-conditioned many-to-one problem since any point along the projection line will project onto the X-ray plane at the exact same spot. Oppositely, there is an ill-conditioned one-to-many problem for back-projection algorithms since the point from the X-ray image can be mapped to any point along the extruded line segment. These problems can be alleviated by taking multiple X-ray views of the target, calculating a metric using each view and combining the measurements in a synergetic way. This allows out-of-plane translational components in one view to project as in-plane translations in another view (Figure 3.3a).

Using multiple X-ray views for registration also allows reconstruction, which is the third image dimensionality option. In reconstruction approaches, the constraining feature must be segmented from each X-ray view, which is then back-projected into the X-ray coordinate system. The intersection of the back-projection lines locates the feature in 3D space, and this location can then be matched to the feature segmented from the 3D image via 3D-3D image

registration (Figure 3.3b). If the X-ray C-arm is tracked and calibrated, then the epipolar constraint can be applied to aid with the segmentation in the information extraction step and establish point correspondences between the views. According to epipolar geometry, given a point $\vec{p}$ in one X-ray view, its corresponding point in another X-ray view must lie along the projection of the back-projection line of $\vec{p}$ (Figure 3.3a). The mathematics of projection, back-projection and reconstruction is outlined in the next chapter.

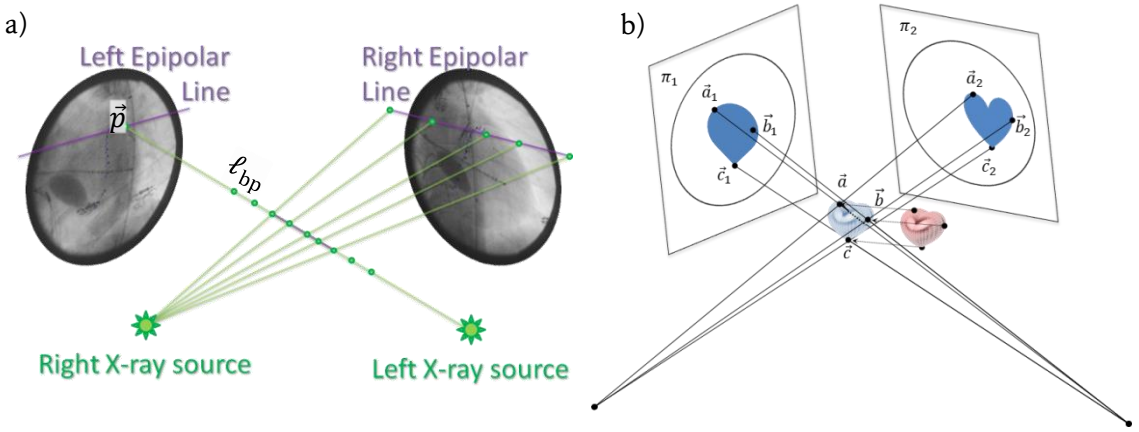


Figure 3.3 a) The epipolar concept. For any point $\vec{p}$ in the left 2D image is a projection line between itself and the left X-ray source ($\ell_{\mathrm{bp}}$). The projection of this line from the right X-ray source onto the right image is the epipolar line. b) Multiple projective images of an object (*blue flat hearts*) from different views can be used to reconstruct the original object in 3D space (*blue volumetric heart*) by taking corresponding points ($\vec{a}_1$ and $\vec{a}_2$, $\vec{b}_1$ and $\vec{b}_2$, $\vec{c}_1$ and $\vec{c}_2$) on the projective images and back-projecting them to their source. The intersection of their back projections, or the point closest to them if they form skew lines, reconstructs the corresponding point in 3D ($\vec{a}$, $\vec{b}$ and $\vec{c}$). The reconstruction can be registered to the same object acquired with a 3D modality (*red volumetric heart*), usually by minimising some measure of distance in reconstruction-based algorithms.

#### 3.1.2.2. Intensity-based Approach

The segmentation step in feature-based approaches may introduce the need for manual interaction, added processing time, and a propagation of uncertainty. *Intensity-based* algorithms avoid this by not requiring segmentation during the information extraction step and instead use a function of the image intensities to constrain the registration. The function can be, for example, the identity, a derivative such as the spatial gradient of the pixels, histogram equalization, edge detection or intensity re-mapping.

Spatial correspondence for intensity-based approaches can be achieved by using either a *projection* or *reconstruction* strategy. In *projection* strategies, the common approach is to make an initial estimate at the rigid-body transformation needed to align the 3D image to the 2D X-ray images (Figure 3.1). Based on this estimate, the 3D image is spatially transformed and then ray-cast onto the X-ray projective plane to produce a digitally reconstructed radiograph (DRR). A *similarity measure* metric is then computed which, quantitatively determines how similar the

DRR and X-ray image are. The rigid-body transformation is then perturbed either systematically or according to measured similarity, until the measure reaches an optimum and the algorithm is said to have converged. Where multiple intraoperative X-ray views are available for registration, a *reconstruction* strategy can be employed. The optimal transformation to align the reconstructed 3D image and the original 3D image is determined by optimising a similarity measure in a similar way to the projection approach.

#### 3.1.2.3. Hybrid Intensity/feature-based Approach

In intensity-based approaches, generating multiple DRRs or performing tomographic reconstructions requires calculation, which may be too time-consuming for clinical applications due to the large number of voxels in a 3D data set. Feature-based approaches significantly reduce the amount of data to be processed by cutting out only the geometric shapes necessary for registration during the segmentation step. On the other hand, automatic segmentation of the corresponding features in the X-ray images can be difficult and sometimes unreliable. Hybrid approaches avoid these issues by segmenting the constraining feature in the 3D modality and matching it with X-ray intensity information. This way, generating DRRs, tomographic reconstructions and segmentation of the intraoperative X-ray are avoided.

#### 3.1.2.4. Calibration-based Approaches

A fourth basis for registration does not use the perioperative images to perform the registration at all; neither its features nor intensity information. These approaches bypass the entire registration pipeline (Figure 3.1) and instead rely on a careful calibration of the imaging systems. The simplest form of calibration-based registration is if the 2D imaging device is the same one used to acquire a 3D image, for example 3D rotational X-ray (3DRx). The approach can use feature- or intensity-based techniques for the initial registration and then rely on continuous spatial tracking of the equipment to maintain registration throughout the procedure using motion sensors.

### 3.1.3. Optimisation procedure: Search Space and Search Strategy

The third defining feature of an image registration algorithm, except in the case of calibration-based approaches, is the optimisation procedure used. All 2D-3D registration algorithms attempt to find a transformation $\mathcal{M}_{\text{reg}}$ that aligns the volumetric 3D data to the projective 2D images – X-ray images, in the context of this thesis – and follow the flow chart in Figure 3.1. Since there is a dimensional mismatch between the images, spatial correspondence must be restored using the C-arm's intrinsic projection parameters $\mathcal{P}$ by projection, back-projection or reconstruction. Where multiple views are used for registration, the projection may need to be determined for each view $\mathcal{P}_n$ where $n$ is the view number, in addition to the pose $\mathcal{M}_n$ of the C-arm gantry of each view. The parameters that define the projections are known as the *intrinsic calibration*

*parameters* of the X-ray, and the parameters that define the pose of the C-arm gantry are known as the *extrinsic calibration parameters* (Figure 1.1).

The actual parameters that make up the transformations $\left(\mathcal{M}_{\text{reg}}, \mathcal{M}_n, P_n\right)$ can vary depending on the assumptions and restrictions used. The most common assumptions associated with $\mathcal{M}_{\text{reg}}$ is that the constraining features do not change shape between the image acquisitions, and therefore $\mathcal{M}_{\text{reg}}$ is a rigid-body transformation that can be decomposed into translations in the direction of, and rotations about, the three independent axes of space, $\mathcal{M}_{\text{reg}}(x, y, z, \alpha, \beta, \gamma)$. The X-ray system used in cardiac catheterisation procedures is usually encased in a C-arm gantry that can be translated in any direction, but constrained to rotate about the sagittal plane in the direction of either the head (*cranially*) or foot (*caudally*) and in the transverse axial plane either to the left (*left anterior oblique*) or to the right (*right anterior oblique*), $\mathcal{M}_n(x_n, y_n, z_n, \alpha_n, \beta_n)$ (Figure 2.8). The generation of an X-ray image can be modelled with a pin-hole camera $\mathcal{P}_n$ and parameterised by $\mathcal{P}_n(c_s, l_s, k_1, k_2)$. $(c_s, l_s)$ are the coordinates of the pixel where the beam strikes at a normal to the imaging plane, and $k_1$ and $k_2$ are ratios of the focal length $f$ and row $\Delta u$ and column pixel pitches $\Delta v$ respectively of the X-ray sensor (Figure 4.1).

Most modern X-ray imaging systems can track the rotation of the C-arm and with their intrinsic parameters pre-calibrated, so their pose $\mathcal{M}_n$ and projection $\mathcal{P}_n$ parameters are known for every view. In systems that do not provide this information, these parameters can be measured using a calibration phantom [30] [79]. All parameters that define the transformation between the volumetric and projective data define the algorithm's *search space*, technically a *vector space* [80], and these parameters are known as *search parameters* or *degrees of freedom* (DOF). Each point in the search space corresponds to an estimate of the search parameters, which corresponds to an estimate of the transformations and can be used to evaluate the metric. The metric, as defined in the previous section, can be used to measure how similar, or how close, constraining features are to one another, in which case the measure is called a *similarity measure*. Alternatively, it can measure how far or dissimilar the features are, in which case the metric is known as a *cost function*. The transformations that correspond to the optimal value of the metric – the highest value if looking for similarity or lowest value if calculating cost – are the transformations used for registration. In a good registration algorithm, this transformation will correctly align the volumetric data to the projective one.

How the algorithm finds the optimal parameters as quickly as possible while avoiding local optima is decided by the algorithm's *search strategy*. These can either be manual, analytic or iterative. Manual approaches rely on the user to visually align the constraining features, which makes them susceptible to inter- and intra-user variability. In analytic approaches, the metric is

only dependant on the geometry or intensity of the constraints and the registration transformations are unique.

The most common strategies are iterative approaches. Search parameters are usually continuous and therefore uncountable. Iterative approaches start by discretizing the parameters, usually into evenly spaced intervals, resulting in a discretised search space. A *global* method is one that seeks to find the unique optimum of the search space. A simple, but computationally expensive way of doing this is by evaluating the metric at every point in the discretised search space in order to find the optimal value. These are known as brute-force algorithms that, at the expense of being computationally expensive and potentially time-consuming, guarantee that the optimal solution is found. A *local* method starts at a point in the space and travels through the space in an intelligent way until an optimum is found. The starting point $\vec{X}_0$ is decided by the initial estimate position of the patient and imaging systems, for example, many algorithms assume that the patient is lying supine on both imaging tables and that the heart is at the isocentre of the imaging system. Because the metric only needs to be computed at the points along the search trajectory, this should be computationally less demanding than a global method. However, the global optimum is not guaranteed.

Local iterative methods can be formulated as finding the point $\vec{X}$ which maximises a similarity measure $S = S(\vec{X})$ or minimises a cost function $C = C(\vec{X})$.

$$\mathcal{M}_{\text{reg}} = \underset{\mathcal{M}(\vec{X}')}{\arg\max}\, S\left(\mathcal{M}(\vec{X}')\right) \quad , \qquad \mathcal{M}_{\text{reg}} = \underset{\mathcal{M}(\vec{X}')}{\arg\min}\, C\left(\mathcal{M}(\vec{X}')\right) \quad . \tag{3.1}$$

Note that $\vec{X}$ is a generalised point, $\vec{X} = \left(X^0, X^1, \dots, X^i, \dots, X^{N-1}\right)$, where the superscript $i$ indexes the coordinates of the point and $N$ is the dimension of the point, in a coordinate system spanned by the unit basis vectors $\{\hat{e}_i\} = (\hat{e}_0, \hat{e}_1, \dots, \hat{e}_i, \dots \hat{e}_{N-1})$.

In local iterative methods, it is not always possible to find the global optimal value of $S$ or $C$ with an optimisation strategy. Usually, a sufficiently optimal value is found instead. This can happen when the optimisation strategy has found a local optimum within the search space and any further movements result in negligible, or zero, increase in the metric, or when the strategy has depleted a supply of resources which are consumed per iteration and therefore reports its current location in the search space. Examples of resources could be a given amount of time or a maximum number of iterations. Depletion of the resources terminates the search and the algorithm is said to have *converged*. Local iterative searches are dependent on an initial position

$\vec{X}_0$ where the search begins: $\vec{X} \leftarrow \vec{X}_0$. The registering transformation $\mathcal{M}_{\text{reg}}$ is made up of the search parameters at the point of convergence: $\mathcal{M}_{\text{reg}} \leftarrow \mathcal{M}(\vec{X})$.

Four iterative search strategies are used throughout the papers reviewed. These include the *best neighbour hill climbing* [81], *downhill simplex* [82], *conjugate direction method* [83] and *iterative closest point* (ICP) [84]. These will be discussed in the following four subsections, and these sections will be referred back to as these strategies are encountered in this review.

#### 3.1.3.1. Powell's Conjugate Direction Search Strategy [83]

Powell's method starts in the search space at a generalised point. The local shape of the cost function $C$ around $\vec{X}$ is assumed to be a multivariate quadratic function of the form:

$$C(\vec{X}) \approx \overleftarrow{X} A \vec{X} + \overleftarrow{B} \vec{X} + c \quad , \qquad (3.2)$$

where $A$ is an $N \times N$ matrix, $\overleftarrow{B}$ is an $N$-dimension pseudovector, and $c$ is a constant. The backward arrow represents that the equality is a pseudo- or row vector, $\overleftarrow{X} = \vec{X}^T$, and the juxtaposition between a pseudovector and a vector is the inner product, $\overleftarrow{X}\vec{Y} = \vec{X} \cdot \vec{Y}$. The search strategy iteratively tries to move $\vec{X}$ towards the minimum of the quadratic. Before each move, $N$ one-dimensional searches are made on the cost function along lines that intersect $\vec{X}$ and parallel to a set of $N$ conjugate vectors. Initially, the vectors are the coordinate directions $\{\hat{e}_i\}$. The location of the minimum evaluation of the cost function along the lines becomes the new point, and the vector $\hat{v}_{\text{min}}$ associated with the line containing the minimum replaces the last vector in the conjugate basis. The first vector in the basis is discarded and each vector in-between is shifted left, forming a new basis $(\hat{e}_1, \dots, \hat{e}_i, \dots \hat{e}_{N-1}, \hat{e}_{N-2}, \hat{v}_{\text{min}})$. Iteration continues until no new minimum can be found beyond the current location, and converges.

#### 3.1.3.2. Best Neighbour Hill Climbing

This strategy requires a vector of step sizes, $\Delta\vec{X} = (\Delta X^0, \Delta X^1, \dots, \Delta X^i, \dots, \Delta X^{N-1})$, with all elements positive. From the current location $\vec{X}$, optimisation involves computing the similarity function $S$ for $2N + 1$ variants of $\vec{X}$. $N$ variants include a small positive incremental change in each one of its $N$ parameters, $N$ negative changes in each parameter; and in the last variant there is no change,

$$s_j = \begin{cases} S(\vec{X} + \Delta\vec{X} \cdot \hat{e}_j) & j = [0, N-1] \\ A(\vec{X} - \Delta X_{j-N} \cdot \hat{e}_{j-N}) & j = [N, 2N-1] \\ A(\vec{X}) & j = 2N \end{cases} \quad , \qquad (3.3)$$

where $\hat{e}_j$ is a basis unit vector of the search space in direction $j$.

The variant that corresponds to the largest computed value of $S$ becomes the new variant.

$$j = \arg\max_{j'} s_{j'}, \quad (3.4)$$

$$\vec{X} \leftarrow \begin{cases} \vec{X} + \Delta\vec{X} \cdot \hat{e}_j & j = [0, N-1] \\ \vec{X} - \Delta X_{j-N} \cdot \hat{e}_{j-N} & j = [N, 2N-1] \\ \vec{X} & j = 2N \end{cases}. \quad (3.5)$$

$\vec{X}$ is refined in this way until the highest similarity measure is from the no-change variant. In this case, the step sizes $\Delta\vec{X}$ are halved and iteration resumes until the increments have been halved a specified number of times, at which point the algorithm ends and is said to have converged.

#### 3.1.3.3. Downhill Simplex [82]

The downhill simplex method uses a $N$-simplex, a $N$-dimensional analogue of a tetrahedron to explore the local neighbourhood around $\vec{X}$. The simplex has $(N+1)$ vertices $\vec{V}_j$ with $\vec{X}$ being one of them. Initially, $\vec{X} = \vec{X}_0$, and the vertices are

$$\begin{aligned} \vec{V}_i &= \vec{X} + \lambda_i \hat{e}_i \quad , \\ \vec{V}_N &= \vec{X}_0 \quad . \end{aligned} \quad (3.6)$$

where $\hat{e}_i$ is a unit vector of the $i^{\text{th}}$ coordinate axis and $\lambda_i$ is its characteristic length scale.

At each iteration, the cost function $C$ is evaluated for each vertices $\vec{V}_i$. Based on the relative values of the evaluations, the simplex is allowed to deform in specific patterns that migrates it towards the nearest maximum. At each vertex, the cost function is evaluated and the vertices that evaluate to the highest and lowest cost functions are noted,

$$\begin{aligned} \vec{H} &= \max_j C(\vec{V}_j) \quad , \\ \vec{L} &= \min_j C(\vec{V}_j) \quad . \end{aligned} \quad (3.7)$$

The highest evaluated vertex is then reflected about the centroid and the cost function at the reflected point $\vec{R}$ is re-evaluated; if this lies between the highest and lowest evaluation, then this new vertex replaces the highest vertex and the reflection process is repeated but with a new simplex having moved toward the minimum. If $C(\vec{R})$ is higher than $C(\vec{H})$, then a minimum exists within the simplex and so the reflected vertex is pulled towards the centroid, contracting the polytope. If $C(\vec{R})$ is lower than $C(\vec{L})$, this indicates that the simplex needs to be bigger to capture the minimum, so the reflected vertex is pulled away from the centroid. After a series of reflections, expansions and contractions, the optimisation strategy halts when the change in error falls below a user pre-set value, and the vertex $\vec{X} = \vec{V}_N$ is returned as the point that minimises $C$.

#### 3.1.3.4. Iterative Closest Point [84]

The iterative closest point (ICP) algorithm finds a rigid-body transformation (RBT) between two sets of points, $L = \{\vec{L}^j\}$ and $R = \{\vec{R}^k\}$, with $\vec{X} = (x, y, z, \alpha, \beta, \gamma)$ being the translational and

rotational parameters in 3D space. During each iteration, the algorithm assumes point correspondences between $L$ and $R$ using the nearest neighbour criteria and finds the RBT between the corresponding points by minimising the root-mean-square (RMS) distance error [85] [86] between them. The points are transformed using the RBT such that error is minimised, and the iteration is repeated with the new set of points, until the RMS error is sufficiently small, at which point the algorithm is said to have converged.

## 3.2. Relevant Publications

Using the classification criteria outlined above, a number of relevant papers are reviewed. In the work behind this thesis, two feature-based algorithms are proposed which register images using catheters inserted into the heart. Justification of this choice is provided in this review, which starts with a calibration-based approach, and then describes intensity-based approaches and ends with feature-based approaches. Imaging modalities involved in this work include X-ray, MR, CT and EAM, and therefore will be the primary focus of this review.

### 3.2.1. Rhode et al. 2005 [30]: System for Real-Time XMR Guided Cardiovasc. Interv.

In cardiac catheterisation procedures, continuous visual feedback is required to carefully manipulate a catheter through the heart. Currently, registration for these procedures can be performed automatically and in real-time using a hybrid X-ray/MR guidance system proposed in [30], which combines an MR scanner and a calibrated and tracked X-ray fluoroscope. The two imaging devices share a single patient bed which can slide between them. This allows the patient to be moved between the two devices in under one minute. Additionally, infrared (IR) light emitting diodes (LEDs) are affixed onto the table and the C-arm of the fluoroscope. The IR LEDs are monitored at all times throughout the procedure by a camera so that any motion is recorded. As a result, registration between the MR scanner and the X-ray can be performed in real-time since the extrinsic parameters are always tracked. This type of system describes a full *calibration-based* multi-modal registration approach.

In the paper, this imaging solution had reported use in 13 live cardiac catheterisation procedures to overlay 3D MR images acquired preoperatively onto the intraoperative X-ray in real-time. The error of this registration method was between 3.3 ± 0.9 mm in 2D, and 4.85 ± 0.25 mm in 3D. This does not include bulk patient motion, which would compromise accuracy and require manual adjustment.

The system is currently deployed in around 20 to 30 research hospitals where they are used to guide cardiac catheterisations. Registration can be performed in real-time, and within the 5-mm clinical accuracy. However, the combination of the two modalities requires a dedicated suite with a shared patient table, limiting its applicability beyond the research environment.

### 3.2.2. Gutiérrez et al. 2007 [16]: X-ray Fused with MRI (XFM) Catheter Roadmaps

The use of fiducial skin markers is another approach to registration and is demonstrated in [16] for fusing X-ray and MR images during invasive cardiovascular procedures. In the work by Gutiérrez *et al.*, 13 to 19 multimodality skin markers were placed on the chest of patients undergoing invasive cardiovascular procedures including graft coronary arteriography, right ventricular free-wall biopsy, iliac/femoral artery recanalization and stenting. The skin markers are visible in both MR and X-ray and are easily identifiable in the images so that their positions could be manually selected. The markers from MR were projected onto X-ray where during the registration process.

Three types of preoperative images were acquired. Contrasted enhanced ECG-gated cine steady-state free precession images were acquired to obtain the cardiac region of interest. 3D contrast enhanced MR Angiograms (MRA) were obtained for the arterial structure around the heart. For fiducial localisation, a 3D $T_1$-weighted gradient echo sequence was used to acquire an image, after which their centres were selected manually from the image.

The X-ray system was previously calibrated and its distortions (pincushion, sigmoidal and gantry sagging) were corrected for using 2D $5^{th}$-order polynomials. The centres of the markers were selected manually.

In order to achieve registration, the markers from both modalities were matched for correspondence and a transformation was found between the 3D and 2D points by iteratively fitting the six RBT parameters that make up $\mathcal{M}_{\text{reg}}$ until the distance between the 3D projected points and the 2D points were minimised. Since cine images were obtained of the heart, the roadmap could in principle be valid throughout the entire cardiac cycle, but registration would be most accurate when performed at end-expiration and end diastole.

This registration algorithm was applied to 20 procedures in 19 subjects, comprising eight femoropopliteal revascularization procedures, six iliac procedures and six diagnostic cardiac procedures. The authors reported that in intracardiac mass biopsy procedures, XFM was useful in helping to avoid inadvertent atrial free wall and aortic biopsy and roadmaps of the MRA images were successful. Roadmaps during femoral artery recanalization and coronary arterio/ventriculography were also successful. However, XFM was unsatisfactory in some of the iliac cases, which was attributed to displacement of the skin fiducial markers. The robustness of this technique was not quantified but accuracy was reported to be between 1.6 and 5.2 mm and summarised in Table 3.2.

The main issue with using fiducial skin markers to register the heart is that accuracy may be lost if there is motion between the heart and the markers, which occurs throughout the entire

cardiorespiratory cycle. Additionally, the skin is highly deformable and motions of the body could change the location of the markers on the chest. In cases where the preoperative image takes place days prior to the procedure, the markers may have to be removed from the patient to prevent discomfort and then replaced during the catheterisation. Marker repositioning can introduce fiducial localisation errors in the registration which will add to the registration error.

### 3.2.3. Lemieux et al. 1994 [87]: Digitally Reconstructed Radiographs

Lemieux *et al.* was the first to publish an intensity-based registration algorithm. In this paper, the author registered images of a skull phantom from CT to two X-ray images. The skull was embedded in rubber, and fiducial markers, visible in both imaging modalities, were attached and used for validation.

The relationship between the CT and X-ray views was approximated by assuming that the skull was in the supine position and that the plane embedding the arc of the X-ray C-arm was parallel to the CT imaging slices. If there was a misalignment, the user was allowed to manually adjust the orientations to ensure that they were parallel. Based on an initial estimated pose, a DRR was produced from the CT image in both X-ray views, which were then compared to the corresponding X-rays using two metrics. One of them measured the cross-correlation using:

$$L_{\text{cc}} = \frac{-(r_1 N_1 + r_2 N_2)}{(N_1 + N_2)} \quad , \quad (3.8)$$

where $r_{1,2}$ are the Pearson's product-moment correlation coefficient between the X-ray and DRR images, and $N_{1,2}$ are the number of pixels in the DRR.

A second metric measured the correlation between the gradients:

$$L_{\text{gp}} = \frac{-1}{(N_1 + N_2)} \left( \sum_{i=1}^{N_1} |\nabla I_1(i) \cdot \nabla J_1(i)| + \sum_{i=1}^{N_2} |\nabla I_2(i) \cdot \nabla J_2(i)| \right) \quad , \quad (3.9)$$

Where $I_{1,2}$ are the X-ray images, $J_{1,2}$ are the DRR images and $N_{1,2}$ are the number of pixels in the images. Both (3.8) and (3.9) are cost functions to be minimised. The algorithm makes use of both metrics. The cross-correlation metric (3.8) is used with a coarse discretization of the search space to obtain a refined estimate pose. This is then used to initialise a second search using the gradient-correlation metric (3.9) with a refined discretisation of the search space.

With both metrics, the search strategy used was Powell's conjugate direction method (§3.1.3.1, [83]). The registration algorithm was applied to the skull phantom and the embedded fiducial markers were used to establish a *gold standard* registration. Compared to this standard, registration could be achieved within 1-mm accuracy in terms of a mean 3D target registration error (3D-TRE) with a success rate of 92% with an average capture range of 21.3 mm.

### 3.2.4. Penney et al. 1998 [79]: Similarity Measures for Use in 2D-3D Medical Im. Reg.

Since [87], a number of metrics have been devised to register between CT and X-ray, but a fair comparison of their performance is difficult due to the differences in the studies, initialisation and choice of search strategies. In [79], Penney *et al.* eliminates these variations and evaluates the performance of six metrics in a lumbar spine phantom study. Twelve fiducial markers were placed around the spine phantom to establish a gold standard registration, and the phantom was subsequently imaged in CT and X-ray. Although X-rays were taken from multiple views, only one view was used for registration at a time. The spine phantom was assumed to be rigid throughout the study and the X-ray system was intrinsically calibrated so that the projection parameters were known and fixed. Therefore, only a rigid-body transformation between the CT and X-ray needed to be determined. A projection strategy was used to achieve spatial correspondence. The six metrics explored in this paper were the normalised cross correlation, entropy of the difference image, mutual information, gradient correlation, pattern intensity and gradient difference. The metrics were all measures for similarity and the algorithm attempted to maximise them. The best two performing metrics in terms of accuracy were the pattern intensity and gradient difference, and are described here.

The pattern intensity metric was calculated by first computing a difference image $I_{\text{dif}}$ between the X-ray $I_{\text{fl}}$ and a scaled DRR $I_{\text{DRR}}$,

$$I_{\text{dif}} = I_{\text{fl}} - sI_{\text{DRR}} \quad , \quad (3.10)$$

where $s$ is an entropy-minimising scaling factor which minimises a measure of entropy $H$ of the difference image,

$$s = \arg\min_{s'} H(s') \quad . \quad (3.11)$$

The entropy of the difference image is computed at:

$$H(s) = -\sum_{x} p(x) \log p(x) \quad , \quad (3.12)$$

where $p(x)$ is the probability of finding a pixel with intensity value $x$ in the difference image.

High contrast patterns in the difference image indicate the presence of regions that do not share the same structures between the images, reducing the measure of similarity. The measure is

$$P_{r,\sigma} = \sum_{i,j} \sum_{d^2<r^2} \frac{\sigma^2}{\sigma^2 + \left(I_{\text{dif}}(i,j) - I_{\text{diff}}(v,w)\right)^2} \quad , \quad (3.13)$$

$$d^2 = (i-v)^2 + (j-w)^2 \quad . \quad (3.14)$$

where $\sigma$ is chosen to dampen the asymptotic nature of the function when deviations between neighbouring pixels are small due to thin structures and $r$ defines the size of the neighbourhood.

Large changes in the difference image within a small region $r$ compute as low values of similarity.

The second of the two top performing metrics, in terms of accuracy and robustness, is the gradient difference, and it measures the combined similarity of the gradients between the two images:

$$G(s) = \sum_{i,j} \frac{A_i}{A_i + \partial_i I_{\text{dif}}} + \sum_{i,j} \frac{A_j}{A_j + \partial_j I_{\text{diff}}} \quad , \quad (3.15)$$

where $\partial_i$ and $\partial_j$ indicate partial derivatives in the subscript direction and $A_{i,j}$ are constants used to dampen any asymptotic behaviour due to thin structures.

To find the best search parameters for obtaining the transformation that maximises a single similarity metric, Penney *et al.* uses the best neighbour hill climbing optimisation strategy (§3.1.3.2) to search for the RBT pose parameters $\vec{X} = (x, y, z, \alpha, \beta, \gamma)$.

The search strategy was applied between CT and four X-ray data for each of the six metrics on the spine phantom with their results averaged. Soft tissue and medical devices were overlaid on the X-ray to simulate the realism of a live clinical case. The success of the registration was defined as being within $\Delta\vec{P} = (50.8\text{ mm}, 3.6\text{ mm}, 2.4\text{ mm}, 3.4°, 7.6°, 7.8°)$. Measures were from a gold standard obtained using fiducial marker registration, with $\Delta\vec{P}$ chosen so that the algorithm needed to be at least half as good as a manual registration of the same images. Mutual information performed the worst with only a 5% success rate, entropy 47%, cross correlation 55%, gradient correlation 95% and both pattern intensity and gradient difference achieved 100% success. For comparison in Table 3.2, the accuracy is approximated as being within 1.8 mm, which is half the largest in-plane component of $\Delta\vec{P}$, the estimated error for manual registration. The average computational time for each registration was 74 s.

Intensity-based methods have been shown to yield high accuracy and success rates [79] [87]. Intensity-based methods work best when the underlying physics between 3D and 2D modalities are similar since contrast ratios of the different tissue types are relatively similar and the grey level values between them share a linear relationship [87]. In these cases, normalizing the two images with a scale factor, using the intensity distribution or the gradient of the image is sufficient [79]. These are known as *quasi-multimodal registrations* [21]. In cardiac catheterisation procedures, which are the focus of the research discussed in this thesis, preoperative images are commonly acquired using MR and need to be matched with X-ray, requiring true *multimodal* registration.

### 3.2.5. Tomaževič et al. 2003 [88]: 2D-3D Registration of CT and MR to X-ray Images

Another approach to achieving multi-modal registration issue is to introduce a segmentation step into the registration pipeline. The algorithm presented in this paper was the first to illustrate a hybrid feature/intensity-based registration. Instead of registering with image intensities, this paper demonstrates the use of gradients to constrain registration and is known as a *gradient*-based algorithm.

To demonstrate the registration, a lumbar spine phantom was scanned in both CT and MR. The spine was then segmented using thresholds and edge-detection, and surface normal vectors $\vec{v}_A(\vec{r})$ were estimated for each modality. Subsequently, 18 X-ray images of the phantom were acquired and their gradients computed using:

$$\vec{v}(\vec{p}) = \nabla I(\vec{p}) \quad , \quad (3.16)$$

where $I(\vec{p})$ is the intensity of an acquired X-ray image at a point $\vec{p}$ on its projection plane. As long as the X-ray C-arm has been previously calibrated for its intrinsic and pose parameters the vectors can be back-projected to the X-ray source location $\vec{s}$ or to any point $\vec{r}$ along its projection line according to,

$$\vec{v}_B(\vec{r}) = \frac{|\vec{p} - \vec{s}|}{|\vec{r} - \vec{s}|} \frac{\hat{n} \times \vec{v}(\vec{p}) \times \hat{e}}{\hat{n} \cdot \hat{e}} \quad , \quad (3.17)$$

with unit vector $\hat{n}$ parallel to the projecting line striking the point normal to the projection plane and unit vector $\hat{e}$ parallel to the point position $\vec{p}$ . The constraining metric of this algorithm is a measure of how well the gradients of each point on the segmented spine surface line up in magnitude and direction to the back projected gradients of the X-ray images. Any pairs with angles more than 90˚ apart are ignored.

$$\text{measure of constraint} = \frac{\sum_i^N \{|\vec{v}_A(\vec{r}_i)||\vec{v}_B(\vec{r}_i)| f(\alpha)\}}{\sum_i^N |\vec{v}_A(\vec{r}_i)| \cdot \sum_i^N |\vec{v}_B(\vec{r}_i)|} \quad , \quad (3.18)$$

$$f(\alpha) \equiv \begin{cases} \cos^4 \alpha = \left[\frac{|v_A(\vec{r}_i) \cdot \vec{v}_B(\vec{r}_i)|}{|\vec{v}_A(\vec{r}_i)||\vec{v}_A(\vec{r}_i)|}\right]^4, & \alpha \in [0, 90°] \\ 0, & \text{otherwise} \end{cases} \quad . \quad (3.19)$$

The algorithm used Powell's method (§3.1.3.1) [89] as its search strategy to maximise (3.18) and find the rigid-body transformation between 3D image modalities and the X-ray's table space. If multiple X-ray views are available, the metric becomes the sum of metrics measured from each view. Results reported in this paper were gathered using two X-ray views per registration, with each view 80˚ apart.

Prior to imaging, six fiducial markers were placed around the spine that were visible in CT, MR and X-ray, which were used to obtain a gold standard registration for validation. Compared against this gold standard, results of the phantom study showed that registration could be

achieved between CT and X-ray with a mean 3D-TRE within 2 mm using a capture range of 6 mm, 91 % of the time. More importantly, multimodal registration between MR and X-ray could also be achieved with a mean 3D-TRE of 2-mm or less with a reduced capture range of 3 mm and an average success rate of 78.8%.

### 3.2.6. van de Kraats et al. 2005 [90]: Multispectral MR to X-Ray Reg. of Vertebra

To improve the results of MR to X-ray registration in [88], the generation of a CT-like data set from MR was proposed in this paper. This was done by attempting to obtain a look up table (LUT) which mapped the intensities of homologous anatomy between MR and CT from training data sets which was used to re-map the MR intensities to look like CT. The CT-Like image was then registered to the X-ray image using the gradient-based registration algorithm proposed in [88]. In a spine phantom study, registration with the CT-like dataset could be achieved within an accuracy of 2 mm with a success rate of 90% within a 5-mm capture range, bettering the results that registration with the MR alone could achieve, which only had a capture range of 1 mm (Table 3.2).

### 3.2.7. Markelj et al. 2008 [91]: Robust Gradient-Based 2D-3D Reg. of CT, MR to X-ray

One disadvantage of using projection or back-projection for spatial correspondence is the loss of depth information resulting in a one-to-many or many-to-one problem, which is ill-conditioned. Using multiple views of the object can recover some of this information since out-of-plane translations in one view project as in-plane translations in another view (Figure 4.2). When multiple views are available, projection and back-projection-based approaches can compute the constraining metric from each view and sum them as in [88]. An alternative is to first perform a reconstruction step then constrain the registration in 3D via a 3D-3D registration algorithm. In [91], Markelj demonstrated this reconstruction approach on a post-mortem spinal column study using a gradient-based method similar to the one in [88].

In this study, two spines were scanned under CT and MR. A set of 100 X-ray images was acquired in a 180˚ arc around each spine phantom which was used to create a third 3D image using 3DRx reconstruction. Registration was performed independently between the X-ray views and the three 3D images. From each 3D image, the spine was segmented using thresholds and edge-detection and their 3D surface normal vectors $\vec{v}_A(\vec{r})$ were estimated. The gradients of the X-ray images used for registration were computed using (3.16) and they were back projected according to (3.17). The back-projected gradients from each view were then summed together to produce a coarse reconstructed gradient vector field according to:

$$\vec{v}_B(\vec{r}) = \sum_{j=1}^{J} \frac{|\vec{p}_j - \vec{s}_j|}{|\vec{r} - \vec{s}_j|} \frac{\hat{n}_j \times \vec{v}(\vec{p}_j) \times \hat{e}_j}{\hat{n}_j \cdot \hat{e}_j} \quad . \quad (3.20)$$

Using the same notation, this equation is essentially the same equation as (3.17) but is extended to perform the reconstruction from multiple views with subscript $j$ denoting which X-ray the quantity belongs to. The metric to constrain the gradients is identical to (3.18) and (3.19) in [88], but the principle difference in paradigm between this algorithm and the previous one in [88] is the inclusion of a reconstruction step.

An advantage that reconstruction can provide over a projection or back-projection approach is that 3D-3D registration can be performed where the one-to-many condition is lifted. This is advantageous during the optimisation stage as it enables adoption of the random sample consensus algorithm [92] as an initial search strategy. This increases the capture range and results in a coarse registration which is then refined using Powell's method [83] [89].

For validation, since the 3DRx image was derived from the X-ray images used for registration, the images were already aligned and provided a calibration-based reference registration. The CT and MR images were then aligned to the 3DRx via a 3D-3D registration algorithm based on maximization of mutual information [93]. Using two X-ray views, quasi-modal registration with CT and 3DRx yielded accurate TREs of 0.32 and 0.17 mm at 90% success in an 11 mm capture range. Multimodal registration with MR achieved 0.48 mm TREs and 69% success rate at a 6 mm capture range.

### 3.2.8. Ector et al. 2005 [68]: 3D MRI and Fluoroscopy Merging

Another feature of the heart commonly used for registration is the cardiac border which consists of the chambers, large vessels and the pericardial sac. Compared to registering with vasculature, the use of cardiac borders for registration means the use of much simpler geometric shapes and therefore considerably fewer constraints for registration. On the other hand, the simple geometry usually leads to an easier segmentation step.

In this paper, Ector *et al.* uses the endocardial contours of the right atrium and venae cavae of the heart, manually segmented from a balanced fast-field echo (bFFE) volumetric MR cardiac scan, and aligns it to a contrast-enhanced silhouette of the heart in X-ray. Registration is performed manually by adjusting the translations and rotations until the gap between the projected MR contours and the silhouette of the contrast-enhanced X-ray shadow is visually minimised in two X-ray views. Both the projected MR contours and the silhouette outlines were manually delineated. The size of the gap was measured as the number of pixels between the two manually delineated contours, divided by the perimeter of the cardiac silhouette. The registration method was applied between a plastic endocardial phantom model and simulated fluoroscopy images of the heart, and then on nine clinical data sets from patients who underwent radiofrequency catheter ablation. Clinical validation reported that registration accuracy was

high but could not be quantified. Since 5 mm is the clinical tolerance for radiofrequency ablation [14], this is the value listed in Table 3.2.

### 3.2.9. Daul et al. 2009 [67]: 3D Cardiac Data Superposition using 2D Image Reg.

Daul *et al.* also present a registration algorithm using the cardiac borders, but performs this semi-automatically. In this paper, the authors aim to register functional 3D tomoscintigraphy data, which represents myocardial perfusion, to contrast-enhanced cardiac X-ray sequences. The registration algorithm was applied to a plastic heart phantom study to quantify the algorithm's accuracy, and was then applied to 21 sets of data from patients suffering from stenoses.

The 3D tomoscintigraphy data was acquired with the single photon emission computed tomography (SPECT) modality using radioisotope thallium-201. The images were acquired such that each slice in the image stack showed a parasternal short axis view of the heart with the origin at the centre of the heart. Intraoperatively, contrast dye was injected into the heart and a sequential biplane X-ray pair was taken with the heart at the isocentre and the patient lying supine. The X-ray C-arm was tracked and calibrated so that its projection and pose parameters were known at all times throughout the procedure. Since the heart was isocentred in both modalities, an initial rigid-body registration was obtained by re-orientating the 3D SPECT volume from parasternal short axis to supine, and then translating the volume so that its isocentre was at the isocentre of the X-ray. Using the X-ray's intrinsic parameters from its calibration, the SPECT volume was projected into each X-ray view to achieve spatial correspondence. In each view, the myocardial edges of the SPECT and X-ray images were segmented from both views using thresholds, edge-detection operations and energy minimising snakes [94]. The cardiac borders segmented from each modality were used as the constraining features for registration. Registration was performed independently in each X-ray view by finding the transformation $\mathcal{M}(\lambda, \delta_u, \delta_v, \theta)$ that consisted of a 2D translation $\vec{\delta} = (\delta_u, \delta_v)$, rotation $\theta$ and scale factor $\lambda$ that aligned the SPECT cardiac border to the X-ray one.

Initially, the transformation was $\mathcal{M}|_0 = \mathcal{M}(1, 0, 0, 0°)$. The algorithm starts by computing the distance image $\mathcal{I}$ from the SPECT contour using a distance transform such that each pixel is given a grey-value proportional to the distance to the closest point along the SPECT border (Figure 3.4). The points along the segmented X-ray cardiac border $\vec{q}_i$ are superimposed onto the distance image and a cost function is computed:

$$S(\lambda, \vec{\delta}, \theta) = \frac{1}{N} \sum_{i=1}^{N} \mathcal{I}(\mathcal{M}\vec{q}_i) \quad , \quad (3.21)$$

where $N$ is the number of points in $\vec{q}_i$.

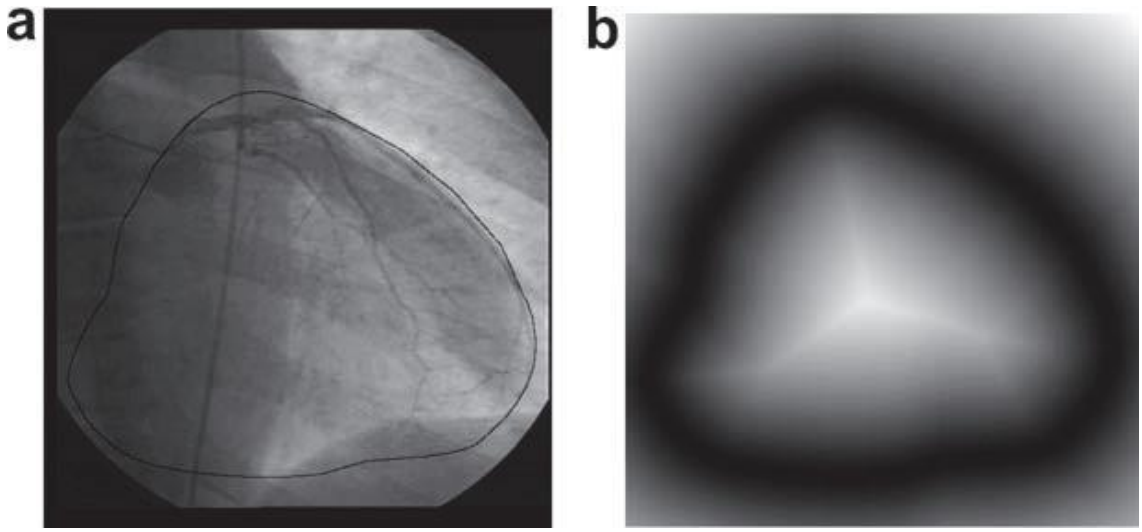


Images taken from [67].

Figure 3.4 a) Example of the distance transform, taken from [67]. A contrast-enhanced X-ray coronary angiogram with the segmented perimeter of the SPECT volume outlined (*black solid closed loop*). b) Applying a distance transform on the segmented contour creates a distance image with pixel grey-levels proportional to how far that pixel is away from the closest point on the perimeter.

Following the pattern in Figure 3.1, the cost function (3.21) is the metric to be minimised, and the minimisation strategy employed is the downhill simplex [82]. In this case, the method is used to find the minimum intensity of the distance image (Figure 3.4b) and the search space is the set of parameters $(\lambda, \delta_u, \delta_v, \theta)$ with initial conditions $\vec{X} = (1, 0, 0, 0°)$. The optimisation strategy halts when the change in error falls below a pre-set value. The error is given as:

$$\varepsilon = \sqrt{\frac{\sum_i \left(S(\vec{v}_i) - S(\vec{v}_c)\right)^2}{N}} \quad . \qquad (3.22)$$

To avoid local minima, translations were optimised first while keeping the rotation and scaling constant. Then translation and rotations were combined and optimised while keeping scaling constant, and finally all four parameters were optimised together.

Once the optimisation is complete, the centroid of the last generated polytope defines the transformation used to align the X-ray to the projected SPECT cardiac borders. After alignment, information from the X-ray biplane, for example a segmented coronary tree, can then be back-projected and reconstructed into the SPECT volumetric space.

In the paper, the registration algorithm was applied to two phantom cases modelling the heart. This was filled with a radioactive tracer to simulate heart perfusion in a tomoscintigraphy scan, and set with a copper arterial tree pattern on the surface of the phantom to simulate contrast injection of the coronaries in a biplane X-ray acquired with a 90˚ separation angle. A single landmark visible in both modalities was used to assess a 2D-TRE. After applying the registration

algorithm to the phantom scans, results of the study yielded a 6-mm TRE, which was reduced to 2-mm by performing the registration on 20 views instead of two. Daul *et al.* demonstrated clinical feasibility in 34 sets of data from 21 patients suffering from stenoses. In 20 of the 34 data sets, the patients were at rest during tomoscintigraphy acquisition and the remaining 14 data sets were obtained while under stress. Clinical experts were used to localise the landmarks in the clinical studies. The registration algorithm applied to the clinical studies was reported to yield 2D-TREs of 5.3 ± 4.4 mm for the patients at rest with 60% of them falling below the 5 mm, and 5.5 ± 4.7 mm for the patients at stress, with 57% of them falling below 5 mm. 5 mm is the isotropic spatial resolution of the tomoscintigraphy scan and also the clinical tolerance for catheterisation procedures such as coronary artery disease (§1.5). For compatibility with the other results in (Table 3.2), these accuracies were re-calculated to be 7.8 ± 4.0 mm and 6.4 ± 3.4 mm for rested and stressed patients respectively. From the 34 rest and stress registrations, 29 used sequential biplane while 5 cases used sequential tri-plane X-ray. Regardless of rest or stress, the average 2D-TRE for biplane registration was 6.7 ± 3.7 mm, of which ten were at or below the 5-mm threshold, and for triplane registration was 9.9 ± 3.5 mm, with none of them at or below 5-mm. Each case using biplane X-ray required about 8 minutes to perform the segmentation, registration and 3D reconstruction and rendering. These results are summarised in Table 3.2.

### 3.2.10. Kita et al. 1998 [95]: Real-time Reg. of 3D Cerebral Vessels to X-ray

The alternative feature-based approach to fiducial markers is to use anatomical landmarks. These landmarks are regions of the anatomy that are relatively easy to identify in both registration modalities, such that a correspondence can be made. Prominent anatomical landmarks in the cardiac vicinity are the chambers, the vasculature (particularly, bifurcations in the vasculature), and the epicardium.

Anatomical landmark registration algorithms have the advantage of not requiring insertion of fiducials and hence minimizing disturbance to the preoperative workflow. Additionally, relative motion between the landmark points and the target organ may be avoided if landmarks are chosen from the target itself. However, there are two major disadvantages to this approach. One is that this has a high reliance on a good segmentation of the target in both registration modalities. The other is that since most target organs deform in complex ways, non-rigid motion may occur. This may compromise the accuracy and precision of the registration if rigid-body motion is assumed.

With the aid of angiography, the vasculature of the brain has been used to provide features that are used for 2D-3D registration [95] aiding in visualization of endovascular treatment of intracranial aneurysms using fluoroscopy guided coil embolization procedures. While the brain

and heart are two very different organs, they are both surrounded by a large amount of vasculature; hence it should not be difficult to adopt the cerebral image registration using angiograms to that of cardiac. In this paper, Kita introduced a 2D-3D registration method between MR and X-ray angiographs of the brain.

The algorithm requires that the intrinsic and extrinsic calibration parameters of the X-ray system, and the pose of the brain between the two angiographs are already known. Subsequent rotations of up to 20˚ of the head and translations within ±10 cm in the directions perpendicular to the X-ray beam and ±20 cm in the direction of parallel to the projection may be determined.

The subsequent changes in the $\mathcal{M}_{\text{reg}}$ are determined by first extracting regularly sampled points along the medial line of the cerebral vessels from the MRA and projecting them onto the X-ray. Using these projected points, a Voronoi-like diagram [96] is generated in their vicinity; the resultant tessellation results in an associated territory assigned to each projected point. The corresponding point on the X-ray angiograph is chosen within the intersection of a skeletonisation of the X-ray vessels and the Voronoi area of the MRA projected points. Erroneous matches were manually removed. With the point-to-point correspondence determined, the subsequent extrinsic parameters were determined using the iterative closest point (ICP) algorithm (3.1.3.4) [84].

The registration method was applied to nine images of two 3D models, where the MRA data was rotated and translated within its working bounds. In eight cases, the amount of rotation and translation was correctly determined – the one failure case was due to poor 2D skeleton extraction. A registration to clinical accuracy of 5mm was obtained in 18 iterations, taking 5.7 seconds. Results are summarised in Table 3.2.

### 3.2.11. Turgeon et al. 2005 [97]: Coronary Angiogram Registration

In this paper, Turgeon presents a 2D-3D registration method using the cardiovascular system. The motivation behind this paper was to improve minimally invasive robotic coronary artery bypass procedures. The registration in this paper was between 3DRx angiograms (3DRA) of the heart, and the DRRs produced from them. The 3DRA data were segmented while the 2D data were DRRs produced by ray-tracing the segmentation on top of a realistic background, i.e. a DRR of another heart in the appropriate orientation without contrast enhancement. The resultant DRR with the background and the ray-traced segmentation were then converted to a binary image to increase its contrast. All images were cardiac and respiratory gated.

This approach does not fall under feature- or image-based registration since a segmentation step is used to extract the cardiovasculature, a step indicative of feature-based approaches. However, the projection of the extracted cardiovasculature is used to generate a new binary image and a

standard image-based registration method is then applied. The segmented 3DRA is given an arbitrary initial pose and is projected onto the binary DRR, and the entropy correlation coefficient (ECC) similarity measure is calculated between it and the projection and the pose is refined using the downhill simplex method (§3.1.3.3) [82].

The authors reported a 3D-RMS error of 1.60 ± 0.21 mm and a robustness of 79% in 80 registration tests, derived from 8 datasets. The authors also experimented using two DRRs for the registration and found a 3D-RMS error of 0.53 ± 0.08 mm and a robustness of 99% in 80 tests. Adding a 10% timing offset between the two DRRs in order to mismatch their phase, as well as creating artificial reconstruction errors, the algorithm was found have an accuracy of 2.19 ± 0.77 mm and a robustness of 94% using two planes in 80 tests. Additionally, the authors report that the ECC similarity measure was the most accurate compared to, in decreasing accuracy order, normalised mutual information, mutual information, mean absolute difference, mean square distance, and normalised cross correlation.

### 3.2.12. Duong et al. 2009 [71]: 2D–3D co-reg. of MSCT seg. with 2D angiograms

In this paper, Duong presents a registration algorithm that also matches on cardiovasculature with application to percutaneous coronary interventions (PCI). Registration was performed between preoperative CT and intraoperative contrast-enhanced coronary angiograms using the coronary arteries to constrain the registration. In this feature-based approach, the left anterior descending (LAD), left circumflex artery (LCx) and right coronary artery (RCA) were segmented from the CT volume by selecting points at their ostia to seed a front propagation method, which extracts the centreline and cross-sectional radius of the vessels. The same vessels were segmented from intraoperative contrast-enhanced X-ray angiograms by first selecting a point at both the proximal and distal ends and then moving the computer mouse, or pointing device, over the vessel. A semi-automatic software found vessels by applying a vesselness transform [98] over the X-ray image and finding the path between selected proximal and distal points that followed the path of maximum vesselness and lay closest to the mouse position as it was moved along the vessel.

An initial alignment, represented by the rigid-body transformation $\mathcal{M}$, between the CT and X-ray was made by placing the CT at the isocentre of the X-ray and assuming the patient was lying supine during both image acquisitions. The X-ray C-arm was assumed to be tracked for its pose parameters and pre-calibrated for its projection parameters. The centrelines of the vessels extracted from CT were projected onto the X-rays and the registration was achieved by finding the rigid-body transformation that minimised the root-mean-square distance error between the projected CT vessel centrelines and the X-ray vessel centrelines, according to the following:

$$\mathcal{M}_{\text{reg}} = \underset{T}{\text{argmin}}\left(\frac{1}{N}\sum_{n}^{N}\sum_{i}\left|\vec{U}_{n,i} - \mathcal{C}\mathcal{M}\vec{V}_{n,i}\right|\right) \quad , \quad (3.23)$$

where $\vec{U}_{n,i}$ are the points along the $n^{\text{th}}$ vessel centreline segmented in X-ray, $\vec{V}_{n,i}$ are the points along the vessel centrelines segmented from CT, $\mathcal{C}$ is the matrix encoding the projection parameters of the C-arm and $\mathcal{M}$ is the estimate transformation used during optimisation. Any number of vessels $N$ can be used in the registration, with each adding additional constraints to the registration. To find the best rigid-body transformation between the imaging modalities, the iterative closest point (ICP) optimisation strategy is used (§3.1.3.4) [84]. To avoid local minimums, the optimisation is run twice, once only optimising for the three translations, and using the result of this optimisation as the new initial estimate, a second optimisation is run with the full six pose parameters.

The registration algorithm was applied to five clinical data sets from patients undergoing PCI of their coronary arteries. For validation, the preoperative CT datasets were first manually aligned with the intraoperative fluoroscopy by a clinical expert. From the five data sets, the automated registrations were performed using four different CA configurations; registration based only on the LAD was performed in three of the sets, on the LCx in two, on the RCA in two and on both the LAD and LCx together in one set. The accuracy of the algorithm in terms of average 3D-TREs, compared with the clinical alignment as the standard registration, were 3.9 mm with the LAD, 4.7 mm with the LCx, 7.3 mm with the RCA and 3.0 mm with both the LAD and LCx. Aggregating these results, the average TRE using a single vessel was 5.1 mm compared to 3.0 mm using two vessels, indicating that the more vessels used to provide constraints the more accurate the registration.

In one of the data sets, Duong shows that the method can still be applied if an X-ray coronary angiogram is not available but instead there is a catheter inserted into one of the CAs. In one of the patients, points along the catheter lying inside the LAD were extracted from the X-ray using the same method used to segment the CA, and these points were used in place of the vessel centreline in (3.23). The mean 3D-TRE of the catheter-vessel constrained registration compared to the clinical standard was 3.4 mm, comparable to registering with vessel centreline-to-centreline.

### 3.2.13. Sra et al. 2005 [17]: CT-Fluoro Registration

In cardiac catheterisations, the use of the catheters for registration is attractive since these devices are the main instruments of the procedure and are placed directly into the heart with excellent visibility in X-ray. Sra *et al.* was the first to propose using the CS catheter for 2D-3D registration of both a phantom model and clinical study of 20 patients undergoing RF ablation for paroxysmal atrial fibrillation. In this approach a catheter was placed in the CS via the superior

vena cava (SVC). The CS and the SVC were segmented from CT data and then projected onto the X-ray. The patient was assumed to lie in a similar manner on both the CT and X-ray table during imaging and isocentre-supine constraints were used as an initial registration. The CT data was then projected onto the X-ray so that translational and scaling parameters of the X-ray system could be approximated using the SVC and CS catheters as constraints. Projection onto a second X-ray view at a different angle was used to manually correct rotational errors in the registered 2D image, which occurred in 9 out of the 20 cases. Of these cases, 51% of 79 image sequences registered required manual rotational correction, giving a registration success rate of 49%. Rotational and translational corrections would have been needed every time the X-ray C-arm, patient or patient table was moved. In a phantom study, the authors reported a 2D-TRE of 1.43 ± 0.53 mm using beads placed along the CS which was used for registration. The accuracy of this algorithm is summarised in Table 3.2.

### 3.2.14. Liao et al. 2008 [99]: Catheter Based 2D-3D Reg. of Fluoro. And CT for EP

The work presented in Sra [17] used a projection strategy to constrain a catheter inserted intraoperatively into the CS via the SVC to its corresponding vessel for registration in EP procedures. However, registration was performed manually and in a single view. In this paper by Liao, an automatic registration algorithm was proposed which matched the CS vessel segmented from CT to its indwelling catheter in intraoperative X-ray for EP procedures. The algorithm was initially applied to a simulated data set to quantitatively assess its accuracy, and then to a clinical data set which was assessed for accuracy through visual inspection.

In the preoperative stage of the study, a CT cardiac scan of the patient was taken and the CS was segmented automatically using the method presented in [100]. In the subsequent intraoperative stage, the CS catheter was segmented semi-automatically from each X-ray by first enhancing the contrast of tubular structures using a Hessian-based imaging filter. Points were manually picked on the enhanced CS catheters which were used to seed a fast marching method to extract the remainder of the catheter.

The paper presents two approaches to achieve spatial correspondence between the 2D and 3D modality. The first is a projection strategy where the CT data is projected onto a biplane X-ray image pair using isocentre and supine constraints. A transformation is then found that minimises a distance-based cost function metric

$$\mathcal{M}_{\text{reg}} = \underset{T}{\operatorname{argmin}} \left( \sum_i \left| \vec{A}_i - \mathcal{C}_A \mathcal{M} \vec{D}_i \right| + \sum_i \left| \vec{B}_i - \mathcal{C}_B \mathcal{M} \vec{D}_i \right| \right) \quad , \qquad (3.24)$$

where $\vec{D}_i$ are the points along the centreline of the 3D CS, $\vec{A}_i$ are the points along the CS catheter in the first view, $\vec{B}_i$ are the 2D points along the CS catheter from the second view, $\mathcal{C}_A$ is the

projection matrix of the first view, $\mathcal{C}_B$ is the projection matrix of the second view and $\mathcal{M}$ is the estimate rigid-body transformation during optimization. The *best neighbour hill climbing* optimisation strategy (§) is used here with the search space being the six pose parameters that make up the rigid-body transformation, i.e. three translations and three rotations, $\mathcal{M} = \mathcal{M}(x, y, z, \alpha, \beta, \gamma)$. To avoid local minima, the optimisation is run twice, once only optimising for the three translations, and using the result of this optimisation as the new initial estimate, optimisation is repeated using the full six pose parameters. This projection strategy is applicable to single-view registration by dropping the second term in (3.24).

Reconstruction is the second approach to achieve spatial correspondence when biplane information is available, by minimising the following cost function in place of (3.24):

$$\mathcal{M}_{\text{reg}} = \underset{T}{\operatorname{argmin}} \left( \sum_i \left| \vec{C}_i - \mathcal{M}\vec{D}_i \right| \right) \quad , \quad (3.25)$$

$$\vec{C}_i = \text{reconstruction of } \vec{A}_i \text{ and } \vec{B}_i \quad . \quad (3.26)$$

Correspondence between $\vec{A}_i$ and $\vec{B}_i$ is maintained using epipolar geometry (Figure 3.3, Figure 4.2) and $\vec{C}_i$ is the reconstruction of the CS catheter in space from these corresponding 2D points (Figure 3.3). To find the best rigid-body transformation between the sets of points $\{\vec{C}_i\}$ and $\{\vec{D}_i\}$, the iterative closest point (ICP) optimisation strategy is used [84] (§3.1.3.4).

Liao first applies the registration on simulated data using a 3D CT image of the heart. The CS is segmented from the image and its centreline is found. Points along the centreline were smoothed and elongated to simulate a catheter, which was then projected onto two projective planes around the centre of the CT image to simulate biplane X-rays. This setup was used as a ground truth for validation. The pose of the CT volume was then adjusted two hundred times randomly within ±8° and ±20 mm isotropically from the ground truth and then registered to the simulated X-rays. Salient points 15 cm away from the CS were picked on the CT volume to act as targets for registration. On average, registration could be achieved with an accuracy of 14.08 mm mean 3D-TRE in 6.93 seconds using a single X-ray view, 3.82 mm TRE in 75.26 s using biplane X-rays, and 3.19 mm TRE in a significantly faster time of 0.62 s with the reconstruction method.

The algorithm assumes that the catheter lies along the centreline of the CS, which may not necessarily be true. To test how much violations of this assumption would affect the registration, local variations of the CS catheter from the centreline were generated by randomly moving points of the catheter within 5 mm from the centreline of the CS, i.e. half of the diameter of the CS, and projecting onto the X-ray to use for registration with the CS centreline. This increased

the average target registration errors slightly for to 14.12 mm with a single view, 4.00 mm using biplane, and decreased the target registration error to 2.34 mm with the reconstruction method.

Finally, registration was applied to *in vivo* clinical data taken from an EP procedure. Registration using biplane X-ray for both the projection and reconstruction strategies was considered achievable according to clinical experts. However, registration failed using only a single view. There were no accuracy value estimates for the clinical data.

### 3.2.15. Ma et al. 2010 [23]: MRI to X-ray Fluoro Overlay for Guidance of CRT

In current clinical settings, a common registration technique is to insert a catheter and loop it inside a target chamber, such as the left atrium (LA), and then manually align the preoperative CT data from several X-ray views. This is demonstrated in this paper by Ma *et al.* using a specially designed software platform (EP navigator, Philips Healthcare, Best, Netherlands).

The platform displays up to four different X-ray views of the heart on a single screen acquired intraoperatively, and requires that the C-arm is precalibrated and tracked so that its projection parameters and pose are known for each view. The patient was assumed to be lying supine and the centre of his or her heart is roughly at the isocentre of the C-arm. Volumetric surface data of the heart, typically whole-heart segmentation from MR, can be loaded into the platform which is then placed at the isocentre of the heart in a supine position and projected onto the X-ray views using the projection and pose parameters supplied by the C-arm. The user is then allowed to modify the pose of the surface data in any of the views which will automatically update in the other views. By iterating through each view and adjusting the pose so that corresponding features from the surface data and X-ray constrain one another, a manual registration can be achieved.

Using this platform, Ma *et al.* was able to perform accurate registrations in seven live cardiac resynchronisation therapy (CRT) cases. Each patient underwent a preoperative MR cardiac scan and the resultant image was segmented for the four chambers of the heart, coronary venous anatomy and any scarring of the heart. Intraoperatively, a looped catheter was placed inside the right atrium, providing a constraint for manual registration by constraining the catheter loop to be entirely enclosed within the perimeter of the projected right atrium in each X-ray view. At least three views were used to perform the registration for each case. For validation, multiple venograms with contrast-enhancement in the coronary sinus (CS) were taken from multiple views and ten points along their centrelines extracted in each view. Points along the centrelines of the projection of the CS segmented from MR were also extracted in each view. The error was measured as the root-mean-squared (RMS) distance error between the 10 X-ray CS centreline points to their nearest projected CS centreline points. Averaging over each view, the mean 2D

distance error for each case was determined to be 1.3 ± 0.68 mm. Registration was successful in all seven cases.

## 3.3. Summary

Intensity-based algorithms can provide very accurate 2D-3D registration by maximising the quantity of image data available for registration [87], [79], but are ideally suited for quasi-intra-modal registration. Intensity-based registration of multimodal images can be achieved by matching on the spatial derivatives of the intensities [88] [91] or by applying a re-mapping function to revert the multimodal problem back into one of quasi-intra-modal [90], but these methods have only been shown to work on the spine. Registration of the heart with intensity-based approaches remains elusive.

Currently, registration can be performed automatically and in real-time using a hybrid X-ray/MR guidance system proposed in [30] to within 5-mm accuracy. However, this requires a specially designed hardware that is not available in many hospitals. The use of fiducial skin markers or other surrogate structures is another approach to registration [16], but accuracy may be lost if there is motion between the heart and the markers. This source of error can be avoided by using anatomical landmarks from the target itself for registration, such as vessel bifurcation points and ostia [95] [97], or the cardiac shadow [68] [67]. However, repeat contrast agent injections may be needed for their reliable segmentation. In cardiac catheterisations, the use of the catheters for registration is attractive since these devices are the main instruments of the procedure and are placed directly into the heart with excellent visibility in X-ray [17].

Among the existing catheter-based approaches, the method used in [70] is a manual approach, and therefore there would require the special attention of an operator. Sra *et al.* report in [17] [23] that manual registration was required in nine out of 20 cases and therefore does not satisfy the criteria of being highly robust. Likewise, the method presented in [71] using an iterative search strategy to perform registration. For cardiac catheterisation procedures where robustness is crucial, a global search strategy may be a better choice. Furthermore, the methods in [17] [23] [71] perform registration in 2D and so their accuracy would be affected by out-of-plane translation and rotation errors.

In current clinical settings, a common registration technique is to insert a catheter and loop it inside a target chamber, such as the left atrium (LA), and then manually align the preoperative CT data from several X-ray views (EP navigator, Philips Healthcare, Best, Netherlands) [23].

The algorithms reviewed in this chapter are summarised according to their problem statement, paradigm and optimisation strategy according to Table 3.1, and their accuracy, robustness and computational times are listed for numerical comparison (Table 3.2).

Accuracy is given in terms of a mean 2D- or 3D-TRE if available. TREs need to be assessed compared to a standard reference registration. For phantom experiments, fiducial markers are usually used to provide an independent gold-standard registration against which the accuracy of the algorithm can be measured. For registration on clinical datasets however, obtaining a gold standard registration is difficult. The use of techniques such as XMR [30] or skin fiducials [65] can provide registrations accurate enough for routine clinical practice, however the accuracy of these methods are adversely affected by cardiorespiratory motion and other sources of error. Therefore, these techniques would not be suitable to provide a gold standard registration. Instead, registration is usually assessed by generating a 2D-3D overlay and measuring the distances between corresponding anatomical features from the 2D image and the projection of the 3D data.

Robustness is measured in terms of a success rate percentage, with success defined as achieving accuracy within a clinical tolerance – 5 mm for most targets in the heart – or being deemed successful by a clinical expert. In iterative approaches which depend on initial positioning, the capture range is also provided, which gives an approximate measure of how close the initial alignment must be in order to converge to a successful registration. Computational times only include the amount of time required to perform the registration within the intraoperative step where time is of the essence. It is assumed that there is ample time in the preoperative stage to perform any necessary processing of the 3D preoperative images.

| method | study | target | *n* | modality | basis | constraint metric | search | projection | back-projection reconstruction | # views | accuracy (mm) | success (%) | range (mm) | time (s) |
|---|---|---|---|---|---|---|---|---|---|---|---|---|---|---|
| Rhode 2005 | clinical | heart | 13 | MR | calibration | external tracking | analytic | | | -- | 4.9 | 100 | ∞ | 0 |
| Gutiérrez 2007 | clinical | vasculature | 3 | MR | feature | skin markers | analytic | ✓ | | 1 | 1.6 | 100 | ∞ | 0 |
| | | Iliac | 6 | | | | | | | | 3.5 | 33 | | |
| | | femoral | 8 | | | | | | | | 2.3 | 100 | | |
| | | chamber | 3 | | | | | | | | 5.2 | 100 | | |
| Lemieux '94 | phantom | skull | 1 | CT | intensity | gradient correlation | Powell | ✓ | | 2 | 1.0 | 92 | 21 | 1800 |
| Penney 1998 | phantom | spine | 4 | CT | intensity | cross correlation | neighbour | ✓ | | 1 | 1.4 | 55 | 2 | 74 |
| | | | | | | entropy difference | | | | | 1.5 | 47 | | |
| | | | | | | mutual information | | | | | 5.1 | 5 | | |
| | | | | | | gradient correlation | | | | | 0.5 | 95 | | |
| | | | | | | pattern difference | | | | | 0.5 | 100 | | |
| | | | | | | gradient difference | | | | | 0.5 | 100 | | |
| Tomaževič 2003 | phantom | spine | 1 | CT | hybrid | spine gradient matching | Powell | | ✓ | 2 | 2.0 | 91 | 6 | 20 |
| | | | | MR | | | | | | | 2.0 | 79 | 3 | 32 |
| van de Kraats 2005 | cadaver | spine | 2 | CT | hybrid | spine gradients matching *MR to CT | Powell | | ✓ | 2 | 2.0 | 90 | 6 | -- |
| | | | | MR* | | | | | | | 2.0 | 90 | 5 | |
| | | | | MR | | | | | | | 2.0 | 90 | 1 | |
| Markelj 2008 | phantom | spine | 1 | 3DRx | hybrid | spine gradient matching | Powell | | ✓ | 2 | 0.2 | 90 | 11 | 25 |
| | | | | CT | | | | | | | 0.3 | 90 | 11 | |
| | | | | MR | | | | | | | 0.5 | 69 | 6 | |
| Ector 2005 | clinical | heart | 9 | MR | manual | cardiac border | manual | ✓ | | 2 | 5.0 | -- | -- | -- |
| Daul 2008 | phantom | heart | 1 | SPECT | feature | cardiac border | simplex | ✓ | | 2 | 6 | -- | -- | 480 |
| | clinical | | 29 | | | | | | | | 6.7 | 34 | | |
| | | | 5 | | | | | | | 3 | 9.9 | 0 | | |
| Kita 1998 | clinical | brain | 21 | MR | feature | vasculature | ICP | ✓ | | 1 | 5.0 | 89 | -- | 6 |
| Turgeon 2005 | computer | heart | 80 | model | hybrid | coronary arteries entropy correlation | simplex | ✓ | | 1 | 1.6 | 79 | | 32 |
| | | | | | | | | | | 2 | 0.5 | 99 | | 17 |
| Duong 2009 | clinical | heart | 7 | CT | feature | vessel centrelines | ICP | ✓ | | 1 | 5.1 | 100 | -- | 2 |
| | | | 1 | | | 2 vessel centrelines | | | | 1 | 3.0 | 100 | | |
| | | | 1 | | | catheter-vessel | | | | 1 | 3.4 | 100 | | |
| Sra 2005 | phantom | heart | 1 | CT | feature | catheter-vessel | manual | ✓ | | 1 | 1.4 | -- | -- | 5 |
| | clinical | | 20 | | | | | | | | 5.0 | 49 | | |
| Liao 2009 | computer | heart | 1 | CT | feature | catheter-vessel | neighbour | ✓ | | 1 | 14.1 | -- | -- | 7 |
| | | | | | | | neighbour | ✓ | | 2 | 3.8 | | | 75 |
| | | | | | | | ICP | | ✓ | 2 | 3.2 | | | 1 |
| | clinical | | -- | | | | neighbour | ✓ | | 1 | -- | 0 | | |
| | | | | | | | neighbour | ✓ | | 2 | 5.0 | -- | | -- |
| | | | | | | | ICP | | ✓ | 2 | 5.0 | -- | | |
| Ma 2010 | clinical | heart | 7 | CT | feature | catheter-chamber | manual | ✓ | | 4 | 1.3 | 100 | -- | 300 |

Table 3.2 – A comparison of relevant registration techniques categorised by the type of study, target of registration, number of registrations (*n*), 3D modality, nature of registration basis, constraint and metric, search strategy and image dimensionality. Accuracy in terms of a TRE, success rate, capture range and computation time are listed for quantitative comparison. Shaded grey values under accuracy used the clinical tolerance of 5 mm in place of a clinical expert's visual inspection that the accuracy is good enough.

## 3.4. Conclusion

Based on the review, two 2D-3D image registration algorithms are proposed and described in terms of their problem statement, paradigm and optimisation procedure (Table 3.1). Major design choices in the paradigm and optimisation procedure are discussed with evidence based within the literature.

### 3.4.1. Problem Statement

The problem statement in the work behind this thesis is to register 3D CT or MR image data from any pre- or perioperative modality and overlay it onto intraoperative X-ray. This has applications in cardiac catheterisations procedures where the overlay can act as a roadmap to help guide the procedure, and in biophysical modelling applications where further co-registration allows complementary data to be used in the models. The three main cardiac catheterisation procedures focused in this thesis are percutaneous coronary interventions (PCI), cardiac resynchronisation procedures (CRT) and RF ablations (RFA). The aim is to develop a clinically robust method to perform 2D-3D registration of volumetric cardiac data obtained preoperatively to projective fluoroscopy for cardiac catheterisation purposes. In current practice, CT is more common for preoperative imaging due to wider availability and low per-patient cost [101]. However, there is a growing trend in usage of MR for preoperative imaging, owing to the versatility of MR and its ability to acquire both anatomical and functional images of the heart, without the risks of exposure to ionising radiation [61]. 3DRx is also gaining in popularity as a modality able to acquire high-quality 3D cardiac images intraoperatively [102].

### 3.4.2. Paradigm: Registration Basis

The 2D-3D registration problem in this thesis is *multi-modal*, and therefore a feature-based approach is chosen over an intensity-based one. Multi-modal 2D-3D intensity-based approaches are generally difficult to achieve and tend to show less accuracy and robustness [90]. Intensity-based approaches also tend to be slower since a large number of data elements are compared during optimisation instead of a smaller number of extracted points [103]. Speed is important in the clinical environment in order to avoid the clinical team waiting on the registration algorithm and causing disruption to the clinical workflow. A calibration-based approach was excluded since it may require expensive and dedicated equipment, limiting clinical applicability [30].

### 3.4.3. Paradigm: Registration Constraint

To address the main source of error caused by the rapid change in shape and pose throughout the cardiac and respiratory cycle, the use of catheters as a feature to constrain registration is attractive since they remain relatively stationary with respect to the target of registration, which is the heart itself [17] [23] [71] [99]. With catheters as the main feature for registration, there would be no additional devices or images required, partially satisfying the criteria of minimal disruption to the clinical workflow. The clear visibility in X-ray also means that no nephrotoxic contrast agent injections are needed, further satisfying this criteria.

Therefore, in this thesis, a catheter-based approach is chosen as the main feature for registration. Two novel catheter-based algorithms are proposed and validated in this thesis. The algorithm

are designed to be suitable for the cardiac catheterisation workflow. The first algorithm performs registration by constraining catheters to lie within vessels, and the second performs registration by constraining looped catheters to lie within chambers of the heart.

The focus is on the use of the catheters that are already found in the clinical workflows of cardiac interventional procedures.

In PCIs, the stenotic CA will need to be cannulated. In order to access the CA, the catheter must enter via the Ao and into the ostium (Os) of the CA. These parts of the vessel can be used to constrain a 2D-3D registration, which can provide overlays to aid the guidewire navigation into various branches of the CA. After treatment is complete, the guidewire can remain in the treated CA and can be used in conjunction with the DAo to provide more constraints for registration which is useful for postoperative treatment validation or biophysical modelling.

During CRT, pacemaker leads are inserted into the LA, RA, RV and CS via the SVC depending on the optimal lead placement, determined preoperatively. The leads can be first placed into the chambers and CS Os to provide constraints for a 2D-3D overlay, which can assist the navigation of the LV lead into the various branches of the CS. Once the CS lead is in place, this can be used in conjunction with the other leads to provide a better constrained registration for treatment validation and biophysical modelling.

For RFA, catheters enter into the heart via either SVC or IVC. In some cases, for example when treating right ventricular (RV) outflow tract tachycardia [104], the catheter will need to be navigated towards the pulmonary artery (PA) by going through the tricuspid valve and then into the RV outflow tract. A trans-septal puncture is necessary to access and treat the left side of the heart (LH). LH treatments include PV isolation for AF which takes place in the LA, and LV mapping and ablation for ventricular tachycardia.

In both RFA and PCI, a catheter is usual placed inside the CS to collected essential intra-cardiac signals (ICS) information which are monitored and interpreted throughout the procedure by a dedicated technician. The CS is accessed via the IVC or SVC and can be used as registration constraints.

The list of catheterised vessels relevant to each procedure is summarised in Table 3.3.

| | LA | LV | RA | RV | DAo | AAo | CA | PA | PV | IVC | SVC | CS | CA |
|---|---|---|---|---|---|---|---|---|---|---|---|---|---|
| **PCI** | | | | | G | G | | | | | | | G |
| **CRT** | | | $L_1L_2L_3$ | $L_2$ | | | | | | | $L_1L_2L_3$ | $L_3$ | |
| **RFA in LH** | | | AE | A | | | | A | | AE | AE | E | |
| **RFA in LA** | A | | AE | | | | | | A | AE | AE | E | |
| **RFA in LV** | A | A | AE | | | A | | | | AE | AE | E | |

Table 3.3 – Summary of catheterised vessels and chambers according to the intervention. Catheters are labelled as A for ablation, L for CRT lead, G for guidewire, and E for ICS lead.

### 3.4.4. A Catheter-Vessel-Based Registration Algorithm

The first registration algorithm proposed, which will be explored in Chapters 6 and 7, uses catheters reconstructed in 3D space from a sequential biplane X-ray pair and matches them to their corresponding vessels segmented from 3D data. This work is most similar to the catheter-based algorithms presented in [17], [71] and [99]. However, the approach differs from that of Sra *et al.* [17] and Duong *et al.* [71] by the inclusion of a biplane X-ray reconstruction step, and performs the registration in 3D to eliminate the errors associated with projections [91] [99]. After registration, the aligned 3D data is projected onto the X-ray image using the pre-calibrated projection parameters of the X-ray system. Liao *et al.* [99] also presents a catheter-based approach using reconstruction; however Liao only uses a single catheter for registration, which may not be sufficient as a constraint. In the algorithm developed in this thesis, a second catheter is introduced.

The novelty of this method will be to use a global search strategy when trying to match catheters to corresponding vessels, which may have an extensive number of branches which should increase the robustness of the algorithm and also avoids the need for a knowledgeable user to identify the branch containing the catheter. The reliance of user input [105] may limit the practicality of an algorithm for clinical practice. Global strategies are superior to local iterative schemes in terms of finding the best registration according to the defined metric since they avoid falling into local optima in the search space, and do not need to initialise the alignment, which may again require user input.

Another contribution to knowledge in Chapter 6 is the exploration of various configurations in order to determine which combination of catheters performs the best in terms of accuracy, and which combination performs the worst.

### 3.4.5. A Looped-Catheter-Based Registration Algorithm

The second catheter-based approach, which will be presented in Chapter 7 of this thesis, extends the novelty of exploring various catheter configurations of Chapters 5 and 6.

The algorithm is an automated algorithm that makes use of catheter loops formed inside target chambers of the heart, and uses these loops to align the preoperative data to one or more X-ray views [23]. The main advantage to this approach is that it makes use of a common clinical technique of looping catheters for visual reference. To achieve the accuracy and robustness necessary for automation, the cardiac shadow adds an additional constraint as in the algorithms presented by both Ector [68] and Daul [67]. However, in order to avoid the need for a contrast agent injection, only the upper border of the shadow is used since it is readily visible in X-ray images of the heart without contrast agents. For versatility, the projection strategy is used to achieve spatial correspondence so that the algorithm can be applied to both single view and biplane X-ray image acquisitions.

An advantage of the proposed registration catheter-based methods is that it only needs to be performed at the beginning of the procedure and is then updated automatically by tracking the motion of the X-ray C-arm and table. Repeat registration is only required if the patient moves on the X-ray table. A single view registration would be useful for detecting when the registration is no longer valid, for example due to bulk patient motion, and can be used to apply small corrections to the registration as necessary.

# Chapter 4

## 4. Spatial Correspondence and Information Extraction

This purpose of this chapter is to provide a reference for Chapters 5, 6 and 7, which are the technical chapters of this thesis and is composed of two parts. The first part describes a mathematical framework to achieve spatial correspondence, and subsequently registration, between 2D and 3D features. It will also describe how to measure the accuracy of the registration and tie it to the clinical accuracy objectives set in [14]. The framework will be based on the *pin-hole camera model* and *rigid-body motion model*, which are the two assumptions used throughout this thesis to describe the X-ray fluoroscopy system and the relationship between coordinate systems defined by the imaging modalities. The second part describes two software tools used in this thesis to extract 2D and 3D features from images during the information extraction step.

### 4.1. Spatial Correspondence

The problem in 2D-3D image registration is that features extracted from the 3D image will have a different dimensionality from those extracted from the 2D image, and so will need to be brought into spatial correspondence. This can be achieved via forward or backward projections.

Projective imaging modalities, such as X-ray fluoroscopy, are usually assumed to follow the pin-hole camera model [22]. The pin-hole camera has a singular point of focus called the source from which a cone-shaped capturing beam is projected towards the imaging target (Figure 4.1). The base of the cone is intersected by a plane placed behind the target, called the projection plane, where the image is captured. Lines emanating from the source to the plane are known as projection lines, and the imaging target information travelling along these lines is integrated before reaching the plane, resulting in a loss of depth information. This type of projection is known as a perspective projection. The pin-hole camera model has ten degrees of freedom (DOF), four DOFs describe the perspective projection and are known as the *intrinsic* parameters of the system, $\vec{I} = (c_s, l_s, k_1, k_2)$. The remaining six DOFs describe the pose of the system in terms of a rigid-body translation and rotation $\vec{E} = (\delta_x, \delta_y, \delta_z, \alpha, \beta, \gamma)$, and are known as the *extrinsic* parameters of the system.

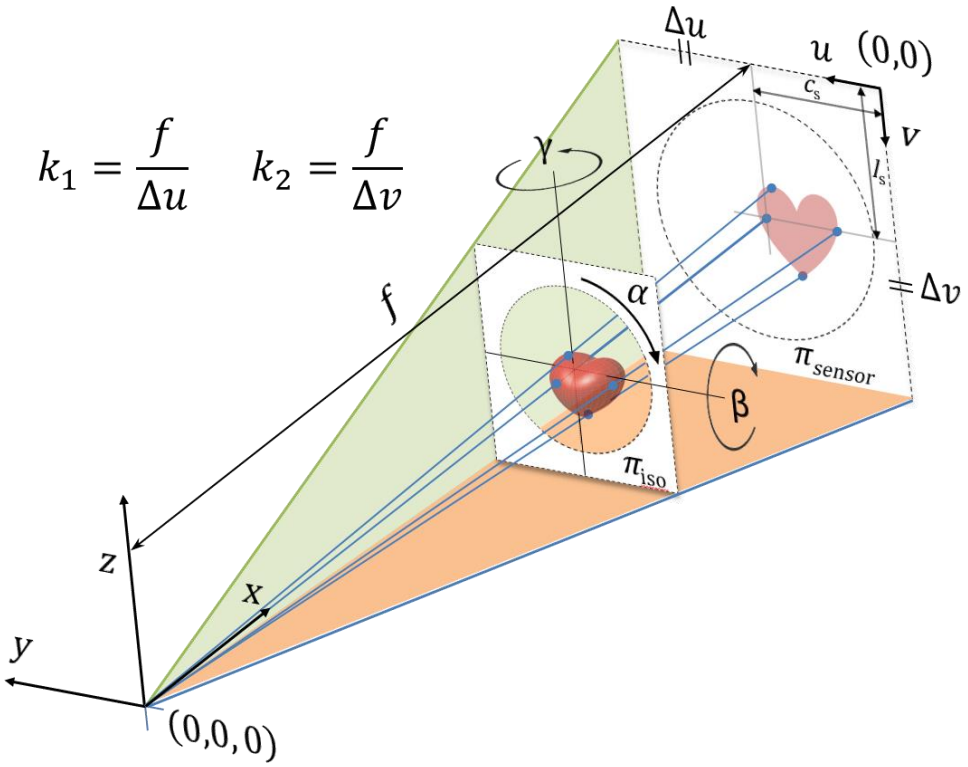


Figure 4.1) A 3D surface model of a Valentine heart [106] located at the isocentre of the projective imaging system ($\pi_{\text{iso}}$) is projected onto the projective plane ($\pi_{\text{sensor}}$) using the pin-hole camera model. Translations along the coordinate axis $(x, y, z)$ and rotations about the isocentre $(\alpha, \beta, \gamma)$ define the pose of the imaging system in relation to the heart, while projection parameters $(c_s, l_s, k_1, k_2)$ define the perspective projection.

### 4.1.1. Intrinsic Parameters

The perspective projection of the 2D modality can be encoded as *projection matrix* in the form,

$$\mathcal{P} = \mathcal{P}(c_s, l_s, k_1, k_2) = \begin{bmatrix} c_s & k_1 & 0 & 0 \\ l_s & 0 & -k_2 & 0 \\ 1 & 0 & 0 & 0 \end{bmatrix} = [P \quad \vec{0}] \qquad , \quad (4.1)$$

$$k_1 = \frac{f}{\Delta u} \qquad k_2 = \frac{f}{\Delta v}$$

where $(c_s, l_s)$ are the coordinates in the image where the beam is normal to the projection plane, $f$ is the distance between the source and the projection plane called the focal length, and $\Delta u$ and $\Delta v$ are the pixel spacing in the $(\hat{u}, \hat{v})$-axes respectively on the projection plane (Figure 4.1).

The relationship between a 3D point on the imaging target with position $\vec{r} = (x, y, z)$ and its corresponding point on the 2D projection plane with pixel position $\vec{p} = (u, v)$ is,

$$\begin{bmatrix} c_s & k_1 & 0 & 0 \\ l_s & 0 & -k_2 & 0 \\ 1 & 0 & 0 & 0 \end{bmatrix} \begin{bmatrix} \vec{r} \\ 1 \end{bmatrix} = \lambda \begin{bmatrix} \vec{p} \\ 1 \end{bmatrix} \qquad , \quad (4.2)$$

where $\lambda$ is a scaling factor. The equation makes use of homogenous coordinates [107].

#### 4.1.1.1. Forward Projection

Finding the 2D projection $\vec{p}$ of a 3D position $\vec{r}$ is known as forward projection. This can be done by solving (4.2) for $\vec{p}$,

$$\begin{bmatrix} c_s x + k_1 y \\ l_s x - k_2 z \\ x \end{bmatrix} = \begin{bmatrix} u \\ v \\ 1 \end{bmatrix} \lambda \quad , \qquad (4.3)$$

$$\vec{p} = \begin{bmatrix} u \\ v \end{bmatrix} = \begin{bmatrix} c_s + k_1(y/x) \\ l_s - k_2(z/x) \end{bmatrix} \quad . \qquad (4.4)$$

Projection depth is defined as the positive $x$-axis (Figure 4.1) and the scaling factor is set to $x$ in the last row of (4.3). In (4.5) the components of $\vec{p}$ are not directly dependent on the components of $\vec{r}$ but on their ratios, revealing the many-to-one problem found when dealing with projections.

#### 4.1.1.2. Back-Projection

The back-projection of a 2D point position $\vec{p}$ is a line, called the *projection line*. The back projection can be found using the Moore-Penrose pseudoinverse of $\mathcal{P}$ [108],

$$\mathcal{P}^+ = \begin{bmatrix} 0 & 0 & 1 \\ \frac{1}{k_1} & 0 & -\frac{c_s}{k_1} \\ 0 & -\frac{1}{k_2} & \frac{l_s}{k_2} \\ 0 & 0 & 0 \end{bmatrix} = \begin{bmatrix} P^{-1} \\ \overleftarrow{0} \end{bmatrix} \quad , \qquad (4.5)$$

where a backward-arrowed vector $\overleftarrow{x}$ denotes the transpose of $\vec{x}$, and $\overleftarrow{0} = [0 \quad 0 \quad 0]$ is a row vector.

In this thesis, pseudoinverse will refer specifically to the Moore-Penrose pseudoinverse unless otherwise stated. Applying the pseudoinverse to both sides of (4.2), and removing the indeterminate last row, reveals the parametric equation for projection lines with $\lambda$ as the parameter,

$$\vec{r} = P^{-1} \begin{bmatrix} \vec{p} \\ 1 \end{bmatrix} \lambda = \begin{bmatrix} 1 \\ (u - c_s)/k_1 \\ (l_s - v)/k_2 \end{bmatrix} \lambda \quad . \qquad (4.6)$$

For simplicity the back-projection of a 2D point $\vec{p}$ will be denoted by $\mathcal{P}^+\vec{p}$.

### 4.1.2. Extrinsic Parameters

A rigid body transformation (RBT) represents the motion of an object that does not change shape or size as it moves through space. The RBT $\mathcal{M}$ is composed of a rotation $\mathcal{R}$ and a translation $\mathcal{T}$

$$\mathcal{M} = \mathcal{M}(\theta, \phi, \alpha, x, y, z) = \mathcal{T}(x, y, z)\mathcal{R}(\theta, \phi, \psi) = \begin{bmatrix} I_3 & \vec{\delta} \\ \overleftarrow{0} & 1 \end{bmatrix} \begin{bmatrix} R & \vec{0} \\ \overleftarrow{0} & 1 \end{bmatrix} = \begin{bmatrix} R & \vec{\delta} \\ \overleftarrow{0} & 1 \end{bmatrix} \quad , \qquad (4.7)$$

where $R$ is a rotation matrix and $\vec{\delta}$ is a displacement vector indicating the amount of translation.

Rotation is described in terms of direction and angle,

$$R = R(\theta, \phi, \psi) = I_3 + [\hat{k}]_\times \sin\psi + (1 - \cos\psi)[\hat{k}]_\times^2 \quad , \qquad (4.8)$$

where $\hat{k} = (\sin\theta\cos\phi\,, \sin\theta\cos\phi\,, \cos\theta)$ is the rotation axis and $[\vec{k}]_\times$ is the matrix,

$$[\vec{k}]_\times = \begin{bmatrix} 0 & -k_z & k_y \\ k_z & 0 & -k_x \\ -k_y & k_x & 0 \end{bmatrix} \quad . \qquad (4.9)$$

According to Euler's rotation theorem, the rotation can also be described in terms of three consecutive rotations around the $x$-, $y$- and then $z$- axes of Euler angles $\alpha$, $\beta$, and $\gamma$ respectively. Rotations can be represented as the following matrix,

$$\begin{aligned} R &= R(\alpha, \beta, \gamma) = R_z(\gamma) R_y(\beta) R_x(\alpha) \\ &= \begin{bmatrix} \cos\gamma & \sin\gamma & 0 \\ -\sin\gamma & \cos\gamma & 0 \\ 0 & 0 & 1 \end{bmatrix} \begin{bmatrix} \cos\beta & 0 & -\sin\beta \\ 0 & 1 & 0 \\ \sin\beta & 0 & \cos\beta \end{bmatrix} \begin{bmatrix} 1 & 0 & 0 \\ 0 & \cos\alpha & \sin\alpha \\ 0 & \sin\alpha & \cos\alpha \end{bmatrix} \\ &= \begin{bmatrix} \cos\beta\cos\gamma & \cos\alpha\sin\gamma - \sin\alpha\sin\beta\cos\gamma & \sin\alpha\sin\gamma - \cos\alpha\sin\beta\cos\gamma \\ -\cos\beta\sin\gamma & \cos\alpha\cos\gamma + \sin\alpha\sin\beta\sin\gamma & \sin\alpha\cos\gamma + \cos\alpha\sin\beta\sin\gamma \\ \sin\beta & \sin\alpha\cos\beta & \cos\alpha\cos\beta \end{bmatrix} \end{aligned} \quad . \qquad (4.10)$$

#### 4.1.2.1. Finding Rigid Body Transformation between Unweighted Points

Finding the RBT $\mathcal{M}$ between two sets of $N$ corresponding 3D points $\{\vec{p}_i\}$ and $\{\vec{q}_i\}$ is a problem of *absolute orientation*, and can be found by a least-squares fitting [85] [86] of the form,

$$\begin{bmatrix} \vec{q}_i \\ 1 \end{bmatrix} = \mathcal{M} \begin{bmatrix} \vec{p}_i \\ 1 \end{bmatrix} + \begin{bmatrix} \vec{e}_i \\ 1 \end{bmatrix} \quad , \qquad (4.11)$$

where $\vec{e}_i$ is the residual distance error of the transformation between the individual registered points. The total error is the metric; a cost function to be minimised:

$$e = \left\| \sum_{i=0}^{N-1} \vec{e}_i \right\| \quad . \qquad (4.12)$$

The points are first recentred so that their centroids $\vec{p}_c$ and $\vec{q}_c$ coincide with the origin,

$$\vec{p}_c = \frac{1}{N} \sum_{i=0}^{N-1} \vec{p}_i \qquad \vec{q}_c = \frac{1}{N} \sum_{i=0}^{N-1} \vec{q}_i \quad , \qquad (4.13)$$

$$\vec{p}_i' = \vec{p}_i - \vec{p}_c \qquad \vec{q}_i' = \vec{q}_i - \vec{q}_c \quad , \qquad (4.14)$$

$$P = [\vec{p}_0' \quad \vec{p}_1' \quad \vec{p}_2' \quad \dots \quad \vec{p}_{N-1}'] \qquad Q = [\vec{q}_0' \quad \vec{q}_1' \quad \vec{q}_2' \quad \dots \quad \vec{q}_{N-1}'] \quad , \qquad (4.15)$$

where $P$ and $Q$ are $3\times N$ matrices representing the points by augmenting their column vectors.

The rotation between $\{\vec{p}_i'\}$ and $\{\vec{q}_i'\}$ can be found by re-arranging the singular value decomposition (SVD) of the correlation matrix $K$ [109],

$$K = PQ^T = U\Sigma V^T \quad , \quad (4.16)$$

$$R = V\begin{bmatrix}1 & 0 & 0\\ 0 & 1 & 0\\ 0 & 0 & |VU^T|\end{bmatrix}U^T \quad . \quad (4.17)$$

where $U$ and $V$ are 3×3 unitary matrices, and $V^T$ denotes transpose of a matrix $V$.

The final RBT between the points is,

$$\mathcal{M} = \begin{bmatrix}R & \vec{q}_i' - \vec{p}_i'\\ \overleftarrow{0} & 1\end{bmatrix} \quad , \quad (4.18)$$

#### 4.1.2.2. Finding Rigid Body Transformation between Weighted Points

When finding the rigid-body transformation, some points within a set may have larger errors than the others and therefore, it would be desirable to reduce the weighting $\{w_i\}$ of these points. Finding the RBT between corresponding points with a weighting function is equivalent to the *weighted orthogonal Procrustes* problem. The problem is formulated as (4.11) but uses an $N\times N$ diagonal weight matrix based on $\{w_i\}$,

$$W = \begin{bmatrix}w_0 & 0 & 0 & \cdots & 0\\ 0 & w_1 & 0 & \cdots & 0\\ 0 & 0 & w_2 & \cdots & 0\\ \vdots & \vdots & \vdots & \ddots & 0\\ 0 & 0 & 0 & 0 & w_{N-1}\end{bmatrix} \quad . \quad (4.19)$$

Point matrices are constructed with $\{\vec{p}_i\}$ and $\{\vec{q}_i\}$ as in (4.13)-(4.15) but with weighting applied,

$$P = W[\vec{p}_0' \quad \vec{p}_1' \quad \vec{p}_2' \quad \dots \quad \vec{p}_{N-1}'] \qquad Q = W[\vec{p}_0' \quad \vec{p}_1' \quad \vec{p}_2' \quad \dots \quad \vec{p}_{N-1}'] \quad , \quad (4.20)$$

and the rest of the problem is the same as absolute orientation with (4.20) in place of (4.15).

### 4.1.3. Intrinsic and Extrinsic Parameters

Together, the intrinsic and extrinsic parameters are known as *camera parameters* and used to form the 3×4 *camera matrix*,

$$\mathcal{C} = \mathcal{C}(c_s, l_s, f, \Delta u, \Delta v, \delta_x, \delta_y, \delta_z, \theta, \phi, \psi) = \mathcal{PTR} = [P \quad \vec{0}]\begin{bmatrix}R & \vec{\delta}\\ \overleftarrow{0} & 1\end{bmatrix} \quad . \quad (4.21)$$

The pseudoinverse of $\mathcal{C}$ cannot be found analytically since $\mathcal{C}$ is a projection, but it can be computed numerically by applying the pseudoinverse of its SVD [89],

$$\begin{aligned}\mathcal{C} &= \mathcal{PTR} = U\Sigma V^T\\ \mathcal{C}^+ &= (\mathcal{PTR})^+ = V\Sigma^+ U^T\end{aligned} \quad . \quad (4.22)$$

The $\Sigma^+$ is a 4×3 diagonal matrix with entries reciprocal to $\Sigma$'s diagonal entries.

The camera matrix is a type of projection that maps a point $\vec{r} = (x, y, z)$ onto 2D as follows,

$$\vec{p} = \begin{bmatrix} c_s + k_1(y'/x') \\ l_s - k_2(z'/x') \end{bmatrix} \qquad \begin{bmatrix} x' \\ y' \\ z' \\ 1 \end{bmatrix} = \mathcal{TR} \begin{bmatrix} x \\ y \\ z \\ 1 \end{bmatrix} \quad , \qquad (4.23)$$

Back projection lines are obtained by rearranging (4.21) to obtain parametric equations,

$$\vec{r} = (PR)^{-1} \begin{bmatrix} \vec{p} \\ 1 \end{bmatrix} \lambda - R^{-1}\vec{\delta} \quad , \qquad (4.24)$$

will be denoted as $\ell(\lambda) = \mathcal{C}^{+}\vec{p}$ in this thesis.

### 4.1.4. Parameters from a Tracked and Pre-Calibrated System

Most modern X-ray C-arm fluoroscopy systems track the angular rotation of their C-arm and have their *intrinsic* projection parameters precalibrated. These parameters are usually with the X-ray images in the Digital Imaging and Communications in Medicine (DICOM) file format [110]. The DICOM parameters used to generate the camera matrix are listed in Table 4.1

| Symbol | DICOM attribute | (Group, Element) |
|---|---|---|
| $SID$ | Distance Source to Detector | (0018, 1110) |
| $SOD$ | Distance Source to Patient | (0018, 1111) |
| $\Delta u, \Delta v$ | Imager Pixel Spacing | (0018, 1164) |
| $\beta$ | Imager Primary Angle | (0018, 1510) |
| $\gamma$ | Imager Secondary Angle | (0015, 1511) |
| $W$ | Rows | (0028, 0010) |
| $H$ | Columns | (0028, 0011) |

Table 4.1 – DICOM tags used to determine the camera matrix.

Positive values of the primary angle $\beta$ measures represent rotation towards the left and results in acquisition of a left anterior oblique (LAO) view. Negative values indicate rotation towards the right and acquisition of right anterior oblique (RAO) view. The secondary angle $\gamma$ measures rotation *cranially* (CRAN) towards the head or caudally (CAUD) towards the feet. When both angles are zero, the fluoroscopy image is acquired in the posterior-anterior (PA) view. Otherwise, the rotation matrix to describe the C-arm orientation is,

$$\begin{aligned} R &= \begin{bmatrix} \cos\gamma & -\sin\gamma & 0 \\ \sin\gamma & \cos\gamma & 0 \\ 0 & 0 & 1 \end{bmatrix} \begin{bmatrix} \cos\beta & 0 & -\sin\beta \\ 0 & 1 & 0 \\ \sin\beta & 0 & \cos\beta \end{bmatrix} \\ &= \begin{bmatrix} \cos\gamma\cos\beta & -\sin\gamma & -\cos\gamma\sin\beta \\ \sin\gamma\cos\beta & \cos\gamma & -\sin\gamma\sin\beta \\ \sin\beta & 0 & \cos\beta \end{bmatrix} \end{aligned} \quad , \qquad (4.25)$$

Assuming the imaging target, i.e. the heart is approximately at the isocentre of the fluoroscope and so no translation is necessary, and that the X-ray beam is normal to the detector at its centre, the camera matrix $\mathcal{C}$ is can computed directly from the DICOM parameters,

$$\mathcal{C} = \begin{bmatrix} \frac{(W-1)}{2} & \frac{SOD}{\Delta u} & 0 & 0 \\ \frac{(H-1)}{2} & 0 & -\frac{SOD}{\Delta v} & 0 \\ 1 & 0 & 0 & 0 \end{bmatrix} \begin{bmatrix} \cos\gamma\cos\beta & -\sin\gamma & -\cos\gamma\sin\beta & SID \\ \sin\gamma\cos\beta & \cos\gamma & -\sin\gamma\sin\beta & 0 \\ \sin\beta & 0 & \cos\beta & 0 \\ 0 & 0 & 0 & 1 \end{bmatrix} \quad . \quad (4.26)$$

### 4.1.5. Epipolar Reconstruction

Epipolar reconstruction allows lost depth information to be recovered from a 2D image if another 2D image is taken of the same imaging target from another view. The images will be referred to as the left and the right image with camera matrices $\mathcal{C}_L$ and $\mathcal{C}_R$. This requires that we know the complete camera parameters of the projective modality, and that corresponding anatomical features within the image can be identified (Figure 4.2). Any point $\vec{p}$, called an *epipole*, in the right image has a corresponding projection line $\ell_{\mathrm{p}} = \mathcal{C}_R^{+}\vec{p}$ between itself and its pinhole source. The forward projection of $\ell_{\mathrm{p}}$ onto the left view creates a line in 2D called the epipolar line, $\ell_{\mathrm{epi}} = \mathcal{C}_R \ell_{\mathrm{p}}$.

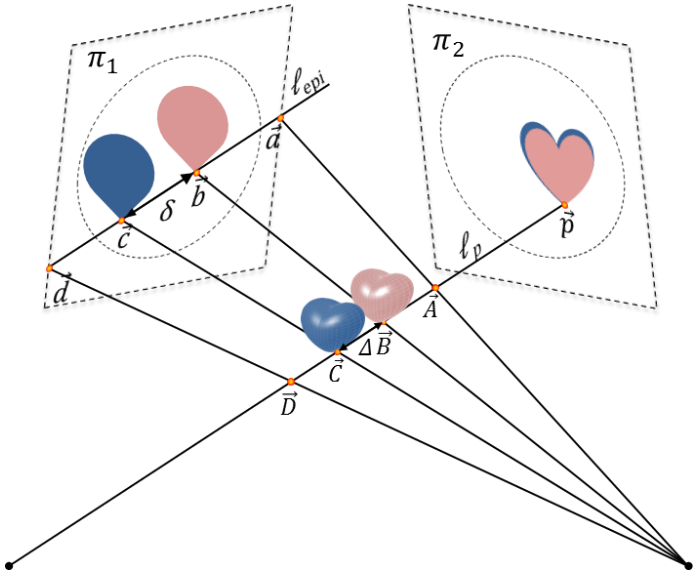


Figure 4.2) This illustrates the concept of epipolar geometry. The back-projection of a point $p$ in one projective plane $\pi_1$ yields the line $\ell_p$. Forward projection of $\ell_p$ onto another plane $\pi_2$ results in a new line $\ell_{\mathrm{epi}}$, the epipolar line. The epipolar constraint dictates that the point $\vec{b}$ that corresponds to $\vec{p}$ in $\pi_2$ must lie on the epipolar line. Also illustrated is the loss of depth information. A large out-of-plane translation $\Delta$ of the 3D object (*red and blue volumetric hearts*) shows very little change of its projections (*red and blue flat hearts*) on $\pi_1$, but shows up as a large displacement $\delta$ in $\pi_2$ where the translation is in-plane.

According to the epipolar constraint, the epipole in the first image has a corresponding point $\vec{q}$ in the second image, which lies on the epipolar line,

$$\vec{q} \in \mathcal{C}_R \mathcal{C}_L^{+} \vec{p} \quad , \quad (4.27)$$

This is useful for finding point-to-point correspondences between the two images as long as the corresponding anatomical point is inside both images. The intersection between the back projection of the points $\vec{p}$ and $\vec{q}$ is the corresponding point in 3D,

$$\vec{r} = \mathcal{C}_L^+ \vec{p} \cap \mathcal{C}_R^+ \vec{q} \quad , \quad (4.28)$$

### 4.1.6. 2D–3D Image Registration

Registering between features from a 2D and 3D image involves the intrinsic and extrinsic matrices $\mathcal{C} = \mathcal{PTR} = \mathcal{PM}$, and a matrix describing the relationship between 2D and 3D images, $\mathcal{M}_{\text{reg}}$. In this thesis, which focuses on 2D-3D image registration of cardiac images, an assumption is made that the heart returns to the same shape and pose when at the same stage of the cardiorespiratory cycle (2.1). Assuming that the 2D and 3D image are acquired at the same cardiorespiratory phase, the relationship between the two images can be described as an RBT so that $\mathcal{M}_{\text{reg}} = \mathcal{T}_{\text{reg}}\mathcal{R}_{\text{reg}}$. The 2D-3D registration problem, including spatial correspondence, is formulated as,

$$\mathcal{PM}\mathcal{M}_{\text{reg}} \begin{bmatrix} \vec{r}_i \\ 1 \end{bmatrix} = \lambda \begin{bmatrix} \vec{p}_i \\ 1 \end{bmatrix} \quad , \quad (4.29)$$

where $\lambda$ is a scaling factor, and $\{\vec{r}_i\}$ and $\{\vec{p}_i\}$ are sets points corresponding to the same anatomical feature extracted from the 3D and 2D image respectively. This equation is valid when registering with a single 2D view. In this case, the two RBTs can be combined: $\mathcal{M}_{\text{reg}} \leftarrow \mathcal{M}\mathcal{M}_{\text{reg}}$. When multiple 2D views are involved, each view has its own camera parameters and the equation becomes,

$$\mathcal{P}^j\mathcal{M}^j\mathcal{M}_{\text{reg}} \begin{bmatrix} \vec{r}_i \\ 1 \end{bmatrix} = \lambda \begin{bmatrix} \vec{p}_i \\ 1 \end{bmatrix} \quad , \quad (4.30)$$

if for variable focal length 2D imaging system, and

$$\mathcal{P}\mathcal{M}^j\mathcal{M}_{\text{reg}} \begin{bmatrix} \vec{r}_i \\ 1 \end{bmatrix} = \lambda \begin{bmatrix} \vec{p}_i \\ 1 \end{bmatrix} \quad , \quad (4.31)$$

for 2D systems that have a fixed focal length and so the intrinsic parameters do not change. The superscript $j$ indexes the 2D view.

### 4.1.7. Measuring Registration

In this thesis, accuracy of the registration $\mathcal{M}_{\text{reg}}$ is assessed in terms of a 2D or 3D *target registration error* (2D- or 3D-TRE) [24], or *reprojection distance* (RPD) [111] of anatomical points of interest $\{\vec{l}_i\}$, not used for registration, from the 3D image (Figure 4.3).

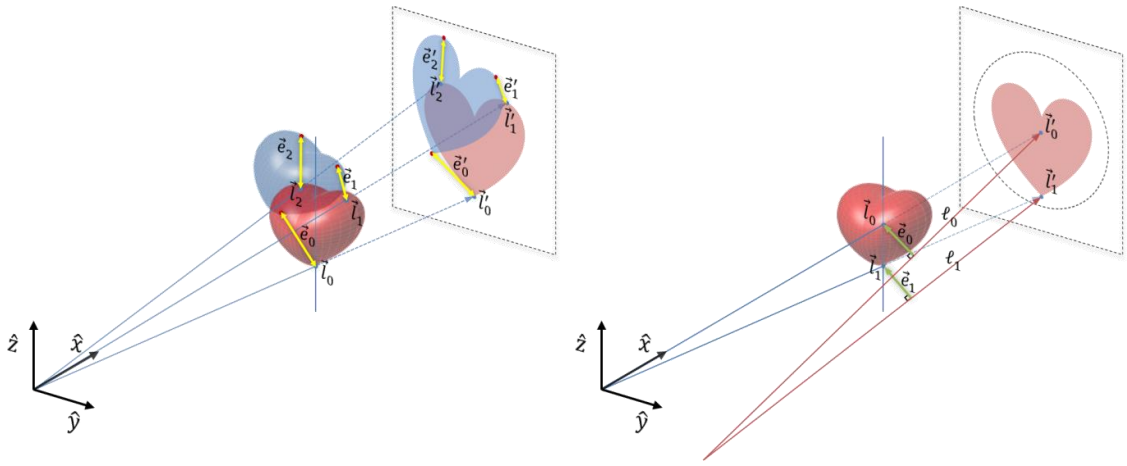

Figure 4.3) Two methods of measuring accuracy of anatomical points of interest $\{\vec{l}_i\}$ from the 3D red heart. Position of heart relative to the 2D imaging system is determined by the registration algorithm. a) The 3D-*target registration error* (3D-TRE) $e_i$ of each anatomical point $\vec{l}_i$, three in this illustration, is the length of the vector $\vec{e}_i$ (*yellow line segments*) to the corresponding anatomical point in the 3D blue heart. The position of the blue heart is determined a gold standard registration. The 2D-TRE $e_i'$ is measured in a similar way but on the 2D image plane. b) The *reprojection distance* (RPD) $e_i$ of each anatomical point $\vec{l}_i$, two in this illustration, is determined by projecting them onto the 2D image $\vec{l}_i'$ and then back projecting them using the gold standard registration ($\ell_i$, *red lines*) and finding the minimum length of the shortest vector $\vec{e}_i$ between $\vec{l}_i$ and $\ell_i$ (*green line segments*).

The error can be measured by comparing the registration to a gold-standard registration $\mathcal{M}_{\text{gold}}$ that can be obtained using fiducial marker locations measured from the 3D image $\{f_i^{3D}\}$ and corresponding fiducial locations measured, and reconstructed, from the 2D images $\{f_i^{2D}\}$. Finding $\mathcal{M}_{\text{gold}}$ between $\{f_i^{3D}\}$ and $\{f_i^{2D}\}$ requires solutions to the problem of absolute orientation without scaling [86]. The mean 3D-TRE can is evaluated as a root-mean-square distance error between the registered anatomical points (Figure 4.3a),

$$\text{3D-TRE} = \sqrt{\frac{1}{N}\sum_i \left\| \mathcal{M}_{\text{gold}}^{-1}\mathcal{M}_{\text{reg}}\vec{l}_i - \vec{l}_i \right\|^2} \quad . \qquad (4.32)$$

Accuracy of the gold standard itself is measured in terms of a *fiducial registration error* (FRE),

$$\text{FRE} = \sqrt{\frac{1}{N}\sum_i \left\| \mathcal{M}_{\text{gold}} f_i^{3D} - f_i^{2D} \right\|^2} \quad . \qquad (4.33)$$

A low FRE values represent an accurate gold standard, but is uncorrelated with the TRE [25].

If a gold-standard registration cannot be obtained due to practical limitations, the error can be estimated by other means, such as visual inspection.

For projection based approaches, the projective nature of X-ray makes it difficult to recover 3D information when registering from a single view. Therefore, single view registration is usually

limited to providing 2D-3D image overlays. Accuracy for overlays is measured in terms of a mean reprojection distance (RPD) [111], which is the RMS of the shortest distance between the points of interest $\vec{l}_i$, and the back-projection with $\mathcal{M}_{\text{gold}}$ of their forward projection with $\mathcal{M}_{\text{reg}}$ (Figure 4.3b),

$$\ell_i = \vec{q}_i + \tau_i \vec{v}_i = \left(\mathcal{C}\mathcal{M}_{\text{gold}}\right)^{+} \mathcal{C}\mathcal{M}_{\text{reg}} \vec{l}_i \quad , \qquad (4.34)$$

$$\text{mean RPD} = \sqrt{\frac{1}{|l|}\sum_{i=0}^{|l|-1} \left\| \left( (\vec{l}_i - \vec{q}_i) - \left( (\vec{l}_i - \vec{q}_i) \cdot \hat{v}_i \right) \hat{v}_i \right) \right\|^2} \quad , \qquad (4.35)$$

where the left hand side of (4.34) represents the back-projection line parameterised by $\tau_i$. The line passes through a point $\vec{q}_i$ and is parallel to unit vector $\vec{v}_i$, which is determined by evaluating the right hand side.

## 4.2. Feature Extraction

Feature-based medical image registration techniques involve the extraction of corresponding geometric features of identifiable anatomy from images in order to register them. Features are typically represented by a set of points with positions $\{\vec{r}_i\}$ relative to the image's coordinate system, where $i$ indexes the points, and the collection consists of $|\{\vec{r}_i\}|$ points, where $|A|$ denotes the cardinality of the set $A$. Features can also be represented as a surface, and a common way of representing such a surface is a set of set of polyhedra $\{V_j\}$. $V_j$ is an index array holding the indices to the points in $\{\vec{r}_i\}$ that it uses as vertices.

In this part of the chapter, two software tools are described to extract registration-constraining features from the 2D and 3D cardiac images. The first is the ITK-SNAP software (© ITK-SNAP Team, www.itksnap.org) [112] used to segment features of the heart from 3D images, and the second is an in-house tool called Sara (© Kawal Rhode, King's College London, London, UK) which is used to manually select catheters from two views, using with the epipolar constraint, and can reconstruct selected catheters in 3D. Both software tools are used throughout Chapters 5, 6 and 7.

### 4.2.1. Image Segmentation with ITK-SNAP

In this thesis, the semi-automatic segmentation of chambers and vessels of the heart from digital tomograms, either from an MR or CT scan, is carried out using ITK-SNAP. This software loads anatomical tomographs and allows the user to pick points that lie within a vessel or chamber of interest. The picked points are then simultaneously region-grown until the region's boundary is reached using active contour methods [113]. Manual adjustments can be made to regions where the image quality is too poor for accurate automatic segmentation.

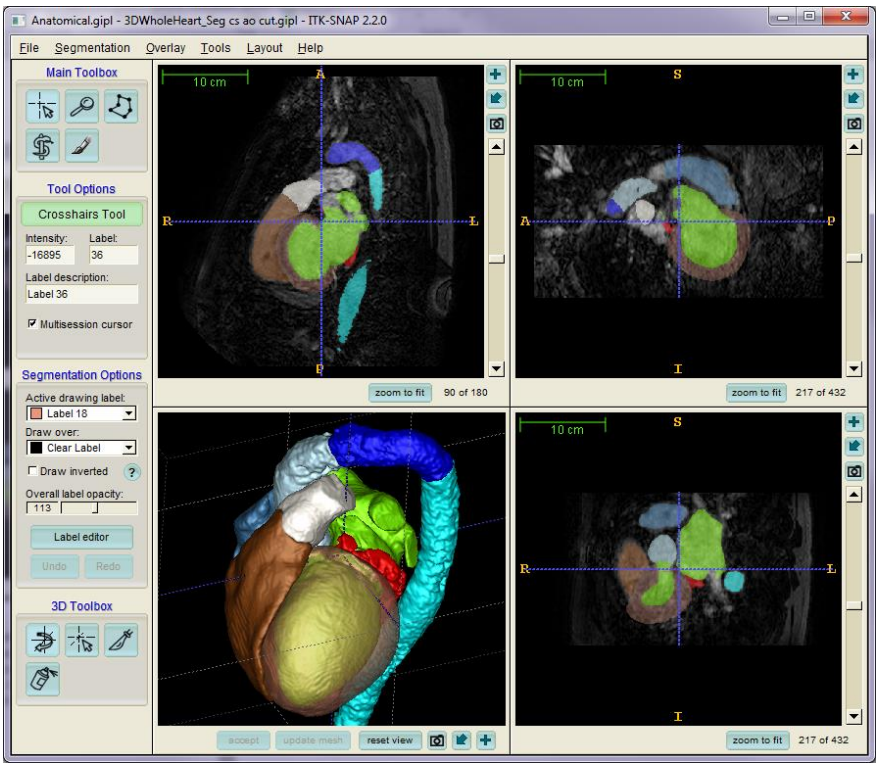


Figure 4.4) Snapshot of the ITK-SNAP segmentation tool showing three orthogonal views (*top left*: sagittal, *top right*: coronal, *bottom right*: axial) of a 3D MR image and a surface rendering of the segmented heart (*bottom left*). Regions segmented from this image include the ascending aorta (*light blue*), aortic arch (*blue*), descending aorta (*cyan*), coronary sinus (*red*), pulmonary artery (*white*), left atrium (*green*), left ventricle myocardium (*bronze, translucent*) and blood pool (*green, embedded*), right atrium (*azure*), and right ventricle blood pool (*brown*).

After segmentation of the vessels and chambers of interest, the software outputs a labelled 3D digital image with intensities corresponding to the $N$ segmented regions. This image can be split into individual 3D binary images. Alternatively, ITK-SNAP has the option to export the geometric hull of a segmented region. This can be extracted using an algorithm such as marching cubes [114], resulting in a collection of points $\{\vec{r}_i\}$ and a set of triangles which tessellate the hull surface $\{V_j\}$.

#### 4.2.1.1. Accuracy of Vessel and Chamber Segmentation

For most automatic cardiac segmentation algorithms, manual vessel and chamber segmentations, performed by expert observers, provide the gold standard for assessing accuracy. There is typically a small degree of variability between observer segmentations. For vessel segmentations in a 3D MR scan, interobserver variability, when delineating narrow vessel lumen to measure the inner diameter of the vessel, was shown to be around 20% in both phantom and clinical datasets [115], and in both high and normal resolution images of the heart. For a narrow 5-mm diameter vessel, such as the coronary artery, this would translate to an error of up to 1 mm. The same 1-mm error can be expected for vessels with larger diameters, since most of the observer discrepancies occurs at the boundary between the lumen and wall of the vessel.

A similar error can be expected for the segmentation of chambers of the heart. In [116], Peters *et al.* show average segmentation errors of chambers and trunks of large vessels of the heart from both CT and MR to be in the order of 0.8 mm, and in the order of 1.3 mm using 3DRx. While segmentations in [116] were performed using automated methods, the errors are expected to be similar in a semi-automatic approaches such as using ITK-SNAP.

The registration algorithms in this thesis rely on segmentations of vessels and chambers of the heart in order to constrain catheters to lie within them. Therefore, the segmentation error should propagate through the algorithm. If the errors only caused a translational error, then its propagation could result in an addition of around 1 mm to the final registration error.

### 4.2.2. Catheter Extraction and Reconstruction with Sara

Software, titled Sara, allows users to load two X-ray views along with the projection and pose parameters of each X-ray view in the form of a camera calibration matrix. The software displays the two views side-by-side and allows points to be picked from either view. When a point is picked in one view, its epipolar line is drawn on the other, and users are able to select the corresponding point in the second view, using the epipolar constraints (Figure 4.5).

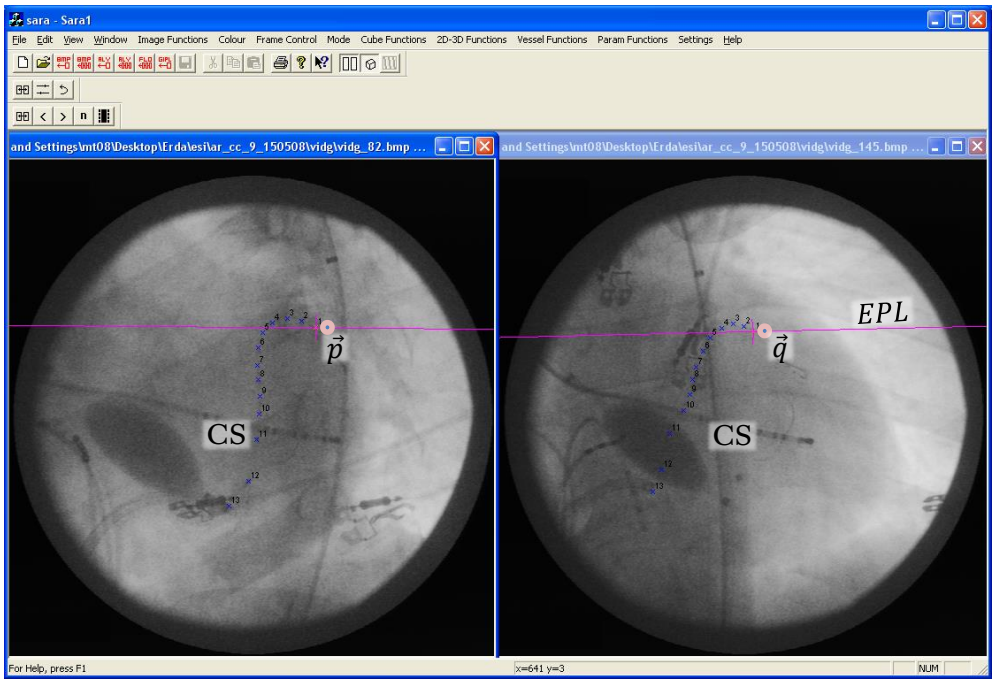


Figure 4.5) Screen shot of the software titled Sara showing X-ray LAO 30˚ and PA views of a patient's heart. Epipolar reconstruction is demonstrated with a with coronary sinus (*CS*) catheter inserted into the CS and into the great cardiac vein branch (*GCV*). A point $\vec{p}$ from the left view generates an epipolar line (*EPL*, *magenta*) in the right view containing its corresponding point $\vec{q}$; their back-projections reconstruct the point in 3D. Points along entire CS catheter can be reconstructed in 3D in this way.

#### 4.2.2.1. Cardiorespiratory Gating of X-ray Video Sequences

When reconstructing catheters from biplane X-ray images taken from clinical data, the image of the heart needs to be in the same cardiorespiratory phase in both views. This assumes that the heart returns to the same shape and size when at the same phase (2.1). The accuracy of this assumption depends on a number of factors, with the two most important ones being the potential deformation of the heart between cardiac and respiratory cycles, and the temporal resolution of the X-ray imaging system. A poor temporal resolution would make it difficult to find the exact corresponding phase in the left and right X-ray views. These potential sources of error culminate to an overall reconstruction error. Using a similar catheter reconstruction setup as outlined in this chapter, Ma *et al.* measured this error to be in the order 0.9 ± 0.4 mm [117]. Without cardiorespiratory gating, reconstructed errors were measured to be 5.2 ± 2.9 mm.

The registration algorithms in this thesis, when dealing with clinical data, relies on the 3D reconstruction of catheters from biplane X-ray images. Therefore, the reconstruction error would propagate through the algorithm and could result in the addition of around 1 mm, if the error was all translational, to the final registration error.

# Chapter 5

## 5. Catheter-Based 2D-3D Registration of Cardiac Phantoms

The aim in this chapter is to develop a novel and clinically robust method to perform 2D-3D registration of cardiac data from a 3D modality such as CT or MR to X-ray fluoroscopy, a projective 2D modality. The method uses catheters that are reconstructed in 3D from sequential biplane X-ray images, and vessels segmented from the 3D data. The approach here differs from that of Sra *et al.* because registration is performed in 3D and then projected onto the X-ray images using a pre-calibration of the X-ray system. Furthermore, the registration only needs to be performed at the beginning of the procedure and is then updated automatically by tracking the motion of the X-ray C-arm and table. Repeat registration is only required if the patient has moved on the X-ray table. Three registration approaches are presented and validated in two experiments using heart phantoms designed to emulate the clinical workflow of a typical cardiac catheterisation procedure.

Imaging the heart and registering cardiac data is challenging due to its highly deformable soft-tissue structure which undergoes many complex motions and deformations throughout the cardiac and respiratory cycle. In this chapter, there is no attempt to model these motions and deformations, but instead rigid and geometrically-realistic models of the heart are used. While the main cause of error in current rigid registration methods are not simulated, the experiments carried out in this chapter are valid and applicable to a cardiac catheterisation procedure if the intraoperative X-ray images are assumed to be phase-matched to the preoperative 3D image with respect to the cardiac and respiratory cycle. Typically, this is the end-diastole phase of the cardiac cycle, when the heart is at maximal expansion and relatively stationary, and at end-expiration phase of the respiratory cycle, since this is the part of the cycle that is most repeatable for the patient.

Applying the algorithm to phantom models of the heart has many benefits that cannot be reproduced in a live clinical environment. Firstly, multi-modal fiduciary markers may be placed directly on a model of the heart to obtain a gold standard registration between the 3D and 2D imaging modalities which is impractical in a live clinical environment. This gold standard registration would allow a quantitative assessment of the algorithm's target registration error (TRE) [24]. Additionally, multiple catheter trajectories can be tested in a single phantom

whereas this would be highly impractical, and potentially dangerous, to practice in a patient. This provides the ability to determine which catheter configuration yields the best results.

## 5.1. Theoretical Method

The general paradigm of the algorithm presented relies on catheters inserted into vessels of the heart where they remain relatively stationary throughout the procedure. These catheters are used to constrain the registration by minimising the 3D root-mean-squared (RMS) (3D-RMS) distance error measured between the catheters and their corresponding vessel centrelines. Ideally, the vessels chosen for this purpose should be relatively narrow in order to minimise the allowable deviance of the catheter from its centreline, the assumption on which this algorithm is based. The ideal vessel should also not possess geometric symmetry, since this may lead to degenerate scenarios where multiple registrations yield competitively low 3D-RMS values with no way of knowing which is correct. For example, if a straight vessel is chosen, then the catheter would be free to translate along the axis of the vessel without affecting the computed 3D-RMS.

In the first approach to this algorithm, a single catheter is constrained to lie within its corresponding vessel. However, in some cases, a single catheter-vessel pair alone may not be sufficient to constrain the registration, for example if the vessel is large, possesses symmetry, or if a there is a high accumulation of errors throughout the algorithm. In clinical settings, a failed registration may translate to poor catheterisation decisions which may jeopardise the procedure and risk the life of the patient; therefore robustness of the algorithm is paramount. The requirement to improve robustness leads to a second approach of the algorithm which simultaneously uses two catheter-vessel pairs to constrain the registration.

Finally, a third approach of the algorithm is introduced due to the fact that in a typical catheterisation procedure, it is rare for two thin vessels to be simultaneously catheterised. It is more common that only one catheterised vessel is thin while the other has a large diameter. Registering with large vessels such as the descending aorta (DAo) increases registration errors due to violations of the assumption that the catheter lies near the medial line of the vessel [118] [119] [120]. Therefore, the method presented in this manuscript attempts to lessen the errors caused by the inclusion of large vessels by introducing a weight function based on the vessel radius. In this final approach, three sensitivity experiments are carried out. The first is designed to find the best pair of catheterised vessels to use for registration, the second is designed to find the balance between the discretisation of catheters with vessel centrelines and the computational time, and the third is designed to find the best weighting to give to the measured radii to constrain the registration.

In order to validate the three approaches of the proposed algorithm, two phantom experiments were carried out with rigid geometrically-realistic models of the heart; one made out of glass (Farlow's Scientific Glassblowing, Grass Valley, CA, US) and the other out of Cyanoacrylate plastic (LFA 5000, Lake Forest Anatomicals, Lake Forest, IL, US). Radio-opaque 0.25-mm diameter lead balls were adhered around the hearts to provide a gold standard registration.

### 5.1.1. Single Catheter Approach

The underlying paradigm of the algorithm presented in this chapter relies on the catheterisation of vessels during the interventional procedure. In terms of image dimensionality, spatial correspondence is achieved between the 2D and 3D image data by reconstructing the 2D points into 3D space, and therefore is a reconstruction-based 2D-3D registration algorithm (§3.1.2.1). The algorithm begins by matching a 3D ordered set of points $V = \{\vec{V}_i\}$ picked along the centreline in a pre-procedural CT scan of the heart, to a set of 3D ordered points along a corresponding catheter $C = \{\vec{C}_i\}$ reconstructed from intra-procedural X-ray, where $i$ indexes the points within the curves. Catheter reconstruction is done by first pre-calibrating and tracking the X-ray system (§4.1.5) to determine the projection parameters $\mathcal{P}_1$ and $\mathcal{P}_2$ of the two views (Figure 4.2) [23] [30] [121]. According to epipolar geometry, a 2D point $\vec{p}$ belonging to a catheter in one view generates an epipolar line $\ell_{\text{epi}} = \mathcal{P}_2\mathcal{P}_1^{+}\vec{p}$ in the other view that contains its corresponding 2D point $\vec{b}$; where $\mathcal{P}^{+}$ denotes the Moore-Penrose pseudoinverse of $\mathcal{P}$. The reconstructed 3D catheter point $\vec{B}$ is at the intersection of the two back projections, ${\mathcal{P}_1}^{+}\vec{p} \cap {\mathcal{P}_2}^{+}\vec{b}$, or at the point closest and equidistant to the back projections if they are skew lines.

This section describes how the registration process works when 3D point sets are picked along the curve at a fixed arclength interval $\Delta$ and have equal point counts, $m = |V| = |C|$, where $|X|$ denotes the cardinality, or the number of points, in $X$. Then the next section describes how equal point counts in the two data sets are obtained.

As described in §4.1.6, the relationship between the coordinate systems of the 2D and 3D images is a *rigid-body transformation* (RBT) represented as a matrix $\mathcal{M}_{\text{reg}} = \begin{bmatrix} R & \vec{\delta} \\ \overleftarrow{0} & 1 \end{bmatrix}$,

$$\begin{bmatrix} \vec{V}_i \\ 1 \end{bmatrix} = \mathcal{M}_{\text{reg}} \begin{bmatrix} \vec{C}_i \\ 1 \end{bmatrix} + \begin{bmatrix} \vec{e}_i \\ 1 \end{bmatrix};\ \forall\, i \in [1, m] \quad . \qquad (5.1)$$

where, $R$ is the 3×3 rotation matrix, $\vec{\delta}$ is the translation vector, and $\overleftarrow{0}$ is a row vector of zeroes, and $\vec{e}_i$ is the residual error between each corresponding points after registration.

The total residual error of this transformation $e$ is calculated with

$$e = \frac{1}{n}\sum_{i=1}^{n}|\vec{e}_i|^2 = \frac{1}{n}\sum_{i=1}^{n}\left|R\vec{C}_i + \vec{\delta} - \vec{V}_i\right|^2 \quad . \quad (5.2)$$

By representing the transformation in this form, it readily identifies itself as the Orthogonal Procrustes problem [85]. The equations (5.1) and (5.2) are only valid if there is a one-to-one point correspondence between the curves $V$ and $C$.

### 5.1.2. Single Catheter Global Search Strategy

When manually picking points along the curve, the points are usually non-uniformly sampled in space, and therefore a natural cubic interpolating spline is fitted through them and re-sampled at an interval $\Delta$ [122]. These evenly sampled points are used with the Procrustes solution to minimise (5.2). As illustrated Figure 5.1 and Figure 5.2 generally $|V| \neq |C|$ and in addition the vessel centrelines may not necessarily be picked in the same direction as their catheters. These are accounted for with a global search strategy which finds the best RBT for $\mathcal{M}_{\text{reg}}$ from a two degree-of-freedom (DOF) search space. The first DOF accounts for the differing number of points between the vessel and catheter, $M = \big||V| - |C|\big| + 1$, by finding the subcurves of the centrelines, $v^j = \{\vec{v}_i^{\,j}\}$ and catheters, $c^j = \{\vec{c}_i^{\,j}\}$, of equal point counts: $m = \left|v^j\right| = \left|c^j\right|$,

$$\left.\begin{array}{rlll} \text{if } |V| < |C|\text{:} & v^j = V, & c^j = C_{(1:m)+j-1} & m = |V| \\ \text{otherwise:} & c^j = C, & v^j = V_{(1:m)+j-1} & m = |C| \end{array}\right\} \forall\, j \in [1, M] \quad . \quad (5.3)$$

where the superscript indexes the subcurve within the set, and a colon in the subscript denotes a range within the original curve, i.e. its subcurve (Figure 5.1),

$$v^{jQ} = \begin{cases} v^j, & Q = 0 \\ \text{reverse}(v^j), & Q = 1 \end{cases}; \forall\, j \in [1, M] \quad . \quad (5.4)$$

with $\text{reverse}(x)$ reversing the order of the points in the subcurve $x$, i.e. $\vec{x}_i = \vec{x}_{|x|-i+1}$. $Q$ represents the second degree of freedom which accounts for whether the $V$ and $C$ in the same order or in an order opposite to one another. A *misregistration* is defined as when the algorithm matches a catheter to a vessel in the wrong direction.

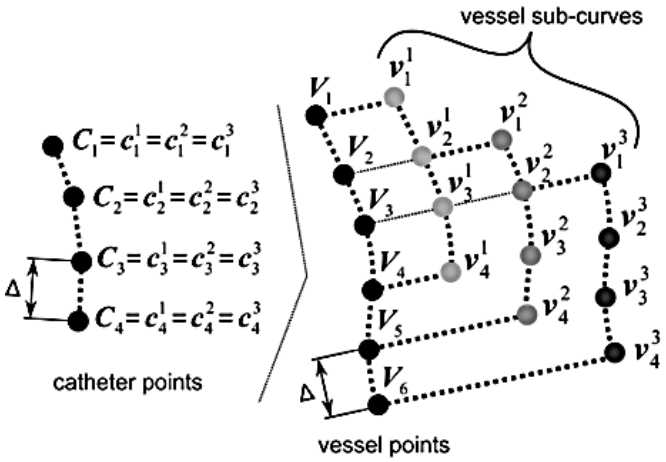


Figure 5.1) A 4-point catheter and 6-point vessel pair generates 3 unique subcurves from the vessel, and 3 catheter subcurves that are replicas of the original.

Subsequently, in the global search strategy an RBT is computed for the $M \times 2$ combinations of subcurves between $v^{jQ}$ and $c^{j}$. The RBT that yields the lowest residual error is the one used for registration so that equations (5.1) and (5.2) are replaced with

$$\begin{aligned} \vec{v}_i^{\,jQ} &= \mathcal{M}^{jQ}\vec{c}_i^{\,j} + \vec{e}_i^{\,jQ} \\ e^{jQ} &= \textstyle\sum_i \left\|\vec{e}_i^{\,jQ}\right\|^2 \quad ; \quad \forall\, j \in [1, M], Q \in [0, 1] \\ \mathcal{M}_{\text{reg}} &= \mathcal{M}^{j'Q'} \text{ where } j', Q' = \underset{j,Q}{\operatorname{argmin}}\, e^{jQ} \end{aligned} \quad . \qquad (5.5)$$

The implementation of (5.3) and (5.5) can be expressed algorithmically with a global-fit pseudo-code algorithm listed in (Listing 5.1).

```
Let C[i] be the ith point of the catheter
Let V[q][i] be the ith point of the qth vessel centreline,
    where q = 0 for forward vessel and 1 for reverse.
Let X[a:b] be the subcurve of X between a and b.
Let e be the error function in eqn. (5.5).
for q = 0, 1
  n = # points in C; m = # points in V[k]
  M = max(m, n) - min(m, n) + 1
  if n > m:
     I = argmin{i}(e(V[q][1:m], C[i:i+m-1])),
     E[k]= e(V[q][1:m], C[I:I+m-1]);
  otherwise:
     I = argmin{i}(e(V[q][i:i+n-1], C[1:n])),
     E[k]= e(V[q][I:I+n-1], C[1:n]);
return ε = argmin{q}(E[q])
```

Listing 5.1 – Global-fit pseudo-code algorithm which determines which vessel direction, when compared against the catheter curve, would yield the lowest error, `e`. The distance Δ between two consecutive points along the catheter and vessel centrelines are assumed to be the same throughout. The distance along the catheters and vessel centrelines is parameterised by the index `i`, and is equal to Δ`i`.

Registration can be performed once the minimum error-yielding transformation is found by applying it to the 3D data and projecting it onto the X-ray images. When finding the subcurves

of catheters and vessel centrelines, there is an assumption that the smaller of the two curves is a subset of the larger curve. Usually the smaller curve should be the catheter, since it is contained within vessel. Therefore, when picking points along the catheter, care should be taken to ensure the catheter at that point is contained within the vessel.

### 5.1.3. Two-Catheter Approach

In some cases, using only a single catheter-vessel pair may not provide enough constraints to overcome the various sources of errors in the registration, resulting in misregistration. Following the framework of the single catheter case, points are picked along the centre of the vessel centrelines, $V_1$ and $V_2$ and along their indwelling catheters, $C_1$ and $C_2$, reconstructed from biplanar X-ray. In order to simultaneously constrain both catheter-vessel pairs, the vessels are combined together and the catheters are combined together. Assuming that the points are picked in order and at an equally spaced distance interval $\Delta$ and that $m_1 = |V_1| = |C_1|$ and $m_2 = |V_2| = |C_2|$, the vessels and catheters are combined,

$$\begin{matrix} V = V_1 \cup V_2 \\ C = C_1 \cup C_2 \end{matrix}; \quad \begin{matrix} |V| = |V_1| + |V_2| = m_1 + m_2 \\ |C| = |C_1| + |C_2| = m_1 + m_2 \end{matrix} \quad . \qquad (5.6)$$

The combined catheter and vessel are treated as a single catheter-vessel pair and the RBT is found using Equations (5.1) and (5.2) as in the single catheter case. However, points in the first catheter only correspond with points from the first vessel, and points from the second catheter only correspond with points from the second vessel. This combination step is performed for computational advantage purposes only. This allows the two catheter-vessel constraints to be calculated in one Orthogonal Procrustes computation (5.2) instead of two separate computations which will then need to be weighted, based on the number of points in the subcurves, and summed.

### 5.1.4. Two Catheter Global Search Strategy

Similar to the one catheter-vessel pair approach, generally $|V_1| \neq |C_1|$, $|V_2| \neq |C_2|$, and the catheters may not necessarily be picked in the same direction as the vessels. In order to simultaneously constrain both catheter-vessel pairs, the global search strategy in the single catheter approach is extended to accommodate all possible ways that the catheters and vessels can be combined, extending the number of DOFs to three. The first two account for the differing number of points in the first vessel, $M_1 = \big||V_1| - |C_1|\big| + 1$, and the second vessel, $M_2 = \big||V_2| - |C_2|\big| + 1$, by finding the subcurves of the centrelines, $v_{1,i}^j$, $v_{2,i}^k$, and catheters $c_{1,i}^j$, $c_{2,i}^k$, of equal point counts: $m_1 = |v_1^j| = |c_1^j|$, $m_2 = |v_2^k| = |c_2^k|$,

$$\begin{matrix} \text{if } |V_1| < |C_1|\text{:} & v_1^j = V_1, & c_1^j = C_{1,(1:m_1)+j-1} & m_1 = |V_1| \\ \text{otherwise:} & c_1^j = C_1, & v_1^j = V_{1,(1:m_1)+j-1} & m_1 = |C_1| \end{matrix} \Big\} \forall\, j \in [1, M_1]$$
$$\begin{matrix} \text{if } |V_2| < |C_2|\text{:} & v_2^k = V_2, & c_2^k = C_{2,(1:m_2)+k-1} & m_2 = |V_2| \\ \text{otherwise:} & c_2^k = C_2, & v_2^k = V_{2,(1:m_2)+k-1} & m_2 = |C_2| \end{matrix} \Big\} \forall\, k \in [1, M_2] \quad . \quad (5.7)$$

The catheter and vessel subcurves are then combined together to create a new set of $M_1 \times M_2$ curves each with $m_1 + m_2$ points similar to (5.6). The catheters are combined as:

$$c^{jk} = c_1^j \cup c_2^k, \quad \forall\, j \in [1, M_1], k \in [1, M_2] \quad . \quad (5.8)$$

The vessel centrelines are also combined but account for the third DOF, $Q$, which allows for the centrelines to be picked in any direction relative to their catheter. In this case, there are four combinations as opposed to two in the single catheter case, resulting in a set of $M_1 \times M_2 \times 4$ vessel curves, each also of length $m_1 + m_2$ (Figure 5.2):

$$v^{jkQ} = \begin{cases} v_1^j \cup v_2^k, & Q = 0 \\ v_1^j \cup \text{reverse}(v_2^k), & Q = 1 \\ \text{reverse}(v_1^j) \cup v_2^k, & Q = 2 \\ \text{reverse}(v_1^j) \cup \text{reverse}(v_2^k), & Q = 3 \end{cases} ; \forall \begin{cases} j \in [1, M_1\text{--}] \\ k \in [1, M_2] \end{cases} \quad . \quad (5.9)$$

A *misregistration* is defined as when the algorithm matches one or both catheters to its corresponding vessels in the wrong direction.

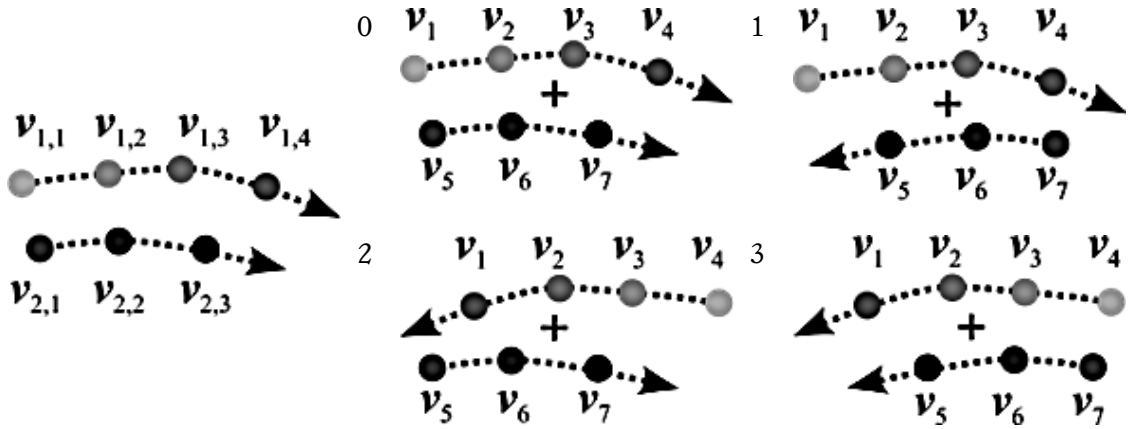


Figure 5.2) The four ways that two vessel centrelines, $\vec{v}_{1,i}$ and $\vec{v}_{2,j}$, can combine; $Q = 0$: head-to-tail, 1: head-to-head, 2: tail-to-tail, and 3: tail-to-head.

Subsequently, in the global search strategy, an RBT is computed for the $M_1 \times M_2 \times 4$ combinations of subcurves between $v^{jkQ}$ and $c^{jk}$.

The RBT that yields the lowest residual error is the one used for registration so that (5.5) is replaced with:

$$\begin{aligned} v_i^{jkQ} &= \mathcal{M}^{jkQ} c_i^{jk} + e_i^{jkQ} \\ e^{jkQ} &= \sum_i \left\| e_i^{jkQ} \right\|^2 \quad ; \quad \forall\, j \in [1, M_1], k \in [1, M_2], Q \in [0, 3] \\ \mathcal{M}_{\text{reg}} &= \mathcal{M}^{j'k'Q'} \text{ where } j', k', Q' = \underset{j,k,Q}{\operatorname{argmin}}\, e^{jkQ} \end{aligned} \quad . \qquad (5.10)$$

A typical surface plot of the residual error over the global search space is shown in Figure 5.3.

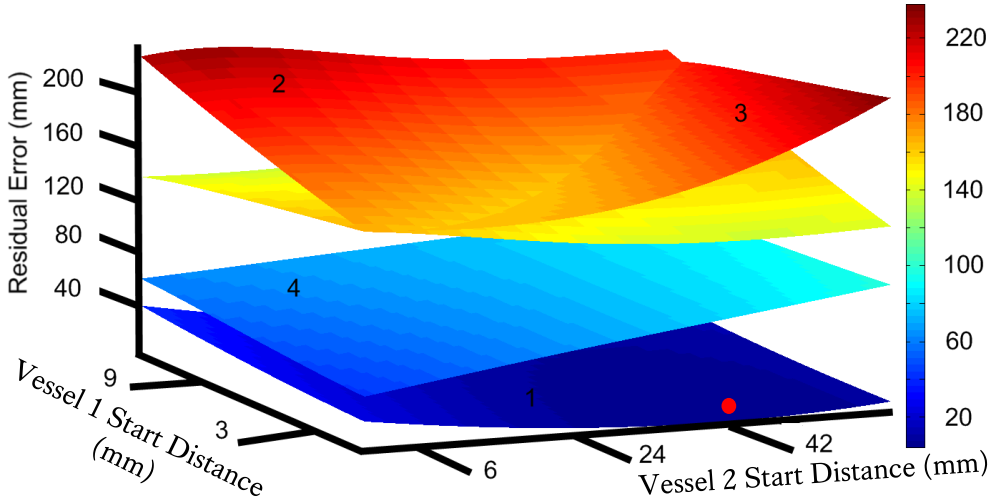


Figure 5.3) A typical residual error function over the search space of the two catheter-vessel pair registration algorithm, with the minimum residual error marked (*red circle*). There are four layers for each of the four ways the two vessels can combine, with the bottom layer ideally being the case when the catheters are picked in the same order as their corresponding vessel's centreline.

### 5.1.5. Vessel-Radius-Weighted Two Catheter Approach

The insertion of two catheters into two narrow vessels is uncommon in catheterisations. Usually only one narrow vessel, such as a coronary vessel, is catheterised while other vessels with catheters inserted in them have large diameters, for example the aorta (Ao), pulmonary veins (PV), and venae cavae (VCs). Registration with large vessels using (5.10) may result in poor accuracy or misregistration since the catheter would have a large volume to move around in. To attempt to lessen these errors, a weighting function based on the inverse of the vessel radius is introduced into the error term in (5.10),

$$e^{jkQ} = \sum_i \rho_i^{-x} \left\| e_i^{jkQ} \right\|^2 ; \quad x \in \mathbb{Z} \quad . \qquad (5.11)$$

where $\rho_i$ is the cross sectional radius of the vessel at the point $i$, and $x$ is a parameter that determines the strength of the weighting, which is to be determined empirically. The problem of finding solutions to (5.11) can be described as that of weighted absolute orientation [86] [123] with no scaling. If $x$ is zero, then (5.11) reduces to the unweighted form (5.10).

## 5.2. Experimental Method

To test the presented registration algorithms, two phantoms experiments were carried out using rigid, geometrically-realistic models of the heart. These experiments were designed to emulate the clinical workflow outlined in Chapter 2, but with the inclusion of fiducial markers placed around the heart. This was done to obtain a gold-standard registration for evaluation of registration accuracy. The experiments are described in three parts to follow the cardiac catheterisation workflow. The first is the preoperative step when the heart is imaged with a CT scanner and the centrelines of vessels which would later be catheterised are extracted. The next is the intraoperative step where the phantom heart is catheterised with typical catheter configurations. For each catheter configuration, a sequential biplane X-ray image pair is taken with a C-arm fluoroscopy system using a separation angle of at least 30˚ in the axial plane between the biplane pairs to allow for the 3D reconstruction of the catheters. Since the catheters are known to lie within the vessel throughout the experiment, they can be used in conjunction with their corresponding vessel as a constraint for registration. The final step is the registration between the CT scan and the X-ray images; this is achieved by finding the transformation that minimises the RMS distance error between the centreline of the vessels to their indwelling catheters' reconstructions in 3D. This transformation combined with the calibration and tracking of the X-ray system, enables the overall 2D-3D registration.

### 5.2.1. Preoperative Step

In cardiac interventional procedures, the preoperative step is the part of the procedure that takes place prior to catheterisation in the operating theatre. During this step, the patient will usually undergo a high-resolution 3D CT or MR scan for diagnostic and treatment planning purposes. Any processing of the 3D data, such as image segmentation and vessel centreline-radius extraction, is performed during this step.

#### *5.2.1.1. Glass Heart Phantom Experimental Setup and Imaging*

In the first of the two phantom experiments, a glass heart model (Figure 5.4a) was used (Farlow's Scientific Glassblowing, Grass Valley, CA, US) which consisted of the endocardial wall of the four chambers of the heart: left atrium (LA), left ventricle (LV), right atrium (RA) and right ventricle (RV); the four PVs: left lower- (LLPV), left upper- (LUPV), right lower- (RLPV) and right upper- (RUPV) branching out of the LA; the Ao, CS and VCs.

Seven 2-mm-diameter lead balls were adhered to the surface of the glass heart, acting as fiducial markers at the locations listed in Table 5.1. These were spaced as far apart as possible so that the distance between each point and three principal axes of the points is maximised, following the optimal marker placement criterion in [24]. This can be visualised as a convex hull formed by these points and encompassing the maximum volume of the heart, which is the target for

registration. The heart with markers underwent a 512×512×384 CT scan (Figure 5.4b) with a $0.78^2 \times 0.62$ mm$^3$ voxel resolution (Helical mode p = 0.53, kVp = 140, mA = 400, SOD = 541, SID = 949; Discovery STE, GE Healthcare, Chalfont St Giles, Buckinghamshire, UK). The chambers and vessels of the heart were subsequently segmented using the ITK-SNAP segmentation software tool [113] [112].

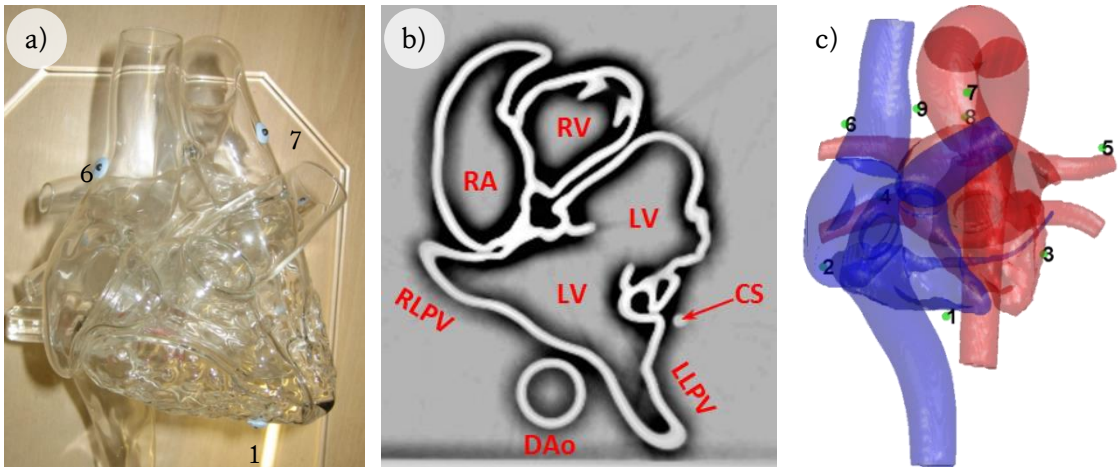


Figure 5.4 a) Anterior-posterior photograph of the glass heart phantom. Fiducial markers 1, 6 and 7 are visible (*numbered*). b) 4-chamber cross-sectional axial slice of the 3D CT image taken of the glass heart looking in foot-head direction. Chambers, lower PVs, DAo and CS are visible and labelled. c) 3D surface rendering of the glass heart endocardium segmented from CT with left heart coloured *red* to represent oxygenated blood and right heart coloured *blue* to represented deoxygenated blood. Seven fiducial markers and two anatomical landmarks are visible (*green*, *numbered*).

| # | Location |
|---|---|
| 1 | RV apex |
| 2 | IVC/RA junction |
| 3 | Mid-LV endocardium |
| 4 | RLPV |
| 5 | LUPV |

| # | Location |
|---|---|
| 6 | SVC/RA junction |
| 7 | ascending/transverse Ao junction |
| 8 | upper LA (*anatomical*) |
| 9 | IVC/ascending Ao junction (*anatomical*) |

Table 5.1 – Seven locations of multimodal fiduciary markers placed around the glass heart and two anatomical landmarks.

#### 5.2.1.2. Plastic Heart Phantom Experimental Setup and Imaging

The second phantom experiment used a rigid and anatomically-realistic Cyroacrylic model of the heart (LFA 5000, Lake Forest Anatomicals, Lake Forest, IL, US). The model consisted of the epicardial surface of the four chambers of the heart, four PVs protruding from the LA, the Ao, and an extensive left and right coronary artery (CA)(LCA, RCA) tree (Figure 5.5a). Nine radio-opaque lead markers were placed around the surface of the heart with their positions listed in Table 5.2, followed by a $512^2 \times 416$-sized 3D image acquisition with a CT scanner ($0.488^2 \times 1$ mm$^3$ voxel resolution; Discover STE, GE Healthcare). The markers positions were located in

the scan (Figure 5.5b), and the chambers and vessels of the heart were then segmented using ITK-SNAP (Figure 5.5c).

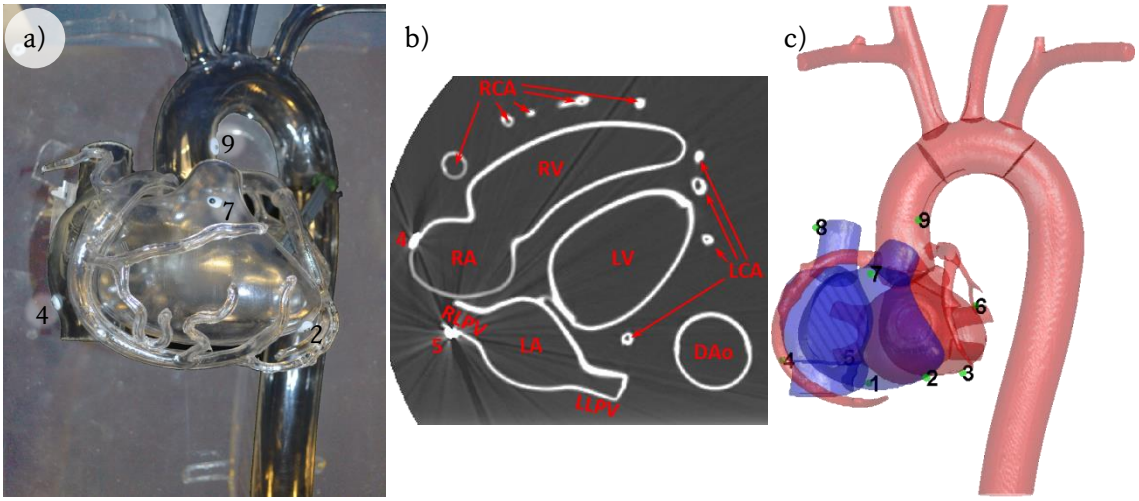


Figure 5.5 a) Anterior-posterior photograph of the plastic heart phantom. Fiducial markers 2, 4, 7 and 9 are visible (*numbered)*. b) 4-chamber cross-sectional axial slice of 3D CT image taken of the plastic heart looking in foot-head direction. Lower PVs, DAo, CAs, chambers and fiducial markers 4 and 5 visible and labelled. c) 3D surface rendering of plastic heart endocardium segmented from CT with left heart coloured *red* to represent oxygenated blood and right heart coloured *blue* to represented deoxygenated blood. Nine fiducial markers are visible (*green, numbered*). Branches of the CAs too narrow to catheterise were not segmented.

| # | Location | # | Location |
|---|---|---|---|
| 1 | lower-mid RV | 6 | LUPV |
| 2 | RV apex | 7 | upper-mid RV |
| 3 | lower-mid LV | 8 | SVC-RA junction |
| 4 | IVC-RA junction | 9 | ascending Ao (left aortic sinus) |
| 5 | RLPV | | |

Table 5.2 – Location of fiduciary markers placed around the plastic heart.

#### 5.2.1.3. Centreline Extraction of Heart Vessels with Cardioclick

The vessel points corresponding to centrelines of the phantom hearts were manually identified in the CT scans using a customised software, Cardioclick (Figure 5.6a, b), which was designed and written by the author for the purpose of this research. This software allows the user to load 3D tomograms and displays axial, coronal and sagittal orthogonal views simultaneously. Voxel positions can then be picked from any of the three views which are recorded and labelled according to the vessel structure they belong to. The points along a centreline are picked in order, which are then smoothed using a triangular weighted moving average and reparameterised at fixed spacing intervals. The radius can also be measured with the help of the software at the proximal, middle and distal ends of the vessel and then linearly interpolated.

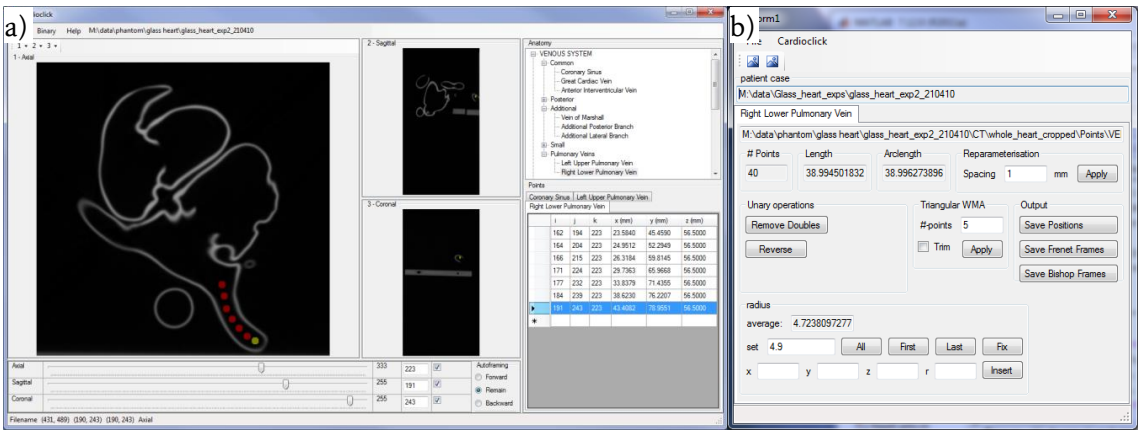


Figure 5.6 a) Screen shot of Cardioclick used to extract the voxel positions corresponding to the centreline of the RLPV (red and yellow dots). b) The space curves corresponding to the vessels are then smoothed using a triangular weighted moving average and reparameterised at fixed spacing intervals. The radius can also be measured with the help of the software at the proximal, middle and distal ends and then linearly interpolated.

Arc-length parameterised natural cubic splines were fitted through the vessel centrelines and sampled at the interval $\Delta$ for use as $V_1$ and $V_2$ in (5.3) and (5.7) so that the number of points in the curve is directly proportional to its length. The vessel's radii $\rho_i$ were measured at the proximal, middle and distal regions and linearly interpolated between measurements.

Using Cardioclick, vessel centrelines of the CS, DAo, AAo, IVC, SVC and LUPV were selected from the glass heart phantom. In the plastic heart phantom, the DAo, RCA and left anterior descending (LAD) branch of the LCA centrelines were extracted. Summary of vessel centreline extraction listed in Table 5.3.

| model | vessel | $\|V\|$ | distal $\rho$ | mean $\rho$ | proximal $\rho$ |
|---|---|---|---|---|---|
| glass heart | CS | 82 | 1.0 | 2.2 | 5.3 |
| | DAo | 183 | 12.8 | 12.7 | 11.0 |
| | AAo | 88 | 12.8 | 13.5 | 14.3 |
| | IVC | 201 | 13.5 | 13.5 | 13.5 |
| | SVC | 61 | 12.0 | 12.0 | 12.0 |
| | LUPV | 36 | 6.0 | 6.0 | 6.0 |
| plastic heart | DAo | 275 | 2.0 | 2.0 | 2.0 |
| | RCA | 220 | 0.5 | 0.5 | 0.5 |
| | LAD | 140 | 0.5 | 0.5 | 0.5 |

Table 5.3 – List of the number of points $|V|$ that make up each vessel centreline, vessel radii at the distal and proximal ends and mean radius $\rho$ (mm).

### 5.2.2. Intraoperative Step

After the preoperative imaging and processing of the 3D image data, the heart is then moved to the X-ray table where it was catheterised under X-ray guidance. To allow biplane reconstructions, the catheters while inside the vessels must be imaged from two different X-ray views.

#### 5.2.2.1. Glass Heart Catheterisation and 2D Imaging

After the 3D CT scan, the heart was placed on a fluoroscopy table equipped with a tracked and pre-calibrated X-ray C-arm with a 25-cm flat panel detector capable of a $0.342^2$ $mm^2$ pixel resolution (Allura Xper FD10, Philips Healthcare). The heart was catheterised with a catheter and guidewire in various configurations involving the CS, AAo, DAo, IVC, SVC and LUPV (Figure 5.7a, b, c). These vessels are typically catheterised during electrophysiology studies and radiofrequency ablations. For each catheter configuration, a biplane X-ray pair of images were taken at posterior-anterior (PA) and left anterior oblique (LAO) 30˚. The catheterisation configurations and corresponding X-ray views taken are summarised in Table 5.4. For all intents and purposes of this algorithm, the words catheter and guidewire are synonymous and used interchangeably.

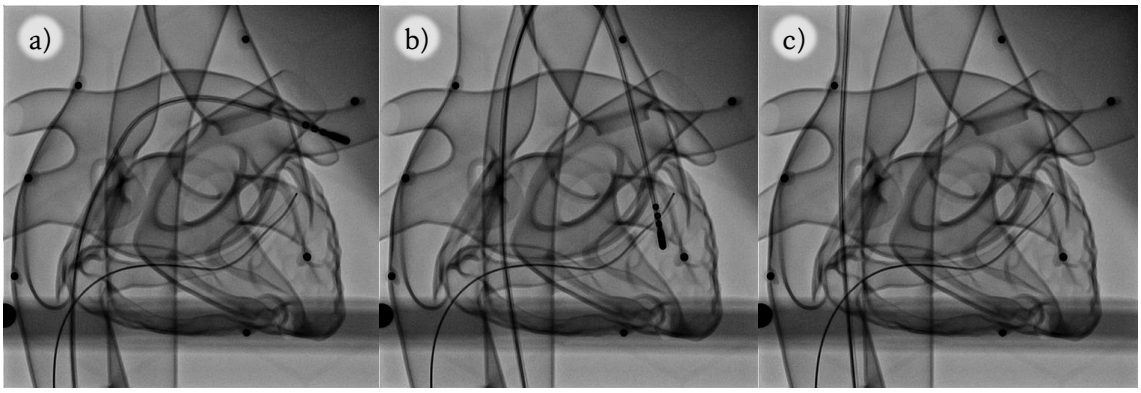


Figure 5.7 a) In this posterior-anterior X-ray view, the CS of the glass heart is catheterised with a guidewire via the IVC and a second catheter is inserted into the LUPV via the IVC, b) the LV via the DAo and c) the SVC via the IVC.

| Pair # | Catheter | Guidewire | View 1 | View 2 | # |
|---|---|---|---|---|---|
| 1 | LUPV via IVC | CS via IVC | LAO 30˚ | PA | 7 |
| 2 | LV via DAo | CS via IVC | LAO 30˚ | PA | 7 |
| 3 | SVC via IVC | CS via IVC | LAO 30˚ | PA | 7 |

Table 5.4 – Catheter configurations in the glass heart. For each configuration, a catheter and guidewire were inserted into the heart and imaged with the trajectories listed. Two x-ray images were taken at the listed angulations. The number of fiducial markers visible in both views and available for reconstruction is listed in the # column.

#### 5.2.2.2. Plastic Heart Catheterisation and 2D Imaging

Similar to the glass heart experiment, the plastic heart phantom was catheterised after the CT scan. In this experiment, two catheter configurations were tested which simulated percutaneous coronary interventions (PCI) where a catheter is inserted into one of the coronary arteries protruding from the ascending aorta (AAo) entering via the DAo (Figure 5.8a, b, c). In the first configuration, the catheter entered the main branch of the RCA and in the other configuration the catheter was placed into the LAD. Once catheterised, biplane images of the phantom were

taken at PA and right anterior oblique (RAO) 45° views (Table 5.5) using a pre-calibrated and tracked X-ray fluoroscopy system (Allura Xper FD20, Phillips Healthcare). The radio-opaque lead markers placed prior to the CT scan were visible in the X-ray.

| Pair # | Catheter | View 1 | View 2 | # |
|---|---|---|---|---|
| 1 | RCA via DAo | PA | RAO 45° | 6 |
| 2 | LAD via DAo | PA | RAO 45° | 8 |

Table 5.5 – Catheter configurations in the plastic heart. For each configuration, a catheter was inserted into the heart and imaged with the trajectories listed. Two X-ray images were taken at the listed angulations. The number of fiducial markers visible in both views and available for reconstruction is listed in the # column.

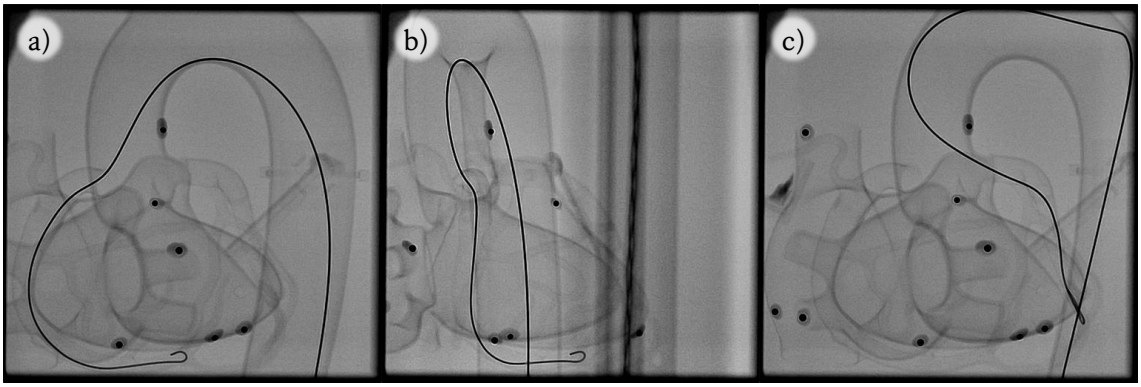


Figure 5.8 a) A guidewire is inserted into the RCA of the plastic heart via the DAo and imaged with X-ray PA and b) RAO 45° views. c) PA X-ray view of the plastic heart with LAD catheterised via the DAo.

#### 5.2.2.3. Catheter Reconstruction

Catheters in the hearts were manually reconstructed in 3D from the biplane views using epipolar geometry and back projection (Figure 4.2, (4.28), §4.1.5) using the software titled Sara (Figure 5.9, §4.2.2). Using the arc-length parameterisation feature of Cardioclick (Figure 5.6b), natural cubic splines were fitted through the vessel centrelines and catheters and sampled at the interval $\Delta$ for use as $C_1$ and $C_2$ in (5.6) so that the number of points in the curve was directly proportional to its length. The reconstructed catheter segments of interest are summarised in Table 5.6.

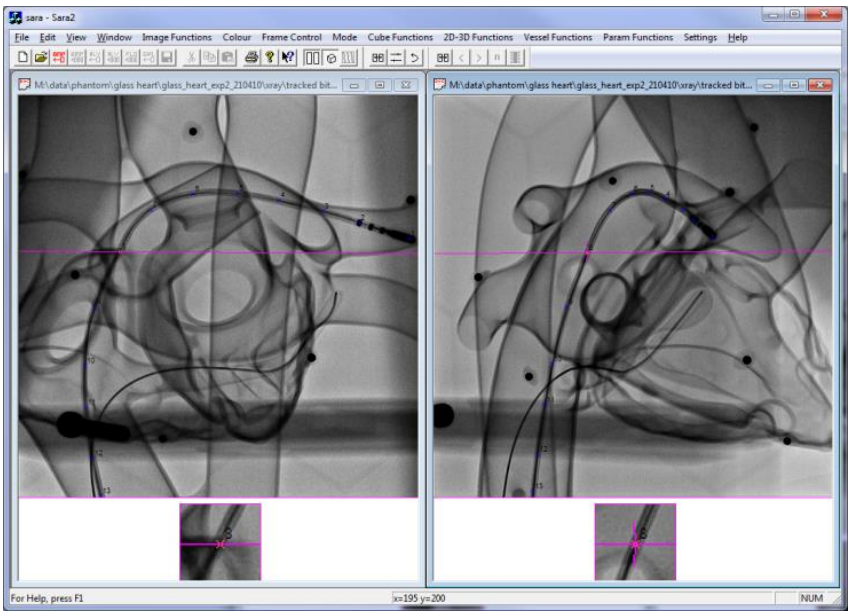

Figure 5.9) X-ray LAO 30˚ and PA views with IVC-CS guidewire and IVC-SVC catheters inserted. A point from one view generates an epipolar line (*magenta*) in the other view containing its corresponding point q; their back-projections reconstruct the point in 3D.

| | vessel | # | pair # | catheter trajectory |
|---|---|---|---|---|
| glass heart | CS | 79 | 1 | CS via IVC guidewire |
| | | 70 | 2 | CS via IVC guidewire |
| | | 80 | 3 | CS via IVC guidewire |
| | DAo | 117 | 2 | LV via DAo catheter |
| | AAo | 35 | 2 | LV via DAo catheter |
| | IVC | 47 | 1 | LUPV via IVC catheter |
| | | 39 | 3 | SVC via IVC catheter |
| | | 22 | 1 | CS via IVC guidewire |
| | | 15 | 2 | CS via IVC guidewire |
| | | 29 | 3 | CS via IVC guidewire |
| | SVC | 33 | 3 | SVC via IVC catheter |
| | LUPV | 28 | 1 | LUPV via IVC catheter |
| plastic heart | RCA | 146 | 1 | RCA via DAo |
| | LAD | 82 | 2 | LAD via DAo |
| | DAo | 115 | 1 | RCA via DAo |
| | | 111 | 2 | LAD via DAo |

Table 5.6 – Listing of the catheter/guidewire segments of interest taken from catheterisations of the glass and plastic hearts. The number of points that make up each segment (#) at 1-mm intervals, and the catheter configuration trajectory from which the segment is taken.

### 5.2.3. Registration Step

With the vessel centrelines selected and their indwelling catheters reconstructed, registration was then carried out between the vessel centrelines and catheters. The three approaches of the catheter-based registration algorithm, comprised of the single-catheter, two-catheter and weighted-two-catheter approaches, were applied to CT and X-ray data acquired from the experiments.

#### 5.2.3.1. Glass Heart Registration

The catheters inserted into the CS, DAo, AAo, IVC, SVC and LUPV were registered to the centreline of their corresponding vessels. Using the single-catheter approach, registration could be applied six times, once for each catheter-vessel pair. In the two-catheter approaches, weighted and unweighted, registration could be performed 15 times, once for each unique two-catheter combination: CS/DAo, CS/AAo, CS/IVC, CS/SVC, CS/LUPV, DAo/AAo, DAo/IVC, DAo/SVC, DAo/LUPV, AAo/IVC, AAo/SVC, AAo/LUPV, IVC/SVC, IVC/LUPV and SVC/LUPV. An initial sampling interval of $\Delta = 1$ mm for all registrations, and for weighted registration, the initial inverse-radius weighting $x = 2$ was chosen. Subsequently, the five configurations with the lowest mean 3D-TRE over the whole heart were used to compare the algorithm's accuracy without weighting ($x = 0$) to weightings inversely proportional to the vessel's cross sectional radius (1), area (2) and volume (3), while fixing $\Delta = 1$ mm. These five configurations were also used to test the effects of changes in the sampling interval on the algorithm's accuracy and computational cost by varying $\Delta$ between 0.2 and 1.8 mm, which covers the typical range of CT voxel resolutions, while fixing $x = 2$.

#### 5.2.3.2. Plastic Heart Registration

Registration of the plastic heart was carried out in the same way as for the glass heart, but with different catheter and vessel combinations. In this experiment, the vessels catheterised were the DAo, RCA and LAD. This allowed for three single-catheter registrations, and three two-catheter registrations with the configurations: DAo/RCA, DAo/LAD and RCA/LAD. However, registration was not performed on the RCA/LAD combination since both vessels are thin and both these vessels would not normally be simultaneously catheterised in PCI procedures. The sensitivity of the registration algorithm to varying $\Delta$ and $x$ was also tested.

#### 5.2.3.3. Gold Standard Registration from Fiducials

To quantify the accuracy of $\mathcal{M}_{\text{reg}}$ (5.1)(5.5)(5.10) in terms of mean 3D-TRE, the markers, seven fiducials and two anatomical landmarks for the glass heart and nine fiducials for the plastic heart, were used to obtain a gold standard RBT, $\mathcal{M}_{\text{gold}}$, between the CT scan and the reconstructed X-ray space, using the method described in [86] without scaling. To obtain 3D-TREs at relevant points of interest, 17 clinically relevant anatomical landmarks $\vec{l}_i$ were selected from the CT scan of both glass heart phantoms and non-exclusively grouped by the chambers of the heart in which they belong (Table 5.7). 3D-TREs were calculated at these positions to calculate the mean 3D-TRE for the four chambers and for the whole heart (4.32).

| LA | RA | LV | RV |
|---|---|---|---|
| mid-LA | mid-RA | mid-LV | mid-RV |
| four PVs | tricuspid valve | mitral valve | tricuspid valve |
| mitral valve | IVC-RA junction | mid-aortic valve | pulmonary valve |
| atrial septum | SVC-RA junction | LV apex | venricular septum |
| | atrial septum | ventricular septum | |

Table 5.7 – Clinically relevant anatomical landmarks categorised by the chambers of the heart.

## 5.3. Results

The single-catheter, two-catheter and vessel-radius-weighted two-catheter approaches were applied to both the glass and plastic heart phantoms. The vessel radii were measured and their centrelines were picked from the 3D data using Cardioclick, smoothed and reparameterised in less than 10 minutes each. The corresponding catheter points from biplane X-ray pairs were picked and subsequently reconstructed in less than 5 minutes each.

### 5.3.1. Gold Standard Registration

In all three reconstructed X-ray biplane pairs of the glass heart experiment, all seven markers were visible in both views. Applying equation (4.32) to the seven markers on the glass heart yielded fiducial registration errors (FREs) between 0.42 and 0.43 mm between the CT coordinate system and the reconstructed X-ray coordinate system (Table 5.8).

| glass heart experiment | | | plastic heart experiment | | |
|---|---|---|---|---|---|
| Configuration | # Fiducials | FRE (mm) | Configuration | # Fiducials | FRE (mm) |
| IVC-LUPV | 7 | 0.43 | Ao-RCA | 6 | 0.37 |
| Ao-LV | 7 | 0.42 | Ao-LAD | 8 | 0.24 |
| IVC-SVC | 7 | 0.43 | | | |

Table 5.8 – Listed for each biplane pair is the number of fiducial markers to obtain a gold standard rigid-body registration between the reconstructed X-ray coordinate system and the coordinate system of the corresponding preoperative CT scanner, and the calculated FRE, for the glass and the plastic heart experiments.

In the plastic heart experiment, the first biplane X-ray pair, taken when the catheter was inserted into the RCA, had only six markers visible in both views, while eight were visible in the second biplane X-ray pair, taken when the catheter was inserted into the LCA. The gold standard registration yielded a fiducial registration error of 0.37 mm with six fiducials, and 0.24 mm with eight fiducials (Table 5.8). Using the gold standard RBTs, the locations of the reconstructed vessels were rotated and translated into the CT coordinate system and it was visually confirmed that all the reconstructed catheters remained inside their respective catheterised vessels for the glass heart (Figure 5.10) and plastic heart (Figure 5.11).

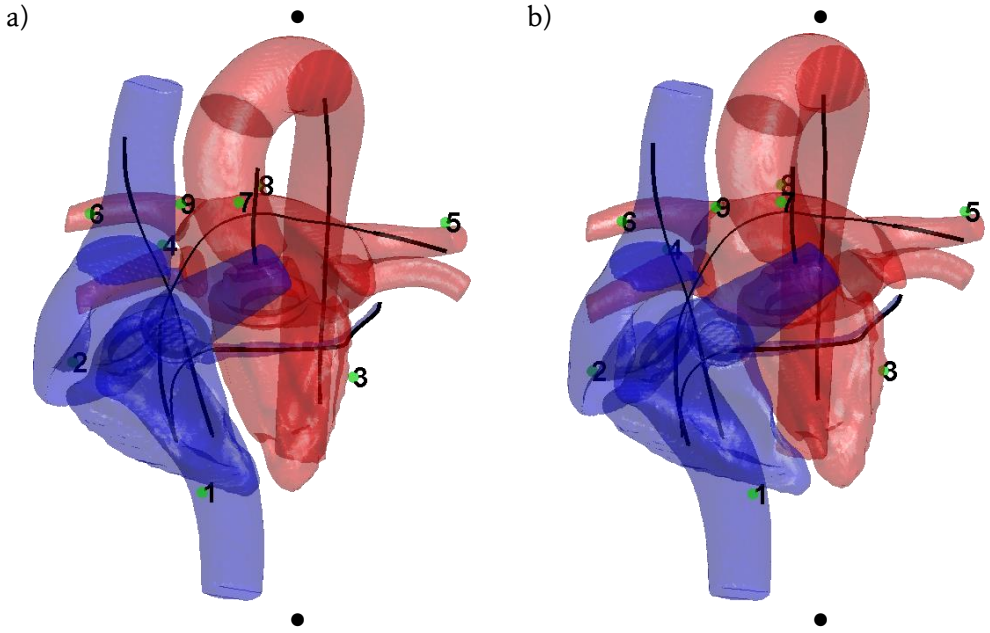


Figure 5.10 a, b) Cross-eyed stereogram pair of 3D surface rendering of glass heart segmented from CT. Left heart (*blue, translucent*) and right heart (*red, translucent*) divided by colour with seven fiducials and two anatomical landmarks located (*green spheres, numbered*). Gold standard registration is applied to catheter and guidewire reconstructions (*black lines, thicker in vessels of interest*) and shown indwelling in the CS, Ao, VCs and LUPV. To visually obtain depth, readers should cross their eyes such the image on the left is seen by the right eye and vice-versa, resulting in a double image of the pair. A 3D image can be formed by overlapping the two middle images of the double pair using the reference dots (●) to help alignment.

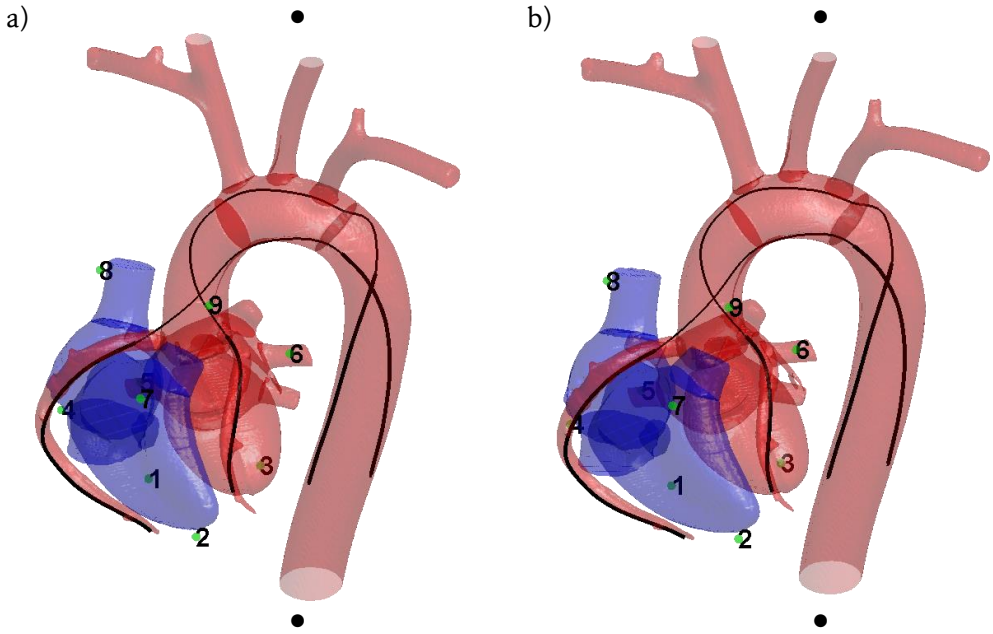


Figure 5.11 a, b) Cross-eyed stereogram pair of 3D surface rendering of plastic heart segmented from CT. Left heart (*blue, translucent*) and right heart (*red, translucent*) divided by colour with nine fiduciary markers located (*green spheres, numbered*). Gold standard registration is applied to catheter and guidewire reconstructions (*black lines, thicker in vessels of interest*) and shown indwelling in the DAo, AAo, LAD and RCA.

### 5.3.2. Catheter-Vessel Registration: Single-Catheter Approach

The single-catheter approach of the registration algorithm outlined in this chapter was applied to the CT and X-ray data of both the glass and plastic heart experiments. In the glass-heart experiments, six different vessels were catheterised (Table 5.6) in three catheter configurations (Table 5.4). In these configurations, the CS was catheterised three times, the IVC was catheterised five times, and the DAo, AAo, SVC and LUPV were catheterised once. In the plastic-heart experiments, 3 different vessels were catheterised (Table 5.6) in two configurations (Table 5.5). In these configurations, the DAo was catheterised twice, and the LAD and RCA were catheterised once. In both experiments, single-catheter registrations were applied to each catheter-vessel pair. After registration using the single-catheter approach, the transformation minimising the RMS distance error between the catheter and its corresponding vessel centreline (5.5) was used to compute a mean 3D-TRE compared to the fiducial marker-based gold standard (4.32). The resultant TREs are listed in Table 5.9; where the same vessel was catheterised multiple times in different configurations, the TREs were averaged.

| | | | Mean 3D-TRE (mm) | | | | | | |
|---|---|---|---|---|---|---|---|---|---|
| **Model** | **Vessel** | **#** | **LA** | **RA** | **LV** | **RV** | **WH** | **R** | ***t* (ms)** |
| **Glass** | **CS** | **4** | 13.8 | 13.7 | 12.9 | 11.1 | 13.3 | ✓ | 3.6 |
| | **DAo** | **2** | 32.8 | 24.5 | 37.7 | 30.6 | 31.8 | ✓ | 32 |
| | **AAo** | **2** | 51.2 | 66.1 | 43.5 | 48.5 | 55.3 | ✓ | 28 |
| | **IVC** | **2** | 184.2 | 170.1 | 139.4 | 135.7 | 162.6 | ✓ | 89 |
| | **SVC** | **1** | 89.4 | 76.0 | 41.8 | 46.5 | 68.2 | ✓ | 4.8 |
| | **LUPV** | **1** | 111.9 | 108.4 | 146.9 | 126.3 | 124.2 | × | 18 |
| **Plastic** | **RCA** | **1** | 114.8 | 144.0 | 58.1 | 95.9 | 106.1 | × | 35 |
| | **LAD** | **1** | 58.1 | 80.3 | 70.6 | 90.5 | 75.3 | × | 23 |
| | **DAo** | **2** | 36.6 | 49.0 | 64.4 | 74.5 | 52.6 | ✓ | 73 |

Table 5.9 – Mean 3D-TRE obtained using the single-catheter registration approach, compared to the fiducial-marker-based gold standard. TREs are computed at the anatomical landmark positions, grouped based on the chambers of the heart (*LA, RA, LV, RV*), and over the whole heart (*WH*). Where a vessel is catheterised multiple times (*#*) the average TRE is reported. Average computational time *t* to perform each registration is also reported in this table. The CS registration that is below the 15 mm clinical tolerance for usefulness is shaded in grey. A checkmark (✓) is placed under the column R if the algorithm registered the corresponding catheter and vessel in the correct direction, or a cross (×) is placed indicating a misregistration.

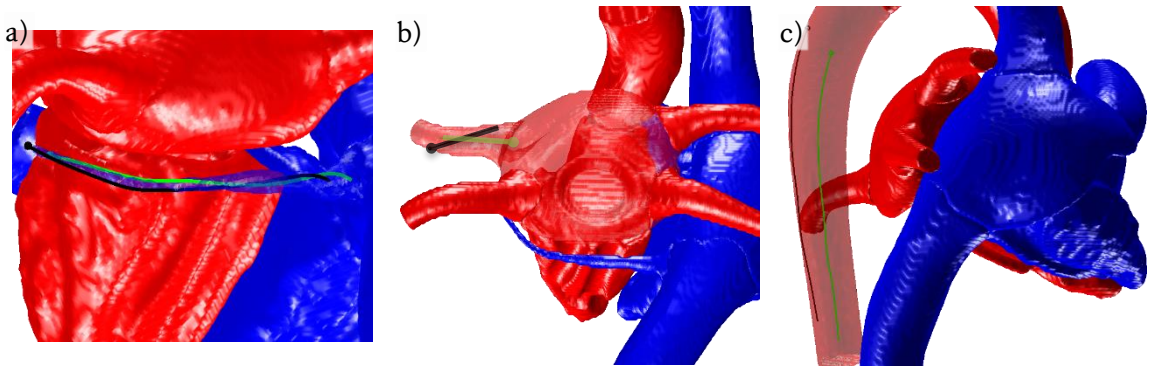


Figure 5.12) Surface rendering of the glass heart with examples of registrations with catheter segments (*green, translucent*) compared to the actual catheter location found by a gold standard registration (*black, solid*). Circle at the end of segment indicate the distal tip. Regions representing the left side of the heart are in red, and the right side in blue. a) Inferior-Posterior view of the heart with catheter in the CS. The curvature of the CS help prevent reflective misregistrations. b) Posterior view of the heart with catheter segment in the LUPV. Distal tip of the algorithm's registration compared to the gold standard registration are oppose one another, indicating a misregistration. The short length and straightness of the catheter are likely to have contributed to the error. c) Registration of the DAo configuration, showing the catheter location lying along the wall of the DAo and not at the centreline.

Registration with the CS performed the best, with accuracy within 15 mm (Figure 5.12a). Registration with the LUPV, RCA and LAD resulted in a misregistration. Misregistration is likely to occur when there is a discrete geometric symmetry of the structures used for registration; for example, a straight line has a reflective symmetry since it can reflect about its midpoint without changing shape. Misregistration of the LUPV configuration is likely due to the short length and straightness of the catheter segment within the LUPV (Figure 5.12b). There were no misregistration of the DAo, AAo, IVC and SVC configurations, however, these registrations were still very inaccurate. This is likely due to the large diameter of the vessel and the catheters not lying along the midline of the vessel, as assumed (Figure 5.12c).

### 5.3.3. Catheter-Vessel Registration: Unweighted Two-Catheter Approach

The two-catheter approach, which extends the single-catheter approach by treating every possible combination of the two catheter-vessel pairs and globally minimising the RMS distance error (5.10), was applied to the data extracted from the glass and plastic heart experiments, setting $\Delta = 1$.

#### *5.3.3.1. Unweighted Registration of the Glass Phantom*

In the glass heart experiment, 15 two-catheter-vessel (2CV) configurations were available from the catheterisations (Table 5.4) using the paired combinations of the CS, AAo, DAo, IVC, SVC and LUPV catheters. The mean 3D-TRE compared against the fiducial-based gold standard registration was computed for each configuration using (4.32), with the landmarks listed in

Table 5.7. These TREs are reported below in Table 5.10, in addition to the average time needed to perform the registration. There were no misregistrations.

| Configuration | | CS /DAo | CS/AAo | CS/IVC | CS/SVC | CS/LUPV | DAo/AAo | DAo/IVC | DAo/SVC | DAo/LUPV | AAo/IVC | AAo/SVC | AAo/LUPV | IVC/SVC | IVC/LUPV | SVC/LUPV |
|---|---|---|---|---|---|---|---|---|---|---|---|---|---|---|---|---|
| TRE (mm) | LA | 6.7 | 6.3 | 20.1 | 12 | 2.2 | 12 | 21 | 17 | 14 | 21 | 36 | 7.6 | 43 | 19 | 21 |
| | RA | 10 | 9.0 | 28.3 | 20 | 3.5 | 9.8 | 21 | 20 | 20 | 21 | 39 | 12 | 18 | 27 | 37 |
| | LV | 5.6 | 8.7 | 18.9 | 7.4 | 3.1 | 11 | 23 | 15 | 15 | 18 | 23 | 5.9 | 64 | 20 | 33 |
| | RV | 7.9 | 8.8 | 25.8 | 17 | 3.8 | 9.2 | 23 | 17 | 19 | 17 | 30 | 3.7 | 50 | 25 | 42 |
| | WH | 7.9 | 8.4 | 23.1 | 15 | 3.0 | 12 | 22 | 17 | 16 | 21 | 35 | 9.2 | 48 | 22 | 29 |
| Time (s) | | 2.3 | 2.3 | 5.0 | 0.28 | 0.45 | 5.4 | 25 | 1.4 | 2.3 | 18 | 0.83 | 1.4 | 2.2 | 2.9 | 0.14 |

Table 5.10 – Mean 3D-TRE (mm) over four chambers of the heart and of the whole heart (WH) for the two-catheter-vessel pairs. The registration pair with accuracy within the 5-mm clinical tolerance for RF ablation is shaded in dark grey, and pairs with accuracy within the 15-mm tolerance for usefulness are shaded grey. Average computation time is also listed.

The CS/LUPV pair yielded the lowest TRE of 3.0 mm over the whole heart. The $\mathcal{M}_{\text{reg}}$ found with this pair was used to perform the 2D-3D registration of the CT heart phantom onto the X-ray PA view (Figure 5.13a, b). 3D-3D co-registration between the reconstructed catheters and the CT heart phantom can also be visualised for purposes such as biophysical cardiac modelling (Figure 5.13c).

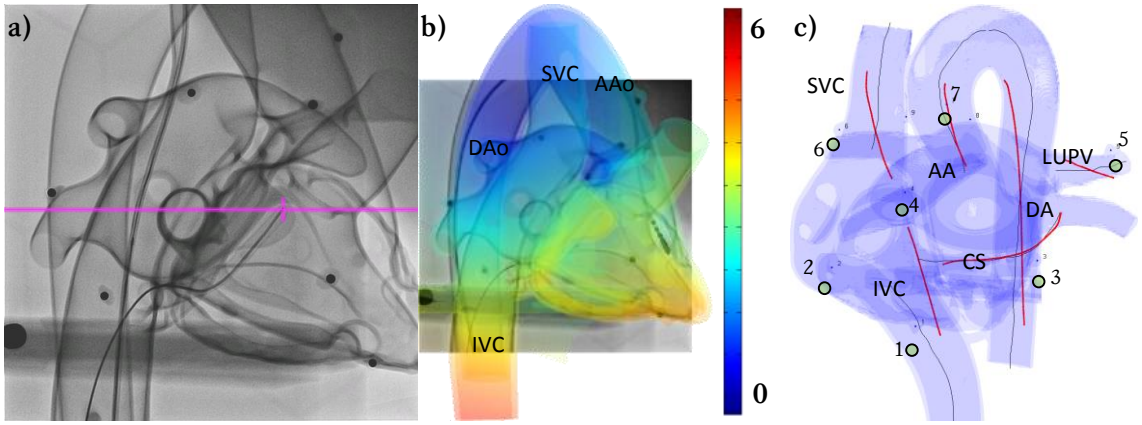


Figure 5.13 a) PA X-ray view of glass heart. b) Colour map showing spatial distribution of 3D-TRE over heart phantom (mm) with great vessels (*labelled*) overlaid onto the PA X-ray view using the CS/LUPV pair for registration. c) 3D view of the glass heart CT scan with registered reconstructed catheters (*thick red lines, labelled*) and medial lines of the vessels (*thin black lines, labelled*) shown. The seven fiducial markers placed around the heart and used to obtain the gold standard registration are also shown (*circled, numbered*).

#### 5.3.3.2. Unweighted Registration of the Plastic Phantom

In the plastic heart experiment, two two-catheter configurations were available from the two catheterisations (Table 5.5): the RCA/DAo and the LAD/DAo. The RCA/LAD combination is rare in the clinical setting and is therefore excluded. The reported mean 3D-TREs and computational time cost of the two configurations is listed in Table 5.11. There were no misregistrations.

| Configuration | | RCA/DA | LAD/DA |
|---|---|---|---|
| TRE (mm) | LA | 15 | 13 |
| | RA | 15 | 14 |
| | LV | 8.5 | 13 |
| | RV | 9.0 | 16 |
| | WH | 12 | 13 |
| Time (s) | | 16 | 11 |

Table 5.11 – Mean 3D-TRE (mm) over four chambers of the heart and of the whole heart (WH) for the two 2CV pairs. Average computing time is also listed. Both registrations yield accuracy below the 15-mm threshold but above the 5-mm threshold.

### 5.3.4. Catheter-Vessel Registration: Weighted Two-Catheter Approach

The third approach to the global-fit registration algorithm that minimises the weighted error (5.11) was applied to the two-catheter configurations of the glass and plastic heart experiments, discussed in the previous section, initially using $x = 2$ and $\Delta = 1$ mm. Based on these results, two sensitivity analyses were conducted. One that varied the weighting constant $x \in \{0, 1, 2, 3\}$ while keeping $\Delta = 1.0$ mm constant, while the other varied the reparameterisation constant $\Delta \in \{0.2, 0.6, 1.0, 1.4, 1.8\}$ mm while keeping $x = 2$ constant.

#### 5.3.4.1. Weighted Registration of the Glass Phantom

For each two-catheter configuration, the mean 3D-TREs were calculated using the anatomical landmarks in and around the four chambers of the heart, and for the whole heart (WH), as in the previous section but minimising the weighted error (5.11) as opposed to the unweighted error (5.10). The TREs calculated for the 15 two-catheter-vessel pairs, and the computational time cost to run the registration algorithm, are giving in Table 5.12. There were no misregistrations.

| Configuration | | CS /DAo | CS/AAo | CS/IVC | CS/SVC | CS/LUPV | DAo/AAo | DAo/IVC | DAo/SVC | DAo/LUPV | AAo/IVC | AAo/SVC | AAo/LUPV | IVC/SVC | IVC/LUPV | SVC/LUPV |
|---|---|---|---|---|---|---|---|---|---|---|---|---|---|---|---|---|
| TRE (mm) | LA | 0.35 | 2.8 | 6.0 | 8.0 | 5.2 | 12 | 20 | 17 | 11 | 21 | 35 | 12 | 42 | 14 | 20 |
| | RA | 0.55 | 3.9 | 10 | 14 | 7.7 | 9.6 | 21 | 20 | 16 | 21 | 39 | 18 | 18 | 22 | 35 |
| | LV | 0.65 | 3.7 | 9.0 | 4.9 | 7.1 | 11 | 23 | 14 | 13 | 17 | 22 | 10 | 63 | 15 | 32 |
| | RV | 0.66 | 3.9 | 11 | 7.7 | 7.7 | 8.7 | 23 | 17 | 17 | 17 | 30 | 7.9 | 49 | 20 | 40 |
| | WH | 0.55 | 3.6 | 9.1 | 8.7 | 6.9 | 10 | 22 | 17 | 14 | 19 | 32 | 12 | 43 | 18 | 32 |
| Time (s) | | 2.3 | 2.3 | 5.0 | 0.28 | 0.45 | 5.4 | 25 | 1.4 | 2.3 | 18 | 0.83 | 1.4 | 2.2 | 2.9 | 0.14 |

Table 5.12 – Mean 3D-TRE (mm) over four chambers of the heart and of the whole heart (WH) for the 2CV pairs for the glass heart phantom using the weighted two-catheter approach. Pairs with TREs within 5-mm are shaded in dark grey while those between 5-mm and 15-mm are shaded light grey. Average computation time is also listed.

Registration of the configurations involving the CS with the DAo or AAo performed best, with accuracy between 0.55 and 3.6 mm 3D-TRE (Figure 5.14a). A possible reason for such a high degree of accuracy is due to the tapering of the CS, which provide very tight constraints for registration. Registration using a single catheter is possible if divided into two separate segments (Figure 5.14b). However, parallel configurations do not provide very accurate registrations, usually in the order of 10 mm or higher. Registration using the IVC and LUPV configurations performed poorly. While there was no misregistration, both these vessels have relatively large diameters and therefore provide less constraints (Figure 5.14c).

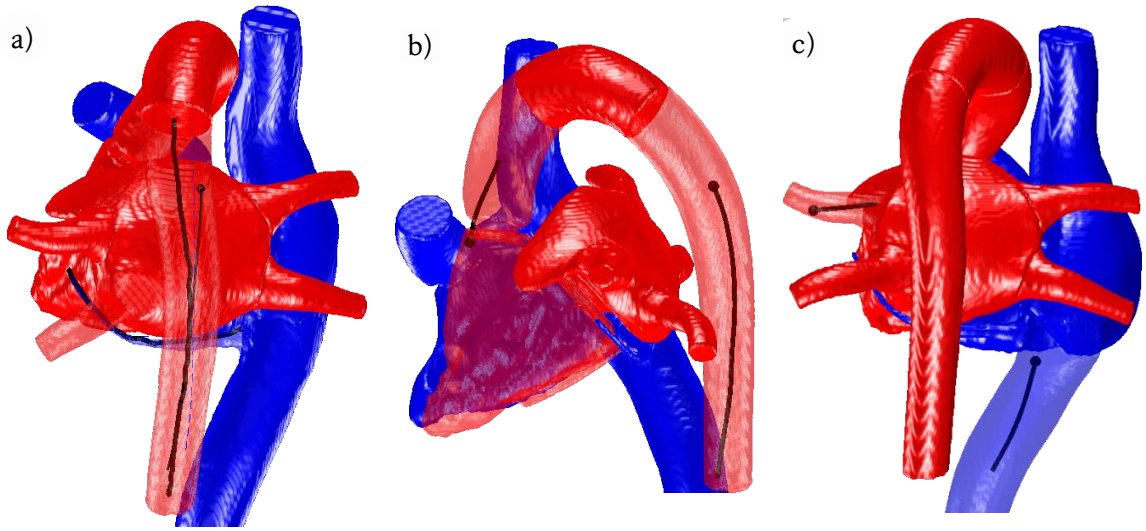


Figure 5.14) Surface rendering of the glass heart with examples of two catheter registrations of catheter segments (black). Circle at the end of segment indicate the distal tip. a) Posterior view of the heart with a catheter in the CS and one in the DAo. Left lateral view of the heart with a single catheter inserted into the Ao, but divided into the DAo and AAo segments. c) Posterior view of the heart with catheter segment in the LUPV and IVC.

#### 5.3.4.2. Weighted Registration of the Plastic Phantom

In the plastic heart phantom experiment the global-fit algorithm, with the parameters set at $x = 2$ and $\Delta = 1$ mm, was also applied to RCA/DAo and LAD/DAo configurations. The TREs and computational times are recorded in Table 5.13. There were no misregistrations.

| Configuration | | RCA/DA | LAD/DAo |
|---|---|---|---|
| TRE (mm) | LA | 2.8 | 6.4 |
| | RA | 4.1 | 7.3 |
| | LV | 2.9 | 6.6 |
| | RV | 4.8 | 8.3 |
| | WH | 3.5 | 7.0 |
| Time (s) | | 16 | 11 |

Table 5.13 – Mean 3D-TRE (mm) over four chambers of the heart and of the whole heart (WH) for the two 2CVs, and the average computational time cost (s). Registration with RCA has accuracy within 5-mm while registration with LAD has accuracy between 5-mm and 15-mm.

#### 5.3.4.3. Sensitivity of Registration to Changes in Weighting (x)

The sensitivity of the algorithm to the inverse-power-of-radius weighting constant $x$ was assessed by applying the algorithm to the five best two-catheter configurations without weighting ($x$ = 0), and with weighting inversely proportional to the vessel radius ($x$ = 1), cross sectional area ($x$ = 2) and volume ($x$ = 3). The mean 3D-TREs were computed for each chamber of the heart and for the whole heart using the anatomical landmarks (Table 5.7).

In the glass heart experiment, using the five configurations which yielded the lowest mean 3D-TRE to test the sensitivity of the algorithm to variations in $x$ (Figure 5.15a), four had lower TREs when using the vessel-radius weighting ($x = 1, 2, 3$) than when not ($x = 0$). The CS/LUPV pair was an exception.

In the plastic heart experiment, for both catheter configurations the weighted approach ($x = 1, 2, 3$) yielded mean 3D-TREs lower than the unweighted approach ($x = 0$) over all four chambers of the heart and over the whole heart (Figure 5.16). Weighting inversely proportional to the cross-sectional area ($x = 2$) yielded the lowest TREs.

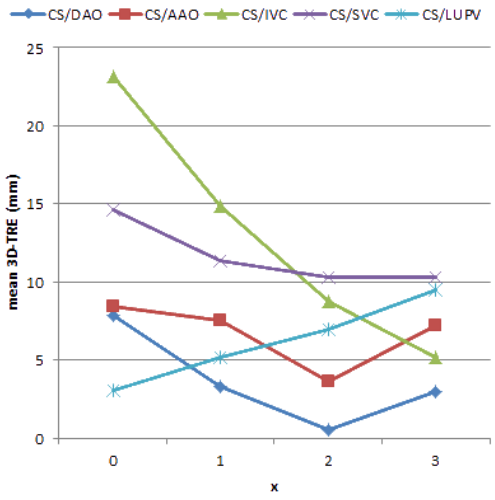


Figure 5.15) Graph showing mean whole-heart 3D-TRE of best 5 configurations of the glass heart as a function of the inverse-power-of-radius-weighting constant $x$.

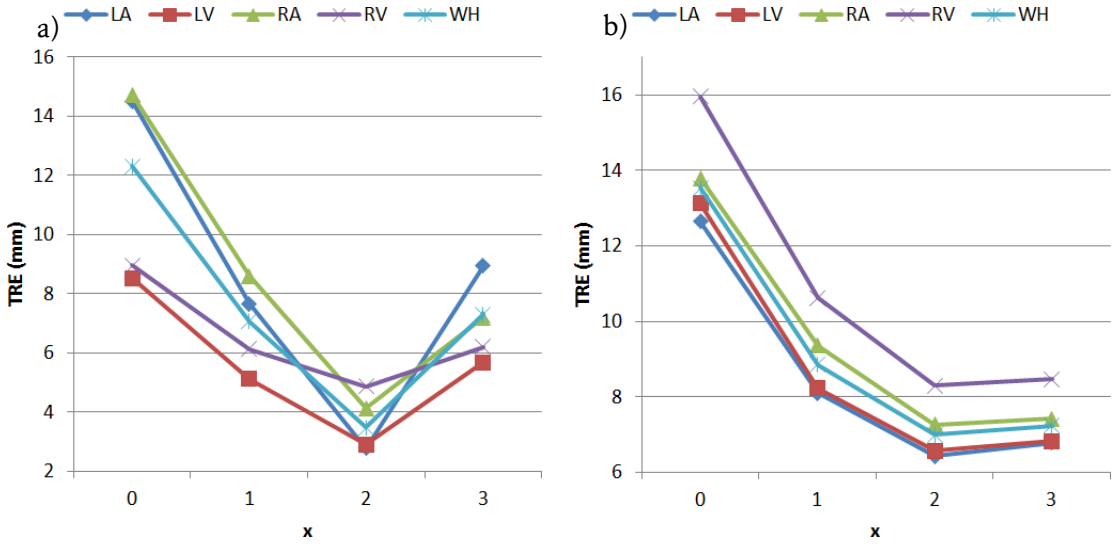


Figure 5.16) Graphs showing mean 3D-TRE over the four chambers of the plastic heart and of the whole heart as a function of $x$ for a) the RCA/DAO and b) the LCA/DAO catheter configurations.

#### 5.3.4.4. Sensitivity of Registration to Changes in Reparameterisation (✪)

In both the glass heart and plastic heart experiments, the algorithm's sensitivity to changes in the reparameterisation spacing constant $\Delta$ was tested by varying the constant in increments of 0.4-mm between 0.2 mm and 1.8 mm, which encompasses the typical range of CT scan resolutions, and applying the registration to each catheter configuration. Weighting inversely proportional to the vessel's cross-sectional-area ($x = 2$) was used. The mean 3D-TRE of the anatomical markers surrounding the whole heart (Table 5.7) were calculated for each of the five catheter configurations involving the CS in the glass heart, and the two catheter configurations involving the CA in the plastic heart (Figure 5.17). $\Delta$ below 0.2 and above 1.8 mm were not considered since these are beyond the resolution of a typical clinical CT scan.

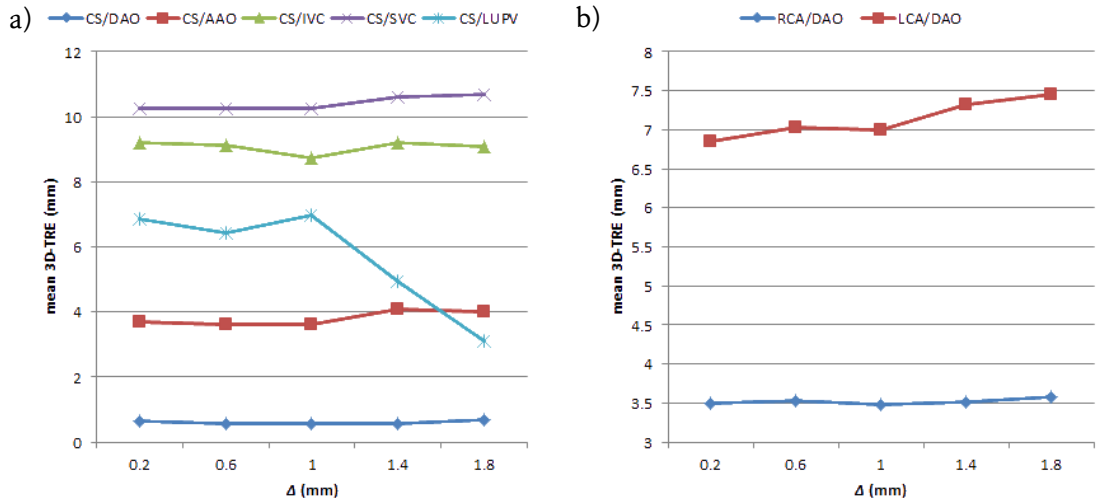


Figure 5.17 a) Graphs showing mean 3D-TRE over the whole heart as a function of the reparameterisation spacing constant Δ for a) the five catheter configurations involving the CS in the glass heart, and b) the two catheter configurations involving the CA in the plastic heart.

For the glass heart, the configurations involving the CS with the DAo, AAo, IVC and SVC had a maximum percentage difference in TRE of 20% or less (Figure 5.17), but this rose to 77% for the CS/LUPV configuration. Reasons for this are speculated in the discussion (§5.4.6). In the plastic heart experiment, the maximum percentage difference in TRE was also within 20%.

Increasing $\Delta$ decreases the number of points that make up the catheters and vessels, thereby reducing the search space that the global-fit algorithm is required to iterate through Figure 5.18.

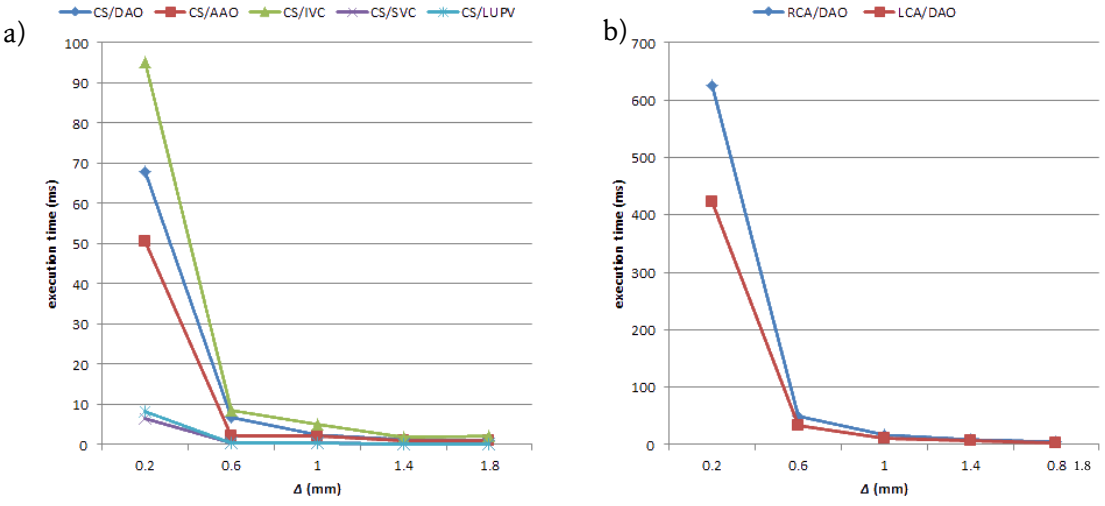


Figure 5.18 a) Graph of execution time of the global-fit algorithm for the five configurations involving the CS in the glass heart, and b) the two configurations involving the CA in the plastic heart.

## 5.4. Discussion

An algorithm has been developed that performs 2D-3D image registration between cardiac images from CT and X-ray. The algorithm relies on catheters placed inside vessels of the heart where they remain relatively stationary throughout the procedure. In these interventions, this is a valid assumption since it is typical to employ several such catheters to collect essential EP data from the patient. A three-DOF global search strategy is used to account for differences in length between the picked catheters and vessels, and in their picking directions. Input requirements for the algorithm are the cross-sectional radius and points along the centreline of the vessel containing the catheter, and points lying on the catheter itself which are found through biplane reconstruction using epipolar geometry. A rigid-body registration is determined by minimising a root-mean-square (RMS) distance error between the points along the catheter and its corresponding vessel centreline. Three approaches have been proposed, the first registers using only a single catheter inserted inside a vessel. The second relies on the insertion of two catheters into two vessels, and the third approach extends this idea by introducing a weighting function which is inversely proportional to the cross-sectional radius of the vessel.

The three approaches to the catheter-based algorithm were applied to two phantom experiments involving the catheterisation of rigid and anatomically-correct models of the heart; one made of glass and the other made of plastic. Both models consisted of the four chambers of the heart, the venae cavae, the aorta, the four pulmonary veins and the pulmonary trunk. The models differed in coronary anatomy; the glass heart included a coronary sinus but not coronary arteries, while the plastic heart included a coronary artery tree but not the coronary sinus. The experiments were designed to emulate the clinical workflow of typical cardiac catheterisation procedures. Preoperatively, CT scans were taken of the models, followed by the intraoperative insertion of catheters into vessels of the model in various configurations, imaged using X-ray fluoroscopy. The image data acquired were then registered using the three approaches of the catheter-based algorithm. To quantify their accuracy, radio-opaque 0.25-mm diameter lead balls were adhered around the heart to act as fiducial markers. These were visible in both the CT scan and X-ray fluoroscopy images to provide a gold standard rigid-body transformation between the two image-spaces using [86] without scaling. For both experiments, the fiducial registration error (FRE) of the gold standard was below 0.5 mm.

### 5.4.1. Single-Catheter Approach

In the single-catheter approach, no catheter-vessel pair was enough to constrain the registration to accuracy within the clinical tolerance of 5-mm for cardiac catheterisations, as described in Chapter 1. In the glass heart experiment, the lowest TRE over the whole heart was achieved using the coronary sinus (CS) catheter, yielding 13.3-mm accuracy while the registration with

the other five vessels, namely the DAo, AAo, IVC, SVC and LUPV yielded accuracy between 31.8 and 162.6 mm over the whole heart. The CS performing better than the other vessels is likely because of the narrow diameter and significant curvature of the CS, allowing for a better registration than when using the other vessels which are straighter and have a wider diameter.

In the plastic heart experiment, all three registrations using the RCA, LAD and DAo catheters performed poorly with TREs between 52.6 and 106.1 mm over the heart. The main cause of misregistration in both the glass and plastic were geometric symmetries. For example, when trying to match a straight catheter to a straight vessel, the global search strategy would be unable to tell where along the vessel the catheter is, since any translation along the vessel would result in similarly low residual errors when calculating a RMS distance error between them. Likewise, the catheter can be flipped upside down, or rotated about the axis of the vessel, and still result in similarly low residual errors. These three scenarios are known as translational, reflective and rotational symmetry respectively. While the narrow vessels do not possess such translational and rotational symmetry, they do possess reflective symmetry with the CS and RCA in the shape of the letter 'C', and the LAD artery in the shape of the letter 'S'. In these cases, the RMS distance error when lining up the catheter with the vessel distal-end-to-distal-end, i.e. the correct orientation, would be as equally low as lining them up distal-end to proximal-end, which is the incorrect orientation; the latter being the case for these misregistrations. In these cases, a second constraint could help choose the correct orientation.

### 5.4.2. Two-Catheter Approach

The second catheter-vessel pair was introduced with the aim of these misregistration scenarios, since the catheter pair is less likely to have geometric symmetry than a single catheter. However, there are some cases that may still exist, for example, using two catheter-vessel pairs that are parallel to each other which allows for translational symmetry. Based on the experiments, results show that two catheters do yield improved accuracy over the single-catheter approach, with TREs between 3.0 and 48.0 mm over the whole heart in the glass heart experiment and between 12.0 and 13.0 mm in the plastic heart experiment. Using the CS/LUPV combination yielded the best result with 3.0-mm accuracy over the whole heart, which is within the clinical tolerance. Registrations using the CS/DAo, CS/AAo, CS/SVC, DAo/AAo, RCA/DAo, LAD/DAo yielded accuracy between 7.9 and 15 mm, while the remaining configurations yielded accuracy between 16 and 48 mm. While misregistration is less frequent using two catheters, the assumption that the catheter lies along the medial line of the vessel may not be accurate, especially when registering with great vessels since they provide more room for the catheter to move around.

### 5.4.3. Two-Catheter Weighted Approach

The third approach introduced a weight function into the RMS distance error measurement (5.11), which increases inversely with the cross-sectional vessel radius, and was designed to address the issue of registering with great vessels by having thin vessels impact the registration more than larger vessels. Using this weighted two-catheter approach, results from the glass heart experiment show that the TRE was highly dependent on which two catheter/vessel pairs were used and indicates that configurations involving the CS catheter resulted in lower TREs (between 0.55 to 9.1 mm) than those that did not (10 to 43 mm). Furthermore, when using the CS in conjunction with the AAo or DAo, TREs below the 5-mm clinical tolerance [65] can be achieved at 0.55 and 3.6 mm respectively. The remaining 13 configurations did not yield TREs below the 5-mm tolerance; this is possibly due to a number of reasons. Among the configurations involving combinations of the DAo, AAo, IVC and SVC, the vessels involved are close to geometrically parallel to each other (Figure 5.10b). Parallel geometries may not be ideal for registration since translations along the parallel vessel direction may result in similarly low residual errors, increasing the probability of a misregistration. All configurations involving the LUPV also resulted in TREs above 5-mm, possibly since the vessel was significantly shorter than the other vessels used for registration (Table 5.6, Figure 5.10b). This may suggest that short catheters are less ideal than long ones for registration since there are fewer points available to minimise the error with (5.11). In the plastic heart experiment, registration with the RCA/DAo configuration achieved an accuracy of 3.5 mm, below the 5-mm clinical tolerance, and can potentially be suitable for RFA procedures. Registration with the LAD/DAo achieved an accuracy of 7.0 which is within 15-mm accuracy suitable for a general X-ray-MR overlay. A reason why the RCA might be better than the LAD for registration may have to do with it being nearly twice as long and therefore have more points available for constrain the registration (Table 5.3, Table 5.6).

As indicated in the unweighted two-catheter approach, the assumption that the catheter lies along the medial line of the vessel may not be accurate, especially when registering with great vessels, since they provide a greater diameter for the catheter to move around in (Figure 5.10b; IVC and SVC). To minimise the loss of accuracy due to this assumption, weighting was used which was a function inversely proportional to the vessel radius. In four out of five configurations involving the CS in the glass heart experiment, and in both configurations involving the coronary arteries in the plastic heart experiments, the vessel-radius-weighting resulted in a more accurate registration (Figure 5.15).

### 5.4.4. Catheter-Vessel-Centreline Assumption

Catheter trajectories tend to follow the path of minimum bending energy [124], and so the assumption that the catheter lies along the vessel centreline is likely to be incorrect (Figure 5.10, Figure 5.11) and add a degree of the inaccuracy to the algorithm. This error is expected to be depended on the radius of the vessels used for registration for the unweighted approach, representing the amount of distance the catheter is allowed to move around. In the weighted approach, the error should be reduced since more weight is given to the smaller diameter vessels that provide better constraints. There is potential to increase the accuracy of the algorithm by registering the catheter to simulated trajectory of the catheter placed within the vessel [118] [119] [120]. However, in clinical practice, being able to provide a robust registration is of utmost importance. Matching the catheter to the vessel-centreline trades off potential accuracy for better robustness compared to matching to an estimated catheter trajectory within the vessel, since using an inaccurately predicted catheter trajectory can greatly amplify registration errors.

### 5.4.5. Clinical Applicability

In the phantom experiments, all possible two-catheter combinations were tested for accuracy. However, not all configurations are clinically practical, for example it is not typical in any interventional procedure to cannulate both the IVC and SVC at the same time. The possible cannulations of interventional procedures are listed in Table 3.3. Furthermore, the clinical tolerance of 5 mm 3D-TRE averaged over the whole heart is only a guideline during the experiment as each type of interventional procedure has different location targets where the catheter needs to be placed, and different accuracy requirements (§1.5). The results of the two-catheter weighted registration experiments in Table 5.12 and Table 5.13 are re-organised to apply to the optimal configuration of specific interventional procedures (Table 5.14). Only the two-catheter weighted results are analysed in this way, since it out-performs the single-catheter and unweighted two-catheter approaches.

| | | | 3D-TRE (mm) | | |
|---|---|---|---|---|---|
| Intervention | Configuration | Target | Ideal | Target | WH |
| PCI | RCA/DAo | LV | 2.5 | 2.9 | 3.5 |
| PCI | LAD/DAo | LV | 2.5 | 6.6 | 7.0 |
| CRT | CS/SVC | LV | 5.5 | 4.9 | 8.7 |
| RFA in RH | CS/SVC | RV | 4 | 7.7 | 8.7 |
| RFA in LH | SVC/LUPV | LA | 3 | 20 | 32 |
| RFA in LH | CS/LUPV | LA | 3 | 5.2 | 6.9 |

Table 5.14 – Registration results of the weighted two-catheter approach according to the applicable intervention, relevant catheter configuration, and target chamber to where catheter navigation is needed, and ideal accuracy at the site. The 3D-TRE is the accuracy achieved by the algorithm at the target chamber, and averaged over the whole heart (WH). Results where the achieved accuracy is within the clinical requirement is shaded, and results where the achieved accuracy is close to the 5.0-mm clinical tolerance is lightly shaded.

The re-organised results in Table 5.14 show that the ideal clinical requirements of CRT are met when the CS catheter is involved. While the clinical requirements defined in §1.5 are ideal, in practice the heart is rapidly beating and moving due to breathing. These motions will tend to dominate the registration, and the interventionist would be trained to read each registration with caution. Therefore, realistically a wider tolerance would be sufficient, generally 5 mm 3D-TRE. With a slightly wider tolerance, a useful registration could be obtained in PCI, CRT and RFA using the shaded configurations in Table 5.14.

### 5.4.6. Clinical Feasibility

The intention is to enable deployment of this algorithm into clinical practice. The operation is time-critical; therefore minimising the computational time needed to perform the registration is paramount. Since the size of the search space decreases with increasing $\Delta$, the computational cost should decrease as well. Results from the sensitivity analysis of the arclength reparameterisation show that when varying $\Delta$ from 0.2 to 1.8 mm, there was a 56-fold decrease in computational time. Meanwhile the maximum difference in accuracy was within 20% for four of five configurations involving the CS and the two configurations involving the CA (Figure 5.18). Based on these results, it can be concluded that computation time can be significantly improved without significantly sacrificing accuracy by increasing $\Delta$, thereby reducing the size of the search space.

In both sensitivity tests with varying x and Δ, the CS/LUPV was the one-in-five outlier. This is possibly due to the two vessels being very close to geometrically parallel while the remaining four were close to perpendicular, and the LUPV could be too short to provide an accurate registration. Aside from the one-in-five outlier, the sensitivity analyses indicate suitable values of $\Delta = 1$ and $x = 2$ for general use. A smaller $\Delta$ would increase the computational time without significantly improving the accuracy, while a larger $\Delta$ may cause a loss of accuracy as in the CS/LUPV (Figure 5.17, Figure 5.18). The choice for $x$ is based on the results shown in Figure 5.15 and Figure 5.16 where there is a decrease in error at $x = 2$. This is likely since it corresponds to a weighting inversely proportional to the cross-sectional area of the vessel within which points along the catheters are largely constrained.

While experiments show that registration with glass and plastic phantoms can yield TREs within the 5-mm clinical tolerance, there are several limitations of this approach. With clinical data, an additional gating step due to cardiac and respiratory motions is needed and will likely decrease the accuracy. The algorithm also assumes that the heart is a rigid-body when at the end-diastole and end-expiration phases. However, the heart undergoes significant motion and deformation throughout the cardiac and respiratory cycles and may not necessarily return to the same shape and size when returning to the same phase. Additionally, the insertion of a rigid catheter into a

soft-tissue vessel may further cause deformations [118] [119] [122]. Both of these issues are likely to add registration errors that are not present when working with rigid hearts. The next step in development of this algorithm is to apply it to clinical data to assess how much the accuracy is lessened by violations of these assumptions. The results of this study are outlined and summarised in the following chapter.

### 5.4.7. Conclusion

A novel catheter-based registration algorithm has been developed and validated on two phantom experiments and has been demonstrated to achieve accuracies within the 5-mm clinical tolerance, a criterion for suitability for deployment in the clinical workflow. A novelty of this algorithm is the global fit approach for finding the best point-correspondence between catheters and vessels and ensuring they are correctly aligned with one another. The global approach has two advantages over a local approach. Assuming that the catheter is entirely contained in the region of its segmented corresponding vessel, the global search strategy is guaranteed to encounter the correct solution during its search whereas a local search might not encounter the correct solution. This not only increases the robustness of the global algorithm, but also avoids the need for a good initial estimate of the registration.

In terms of clinical applicability, using two catheters with weighted inversely proportional to the vessel's cross sectional radius yielded the most accurate registrations. This approach was more accurate than both unweighted approach and the approach using a single catheter. Another contribution to knowledge in this chapter is the testing of which catheter configurations produced the most accurate results. Based on the phantom experiments, the following recommendations could be made for the choice of catheters:

1) Registration with the CS/DAo, CS/AAo and RCA/DAo performed the best with accuracy within the 5-mm clinical tolerance.
2) Registration with the DAo/IVC, DAo/SVC, AAo/IVC, AAo/SVC, IVC/SVC, IVC/LUPV, SVC/LUPV performed poorly, above the 15-mm clinical tolerance and should be avoided.

# Chapter 6

## 6. Catheter-Based 2D-3D Registration of Clinical Interventions

In this chapter, the catheter-based 2D-3D image registration algorithm presented in the previous chapter is adapted to deal with the additional sources of noises and artefacts introduced when registering with clinical data. In the previous chapter, registration was demonstrated and analysed on two rigid, anatomically-correct phantom models in experiments designed to emulate the clinical workflow of a typical catheterisation. Registration relied on catheters being placed in the vessels of the heart and remaining there throughout the procedure. The catheters were then reconstructed from biplane X-ray images and matched to the centreline of their containing vessels segmented from cardiac MR scans. Based on the phantom experiments, it was shown that weighting the registration using a function inversely proportional to the vessels' radii improved the algorithm's accuracy. The experiments also showed that accuracy could be improved by registering using two catheter-vessel pairs instead of one. The algorithm used a rigid-body assumption that was valid when registering with phantom models.

Images from patient data differ from the phantom models in several ways with the most significant being the non-rigidity and non-stationary nature of the heart throughout the cardiorespiratory cycle. This introduces motion artefacts and potential phase mismatch issues between images of the heart. Additionally, patient images usually have lower contrast than images of phantoms and so imaging of the heart usually involves the injection and perfusion of contrast agent into the blood stream for better vessel and chamber visibility. However, the rapid transportation of blood disperses the contrast agent non-uniformly throughout the vessels and chambers, resulting in cardiac images where some regions of interest (ROIs) have little or no contrast at all. With patient data, it is difficult to know for certain which vessel branch has been catheterised due to the poor visibility of fluoroscopy. X-ray angiography provides insight into resolving this matter at the expense of a contrast-agent injection, but even so, the projective nature of X-ray may result in the catheterised branches being overlapped with other branches. This makes it difficult to resolve which branch has actually been catheterised, especially with the complex vasculature of coronary vessels. This is not an issue with phantom heart models since the exact branch of the coronary anatomy that is catheterised in the phantom is visually verifiable as the heart is translucent and not encased. On the other hand, material limitations of

phantom heart models can only provide a small number of branches of the coronary sinus and arteries for catheterisation.

To deal with the uncertainties introduced when registering with patient data, the registration algorithm has been augmented with a number of image processing techniques, which are presented in this chapter. These techniques include image segmentation and morphological operations, skeletonisation, automatic radius detection and topological analysis of the preoperative data; and cardiorespiratory gating of the intraoperative X-ray data. The improved registration algorithm is applied to the images of three cardiac catheterisation procedures and compared to manual registrations. Manual registrations were performed using a modified EP navigator (Philips Healthcare, Best, The Netherlands), a software platform currently employed in routine catheterisation procedures to interactively align the preoperative magnetic resonance (MR) data with the intraoperative X-ray. The purpose is to compare the automatic registration algorithm presented in this chapter to a current standard registration method used in clinical practice.

After treatment, while the patient is still lying on the operating table, electroanatomical mapping (EAM) data of the left ventricle (LV) endocardial wall is acquired. A second registration algorithm is proposed in this chapter to additionally register the EAM data to the already co-registered X-ray-MR space (XMS), and this is demonstrated in an exemplary clinical case. The triple co-registration of X-ray, MR and EAM data is useful for both electrophysiological (EP) validation of the effectiveness of the procedure, and for biophysical modelling purposes [125] [126] [127]. Accuracy of the triple co-registration is demonstrated by comparing regions of scarring of the heart on the LV myocardium obtained from a late gadolinium-enhanced cardiac MR (LGE-CMR) scan to the bipolar voltage data obtained from the intraoperative EAM.

## 6.1. Clinical Data

The extended 2D-3D registration algorithm presented in this chapter is applied to a three clinical cases that exemplify typical cardiac catheterisation procedures as outlined in Chapter 3. The first of these cases involves a patient who underwent radio-frequency ablation (RFA) for atrial fibrillation (AF); the second underwent cardiac resynchronisation therapy (CRT); the third was treated for arteriosclerosis by percutaneous coronary intervention (PCI).

Prior to the catheterisation, 3D scans of the patient were acquired with MR for diagnostic and treatment planning purposes (Figure 6.1a). Two MR scans are used in this chapter for registration, one to obtain 3D anatomical information of the heart and the other for localising regions of scar inside the LV myocardial chamber. Anatomical images were carried out after the administration of a blood pool contrast agent (Vasovist®, Bayer Schering Pharma, Berlin,

Germany) injection using either a 3D steady-state free precession (SSFP) or spoiled gradient echo (SGE) sequence with an inversion recovery preparation RF-pulse. Scar images were acquired using an LGE-CMR protocol which involved the injection of gadolinium contrast agent and an initial SSFP scan, followed by a late SSFP scan which exposes regions of scar within the heart. The preoperative MR scans were respiratory navigator gated at end-expiration and electrocardiogram (ECG)-triggered at late diastole.

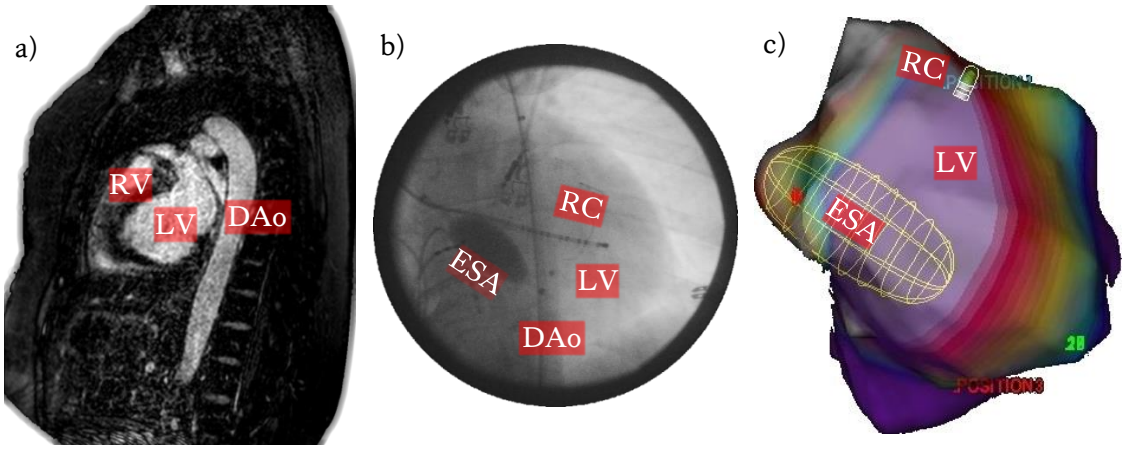


Figure 6.1 a) A sagittal slice of a patient's torso scan taken from a contrast-enhanced MR image. Left (*LV*) and right ventricles (*RV*) and descending aorta (*DAo*) are labelled. b) Posterior-anterior X-ray view of the heart with intracardiac devices, including the EnSite Array™ (*ESA*) and roving catheter (*RC*) in the LV entering via the DAo, and the coronary sinus catheter. c) Example of the EAM information acquired using the EnSite™ System in anterior-posterior views of cardiac action potential depolarisation mapped onto the surface rendering of the LV endocardial wall geometry. The location of the ESA and RC in relation to the LV is also displayed.

Intraoperatively, the catheterisations were guided under X-ray (Figure 6.1b) using a tracked and pre-calibrated fluoroscopy imaging system [30] with the patient lying supine and their hearts approximately at the isocentre of the C-arm-shaped gantry. During the EP procedure, the aorta and at least one small-diameter vessel, either the coronary sinus or one of the coronary arteries, were catheterised followed by the acquisition of sequential biplane fluoroscopy videos at up to 15 frames per second during free-breathing. Approximately four seconds were recorded for both X-ray views so that at least two full breathing cycles were captured. After treatment, but while the patient was still lying on the operating table, the LV endocardial wall was electroanatomically mapped (Figure 6.1c) using the EnSite™ System (St. Jude Medical, St. Paul, MN, USA). All patients were treated at St. Thomas' Hospital, London, UK, and whose consent to the acquisition and use of the data for research purposes was acquired. The catheterisation case is summarised in Table 6.1. MR and X-ray imaging parameters for the clinical case is summarised in Table 6.2 and Table 6.3 respectively.

| Case | Vessels catheterised | EAM System |
|---|---|---|
| **RFA** | Aorta, CS | EnSite™ |
| **CRT** | Aorta, CS | EnSite™ |
| **PCI** | Aorta, LAD | Carto™ XP |

Table 6.1 – Listing of the three catheterisation cases identified by their case type and number. Vessels catheterised during the procedure and used for registration are also listed, along with the voltage mapping system used to collect the EAM data.

### 6.1.1. Radiofrequency-Ablation for Right Atrial Fibrillation

This clinical procedure was performed in a hybrid X-ray and MR (XMR) interventional suite which was equipped with a 1.5T cylindrical bore MR scanner (Intera, Philips Healthcare, Best, The Netherlands) and a single plane X-ray system (BV Pulsera, Philips Healthcare). Gadolinium-enhanced MR angiograms (MRA) were taken of the patient using a balanced turbo field echo (TFE)(bTFE) pulse sequence, a type of SSFP, while the scarring of the patient's heart was imaged using an LGE-CMR scan (Table 6.2). During the EP procedure, a balloon catheter (EnSite Array™ Catheter, St. Jude Medical, St. Paul, MN, USA) and Redel 10-Pin connected catheter (7F Webster® Decapolar Catheter, Biosense Webster, Diamond Bar, CA, USA) was inserted into the left ventricle (LV) via the aorta (Ao) to collect EAM information along the LV endocardium, while an endovascular coronary sinus (CS) catheter was placed within the CS to collect essential ECG and pressure measurements. A pulmonary vein (PV) isolation (PVI) was performed in the left atrium (§2.3.3) which required cannulation of the four PVs. While the catheters were in place, sequential biplane fluoroscopy images (Table 6.3) were acquired using the single plane X-ray system during free-breathing for approximately four seconds.

### 6.1.2. Cardiac Resynchronisation Therapy

The patient who underwent CRT was treated in a dedicated catheterisation laboratory equipped with a tracked and pre-calibrated single-plane X-ray system (Allura Xper, Phillips Healthcare). 3D cardiac images (Table 6.2) of the anatomy and scarring of the patient's heart were acquired with a 1.5T MR scanner (Achieva, Phillips Healthcare) seven months prior to the treatment. During the procedure, the Ao and CS were catheterised followed by the acquisition of sequential biplane fluoroscopy images (Table 6.3) during free-breathing for approximately four seconds. Electroanatomical mapping was performed using EnSite™.

### 6.1.3. Percutaneous Coronary Intervention

The last patient was treated for arteriosclerosis by percutaneous coronary intervention (PCI) in a dedicated catheterisation laboratory. 3D cardiac images were taken of the patient in the morning using a 1.5T MR scanner (Achieva, Phillips Healthcare) imaging both anatomy and scarring of the heart (Table 6.2). Later on the same day, the patient underwent the catheterisation treatment with X-ray guidance in a dedicated catheterisation laboratory

equipped with a tracked and pre-calibration single-plane X-ray system (Allura Xper). During the EP procedure, the Ao and left anterior descending (LAD) branch of the coronary arteries were catheterised followed by the acquisition of sequential biplane fluoroscopy images during free-breathing for four seconds. Electroanatomical mapping was performed using the Carto™ XP EP Navigation System (Biosense Webster, Diamond Bar, CA, USA).

| case | model | scan | sequence | NEX | TE (ms) | TR (ms) | θ (°) | size (vx) | res. (mm³) |
|---|---|---|---|---|---|---|---|---|---|
| RFA | Intera | anatomy | bTFE | 1 | 2.36 | 4.72 | 90 | $384^2 \times 228$ | $0.89^2 \times 1.68$ |
| | | scar | LGE-SSFP | 1 | 1.99 | 5.57 | 25 | $288^2 \times 10$ | $1.25^2 \times 10.0$ |
| CRT | Achieva | anatomy | TFE | 1 | 1.44 | 4.24 | 50 | $432^2 \times 180$ | $0.84^2 \times 2.00$ |
| | | scar | LGE-SSFP | 1 | 1.99 | 5.45 | 25 | $288^2 \times 12$ | $1.25^2 \times 10.0$ |
| PCI | Achieva | anatomy | TFE | 1 | 1.16 | 4.04 | 20 | $400^2 \times 160$ | $0.75^2 \times 0.75$ |
| | | scar | LGE-SSFP | 3 | 1.76 | 3.59 | 15 | $512^2 \times 20$ | $0.76^2 \times 5.00$ |

Table 6.2 – Preoperative MR imaging parameters used to obtain the 3D anatomy and scar data including the model of the scanner for each catheterisation procedure. Pulse sequences for the anatomical imaging were either a bTFE, a type of SSFP, or TFE, a type of SGE. Imaging parameters are listed in terms of the number of excitations (*NEX*), echo time (*TE*), repetition time (*TR*), flip angle (θ), the voxel size of the scans and voxel resolution (*res*).

| case | model | left | right | fps | SOD (mm) | SID(mm) | size (px) | res. (mm) |
|---|---|---|---|---|---|---|---|---|
| RFA | BV Pulsera | LAO 20° | PA | 15 | 651 | 963 | $576^2$ | $0.33^2$ |
| CRT | Allura Xper | LAO 30° | RAO 1° | 7.5 | 765 | 1095 | $512^2$ | $0.34^2$ |
| PCI | Allura Xper | LAO 30° | RAO 30° | 15 | 765 | 1065 | $512^2$ | $0.26^2$ |

Table 6.3 – Intraoperative X-ray Imaging parameters of the fluoroscopy system including its model for each catheterisation procedure. Parameters are listed in terms of the view angles (*left*, *right*) used in catheter reconstruction, the frame rate measured in frames per second (*fps*) of the X-ray sequences, distance between the X-ray source to the isocentre (*SOD*), the distance between the source to the X-ray image detector (*SID*), the image size and pixel resolution (*res*).

## 6.2. Extended 2D-3D Registration Method

The 2D-3D registration algorithm used in this chapter is a clinical adaptation of the previous algorithm in Chapter 5 but is extended to deal with the additional imaging artefacts and distortions introduced when progressing from phantom to clinical data. These adaptations are

- a semi-automatic vessel centreline and radius extraction,
- a global-fit strategy for exploring coronary vessels,
- cardiorespiratory gating of X-ray, and
- further co-registration of EAM data.

A more automated approach to vessel centreline and radius extraction should be more accurate than a manual approach since intra- and interobserver variability are avoided, and fits better with the clinical workflow since the need for an expert user input is lessened. A global-fit strategy which automatically explores all possibly branches of vessel when constraining the registration would also avoid the need for an expert user input, and therefore avoid disruption

to the clinical workflow. This would also provide additional robustness to the registration algorithm by avoiding scenarios where wrong vessel branch is selected for registration. Retrospective cardiorespiratory gating of X-ray images is necessary to match the cardiac and respiratory phase of the preoperative 3D data in order to avoid reconstruction errors of the catheters used to constrain the registration, and also to avoid deformation errors caused by a phase mismatch, since the heart would not be at the same shape and size when not at the same phase (2.1). Finally, with some patient datasets, EAM data may be acquired at the end the procedure. It would be beneficial for the procedure if this information can be fused to the already co-registered MR and X-ray data. The workflow of the modified algorithm is summarised in Figure 6.2 and will be described in the subsequent sections.

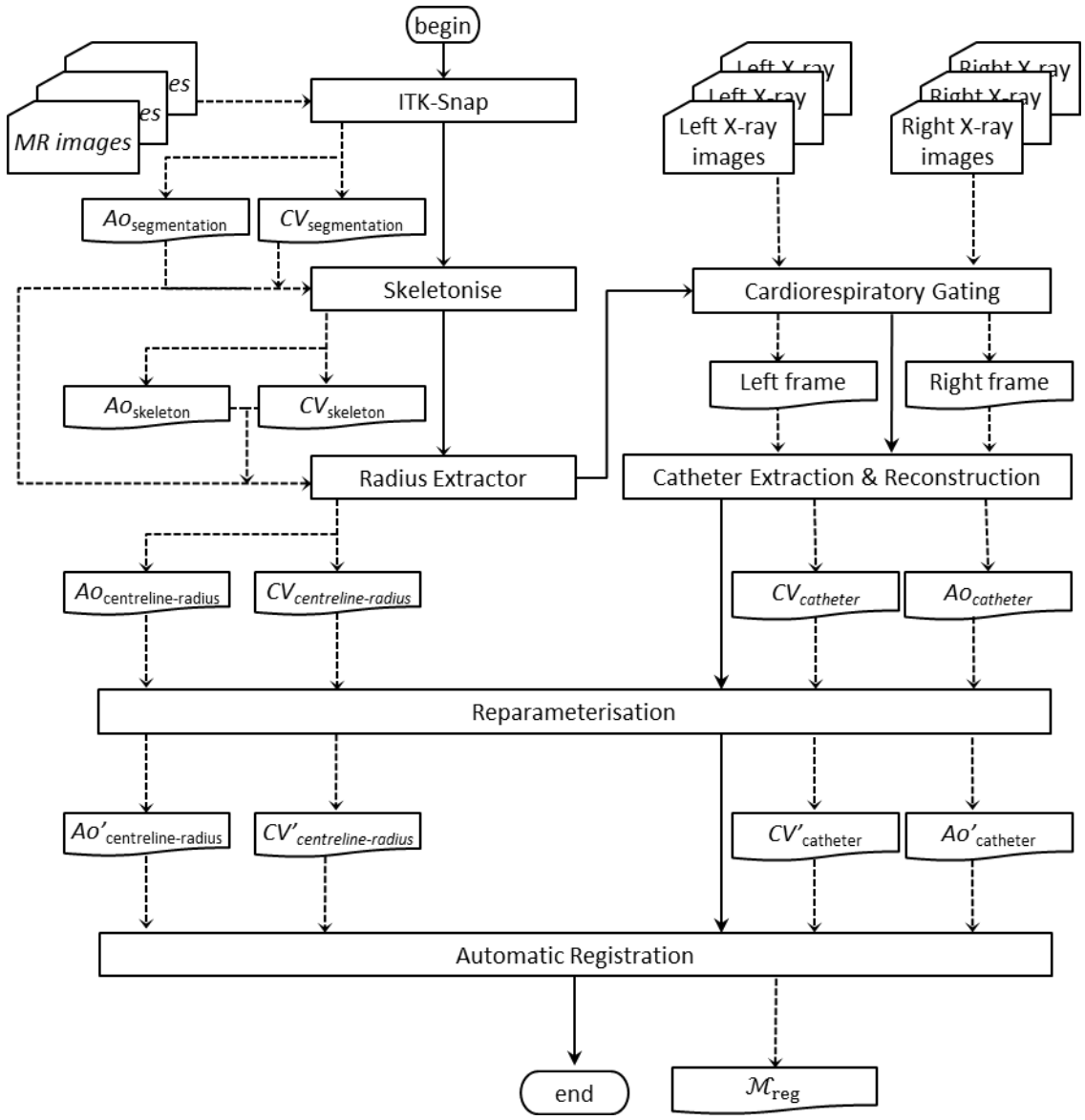


Figure 6.2) Workflow for the adapted catheter-based 2D-3D registration algorithm which fuses X-ray and 3D cardiac data from patients undergoing a catheterisation procedure. Solid lines represent the flow of processes while dashed lines represent flow of data between processes.

As in the previous chapter, the first part of the algorithm's workflow is divided into three stages to mirror those of typical cardiac catheterisation procedures. The first is the preoperative stage where vessels, chambers and scar data of the heart are extracted from the 3D preoperative MR scans. The new approach involves an interactive segmentation, a skeletonisation and an automatic radii measurement step that replaces the manual and less accurate centreline and radii measurement step in the phantom experiments. The second stage involves processing the X-ray fluoroscopy images which are acquired intraoperatively. During the fluoroscopy, the heart undergoes significant changes in shape and pose. These complex changes are addressed by introducing a cardiorespiratory gating step prior to catheter reconstruction, a step not necessary in the phantom studies. Finally, the last stage in the algorithm is the 2D-3D registration. Registration can be performed either intraoperatively, to overlay the segmented 3D heart onto the fluoroscopy as a roadmap, or postoperatively for biophysical modelling purposes.

When registering patient data, there is an uncertainty when determining which branch of the complex coronary anatomy has been catheterised. The novelty of the modified algorithm takes this into account by testing all possible branches, further extending the number of degrees of freedom in an already global-fit search space. Finally, a second part, or fourth stage, is introduced in the algorithm to further co-register EAM data onto the already co-registered XMS. This is useful both intraoperatively to validate the effectiveness of the treatment, and postoperatively for biophysical modelling purposes.

### 6.2.1. Vessel Centreline and Radii Extraction from Preoperative 3D Data

In the phantom case, points along the vessel centrelines were picked manually and then smoothed, while the cross-sectional radius was measured at the proximal, medial and distal regions followed by linear interpolation. The combined centreline-radius (CLR) function of the vessel was then reparameterised prior to registration. Manual CLR extraction and linear interpolation was suitable for the phantom data due to the simplicity of the phantom coronary vasculature. This is not the case with patient data where the coronary vasculature is significantly complex and manual CLR extraction becomes tedious and not clinically feasible. Therefore, a semi-automatic algorithm is used to first segment the vessels of the heart, followed by an automatic skeletonisation and cross-sectional radius detection algorithm.

#### *6.2.1.1. Semi-Automatic Segmentation of Vessels of the Heart*

The semi-automatic segmentation of the coronary anatomy and aorta from the MR scan was carried out using the ITK-SNAP segmentation (§4.2.1) to produce binary images $I_{\text{seg}}$. Binary images can be treated as a set of voxel coordinates $I_{\text{im}} = \{\vec{I}_{\text{im}}^{\,i}\}$, and the number of voxels set in the binary image is $|I_{\text{im}}|$, which is also equal to the cardinality of the set $\left|\{\vec{I}_{\text{im}}^{\,i}\}\right|$. After

segmentation, surface geometry of the hull was generated from the software in the form of triangular tessellations.

#### 6.2.1.2. Vessel Skeletonisation for Centreline Extraction

After segmentation of the vessels $I_{seg}$ their medial skeleton $I_{skel}$ was found using a 3D 6-subiteration curve thinning algorithm [128]. The skeletonisation algorithm preserves topology which means that any cavity within the segmentation results in large nodes and holes in the image result in the formation of loops. Due to imaging and segmentation artefacts, the skeletonisation algorithm may also have extraneous branches (Figure 6.3). Therefore prior to skeletonisation, the image was morphologically closed by first dilating the image using a spherical structuring element and then using it to perform a subsequent erosion operation [129]. Morphologically closing the segmentation prior to skeletonisation produced a simpler skeleton while maintaining the general topology of the vessel (Figure 6.3b, c).

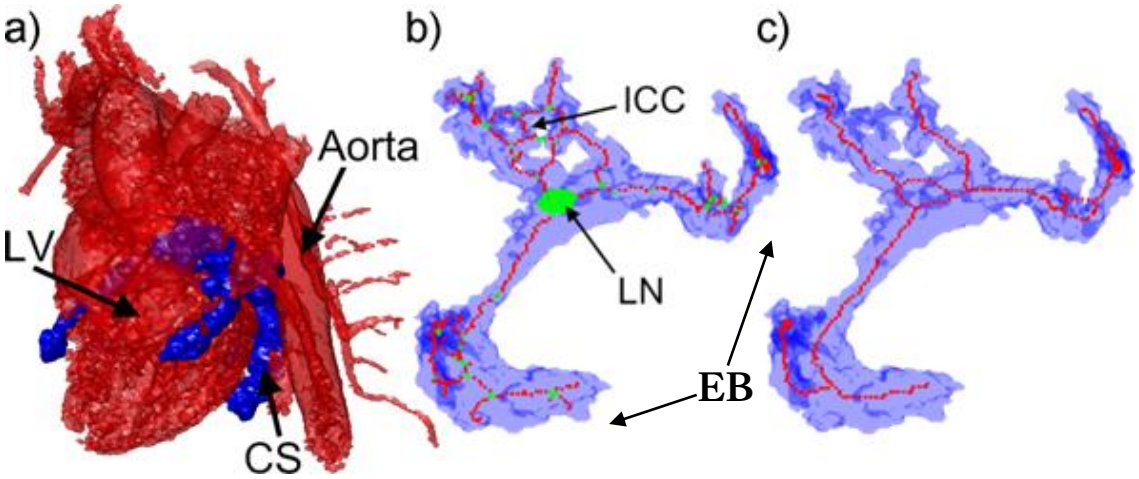


Figure 6.3 a) The CS (*blue*) segmented from the rest of the heart (*red*) with the left ventricle (*LV*) and aorta labelled. b) The CS (*blue, translucent*) and its skeleton divided into branches (*red*) and nodes (*green*). Due to poor image quality, topology preservation usually results in extraneous branches (*EB*) and vessels are ill-defined and can often merge with others to form holes within the image that form internally-closed circuits (*ICC*) in the skeletonisation. Cavities within the vessels due to non-homogenous contrast result in large nodes (*LN*) after skeletonisation. There are 601 distinct pathways in this skeleton. c) Morphologically closing the segmentation prior to skeletonisation removes most of the ICCs and LNs, resulting in a skeleton with only 40 distinct pathways.

#### 6.2.1.3. Vessel Cross-Sectional Radii Extraction

Using the segmented binary images $I_{seg}$ and subsequent skeletonisation image $I_{skel}$, the cross-sectional radius of the vessels at each set voxel of the skeletonisation was automatically measured. This was achieved by aligning the voxels of both images and then growing spherical structuring elements at each set voxel in the skeleton, $I_{skel}$until the boundary of the sphere reached the wall of the segmented vessel, $I_{seg}$ . This was done by considering each set voxel in

the skeleton independently, with coordinates $v_i = \vec{I}^{i}_{\text{skel}} = (x_i, y_i, z_i)$, and dilating them using a growing spherical structuring element $I_{SE}$, with

$$I_{SE} = \left\{x, y, z | \sqrt{(x - x_i)^2 + (y - y_i)^2 + (z - z_i)^2} < r\right\}; r \in \mathbb{N} \quad , \quad (6.1)$$

where $r$ is a natural-numbered radius increased until the sphere reaches the boundaries of the aligned $I_{\text{seg}}$. The sphere is considered to reach the boundary when the ratio of the number of set voxels in the intersection of the dilation and the aligned segmentation to the number of voxels in the dilation is less than 97.5%,

$$\frac{|I_{SE} \cap I_{\text{seg}}|}{|I_{SE}|} < 97.5\ \% \quad , \quad (6.2)$$

where the sphere's radius initially starts at one and increments by one per iteration. The algorithm assumes that the vessel has a circular cross section. The threshold was chosen empirically to be a good estimator of when the sphere reaches the vessel wall by comparing the automatic radius detection method to manual measurements of the radius.

#### 6.2.1.4. Vessel Branching Topological Analysis

When catheterising complex blood vessels containing multiple branches, such as the coronary sinus and coronary arteries, it is difficult to know for certain which branch is catheterised from the X-ray fluoroscopy due to the poor soft-tissue contrast in the images captured. Even with contrast agent injections, the projective nature of X-ray may yield images where multiple branches overlap, making them difficult to resolve. Therefore, to avoid the need for manually picking the containing pathway, entire blood vessels are segmented and then skeletonised. Geometrically the catheter is homeomorphic to a line and thus may only be contained by one skeleton pathway. In order to match catheters to corresponding vessel centrelines with (5.11), the skeleton must be broken down into its constituent pathways (Figure 6.4).

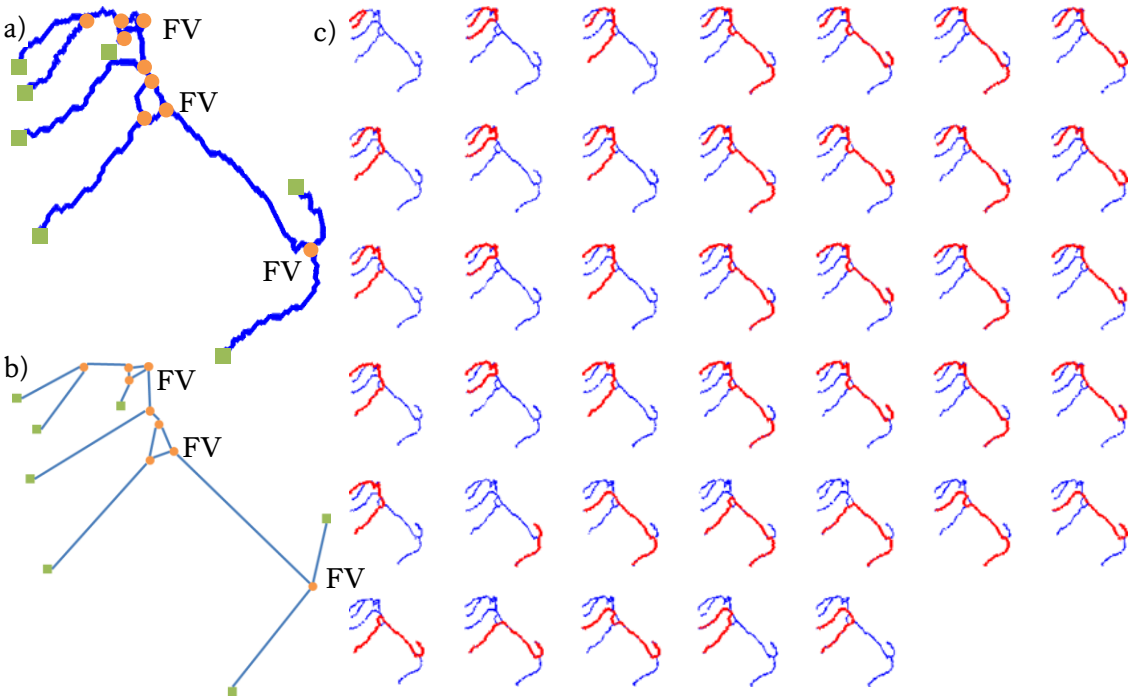


Figure 6.4 a) Skeleton of the coronary sinus with furcation voxels (FV, *orange circles*) and endpoints (*green squares*) identified. b) Representation of the skeleton as a graph with the FV as the vertices, and the connected components between the FV as the edges. c) The graph is traversed for all simple pathways from one endpoint to another to find all 40 unique pathways (*red*) of the skeleton (*blue*) that it represents.

Finding the constituent pathways of the skeletonisation is done by first finding all *furcation* voxels of the skeleton image $I_{\text{skel}}$. These are where the vessel starts to divide into branches, and are topologically defined as voxels 26-connected [128] to three or more other voxels. The furcations are then removed from the skeleton image and the remaining voxels are grouped into their 26-connected components. The skeleton is then represented as an undirected, unweighted and irreflexive graph [130] with furcation voxels stored as vertices and the 26-connected components stored in its edges, thereby preserving the topology of the skeleton within the graph. The graph is then traversed to find all simple paths of the graph. A simple path is a sequence of sequences of non-repeating edges and vertices connected together. Each path is converted back into voxels, of the represented skeleton, representing a potential pathway in the vessel that the catheter can be inserted into. The extended global-fit search strategies considers all these pathways when performing the catheter-vessel registration, as will be described in §6.2.3.

### 6.2.2. Intraoperative X-ray Gating

In the phantom experiments, the relationship between the pose of the phantom model in MR and in X-ray was described using a rigid-body transformation (RBT). In patient images, the heart undergoes significant changes in shape and size throughout the cardiorespiratory cycles, limiting the validity of a RBT relationship. However, an RBT relationship can still be used by assuming that the heart returns to the same shape, size and pose at the same cardiorespiratory

phases. In the MR images, the heart scan is taken at end-expiration and late diastole and therefore the X-ray would also need to be gated at these phases to re-validate the RBT relationship. Gating of the X-ray is performed by manually selecting a frame from the four-second video fluoroscopy sequence in each X-ray view. The frame was chosen by a clinical expert.

Afterwards, the catheters inserted into the narrow coronary vessel, ascending aorta and descending aorta were reconstructed in 3D using epipolar geometry [131] from cardiac and respiratory gated X-ray images. The X-ray C-arm was calibrated using the methods described in [30]. Using the pre-calibration and tracked information of the X-ray system, the catheter points were first selected in one X-ray view and the corresponding points in the other view were selected with the aid of the epipolar constraint (Figure 6.5). Back projection of the corresponding X-ray point pairs was used to determine their 3D positions (Figure 3.3). Reconstructed catheters $\vec{C}_1$ and $\vec{C}_2$ are then used for registration in (5.11).

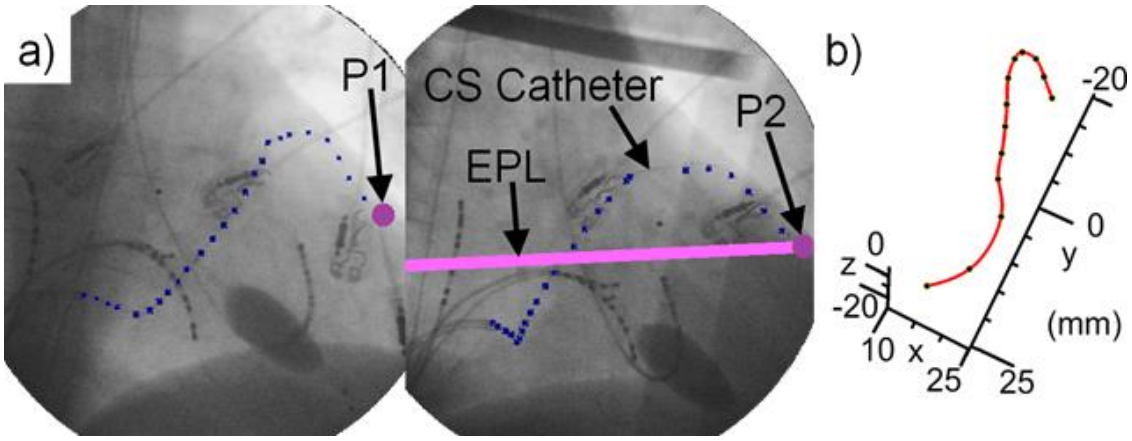


Figure 6.5 a) AP (*left*) and LAO 30˚ (*right*) X-ray views of the heart gated at end-diastole and end-expiration. Points along the CS catheter are selected in both images (*blue dots*). A point from the left image (*P1*) generates an epipolar line in the right image (*EPL*); its corresponding point lies at an intersection of EPL and the catheter (*P2*). b) 3D Spline reconstruction of the catheter.

### 6.2.3. Global-Fit Registration

Registration between the 2D-X-ray and 3D-MR for the clinical datasets uses (5.11) to match between vessel centrelines and catheters employing a similar global-fit search strategy of §5.1.5. However, with clinical data sets, blood vessels are no longer homeomorphic to a line, due to the presence of multiple branches, especially when registering with complex coronary vasculature (Figure 6.3). To deal with this issue, the algorithm extends the global-fit approach to search through all possible pathways of the vasculature using the topological analysis of the vessel's skeletonisation (Figure 6.4).

The advantage of a global search strategy is that, assuming the catheter is lying within the segmented vasculature, the correct solution is guaranteed to be encountered in the search, as opposed to a local search strategy which does not explore the entire search space. If the metric is designed well, and the data is not dominated by sources of error such as rigid-body deformations, optimisation of the search parameters will occur when the correct solution is encountered. Under these assumptions, the multi-pathway global search strategy would be highly robust.

Since the global search explores every unique pathway in the vasculature, pathways that are anatomically unfeasible are also explored. If the metric is designed well, unfeasible pathways should be rejected as they are encountered during the search, but will consume computational resources. This could be avoided if a knowledgeable user is allowed to specify which pathways are unfeasible. However, user interactivity can be very disruptive to the clinical workflow and may limit the suitability of translational applications for deployment in the clinical environment [105]. Therefore, a global search strategy has the advantage of minimising disruptions to the workflow, an important criterion in the thesis objectives.

The multi-pathway global search strategy, combined with the automatic radii extraction method above, results in a set of vessel pathways $V = \{\vec{V}^i\}$ with associated radii functions $\rho^i$. This algorithm registers with two catheter-vessel pairs, and so the branch analysis will need to be performed twice to get two collections of vessel pathways, $V_1 = \vec{V}_1^i$ and $V_2 = \vec{V}_2^j$, with radii functions $\rho_1^i$ and $\rho_2^j$. These branches are matched to points along catheters $\vec{C}_1$ and $C_2^i$ contained within their respective vessels.

The global strategy then considers every unique pairing between the pathways in $V_1$ and $V_2$. For each unique pair, a global-fit RBT is found with (5.11), but with the DOF $Q$ not only taking into account the forward and reverse directions of pairs of vessels, but expanded to take into account the unique pairings of $V_1$ and $V_2$,

$$Q = 4 \times |V_1| \times |V_2| \quad , \qquad (6.3)$$

where $|V|$ denoting the number of pathways in $V$.

A typical surface plot of the residual error over the entire global search space is shown in Figure 6.6, which is similar to Figure 5.3 but with more DOFs due to the multi-pathway global-fit approach.

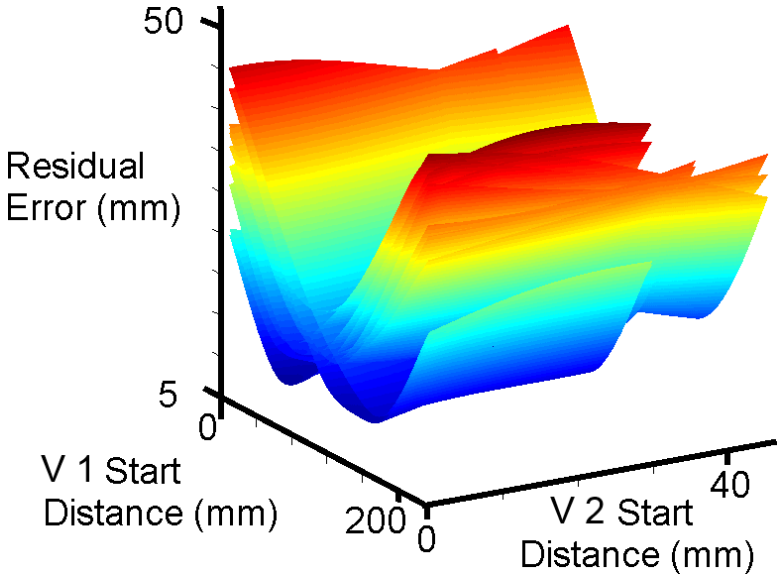


Figure 6.6) A typical residual error function over the search space of the two catheter-vessel pair registration algorithm, with the minimum residual error marked (*red circle*). There are four layers for each of the four ways the two vessels can combine, with the bottom layer ideally being the case when the catheters are picked in the same order as their corresponding vessel's centreline.

## 6.3. EAM Fusion with MR and X-ray of the Left Ventricle

Once the preoperative 3D data is registered with the intraoperative X-ray, additional intraoperative EAM information (§2.2.3.4) collected during the procedure using EnSite™ or Carto XP EP Navigation System, can be co-registered to the already co-registered X-ray-MR space (XMS) (Figure 6.7). For patients who suffered from myocardial infarction, scarring usually occurs in the myocardial wall of the LV, and therefore is usually the region of interest when acquiring EAM data.

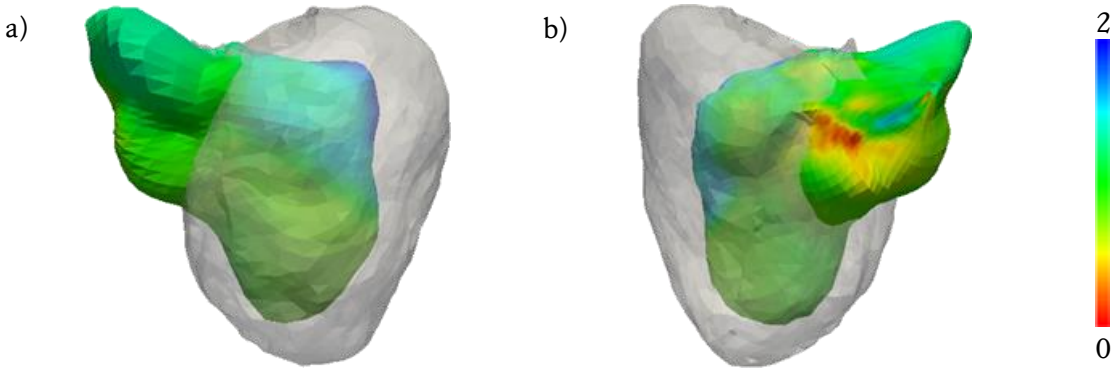


Figure 6.7 a) This figure shows the co-registration of bipolar voltage EAM data from EnSite (*opaque, colour mapped*) onto the MR segmentation of the LV myocardium (*white, translucent*) a an RFA patient's heart in anterior view. The Carto XP anatomical surface is colour mapped to show spatial distribution of voltage (mV) with low voltage regions on the EAM data (*red to yellow*) indicate the presence of scar. b) Same, but showing a posterior view of the heart.

A few methods currently exist to fuse EAM and 3D preoperative information. In [132], Knowles *et al.* use XMR system to obtain a co-registered XMS, and then use the ablation catheter tip locations from biplane X-ray to align with the ablation locations from the EAM. However, XMR systems require specially modified hardware, which limits the applicability of this approach beyond the research environment. Software platforms such as the freely available Vurtigo (The Vurtigo Team, University of Toronto, Toronto, ON, Canada) [133] and commercially available NavX Fusion (St Jude medical, St. Paul, MN, USA) perform registrations using the positions of corresponding anatomical landmarks manually picked from both modalities. However, between 15 and 30 positions need to be picked for an accurate registration in the case of NavX Fusion, adding around 15 minutes to the clinical workflow [127]. Another commercially available software, Cartomerge (Biosense Webster, Diamond Bar, CA, USA), can perform registration using only five landmark locations, however venograms are required to obtain these, involving the injection of nephrotoxic contrast agents into the bloodstream. Registration can be performed by Cartomerge in around 11 minutes [127].

As previously mentioned in §2.1, the blood pool of the chambers can often be modelled using spheroids [34], and for the LV, the spheroid is *prolate*, i.e., is elongated along a line. A method is devised in this section to register EAM and MR data to take advantage of this model by aligning prolate-spheroid-shaped features extracted from both modalities. Using this as a constraint can replace the need for venograms or a large number of landmarks to constrain the registration. However, the spheroid possesses reflection and rotation symmetries about its principle axis, so a small number of corresponding landmarks are still needed to fully constrain the registration.

### 6.3.1. Registration of EAM Data to MR and X-ray using Prolate Spheroids

The collected EAM information used for registration consists of points along the LV endocardial wall $\vec{S}_i$, a bipolar voltage signal $V_i(t)$ at each point over one heartbeat, and the location of various surrogate landmarks $\vec{L}_j$ such as the CS ostium, aortic valve, LV apex and high-right atrium (HRA). The EAM data is then augmented into the co-registered 3D MR and X-ray space. Once co-registered, the bipolar electrical data from the EAM system is interpolated over the previously segmented LV chamber. Accuracy and precision of EAM co-registration are measured according to a binary classification test of scar identification by LGE-MR and by bipolar voltage maps thresholded at 1.5 mV according to [134].

Once the electroanatomical mapping of the LV endocardial wall is complete, it is then aligned to the previously co-registered X-ray-MR space (XMS). The alignment is described as a rigid body transformation $M$ composed of a translation $T$ and two rotations $R_{\text{axis}}$ and $R_{\text{lm}}$ ,

$$M = TR_{\text{lm}}R_{\text{axis}} \quad , \qquad (6.4)$$

where $R_{\text{axis}}$ provides an alignment of the primary axis of the EAM geometry and $R_{\text{lm}}$ is a rotation about the axis using the landmarks as a constraint.

### 6.3.2. Axis Rotation between EAM and XMS

The first rotation $R_{\text{axis}}$ is used to align the primary axis $\vec{V}_{\text{eam}}$ of the EAM geometry to its corresponding axis, $\vec{V}_{\text{xms}}$ in the XMS.

With EAM geometry taken using EnSite™, the axis of the EnSite balloon catheter is used for this purpose, which is the z-axis of the EAM geometry. Its corresponding axis in the XMS is the vector difference between the top, $\vec{T}_{\text{xms}}$, and bottom, $\vec{B}_{\text{xms}}$, points of the balloon reconstructed from a pair of X-ray images,

$$\begin{aligned} \hat{V}_{\text{eam,ensite}} &= \hat{z} \\ \vec{V}_{\text{xms,ensite}} &= \vec{B}_{\text{xms}} - \vec{T}_{\text{xms}} \end{aligned} \quad . \qquad (6.5)$$

When aligning the Carto geometry to the XMS, the primary axis of the Carto geometry is taken as its largest principal component computed using singular value decomposition (SVD) [135], while its corresponding axis in the XMS is the geometric principal component of the points that make up the LV endocardium segmented from MR.

The rotation that aligns the axis is given by the axis-angle formula (6.3) between the vectors $\hat{V}_{\text{eam}}$ and $\hat{V}_{\text{xms}}$ with the axis and angles given by,

$$\begin{aligned} \hat{k} &= \hat{V}_{\text{eam}} \times \hat{V}_{\text{xms}} \\ \alpha &= \text{acos}\left(\hat{V}_{\text{eam}} \cdot \hat{V}_{\text{xms}}\right) \end{aligned} \quad . \qquad (6.6)$$

### 6.3.3. Translation between EAM and XMS

The translation between the EnSite EAM data and XMS is determined by the vector difference between two central points in each geometric space.

The central point in EnSite is chosen to be the centre of the balloon, which corresponds to the origin of the EnSite geometry, while the corresponding point in the XMS is obtained as the midpoint between the top and bottom points of the balloon reconstructed from biplane X-ray:

$$\begin{aligned} \vec{C}_{\text{eam,ensite}} &= (0,0,0) \\ \vec{C}_{\text{xms,ensite}} &= \frac{\vec{B}_{\text{xms}} + \vec{T}_{\text{xms}}}{2} \end{aligned} \quad . \qquad (6.7)$$

In Carto, the central point of the EAM geometry is chosen to be the geometric centroid of the points $\vec{p}_i$ collected by the roving catheter, and its corresponding central point in the XMS is the

geometric centroid of the points $\vec{q}_i$ that make up the tessellation of the LV endocardial surface segmented from MR.

$$\vec{C}_{\text{eam,carto}} = \frac{1}{N}\sum_i \vec{p}_i$$
$$\vec{C}_{\text{xms,carto}} = \frac{1}{M}\sum_i \vec{q}_i \quad . \quad (6.8)$$

The translation vector is the vector difference between the central points [86],

$$T = \begin{bmatrix} I_3 & \vec{C}_{\text{eam}} - \vec{C}_{\text{xms}} \\ \overleftarrow{0} & 1 \end{bmatrix} \quad . \quad (6.9)$$

### 6.3.4. Landmark Rotation between EAM and XMS

The first rotation $R_{\text{axis}}$ aligns the axis of the EAM data within the XMS, leaving a rotation degree of freedom (DOF) $\phi$ around the axis. In order to constrain this last DOF, the surrogate landmarks $\vec{L}_j$ are first brought into the XMS,

$$\begin{bmatrix} \vec{L}'_j \\ 1 \end{bmatrix} = TR_{\text{axis}} \begin{bmatrix} \vec{L}_j \\ 1 \end{bmatrix} \quad . \quad (6.10)$$

The corresponding landmarks locations $\vec{K}'_j$ are then manually selected from either from the MR image or reconstructed from biplane X-ray, and a rigid body transformation between the two sets of landmark locations is found by minimizing the root-mean-square (RMS) distance error $e = \sqrt{\frac{1}{N}\sum_j \|\vec{e}_j\|^2}$ between them,

$$\begin{bmatrix} \vec{K}_j \\ 1 \end{bmatrix} = T_{\text{lm}} R_{\text{lm}} \begin{bmatrix} \vec{L}_j \\ 1 \end{bmatrix} + \begin{bmatrix} \vec{e}_j \\ 1 \end{bmatrix} \quad , \quad (6.11)$$

using the solution found in [86] without scaling, and discarding the translational component $T_{lm}$.

## 6.4. Experimental Method

The adapted 2D-3D image registration algorithm proposed in this chapter is applied to the three clinical datasets described in (§6.1). Following the methods outlined in (§5.1) and extended in (§6.2) the two catheterised vessels (Table 6.1) and four chambers were semi-automatically segmented from the preoperative MR cardiac scans of the three clinical datasets using ITK-SNAP. The aorta was further divided into the ascending aorta (AAo), transverse aorta and descending aorta (DAo). The catheterised coronary vessel, either the CS or a CA, the AAo and the DAo were then skeletonised with their cross-sectional radii detected automatically. Each simple path of the vessel skeletons was extracted resulting in a collection of individual centreline-radius functions for each vessel branch suitable for use with (5.11). Intraoperatively, the catheters that were placed inside the narrow CV, and the catheter segments placed inside the

AAo and DAo, were reconstructed from biplane X-ray gated at end-expiration and end-respiration.

Two registrations were carried out for each case, first using the narrow CV and the AAo along with their corresponding catheters, and a second time using the narrow CV and DAo and their corresponding catheters. Once the X-ray and MR data were aligned into a common X-ray-MR space (XMS), further EAM information was fused onto the XMS using the 3D-3D method outlined in the previous section.

### 6.4.1. Manual Registration with EP navigator

In current clinical settings, registration is usually performed manually using the EP navigator software platform that is integrated into the clinical environment (§4.2). Features in the X-ray image that have a corresponding anatomy can be used to provide registration constraints. These include catheters lying inside vessels [136], catheters looped within chambers [137], radio-opaque dye injected into the coronary anatomy [97] and the cardiac shadow [67]. The corresponding anatomy segmented from a preoperative 3D scan is projected onto the X-ray and can be interactively manipulated until they line-up with their indwelling features. Alignment can be sequentially performed in multiple views, with interactive adjustments saved between each view.

A modified EP navigator is used to manually align the CRT clinical dataset in this chapter. For this dataset, the software platform is provided with the two catheterised vessels and four chambers segmented from the preoperative MR image, and with the two biplane X-ray views used for catheter reconstruction (§6.2.2) that were gated at end-expiration and end-diastole. One of the X-ray views is displayed and the segmentation of the catheterised vessels and four heart cambers are projected onto it with an initially incorrect, random alignment. This setup is presented independently to two clinical experts who have had prior experience with the EP navigator platform for manual registration. The experts are asked to align the segmentations to the X-ray using the two views until they believe that registration is good enough to guide cardiac catheterisation procedures such as RFA. The time allowed for manual registration is limited to ten minutes, since any registration taking any longer is likely to disrupt the clinical workflow of the procedure. Once the expert is satisfied with their registration, or has exceeded the ten minute limit and asked to stop, the time and final alignment is recorded.

The final alignment and time taken for manual alignment is compared to the automatic registration method presented in this chapter. The aim is to answer the question: *can the proposed registration algorithm perform better than a current registration method used in clinical settings in terms of accuracy and speed*?

### 6.4.2. Validation of Automatic and Manual Registration

The 5-mm and 15-mm clinical thresholds set in Chapter 1 are useful when the *target registration error* (TRE) can be quantified (§4.1.7) in comparison to a gold standard registration $\mathcal{M}_{\text{gold}}$ (4.33). Previously in the phantom experiments, registration was validated by placing fiducial markers around the heart which were visible in all images involved in the registration, allowing the computation of accuracy in terms of a 3D-TRE.

This is not a viable option when working with clinical data since the heart is not directly accessible for fiducial marker placement. Skin fiducial markers are safe and can be placed on the chest instead of on the heart [16], but the relatively motion between the heart and the chest throughout the cardiorespiratory cycle, combined with the elasticity of skin allowing the fiducials to move around, can compromise the registration accuracy and limit their suitability to provide a gold standard registration. Currently, it is difficult to obtain a good gold standard registration that is compatible with the clinical environment and therefore the TRE was estimated in this study by clinical experts using visual inspection. The clinical experts assessing accuracy were not the same clinical experts performing the manual registration in §6.4.1.

Once registration is performed, either using the automatic method or manually with EP navigator™, a collection of eight images are generated for each biplane X-ray view. For each view, the first image is the X-ray image, and the remaining seven are the X-ray image with overlays of the 3D models; one for each of the four chambers of the heart, one for each of the two vessels used for registration, and one with the whole heart including the four chambers and two vessels (Figure 6.8). The 16 images are given to the clinical expert, who is asked to estimate a mean 2D-TRE for each of the four chambers of the heart using the scale embedded in the image for both of the biplane X-ray views. Once the errors for both biplane X-ray views have been assessed, the larger of the two mean estimates are recorded for each chamber.

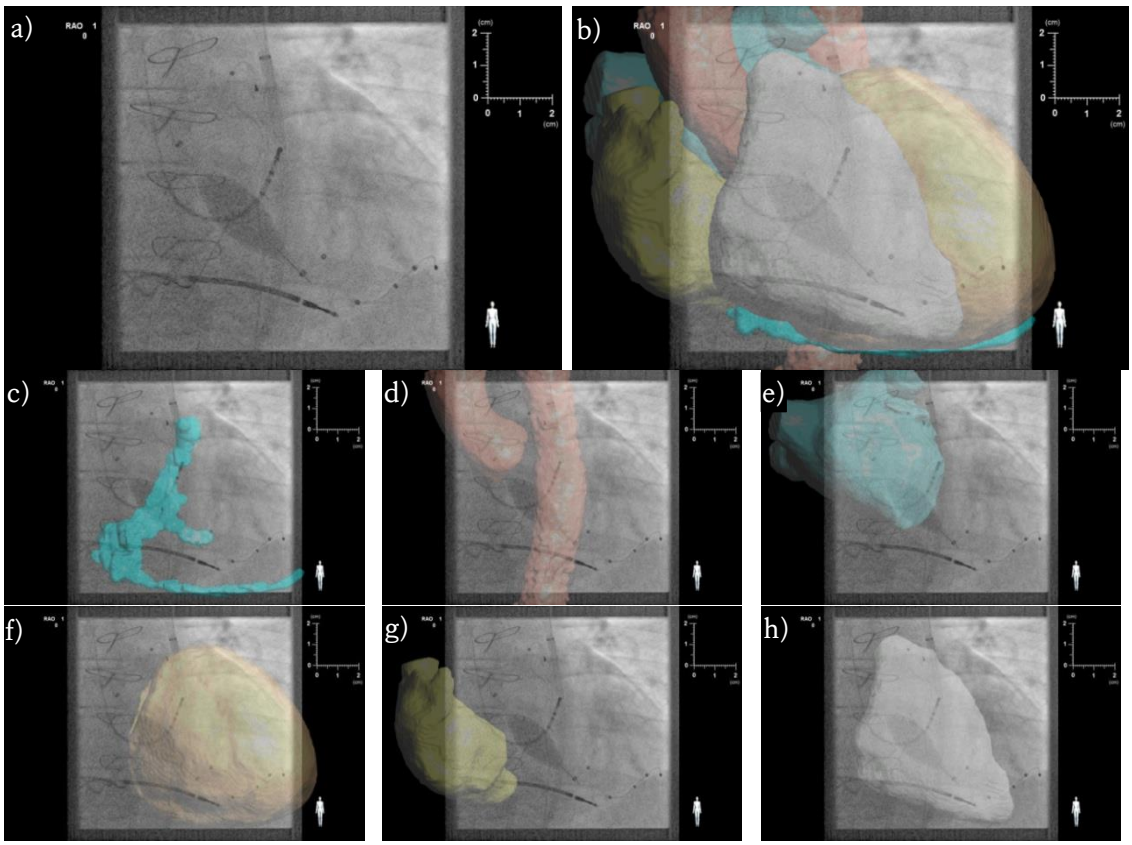


Figure 6.8 a) PA X-ray view of the patient's heart and catheters inserted inside it. Once 2D-3D registration is performed, surface renderings of segmented regions are overlaid onto the X-ray view. b) Overlay showing all regions, which include the c) CS, d) Ao, e) LA, f) LV myocardium, g) RA and h) RV blood pool. All eight images were used by clinical experts to assess the accuracy of the registration of each cardiac chamber and of the whole heart.

The scale drawn on each image indicates the size of the objects within the image, calculated using,

$$\begin{bmatrix}\Delta u' \\ \Delta v'\end{bmatrix} = \begin{bmatrix}\frac{W}{W'} & 0 \\ 0 & \frac{H}{H'}\end{bmatrix} \frac{SOD}{SID} \begin{bmatrix}\Delta u \\ \Delta v\end{bmatrix} \quad , \qquad (6.12)$$

where $\Delta x'$ and $\Delta y'$ is the spatial resolution (mm) of each row and column respectively in the presented image, $W'$ and $H'$ is the number of rows and columns respectively in the portion of the presented image that contains the X-ray image. The remaining symbols are taken from the pre-calibration of the X-ray system, specified according to Table 4.1.

### 6.4.3. Validation of EAM, MR and X-ray Co-Registration

In order to assess the EAM co-registration to XMS of the CRT dataset, the scar on the LV was segmented from the preoperative MR scar imaging from the one exemplar clinical dataset. The anatomical MR scan and the LGE-CMR scan were acquired during the same scanning session. Assuming that the patient did not move between the scans, the anatomical and scar images are

co-aligned to the same MR coordinate system, allowing the scar information extracted from the LGE-CMR scan to be mapped onto the LV endocardial surface.

Once the EAM and MR are aligned via triple co-registration, the EA voltage data is radially projected onto the MR endocardial surface. This is achieved by using the central point of the EA map $\vec{C}_{\text{eam}}$ determined in the registration step. Line segments $\ell_i$ are then computed between the EA map centroid and each point $\vec{r}_i$ on the MR segmented surface of the left ventricle, $\ell_i = \{\vec{C}_{\text{eam}} + t(\vec{r}_i - \vec{C}_{\text{eam}}) | t \in [0,1]\}$. For each of the line segments $\ell_i$, the point closest to it within the EA map point cloud is selected, and the bipolar voltage associated with the EA map is transferred onto the associated MR point $\vec{r}_i$. Bipolar voltages with values lower than 1.5 mV are identified as scar [134] which is then compared to scar segmented from MR obtained from the preoperative late Gadolinium enhanced (LGE) images. Scar is identifiable in the LGE image brighter than the surrounding myocardium [134] and can be segmented using ITK-SNAP (§4.2.1). This segmentation is considered the ground truth for scar and is used to quantify accuracy in terms of a mean 3D-TRE and precision in terms of a percentage overlap.

Accuracy of the EAM-XMS registration is measured in terms of a single mean 3D-TRE value. This is found by finding the centroid of the scar from the LGE-CMR scan mapped onto the MR endocardial surface, and the centroid of the scar measured EAM also mapped onto the surface via radial projection. Assuming that the distribution of scar around the LV myocardium is the same in both MR and EAM, the mean 3D-TRE value is calculated as the distance between the two centroids.

Precision of the registration is measured in terms of a the positive predictive value using a binary classification test, by iterating though each point $\vec{r}_i$ in the MR segmented LV surface and comparing whether the point is identified as scar or not from both EAM and LGE. If a point is identified as scar from LGE and also by EAM, then that point is a true positive (TP) for the test. If the point is identified as scar from LGE and but not identified as scar in EAM, then the point is false positive FP. The number of TPs and FPs are counted and precision is given as,

$$\text{precision} = \frac{\#TP}{\#TP + \#FP} \times 100\% \quad . \quad (6.13)$$

where $\#X$ denotes the number of counts of $X$ [138].

## 6.5. Results

The multi-pathway global-fit registration algorithm presented in this chapter was applied to three clinical cardiac catheterization cases, followed by one co-registration of EAM data to the co-registered X-ray-MR space (XMS) in the CRT case.

### 6.5.1. Catheter-Based Registration of MR and X-ray

Following the method outlined above, the centreline-radius functions were obtained for the CV, AAo and DAo. The length of the centreline $\ell$ and mean radius $\bar{r}$ over the vessel is listed in Table 6.4. For the CV, since there are multiple branches to the vessel, the mean length of the centreline, averaged over all the unique paths $\bar{\ell}$, is given instead. The portions of the catheter inside the vessels were reconstructed from X-ray and their lengths are also listed in Table 6.4. Lastly, the table lists the number of points that make up the segmented chamber, and for the CRT case, the number of points identified as scar projected onto the LV endocardial wall.

| | catheters length (mm) | | | CV (mm) | | | DAo (mm) | | AAo (mm) | | #1000 points | | | | |
|---|---|---|---|---|---|---|---|---|---|---|---|---|---|---|---|
| case | CV | DAo | AAo | # | $\bar{\ell}$ | $\bar{r}$ | $\ell$ | $\bar{r}$ | $\ell$ | $\bar{r}$ | LA | LV | RA | RV | scar |
| RFA | 93 | 107 | 127 | 14 | 69 | 5.1 | 198 | 14.4 | 114 | 16.3 | 25 | 23 | 23 | 22 | N/A |
| CRT | 73 | 111 | 15 | 12 | 141 | 4.5 | 64 | 14.7 | 64 | 14.7 | 20 | 22 | 17 | 21 | 10 |
| PCI | 100 | 101 | 61 | 6 | 20 | 1.9 | 124 | 24.8 | 84 | 21.0 | 32 | 35 | 32 | 41 | N/A |

Table 6.4 – Summary of vessel and chamber data extracted from preoperative MR, and catheters reconstructed from biplane X-ray. From left to right, the 3D arclengths of the catheter portion lying within their corresponding vessels are listed (mm). The centreline arclength ($\ell$) of the vessels, segmented from MR, and its mean radius $\bar{r}$ are given in millimetres. For the CV, the length listed is the average length over all unique branches ($\bar{\ell}$); the number of them listed under #. On the right, the number of points that make up the point clouds of the four chambers are also listed under their respective chamber, in the 1000s, the and where relevant, number of points that are identified as scar according to the LGE image is listed under scar.

Once the catheters and vessels were registered automatically using the CS/DAo and CS/AAo pairs, sets of eight overlays were provided for each biplane view of each registration, which were visually assessed for accuracy by an expert clinician. The expert's accuracy assessment in terms of 2D-TRE and time taken to perform registration is listed in Table 6.5.

| | | | estimated mean 2D-TRE (mm) | | | | | | |
|---|---|---|---|---|---|---|---|---|---|
| | | | observer #1 | | | observer #2 | | | final |
| case | vessels | time (s) | left | right | mean | left | right | mean | mean |
| RFA | CS/DAo | 210.0 | 5.5 | 5.8 | 5.7 | 5.0 | 7.0 | 6.0 | 5.8 |
| | CS/AAo | 184.4 | 4.5 | 4.8 | 4.7 | 5.0 | 7.0 | 6.0 | 5.3 |
| CRT | CS/DAo | 84.3 | 5.0 | 7.0 | 6.0 | 7.5 | 7.5 | 7.5 | 6.8 |
| | CS/AAo | 83.9 | 4.5 | 7.0 | 5.8 | 7.5 | 7.5 | 7.5 | 6.6 |
| PCI | RCA/DAo | 60.1 | 5.0 | 4.0 | 4.5 | 4.5 | 4.0 | 4.3 | 4.4 |
| | RCA/AAo | 64.3 | 6.5 | 5.3 | 5.9 | 6.0 | 8.0 | 7.0 | 6.5 |
| mean | CV/DAo | 118.1 | 5.2 | 5.6 | 5.4 | 7.5 | 7.5 | 7.5 | 5.7 |
| | CV/AAo | 110.9 | 5.2 | 5.7 | 5.4 | 7.5 | 7.5 | 7.5 | 6.1 |
| final mean | | 114.5 | 5.2 | 5.7 | 5.4 | 5.9 | 6.8 | 6.4 | 5.9 |

Table 6.5 – Estimated mean 2D-TRE listed for clinical expert assessment and for each catheter-vessel pair. The time taken to perform each registration is also listed ($t$).

### 6.5.2. Manual Registration of MR and X-ray

Manual registration was performed on the CRT clinical cases by three expert clinicians (registrars) who have had experience using EP navigator. The registrations were assessed for their accuracy by another group of two expert clinicians (observers). The estimated 2D-TREs are listed in Table 6.6, in addition to the time taken for each registration.

| | | | estimated mean 2D-TRE (mm) | | | | | | |
|---|---|---|---|---|---|---|---|---|---|
| | | | observer #1 | | | observer #2 | | | total |
| case | registrars | time (s) | left | right | mean | left | right | mean | mean |
| RFA | registrar #1 | 577 | 4.0 | 5.0 | 4.5 | 7.5 | 10.0 | 8.8 | 6.6 |
| | registrar #2 | 468 | 5.0 | 5.0 | 5.0 | 7.5 | 7.5 | 7.5 | 6.3 |
| | registrar #3 | 231 | 10.0 | 10.0 | 10.0 | 15.0 | 15.0 | 15.0 | 12.5 |
| | mean | 425 | 6.3 | 6.7 | 6.5 | 10.0 | 10.8 | 10.4 | 8.5 |
| CRT | registrar #1 | 428 | 5.0 | 5.0 | 5.0 | 10.0 | 5.0 | 7.5 | 6.3 |
| | registrar #2 | 415 | 4.0 | 6.5 | 5.3 | 5.0 | 10.0 | 7.5 | 6.4 |
| | registrar #3 | 478 | 20.0 | 20.0 | 20.0 | 15.0 | 15.0 | 15.0 | 17.5 |
| | mean | 440 | 9.7 | 10.5 | 10.1 | 10.0 | 10.0 | 10.0 | 10.0 |
| PCI | registrar #1 | 565 | 6.8 | 6.3 | 6.6 | 6.0 | 7.0 | 6.5 | 6.5 |
| | registrar #2 | 276 | 7.8 | 5.5 | 6.7 | 7.0 | 6.0 | 6.5 | 6.6 |
| | registrar #3 | 326 | 9.0 | 6.5 | 7.8 | 9.0 | 15.0 | 12.0 | 9.9 |
| | mean | 389 | 7.9 | 6.1 | 7.0 | 7.3 | 9.3 | 8.3 | 7.7 |
| total mean | | 418 | 8.0 | 7.8 | 7.9 | 9.1 | 10.1 | 9.6 | 8.7 |
| total mean w/o #3 | | 455 | 5.4 | 5.6 | 5.6 | 7.2 | 7.6 | 7.4 | 6.5 |

Table 6.6 – Summary fo the manual registration method by three clinical experts (registrars) between the CT and X-ray data of the clinical data using EP navigator. A mean 2D-TRE was estimated by two independent clinical experts (observers). Time required to perform the registration are listed in this table. A second total mean was computed without (w/o) registrar #3 since, by consensus of the expert observers, these registrations were less accurate.

### 6.5.3. Automatic vs. Manual Registration

For comparison, the 2D-TRE estimates of the CRT case are averaged. For the manual registration, 2D-TRE estimates are first averaged across the two expert registrations, and then across the two expert error assessments and summarised in Table 6.7. For automatic registration, 2D-TRE estimates are averaged across the two expert error assessments and three clinical cases (Table 6.7).

| | estimated mean 2D-TRE (mm) | | | |
|---|---|---|---|---|
| | EP navigator | EP navigator w/o #3 | CV/DAo | CV/AAo |
| RFA | 8.5 | 6.5 | 5.8 | 5.3 |
| CRT | 10.0 | 6.4 | 6.8 | 6.6 |
| PCI | 7.7 | 6.6 | 4.4 | 6.5 |
| mean | 8.7 | 6.5 | 5.7 | 6.1 |

Table 6.7 – Mean estimated 2D-TRE from averaging over the three, and two, expert estimations for each case. The mean 2D-TREs are further averaged over the three clinical cases to result in a final measure of mean 2D-TRE for each method of registration: manually using EP navigator, or automatically using the CV/DAo catheter-vessel pairs or the CV/AAo pairs.

Registration times are also averaged in the same order as averaging the 2D-TREs for both manual and automatic registration. Results are tabulated in Table 6.8.

| | registration time (s) | | | |
|---|---|---|---|---|
| | EP navigator | EP navigator w/o #3 | CV/DAo | CV/AAo |
| RFA | 425 | 523 | 210 | 184 |
| CRT | 440 | 422 | 84 | 84 |
| PCI | 389 | 421 | 60 | 64 |
| mean | 418 | 455 | 118 | 111 |

Table 6.8 – Mean registration time costs averaged over the three clinical cases to result in a final measure of time cost for each method of registration: manually using EP navigator, or automatically using the CS/DAo catheter-vessel pairs or the CS/AAo pairs.

The automatic registration algorithm performed more accurately, according to the independent clinical experts, compared to expert manual registration. Furthermore, the intraoperative phase of the automatic registration algorithm could be performed in 2 minutes on average, while manual registration took on average 7 minutes.

### 6.5.4. Triple Co-Registration of EAM, MR and X-ray

After applying the automatic registration algorithm using the coronary sinus and aorta, electroanatomical data was further registered to the co-registered X-ray-MR space (XMS). For the CRT case, using the CS/DAo for the X-ray-MR registration, further co-registration accuracy with the EAM was measured to be 3.7 mm 3D-TRE with a precision, in terms of percentage overlap of the scar was 83%. Co-registration using the CS/AAo configuration produced the same accuracy and precision, suggesting that the registration problem was largely constrained by the CS and not the Ao. Co-registration between MR data and EAM taken from is shown in Figure 6.9.

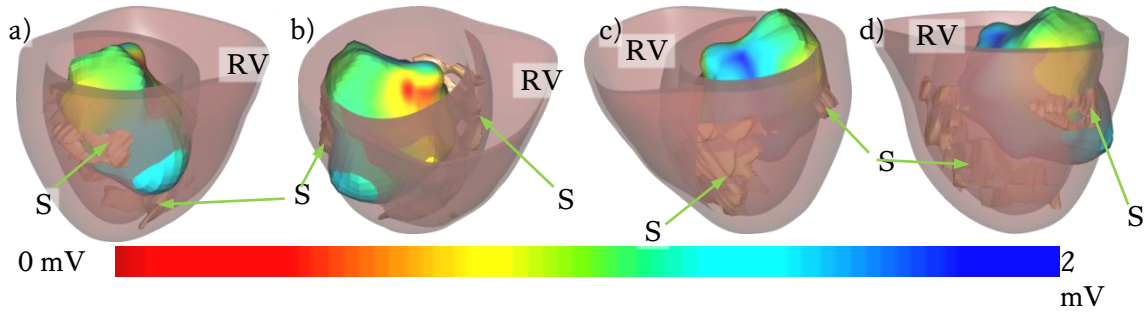


Figure 6.9 a) Co-registration of bipolar voltage EAM (colour mapped, opaque) acquired from EnSite and MR segmented LV and RV (*pink, translucent*). Regions of scar obtained from LGE images (*opaque, white, labelled S, green arrows*) correspond to regions of low voltage (*red to yellow*) in the EAM surface. This is showing a posterior view, b) posterior view with a slight tilt forward, c) anterior view, and d) anterior view with a slight tip backward.

## 6.6. Discussion

In this chapter, the 2D-3D registration algorithm presented in Chapter 5 was adapted to deal with the additional sources of errors introduced when registering with clinical data as opposed to phantom studies. The phantom models also had simpler coronary vasculature than those of the patients and so this also needed to be addressed. The catheter-based pipeline in Chapter 5 was adapted in three ways. The first was a global-fit extension to handle the multiple branches of a more extensive coronary vasculature. The second was to include an automatic centreline and radius extraction method, since the manual method of extraction was no longer practical. The third and was retrospective gating of the fluoroscopy data due the effect of cardiorespiratory motions on the images. The extended method was described and validated on three exemplary clinical cardiac catheterisation procedures, one RFA, one CRT and PCI.

### 6.6.1. 2D–3D Registration

In Chapter 5, it was shown that using the vessel-radius-weighted two-catheter approach was the best of the three approaches tested, and that the best two-catheter configurations to use were the CS or RCA in conjunction with the Ao. Based on these conclusions, these were the configurations used in this chapter. For each case, registration was performed twice, once using the CV in conjunction with the DAo and the second time using the CV with the AAo.

Due to the difficulty in obtaining a ground truth registration for clinical data, accuracy of the registration was independently assessed by two clinical experts in terms of a mean 2D-TRE over the whole heart. For each registration, error estimates were given for each X-ray view (Table 6.5) which was, on average, 6.1 mm mean 2D-TRE using the CV/AAo configuration, and 5.7 mm mean 2D-TRE using the CV/DAo configuration. Automatic registration only required about 114.5 s on average.

The results of the automatic registration method were compared to manual registrations performed independently by three clinical experts (Table 6.6) using a modified EP navigator, a software platform currently used in clinical practice to manually overlay 3D cardiac data to the X-ray fluoroscopy. By consensus of the expert observers, registrar #3 was less accurate and so is excluded in the rest of this discussion. Two clinical experts, #1 and #2, took 455 s, on average, to register each case in two views. The manual registrations were assessed by same two clinical experts who assessed the automatic registrations, and estimated the mean 2D-TRE to be 6.5 mm over the whole heart.

While the accuracy for the automatic registration was not below the 5-mm clinical accuracy required for radiofrequency ablations [14], results show that for all thee clinical cases, automatic

registration performed better than manual registration, which is in current clinical use, in terms of accuracy and speed (Table 6.8).

The algorithm for the clinically adapted catheter-based registration algorithm did not perform as well as the algorithm applied to phantom data in Chapter 5, which had an accuracy of 2.7 mm mean 3D-TRE (WH) averaged over the three catheter configurations used in this chapter. This was expected, however, due to the additional sources of error in patient data not present in phantom data, which will be address in the next section.

### 6.6.2. Sources of Error

The image gating requirement introduces two potential sources of error, an intra-modality phase mismatch between the left and right X-ray images, and an inter-modality phase mismatch between the MR and X-ray. These errors are expected to increase with a decrease in the frame rate of the X-ray videos, since there are fewer images to choose from that match the end-diastole and end-expiration conditions. The intra-modality phase mismatch affects the reconstruction of catheters and other intracardiac devices which will be used for registration. This error can be eliminated by using simultaneous biplane, as shown in [139]. However, this requires a dedicated biplane X-ray system not widely available in most hospitals due to cost. The inter-modality phase mismatch affects the relative shape and pose of the heart vessel compared to its catheter, unavoidably reducing the potential accuracy and robustness of the registration. Another source of error related to the non-rigidity of the heart is that a relatively stiff catheter may deform the vessel it is inserted into during the procedure. This creates a shape mismatch of the vessel between the two modalities.

### 6.6.3. Validation of 3D-3D Registration

Another scenario that is not modelled using a phantom is the presence of scarring due to myocardial infarction and electrical activity. The ability to map EAM data onto a more accurate MR anatomy is desirable for both the clinical setting to improve EP studies and biophysical modelling. The method to do this in this chapter approximates the LV blood to a prolate spheroid and matches it to the prolate spheroid approximation of Carto's LV anatomy or in the CRT case, the EnSite balloon catheter. To validate the registration, scar information was extracted from a LGE-CMR scan and from the bipolar voltage data of the EAM. Both scar extractions were mapped onto the accurate LV geometry from the anatomical MR scan where accuracy, in terms of a centroid distance, and precision in terms of percentage overlap was measured. Average accuracy of the algorithm from the two catheter configurations was 3.7 mm, with an 83% scar overlap (Figure 6.9). The accuracy is comparable to commercially available platforms such as the NavX Fusion and Cartomerge [127], but requires significantly fewer corresponding points and no venogram acquisitions.

Since the co-registration between the EAM and XMS coordinates relies on the initial co-registration between X-ray and MR, errors present in the initial registration propagate into EAM-XMS co-registration. However, the main source of error of the co-registration comes from the EAM data itself; particularly the geometry acquisition techniques employed by the mapping system. In both the Carto XP and EnSite systems, a roving catheter is introduced into the LV to collect points along the endocardial wall. Since points are acquired sequentially, cardiac and respiratory motion may cause deflection of the catheter tip from one point to the next which introduces distortions in the geometry. As a result, the endocardial LV surface generated from EAM is usually very different from the surface segmented from an MR image. This is evident in Figure 6.7 and Figure 6.9, representing a significant contribution to the error.

### 6.6.4. Conclusion

This chapter demonstrates 2D-3D image registration of cardiac images acquired using MR and X-ray fluoroscopy, taken from three routine cardiac catheterisation procedures with an average mean 2D-TRE of 5.9 mm. While the accuracy falls short of the 5-mm clinical requirement, it has been shown to register more accurately than the manual registration using the EP navigator platform which is currently used in clinical practice, which had an average mean 2D-TRE of 6.5 mm. It also performed registration faster, and because the method is mostly automated, it fits better in the clinical workflow.

During two stages of the algorithm, the segmentation of the vessels and the epipolar reconstruction of the catheters, manual interactions are required, prolonging the overall processing time. However, there has been recent research which show promise towards automating these steps [137] [140].

While robustness was not measured in this study, an argument can be made that the algorithm should already be robust, due to the global-fit search strategy employed by the algorithm. The argument is that as long as the catheter is lying within a branch of the corresponding segmented, the global search strategy is guaranteed to encounter the correct solution during the search (§6.2.3).

The 2D-3D image registration of cardiac images provided by the global-fit algorithm can potentially provide the clinical team with a roadmap to guide catheterisation procedures safely and efficiently. Furthermore, it was shown that EAM data could be accurately mapped onto the X-ray and MR images using a 3D-3D image registration algorithm. This second registration can provide the medical team with visual and quantitative evidence of how effective the treatment was, and has many uses in the biophysical modelling applications which may ultimately result in better ways to treat electrical abnormalities of the heart.

While more patient studies will need to be conducted to fully test this algorithm, it is envisaged that both the 2D-3D and 3D-3D methods of image registration of cardiac images will be embedded as a standard part of the clinical workflow in Figure 2.12, ultimately improving the catheterisation procedure to better deal with pathologies of the heart.

# Chapter 7

## 7. Looped-Catheter-Based 2D-3D Registration of Cardiac Data

In current clinical settings, a common registration technique involves inserting a catheter and looping it inside a target chamber (Figure 7.1a, b, c), such as the left atrium (LA), and then manually aligning the preoperative 3D data from several X-ray views using a software platform such as EP navigator [23]. In this chapter, the proposed 2D-3D registration is an automated implementation of this approach but modified to work with a single view if multiple views are unavailable. To improve accuracy and robustness, the upper border of the cardiac shadow is used as an additional constraint as in [67]. Using only the upper border avoids the need for a contrast agent injection since the region is readily visible in typical X-ray images of the heart without contrast agents (Figure 7.1c).

The focus of the previous two chapters was a reconstruction-based 2D-3D image registration algorithm using catheterised vessels. The reconstruction algorithm has the advantage over projection and back-projection approaches that depth information is recovered prior to registration, thereby avoiding the many-to-one or one-to-many geometric relationships; both ill-conditioned problems. On the other hand, reconstruction requires two X-ray views of the catheters placed within the heart. During intervention, it is sometimes not desirable to acquire biplane X-rays.

Sequential biplane acquisitions negatively affect the clinical workflow since it requires the radiographer to rotate and then readjust the C-arm and, possibly, the patient table. This becomes an issue if repeat registrations are required. Sequential biplane images can also cause a number of issues related to gating and catheter movements between images, leading to potential sources of error. These issues can be avoided using a simultaneous biplane fluoroscopy system [139]. However, these dedicated systems are expensive and not in widespread clinical use.

On the other hand, single-view registration would be advantageous where repeat registrations are required, for example due to bulk patient motion. This is a known problem in in 2D-3D image registration of cardiac images [30] when the patient is under sedation but not under general anaesthetics [141]. According to clinical experts, bulk patient motion occurs frequently enough in a catheterisation lab for single-view registration to be desirable, although there is no definitive statement on this matter in the literature. A single view method could be used to detect

when bulk patient motion has occurred, and can potentially correct a prior registration for this motion. The prior, initial registration can be achieved by either the previous catheter-vessel approach, or the using looped-catheter-based proposed in the rest of this chapter with two views.

In this chapter, the looped-catheter-based 2D-3D image registration algorithm is described and applied to the plastic and porcine heart models (Figure 7.1a, b) where fiducial markers placed around the heart are used to quantify the algorithm's accuracy and robustness. The ability to quantify these two values allows variations and refinements of the algorithm to be explored. Based on this exploration, the version of the algorithm that performed the best was used to register a clinical data set of a patient who underwent radiofrequency (RF) ablation (RFA) treatment for left atrial flutter (LAF) (Figure 7.1c).

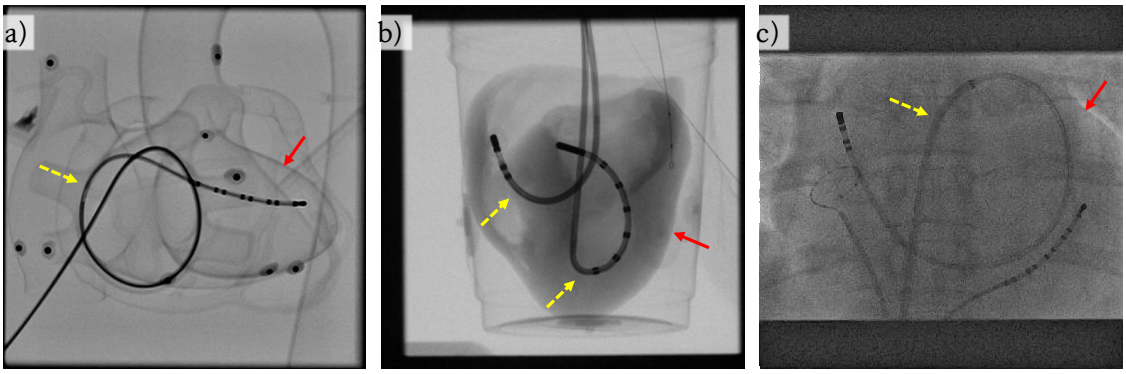


Figure 7.1 a) PA X-ray view of a plastic phantom with catheter inserted into its LA and looped along the arterial wall. b) Anterior X-ray view of an *ex vivo* porcine heart with a catheter loop inside the left ventricle and half loop inside the right ventricle. c) PA X-ray view of a patient's heart with catheter looped inside the LA. The catheter (yellow dashed arrow) and upper cardiac borders (*red solid arrow*) are readily visible in all views.

## 7.1. Theoretical Method

The proposed algorithm is a projection-based approach that is intended to work with any number of X-ray views, and relies on the formation of a catheter loop inside a target chamber of the heart during the procedure. It iteratively searches for the rigid-body transformation (RBT) $\mathcal{M}_{\text{reg}}$ that aligns the preoperative 3D data to X-ray images by maximising the metric,

$$A = \sum_{i=0}^{N-1} \left( A^i_{\text{loop}} - A^i_{\text{border}} \right) \quad . \qquad (7.1)$$

The superscript $i$ indexes the X-ray image within the set, $i \in [0, N-1] \cap \mathbb{Z}$, and $N$ is the number of suitable X-ray views used for registration. The symbols $i$ and $N$ will be used exclusively in this way for the remainder of this chapter. The superscript $i$ will be dropped for clarity when not referring to any specific X-ray view. For each X-ray view, $A_{\text{loop}}$ is the intersecting area enclosed by points manually picked along the catheter loop from the view, and projections of the target chamber surface segmented from the preoperative 3D data, while

$A_{border}$ is the area between points manually picked along the upper border of the X-ray cardiac shadow and the projections of the ventricles segmented from the preoperative 3D data (Figure 7.2).

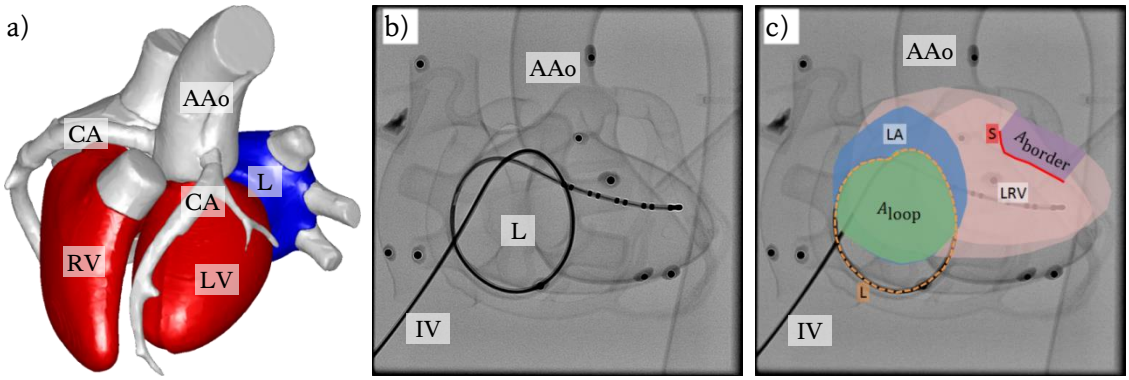


Figure 7.2 a) Surface rendering of a CT scan of a plastic heart phantom after segmentation of its left (LV) and right ventricles (RV) (*red*), left atrium (LA) (*blue*), and other chambers and great vessels (*white*), such as the coronary arteries (*CA*) and ascending aorta (*AAo*). b) X-ray of the phantom in posterior-anterior view with a catheter inserted into its LA via the inferior vena cava (IVC), and exiting the lower right pulmonary vein (*LRPV*). c) Same PA view highlighting the upper cardiac border from X-ray (*red solid arc, labelled S*) and the projected convex hulls of the LA (*blue*) and combined LV and RV (LRV) (*pink*). Projected anatomy is not in registration position; to get there the algorithm attempts to maximise the intersection of the catheter loop (*orange dashed loop, labelled L*) in X-ray and the projected LA (*green*, $A_{loop}$) while minimising the gap between the upper cardiac border from X-ray and the projected LRV (*purple*, $A_{border}$).

The metric is designed to be suitable for any number of X-ray views, although intuitively, the ideal views are the ones where the catheter loop encloses the largest area and closely matches the area of the projection of the target chamber (Figure 7.2). This usually occurs in PA view since the points where the catheter enters and exits the chambers of the heart are almost in-plane. When the loop is viewed from other angles, its minor axis decreases, resembling a flattened ellipse (Figure 7.3a). In these cases, the catheter loop still provides two points of constraints. In some scenarios, the catheter loop may be smaller than its confining chamber if, for example, the catheter does not accurately follow the chamber wall. This would introduce an error $\delta$ which would be equal to the difference between projected diameters of the chamber and the loop (Figure 7.3b), and no greater than the chamber diameter. The error $\delta$ would propagate through the algorithm and could result in the addition of errors of up to $\delta$ in the registration, assuming that the error propagation is all translational. Fitting the loop inside the chamber represents a circular constraint that would lead to errors when registering. The inclusion of the upper cardiac border adds a constraint to prevent this free rotation (Figure 7.3c).

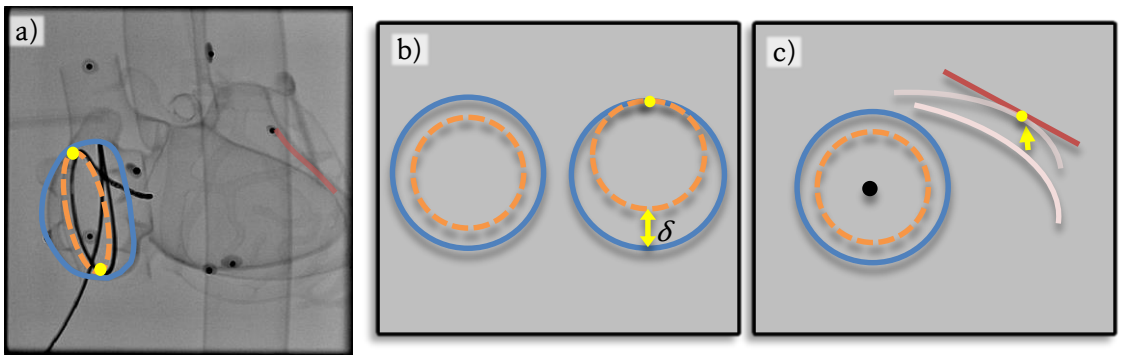


Figure 7.3 a) X-ray image of a plastic heart phantom taken at LAO 30˚. The looped part of catheter (*orange, dashed*) viewed at this angle resembles an ellipse with a short minor axis. The ellipse touches the walls of its confining chamber (*blue, solid*) at the end of its major axes (*orange circles*). b) Diagram of a scenario in PA view when catheter loop (*orange, dashed*) is smaller than its confining chamber (*blue, solid*), then the maximum error $\delta$ is the difference in diameter between the chamber and the loop in this view. This is when the loop touches the chamber at one point (*yellow circle*). c) Diagram of scenario in PA view using both the loop and border constraint (*red line*). The projected confining chamber (*blue, solid*) and LRV (*pink curve*) are free to rotate around the centre of the loop (*black circle*) until it touches the segmented LRV border (*red line*) in X-ray at a point (*yellow circle*).

### 7.1.1. Preoperative 3D Features

Prior to the cardiac catheterisation procedure, a 3D image $I^{3D}$ of the heart is required. In this chapter, tomographs are acquired using magnetic resonance (MR), X-ray computed tomography (CT) and 3D-rotational X-ray (3DRx). The chambers of the heart are then segmented from the image using a semi-automatic segmentation tool (ITK-SNAP) [112], followed by an output of the points that make up their geometric hulls (Figure 7.2a). For the target chamber in which the catheter loop will be formed, the surface corresponding to the endocardial wall is segmented with hull points $\{\vec{C}_j^{3D}\}$ extracted, while for the left and right ventricles (LRV), the epicardial walls are segmented with respective hull points $\{\vec{U}_j^{3D}\}$ and $\{\vec{W}_j^{3D}\}$ extracted. The subscript $j$ indexes the points in each set.

### 7.1.2. Intraoperative 2D Features

During the procedure, once the catheter loop is formed within the target chamber any number of X-ray images $\{I^i\}$ of the heart can be used in the algorithm as long as the catheter loop and upper border of the cardiac shadow are in view, the view is in-phase with the preoperative image $I^{3D}$ in terms of the cardiorespiratory cycle. The X-ray imaging system is required to be geometrically pre-calibrated and tracked so that the intrinsic $\mathcal{P}(c_s, l_s, k_1, k_2)$ and extrinsic $\mathcal{M}_{2D}^i(\delta_x^i, \delta_y^i, \delta_z^i, \theta^i, \phi^i, \psi^i)$ camera calibration parameters, and hence matrices, are known.

For each view, points along the looping catheter that makes up the hull of the loop $L = \{\vec{L}_j\}$, and along the upper cardiac border $S = \{\vec{S}_j\}$, are manually selected (Figure 7.4). Incomplete loops

are closed with a straight line (Figure 7.4b). The subscript $j$ indexes the points in each set and are ordered so that $L$ represents an anticlockwise polygon and $S$ is a discrete arc on the plane.

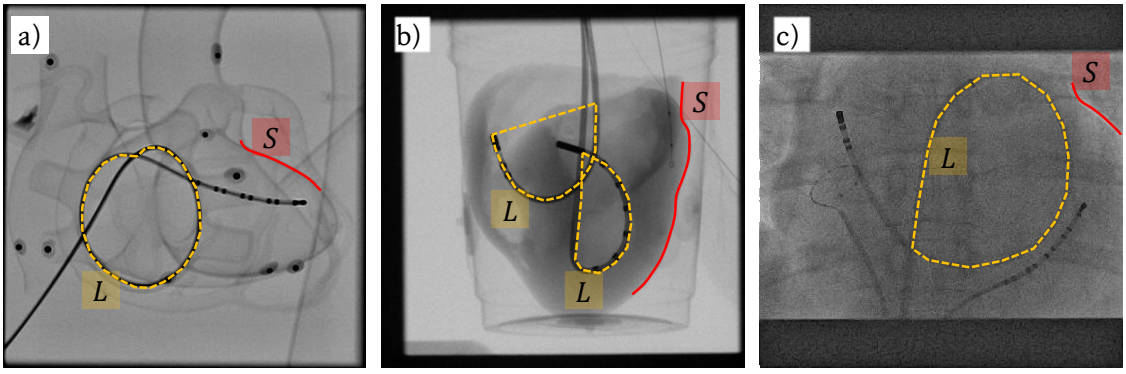


Figure 7.4) X-ray images of a) plastic heart, b) porcine heart and c) human heart with catheter loops (*dashed, dark yellow*) formed within their chambers. The arcs along upper cardiac borders (*solid, red*) are highlighted.

### 7.1.3. Loop Area $A_{\text{loop}}$

The positive part of the metric (7.1) $A_{\text{loop}}$ measures how much of the catheter loop is contained within the projection of the target chamber in each X-ray view (Figure 7.5a). To quantify this, endocardial hull points of the target chamber are projected onto the X-rays (Figure 7.2c),

$$\lambda_j \begin{bmatrix} \vec{C}_j \\ 1 \end{bmatrix} = \mathcal{P}\mathcal{M}_{\text{2D}}\mathcal{M}_{\text{reg}} \begin{bmatrix} \vec{C}_j^{\text{3D}} \\ 1 \end{bmatrix} \quad , \qquad (7.2)$$

where $\mathcal{M}_{\text{reg}}$ is the rigid-body transformation (RBT) describing the relationship between the X-ray's and the 3D scanner's coordinate systems, which changes to maximise $A_{\text{loop}}$. The $\lambda_j$s are the scaling parameters. The convex hulls of the projected chamber and of the catheter loop are extracted using a fast radial sweep hull routine (S-hull, http://www.s-hull.org) [142],

$$\{\vec{c}_k\} = \text{convex hull}(\{\vec{C}_j\}); \{\vec{c}_k\} \subseteq \{\vec{C}_j\} \quad , \qquad (7.3)$$

$$\{\vec{l}_k\} = \text{convex hull}(\{\vec{L}_j\}); \{\vec{l}_k\} \subseteq \{\vec{L}_j\} \quad , \qquad (7.4)$$

with the subscript $k$ indexing points of the hull, which are ordered so that the hulls form anti-clockwise polygons $C$ and $L$. The intersecting polygon $G$ between the catheter loop's and projected chamber's convex hulls is found using a general polygon clipping routine (Clipper, http://www.angusj.com) [143] which is based on [144],

$$G = C \cap L \quad . \qquad (7.5)$$

Finally, the loop area $A_{\text{loop}}$ is defined as the area of this intersecting polygon $G$. If $\{(x_k, y_k)\}$ are the vertices of this polygon, the area is computed with:

$$A_{\text{loop}} = \sum_k (x_k y_{k+1} - x_{k+1} y_k) \quad . \qquad (7.6)$$

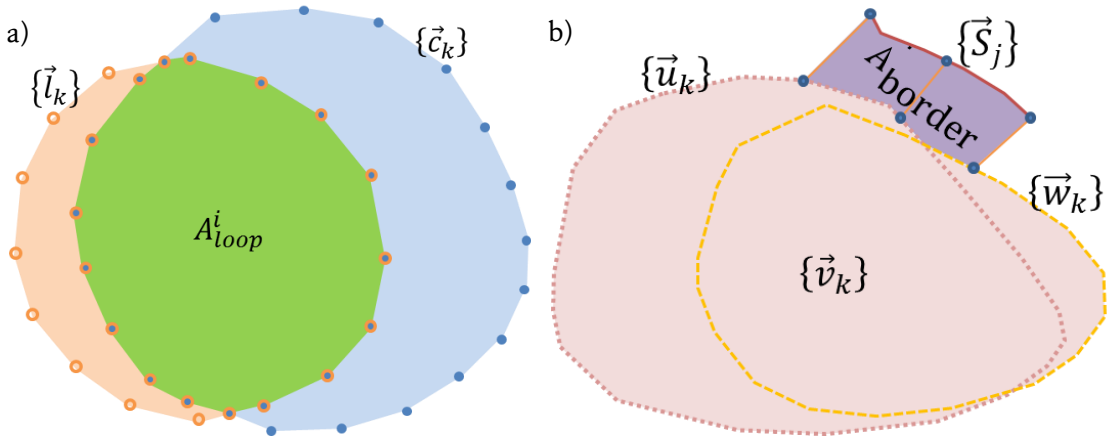


Figure 7.5 a) Intersection area $A_{loop}$ (shaded green, enclosing points shown as concentric circles, blue inside, orange outside) between convex hull of the catheter loop $\{\vec{l}_k\}$ (orange and green shaded areas, enclosed by hollow orange circles) and convex hull of target chamber projection $\{\vec{c}_k\}$ (blue and green shaded areas, enclosed by solid blue circles). b) Separation area $A_{\text{border}}$ (shaded light purple) between X-ray cardiac border $\{\vec{S}_j\}$ (red line) and the combined LRV polygon (shaded light pink) defined by points in $\{\vec{v}_k\} = \{\vec{u}_k\} \cap \{\vec{w}_k\}$ (dotted light red and dashed dark yellow closed paths respectively). Endpoints and midpoint of cardiac border and corresponding points on combined LRV polygon marked (*blue circles at ends of orange lines*).

### 7.1.4. Border Area $A_{\text{border}}$

The negative part of the metric (7.1) $A_{\text{border}}$ measures the amount of separation between the upper cardiac border in X-ray and the combined convex hulls of the projections of the left and right ventricles. This measure is quantified by first projecting points of the epicardial ventricular surfaces onto the X-ray views,

$$\lambda_j \begin{bmatrix} \vec{U}_j \\ 1 \end{bmatrix} = \mathcal{P}\mathcal{M}_{\text{2D}}\mathcal{M}_{\text{reg}} \begin{bmatrix} \vec{U}_j^{\text{3D}} \\ 1 \end{bmatrix} \quad , \qquad (7.7)$$

$$\lambda_j \begin{bmatrix} \vec{W}_j \\ 1 \end{bmatrix} = \mathcal{P}\mathcal{M}_{\text{2D}}\mathcal{M}_{\text{reg}} \begin{bmatrix} \vec{W}_j^{\text{3D}} \\ 1 \end{bmatrix} \quad . \qquad (7.8)$$

The convex hulls of each ventricle projection, $\{\vec{U}_j\}$ and $\{\vec{W}_j\}$, are then computed using [142] to yield anticlockwise polygons $u$ and $w$ with respective vertices,

$$\{\vec{u}_k\} = \text{convex hull}(\{\vec{U}_j\}); \{\vec{u}_k\} \subseteq \{\vec{U}_j\} \quad , \qquad (7.9)$$

$$\{\vec{w}_k\} = \text{convex hull}(\{\vec{W}_j\}); \{\vec{w}_k\} \subseteq \{\vec{W}_j\} \quad . \qquad (7.10)$$

The two convex polygons combine to produce a third concave polygon $v$ with vertices,

$$\{\vec{v}_k\} = \text{concave hull}(\{\vec{u}_k\}, \{\vec{w}_k\}) \quad . \qquad (7.11)$$

The concave hull between two polygons can be expressed as the union of their points $v = u \cup w$, and is computed using the general polygon clipping routines [143] (Figure 7.5).

The next step is to find a minimum-area separating loop in each view between the upper cardiac border arc $S$ and the combined left and right ventricle projection polygonal hull $v$. This step begins by first finding the middle point $\vec{S}_{\text{mid}}$ which lies along an edge of the arc $S$ (Figure 7.5b, Figure 7.6) such that the total linear length along the arc between the first point $\vec{S}_0$ and $\vec{S}_{\text{mid}}$ is exactly half the total linear length of the arc $S$.

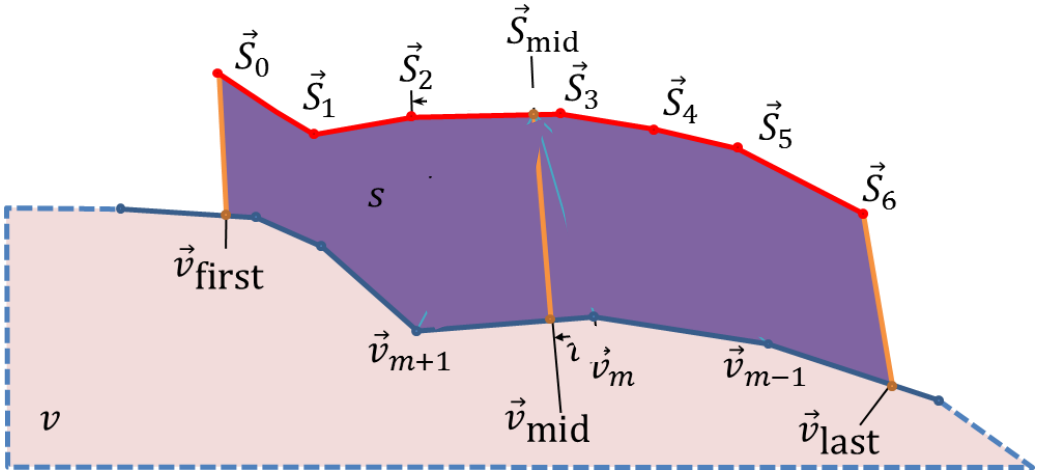


Figure 7.6) Formation of the separation loop $s$ which encloses the area (*purple*) between the discrete arc $S = \{\vec{S}_j\}$ (*solid, red*) and the hull of a polygon $v = \{\vec{v}_j\}$ (*solid and dashed, blue; enclosing pink area*). Loop is determined by finding the middle point $\vec{S}_{\text{mid}}$ along an edge of $S$. In this figure, $|S| = 7$ and $\vec{S}_{\text{mid}}$ lies on the edge between $\vec{S}_2$ and $\vec{S}_3$, corresponding to $k = 2$ in (7.14)(7.2). $\vec{v}_m$ is the vertex in $v$ closest to $\vec{S}_{\text{mid}}$. $\vec{v}_{\text{mid}}$ is the point along the hull of $v$ closest to $\vec{S}_{\text{mid}}$ between the neighbouring points of $\vec{v}_m$: $\vec{v}_{m-1}$ and $\vec{v}_{m+1}$. The Points $\vec{v}_{\text{first}}$ and $\vec{v}_{\text{last}}$ are points on the hull of $v$ which are exactly half the length of $S$ away from $\vec{v}_{\text{mid}}$ and correspond to $\vec{S}_0$ and $\vec{S}_6$ respectively. The arc $S$, line segment between $\vec{S}_0$ and $\vec{v}_{\text{first}}$ (*solid, orange*), line segment between $\vec{S}_6$ and $\vec{v}_{\text{last}}$ (*solid, orange*), and points along the hull of $v$ between and including $\vec{v}_{\text{first}}$ and $\vec{v}_{\text{last}}$ form a closed loop $s$ and the loop's area is the quantity to be minimised in (7.1).

Let the following denote the total linear length along $X$ with vertices $\{\vec{X}_j\}$ between $\vec{X}_u$ and $\vec{X}_v$,

$$\ell_{u,v}(X) \equiv \sum_{j'=u}^{v-1} \left\| \vec{X}_{j'+1} - \vec{X}_{j'} \right\| \quad , \qquad (7.12)$$

then the total linear length of the arc $X$ is

$$\mathcal{L}(X) \equiv \ell_{0,|S|-1}(X) \quad . \qquad (7.13)$$

The point $\vec{S}_{\text{mid}}$ lies along the edge between points $\vec{S}_k$ and $\vec{S}_{k+1}$. $k$ is the point in $S$ that satisfies:

$$\ell_{0,k}(S) < \frac{\mathcal{L}(S)}{2} < \ell_{0,k+1}(S) \quad . \qquad (7.14)$$

Once $k$ is found, the distance between $\vec{S}_{\text{mid}}$ and $\vec{S}_k$ is,

$$\delta = \frac{\mathcal{L}(S)}{2} - \ell_{0,k}(S) \quad , \quad (7.15)$$

which is used to find the location of $\vec{S}_{\text{mid}}$,

$$\vec{S}_{\text{mid}} = \vec{S}_k + \delta \frac{\vec{S}_{k+1} - \vec{S}_k}{\left\|\vec{S}_{k+1} - \vec{S}_k\right\|} \quad , \quad (7.16)$$

The next step is to find the point $\vec{v}_m$ in $v$ that's closest to $\vec{S}_{\text{mid}}$,

$$m = \arg\min_{m'} \left\|\vec{S}_{\text{mid}} - \vec{v}_{m'}\right\| \quad , \quad (7.17)$$

which helps determine the point $\vec{v}_{\text{mid}}$ that is closest to $\vec{S}_{\text{mid}}$ along the edges adjacent to $\vec{v}_m$,

$$\tau = \arg\min_{\tau' \in [-1,1]} \begin{cases} \left\|\vec{S}_{\text{mid}} - \left(\vec{v}_m + \tau'(\vec{v}_{m+1} - \vec{v}_m)\right)\right\| & \tau' \geq 0 \\ \left\|\vec{S}_{\text{mid}} - \left(\vec{v}_m - \tau'(\vec{v}_{m-1} - \vec{v}_m)\right)\right\| & \tau' < 0 \end{cases} \quad , \quad (7.18)$$

$$\vec{v}_{\text{mid}} = \begin{cases} \vec{v}_m + \tau(\vec{v}_{m+1} - \vec{v}_m) & \tau \geq 0 \\ \vec{v}_m - \tau(\vec{v}_{m-1} - \vec{v}_m) & \tau < 0 \end{cases} \quad . \quad (7.19)$$

From $\vec{v}_{\text{mid}}$ a distance exactly equal to half the linear length of $S$ is travelled along the hull of $v$ to find $\vec{v}_{\text{first}}$ in one direction and $\vec{v}_{\text{last}}$ in the other (Figure 7.6),

$$\ell_{\text{first,mid}}(v) = \frac{1}{2}\ell_{0,|S|-1}(S) = \ell_{\text{mid,last}}(v) \quad . \quad (7.20)$$

The arc $S$ and all points on the hull of $v$ between and including $\vec{v}_{\text{first}}$ and $\vec{v}_{\text{last}}$ are then reordered, if necessary, and joined together to form a new polygon which represents the separation between the upper border of the cardiac shadow $S$ and the combined left and right ventricle projection $v$. Finally, the separating area $A_{\text{border}}$ is defined as the area of this polygon.

If $\{(x_k, y_k)\}$ are the vertices of this polygon, the area is computed with:

$$A_{\text{border}} = \sum_k (x_k y_{k+1} - x_{k+1} y_k) \qquad \{(x_k, y_k)\} = \{S_j\} \cup \{v_j | \text{first} \leq j \leq \text{last}\} \quad . \quad (7.21)$$

### 7.1.5. Iterative Search Strategy

The algorithm presented in this chapter requires an initial estimate of the six pose parameters $\vec{X} = (x, y, z, \alpha, \beta, \gamma)$ that make up the RBT $\mathcal{M}_{\text{reg}} = \mathcal{M}(\vec{X})$. The initial estimate assumes that the X-rays were taken with the heart approximately at the isocentre of the C-arm, and that the patient is lying in a supine position both preoperatively for the 3D scan, and intraoperatively on the X-ray table, $\mathcal{M}_{\text{reg}} = \mathcal{M}_{\text{iso-sup}}$. This is known as using isocentre-supine constraints and is a simple form of a *calibration-based* registration approach. While not very accurate, this method provides a good starting point for refinement schemes. The six pose parameters of $\vec{X}$ make up a six-degree-of-freedom (DOF) search space, which is iteratively explored to maximise the area metric $A$ in (7.1).

#### 7.1.5.1. Best Neighbour Hill Climbing Method

The iterative search strategy used in the algorithm is the *best neighbour hill climbing* (BNHC) method as used in [79] (§3.1.3.2). The method uses the isocentre-supine constraints to determine the initial estimate position in the search space, $\mathcal{M}_{\text{reg}} \leftarrow \mathcal{M}_{\text{iso-sup}}$, and requires a set of incremental step sizes $\Delta\vec{X} = (\Delta x, \Delta y, \Delta z, \Delta\alpha, \Delta\beta, \Delta\gamma)$. The method then computes 13 variant RBTs from $\mathcal{M}_{\text{reg}}$ and $\Delta\mathcal{M} = \mathcal{M}(\Delta\vec{X})$: six variants include a small positive incremental change in each one of its six parameters, six negative changes in each parameter; and in the last variant there is no change,

$$a_j = \begin{cases} A\left(\mathcal{M}_{\text{reg}} + \Delta\mathcal{M}_j \cdot \hat{e}_j\right) & j = [0,5] \\ A\left(\mathcal{M}_{\text{reg}} - \Delta\mathcal{M}_{j-6} \cdot \hat{e}_{j-6}\right) & j = [6,11] \\ A\left(\mathcal{M}_{\text{reg}}\right) & j = 12 \end{cases}, \qquad (7.22)$$

where $\hat{e}_j$ is a unit vector of the search space in direction $j$.

For each variant RBT, the area $A$ is computed, and the variant that corresponds to the largest computed value of $A$ becomes the new $\mathcal{M}_{\text{reg}}$. $\mathcal{M}_{\text{reg}}$ is refined in this way until the largest computed area is from the no-change variant. In this case, the incremental amounts are halved and iteration resumes until the increments have been halved 15 times, at which point the algorithm ends and is said to have converged. A flowchart of the BNHC method is shown in Figure 7.7.

In many cases, the supine constraint may provide a good initial estimate for the rotational parameters that make up $\mathcal{M}_{\text{reg}}$, since the patient usually lies on the table bed in the same, repeatable way. However, depending on the individual case, the heart may not lie at the exact isocentre in the 2D or 3D images, and therefore, there may be a large translational error between the images after applying the isocentre-supine constraint. In these cases, it may be better to first find the translational components that make up $\mathcal{M}_{\text{reg}}$ before finding the rotational components. This may increase the efficiency of the optimisation strategy in terms of speed and accuracy, since the initial large translational error can be corrected first without having to spend time considering potentially erroneous rotational corrections.

A variation of the BNHC method as used in [99] first finds the translational components of $\mathcal{M}_{\text{reg}}$ using the same iteration and stopping criteria as the BNHC method described above, with $\Delta\vec{X} = (\Delta x, \Delta y, \Delta z, \Delta\alpha, \Delta\beta, \Delta\gamma)$, but only using the translational components of $\Delta\vec{X}$ in the first stage of iteration. Once converged, the registration then starts to search through the entire set of parameters of $\Delta\vec{X}$. This modification is referred to in this chapter as the two-stage BNHC (2× BNHC), while the former is referred to as the one-stage BNHC (1×BNHC).

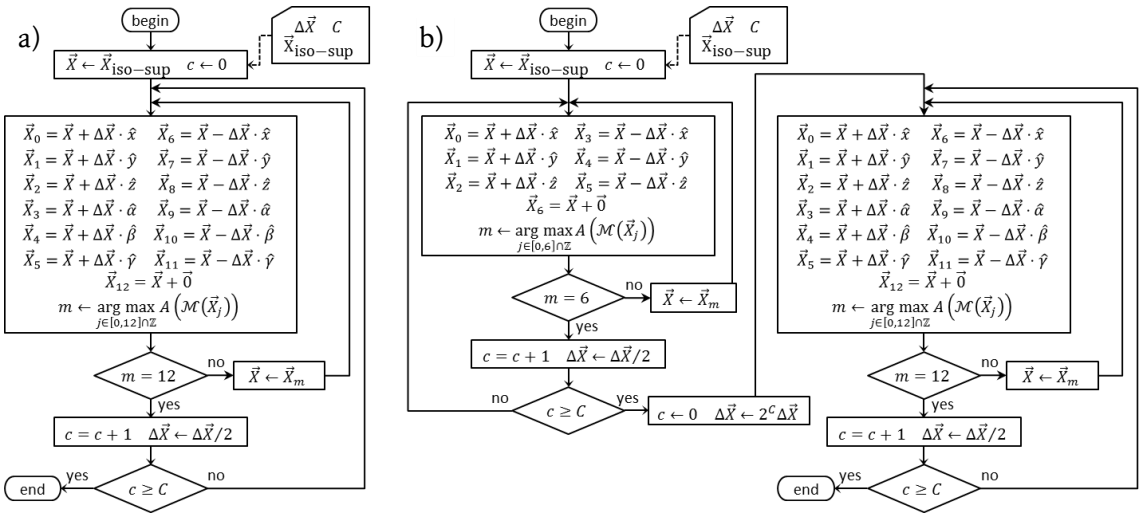


Figure 7.7) a) Flowchart of 1×BNHC optimisation strategy as used in the loop-catheter-based registration algorithm. Starting with the isocentre-supine constraint as an estimate $\mathcal{M}_{\text{reg}}$, the algorithm tests small changes of $\mathcal{M}_{\text{reg}}$ in all twelve directions to find the parameters that maximise the area metric $A$ in (7.1). b) A small modification is the 2×BNHC which first searches the translational directions first before searching through the entire twelve directions.

## 7.2. Non-Clinical Heart Model Experimental Method

To validate the proposed registration algorithm, phantom model and *ex vivo* animal experiments were carried out. These were designed to emulate the workflow of a typical cardiac catheterisation (Figure 2.12) but with the addition of an intraoperative catheter loop formation. Image registration was performed on the collected data (Figure 2.16) using this chapter's proposed algorithm.

### 7.2.1. Preoperative Step

The phantom experiment involved a geometrically-realistic plastic model of the heart (LFA 5000, Lake Forest Anatomicals, Lake Forest, IL, US) (Figure 7.2), the same phantom used in Chapter 5. The *ex vivo* animal experiment involved a previously healthy porcine heart securely placed within a basket and preserved with Formaldehyde. In these experiments, multi-modal fiducial markers placed around the heart were used to obtain a gold-standard registration between imaging modalities. This acted as a ground truth for quantifying the accuracy and robustness of the registration algorithm.

#### *7.2.1.1. Plastic Heart Phantom 3D Tomographic Imaging*

The same tomographic image of the plastic heart used in Chapter 5 was also used in this chapter (§5.2.1.2). This was a 512×512×416-sized 3D CT scanned image (0.49×0.49×1 mm$^3$ voxel resolution; Discover STE, GE Healthcare, Chalfont St Giles, Buckinghamshire, UK) with nine radio-opaque markers placed around the heart visible in the scan at locations listed in Table 5.2.

#### 7.2.1.2. Ex Vivo Porcine Heart 3D Tomographic Imaging

The porcine heart used in the animal experiment originated from a healthy pig and was preserved in Formaldehyde after extraction. The atria were removed, leaving only the two ventricles. The heart was securely placed in a plastic basket and six disposable ECG chest electrodes, visible in both MR and X-ray images, were placed around the basket to act as fiducial markers. The basket containing the heart was then scanned under MR ($256^2 \times 70$ voxels, $0.55^2 \times 2$ $mm^3$ resolution; Signa HDxt 1.5T, GE Healthcare, Little Chalfont, Buckinghamshire, UK) using a spoiled gradient echo pulse sequence (NEX = 1, TE = 2.16 ms, TR = 10.18 ms, $\theta = 30^\circ$).

Subsequently, the basket was placed on an X-ray table where it was catheterised, followed by a 3D rotational X-ray (3DRx) image acquisition ($512^2 \times 460$ voxels, $(0.2276\ mm)^3$ resolution; 196˚ arc, 147 views, $V_p$ = 60 kV, I = 97 mA; Innova $2121^{IQ}$, GE Healthcare). To reduce the streaking artefacts in the 3DRx image due to X-ray photon starvation and an incomplete gantry revolution, the image was isotropically subsampled by a factor of two followed by a convolution with a $3 \times 3 \times 3$ 0.65-voxel-standard-deviation Gaussian kernel. This resulted in a $256^2 \times 230$ voxel image with a new resolution of $(0.4552\ mm)^3$. While the 3DRx scan was performed intraoperatively during this experiment, the features extracted from this image were used as a preoperative data set, and therefore described as being part of the preoperative step.

#### 7.2.1.3. Preoperative Information Extraction

The chambers of the CT, MR and 3DRx scanned images of the plastic and porcine hearts were segmented using a semi-automatic active contour region-filling algorithm (ITK-SNAP) [112]. The four chambers of the plastic heart were segmented, while only the two ventricles of the porcine hearts were segmented since the atria had been removed. In the plastic heart, the chamber walls are thin and so there is no discernible difference between the inner and outer walls of the chambers of the plastic phantom model, and so a chamber segmentation is referring to the total chamber including both myocardium and blood pool. In the porcine heart, however, the myocardium is relatively thick and so a distinction has to be made between the blood pool and the myocardium of the chamber, both of which were segmented for this heart.

Additionally, for each catheter loop configuration, the chamber into which the catheter had been inserted was segmented; the blood pool in the case of the porcine heart. Triangulated meshes of the hull of the chambers were generated from the binary segmentation using ITK-SNAP. To reduce the computational burden, the meshes were decimated so that the average area of each triangular face was comparable to the resolutions of the acquired tomographic scans. The unordered set of mesh vertices of the target chamber's blood pool, and the LV and RV myocardium are $\{\vec{C}_j^{3D}\}$, $\{\vec{U}_j^{3D}\}$ and $\{\vec{W}_j^{3D}\}$ and used in (7.2), (7.7) and (7.8) respectively. The

volumes of the segmented chambers and the numbers of vertices that made up the meshes after decimation are listed in Table 7.1.

| Dataset | modality | target | target chamber | | LV | | | RV | | |
|---|---|---|---|---|---|---|---|---|---|---|
| | | | *b.p. V* | # | *tot. V* | *myo. V* | # | *tot. V* | *myo. V* | # |
| plastic heart | CT | LA | 54.4 | 401 | 99.9 | -- | 612 | 103.2 | -- | 715 |
| porcine heart | MR | LV | 28.4 | 149 | 121.1 | 92.7 | 396 | 85.1 | 36.9 | 400 |
| | | RV | 48.2 | 217 | | | | | | |
| | 3DRx | LV | 29.8 | 498 | 143.2 | 113.4 | 1379 | 78.9 | 28.7 | 998 |
| | | RV | 50.2 | 740 | | | | | | |

Table 7.1 – Summary of chamber segmentations with the blood pool (*b.p.*), myocardium (myo.) and total (*tot.*) volume $V$ ($cm^3$) and the numbers of vertices (#) that make up their hulls. The plastic heart does not model the myocardium, so the ventricular segmentations are for the outer myocardial wall only with the volume encompassing both the myocardium and blood pool.

### 7.2.2. Intraoperative Step

Following the preoperative tomographic scans, the hearts were placed on the X-ray table and catheters were inserted into their chambers and looped around the inner chamber wall prior to the sequential biplane acquisition.

#### *7.2.2.1. Plastic Heart Phantom Catheterisation*

The plastic heart was catheterised in two configurations, both of which passed through the inferior vena cava (IVC) before entering the LA and forming a loop around the chamber's interior wall. In the 1st configuration, the catheter exited the LA via the right lower pulmonary vein (RLPV) and in the 2nd configuration exiting the left upper pulmonary vein (LUPV). Once the catheter loop was in place, a sequential biplane X-ray pair of the heart was taken from PA and RAO 45° views (Allura Xper FD10, Philips Healthcare, The Netherlands) (Figure 7.2).

#### *7.2.2.2. Ex Vivo Porcine Heart Catheterisation*

In the animal experiment, two catheters were inserted into the porcine heart. One catheter was inserted into the LV while the other was inserted into the RV, where they both formed loops within their respective chambers (Figure 7.4b, Figure 7.8a, b). If vessels and atria were still attached to the porcine heart, the LV catheter would typically enter via the Aorta and the RV catheter would normally enter via the SVC. For the purposes of this experiment, the two catheters are treated as two independent looped-catheter configurations. Once catheterised, 147 images were acquired using a rotating X-ray C-arm system which was used for 3DRx tomographic reconstruction (§7.2.1.2). The biplane images corresponding to PA and RAO 45° were used for reconstruction ($500^2$ pixels, $(0.4\ mm)^2$ resolution; SOD = 720 mm, SID = 1188 mm; Innova 2121IQ, GE Healthcare).

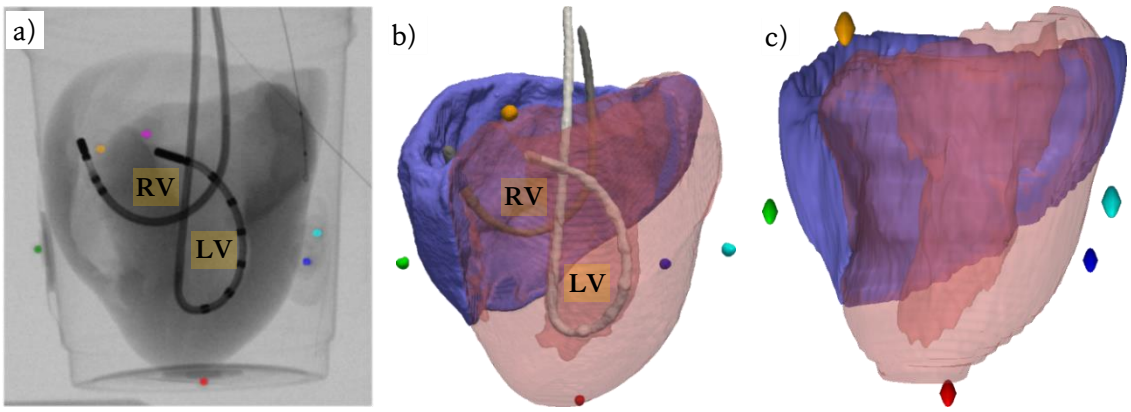


Figure 7.8) Anterior views of the porcine heart's left (*translucent red*) and right (*blue*) ventricles a) in X-ray fluoroscopy and as surface renderings from b) 3DRx and c) MR scan segmentations. Six fiducial markers (*blue, red, green, orange, magenta, cyan*) used to obtain a gold standard registration were visible to each image modality. Catheters inserted into the LV (*white*) and RV (*grey*) and looped were in-place and visible in both X-ray-based modalities but not during the MR scan.

#### 7.2.2.3. Intraoperative Information Extraction

From both biplane X-ray images of the plastic and porcine hearts, points along the looping catheter and upper border of the cardiac shadow were manually picked (Figure 7.4a, b). Points selected from the looping catheter were limited to only those that formed part of the loop and selected in ascending arclength and anti-clockwise order to form vertices of simple polygons $L = \{\vec{L}_j\}$ used in (7.4; §7.1.3). In some X-ray views of a configuration, the image of the catheter did not intersect itself. In these cases, as much of the loop was selected as possible, using only the section reliably within the target chamber, and the selected points were then closed off by a straight line (Figure 7.4b). Points picked on the cardiac shadow were selected in ascending arclength order, forming discrete arcs $S = \{\vec{S}_j\}$ used in (7.15, §7.1.4). A summary of the catheter loop configurations and X-ray 2D images are listed in (Table 7.2).

| dataset | target | configuration | view | catheter loop | | | border | |
|---|---|---|---|---|---|---|---|---|
| | | | | # | $A$(mm$^2$) | $\ell$(mm) | # | $\ell$(mm) |
| plastic heart | LA | IVC-LA-LUPV | PA | 27 | 1900.4 | 156.9 | 8 | 36.1 |
| | | | RAO 45° | 20 | 584.5 | 132.9 | 6 | 36.0 |
| | | IVC-LA-RLPV | PA | 19 | 1459.0 | 140.3 | 8 | 39.2 |
| | | | RAO 45° | 16 | 154.0 | 83.7 | 6 | 33.5 |
| porcine heart | LV | DAo-LV | PA | 12 | 290.1 | 82.7 | 12 | 67.7 |
| | | | RAO 45° | 14 | 494.7 | 94.4 | 17 | 85.8 |
| | RV | SVC-RV | PA | 12 | 1030.2 | 128.2 | 12 | 67.7 |
| | | | RAO 45° | 10 | 843.3 | 114.4 | 17 | 85.8 |

Table 7.2 – Summary of catheter loop configurations, and points picked along catheter loop and upper cardiac border in each X-ray view of the configuration. The number of points (#), encompassing area ($A$) and perimeter ($\ell$) are listed for the catheter loops, and the number of points (#) and total linear arclength ($\ell$) of the border are listed.

The fiducial markers were also manually selected from each X-ray view. In the plastic and porcine heart experiments, fiducial markers were first located in the PA view, and their corresponding location found in the RAO 45° view using the epipolar constraint. Marker locations in 3D were then found using epipolar reconstruction (§4.1.5). In the porcine heart experiment, a larger number of X-ray views were available, therefore allowing a more accurate method of positioning the 3D markers in addition to the biplane marker reconstruction. For each of its six fiducial markers, indexed with $j$, their coordinates $\{\vec{p}_j^{\,i}\}$ in each X-ray image were manually selected and then back projected (§4.1.1.2), forming a bundle of skew lines:

$$L_j^i = \left(\mathcal{P}\mathcal{M}_{2\mathrm{D}}^i\right)^+ \vec{p}_j^{\,i} = \left\{\vec{q}_j^{\,i} + \tau_j^i \vec{v}_j^{\,i} \middle| \tau \in \mathbb{R}\right\} \quad , \qquad (7.23)$$

where $\tau_j^i$ parameterising the back-projection line which passes through the point at $\vec{q}_j^{\,i}$ and parallel to the vector $\vec{v}_j^{\,i}$. The 3D location of the $j^{\text{th}}$ fiducial marker $\vec{f}_j^{\,\text{xr}}$ is at the point that simultaneously minimises the sum of squared errors to each line,

$$\vec{f}_j^{\,\text{xr}} = \left(\sum_i I - \vec{v}_j^{\,i} \tilde{\vec{v}}_j^{\,i}\right)^{-1} \left(\sum_i (I - \vec{v}_j^{\,i} \tilde{\vec{v}}_j^{\,i}) \vec{q}^{\,i}\right) \quad . \qquad (7.24)$$

The juxtaposition $\vec{u}\tilde{\vec{v}}$ is equivalent to the tensor product $\vec{u} \otimes \vec{v}$ and matrix product $[\vec{u}][\vec{v}]^{\mathrm{T}}$. The better set of marker positions, either using biplane epipolar reconstruction or using all available X-ray images, in terms of a lower fiducial registration error (FRE), is the set used to obtain the gold standard.

### 7.2.3. Registration Step

Once all pre- and intraoperative features are extracted, the loop-catheter-based registration is performed between X-ray and CT data in the plastic heart experiment, and between X-ray and 3DRx and between X-ray and MR for the porcine heart experiment (Table 7.1). There are two catheter loop configurations for each experiment (Table 7.2), giving a total of six catheter and modality configurations. For each of these six configurations, the two optimisation strategy variations are employed. The isocentre-supine constraint is used to find an initial starting point prior to iteration. Each optimising strategy is performed three times for each configuration, once using two X-ray views, once using only the left of the two views and once using only the right of the two views. A total of 32 registrations were performed, 8 for the plastic heart and 16 for the porcine heart. For the one-stage and two-stage best neighbour hill climbing (BNHC) method, $\Delta\vec{X}$ was chosen to be $(2\text{ mm}, 2\text{ mm}, 2\text{ mm}, 3.5°, 3.5°, 3.5°)$. The translational step size was chosen to be 2 mm since this was in the same range as the resolution of the images, and 3.5° for the angular step size was chosen as this amount of rotation of a 10-cm diameter heart would cause approximately 2-mm of displacement along its epicardial border.

#### 7.2.3.1. Quantifying Registration Accuracy

The accuracy of the looped-catheter-based registration $\mathcal{M}_{\text{reg}}$ is compared against the fiducial-marker-based registration $\mathcal{M}_{\text{gold}}$ which acts as a ground truth. $\mathcal{M}_{\text{gold}}$ is obtained by solving the problem of *absolute orientation*, without scaling [86], between corresponding fiducial marker locations extracted from the 3D modality $\{\vec{f}_j^{3D}\}$ and from X-ray reconstruction $\{\vec{f}_j^{\text{xr}}\}$.

When registering with biplane X-ray images, 3D information is available by means of epipolar reconstruction and accuracy is assessed in terms of a mean 3D target registration error (TRE) averaged over a region of interest. When only a single view is available for registration, accuracy for overlays is measured in terms of a mean reprojection distance (RPD) [111], which is the total minimum distance between a region of interest, and the back-projection with $\mathcal{M}_{\text{gold}}$ of its forward projection with $\mathcal{M}_{\text{reg}}$. Both the TRE and RPD are as described in §4.1.7.

#### 7.2.3.2. Quantifying Registration Robustness

The gold standard registration $\mathcal{M}_{\text{gold}}$ also allows the quantification of robustness in terms of a *capture range* [31]. To measure this, a set of small perturbations are made around the gold standard $D = \{\vec{D}^i\} = \{(d_x^i, d_y^i, d_z^i, d_\alpha^i, d_\beta^i, d_\gamma^i)\}$. For each perturbation, the accuracy, referred to as the *input accuracy*, is calculated over the whole heart. The optimisation strategy is then applied using the input perturbation as the initial starting point and accuracy is reassessed after the strategy has converged, called the *output accuracy*. The capture range is defined as the largest input accuracy in which the output accuracy is below a certain threshold at least 95% of the time [31]. In this chapter, the threshold is set at 5-mm, which is the desired clinical tolerance for cardiac catheterisation procedures [14]. For biplane registration, accuracy is measured in terms of a mean 3D-TRE and in terms of mean RPD for monoplane registration.

Capture range was measured for each optimisation strategy variation of the registration algorithm and for both biplane and two monoplane views totalling twelve capture range measurements. This was performed on the plastic heart phantom in the IVC-LA-LUPV looped-catheter configuration with 200 perturbations with a uniform distribution of input accuracy between 0 and 25 mm.

#### 7.2.3.3. Registration Algorithm Implementation

The registration algorithm described in this chapter was implemented as a custom visual software application (©Michael Truong, King's College London, London, UK) (Figure 7.9). The software was written in C# and compiled for the .NET™ Framework 4.0 (Microsoft, Redmond, Washington, US) using Visual Studio 2010 (Microsoft) and running on Windows 7 Professional 64-bit (Microsoft) operating system. Features of the software include registration using fiducial markers, the isocentre-supine constraint and manual adjustments of the individual

pose parameters to provide an initial starting position of the looped-catheter-based registration algorithm. The software also allows the user to register using either the one-stage or two-stage best neighbour hill climbing optimisation strategy, and using either biplane or monoplane registration. The machine running the software was equipped with a Core 2 Extreme CPU (Intel, Santa Clara, California, US; 2×3.06 GHz, 4 GB RAM, 64-bit).

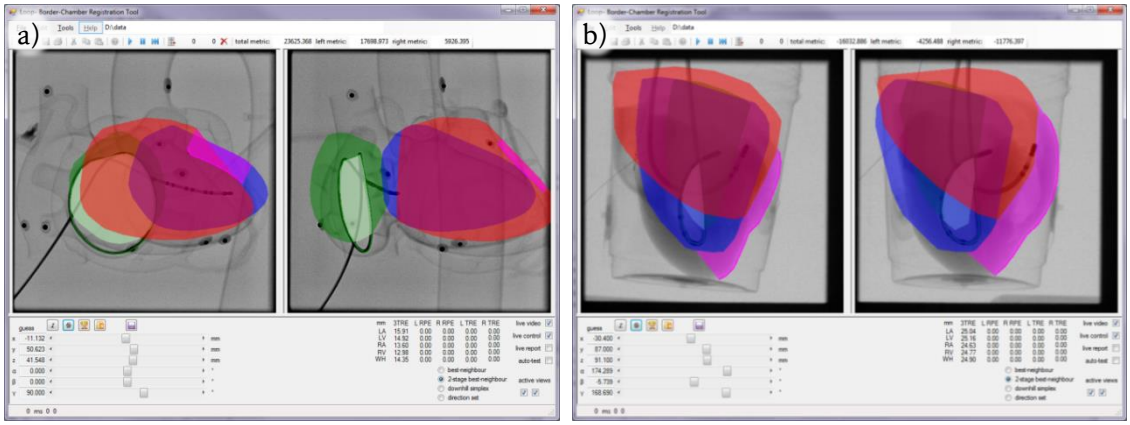


Figure 7.9) Screen shots of the custom software written to perform looped-catheter-based 2D-3D image registration using either 1× or 2×BNHC optimisation strategies, and with either biplane or monoplane X-ray views. Controls allow manual adjustments of $\mathcal{M}_{\text{reg}}$, while updating visual overlays and accuracy provide insight on the algorithm as it executes. a) Plastic phantom and b) porcine heart data loaded in biplane mode after applying the isocentre-supine constraints. Visual ROIs over all X-ray images include the catheter loop (*green solid line*), upper cardiac border (*magenta solid line*), LV (*translucent blue*), RV (*translucent red*), target chamber (*translucent green*), intersection loop (*translucent white*) between the catheter and target chamber, and separation loop (*translucent magenta*) between the upper cardiac border and combined LRV.

## 7.3. Non-Clinical Heart Model Results

The 2D-3D image registration algorithm presented in this chapter was applied to the two looped-catheter configurations of the phantom experiment and of the *ex vivo* porcine heart experiment, providing four different catheter configurations. In the porcine heart experiment, there were two types of preoperative image used and the two catheter configurations were used for each of them, providing a total of six catheter configuration and modality combinations. For each experiment, six variations of the algorithm, based on a combination of two variations of the optimisation strategies and three different view configurations, were tested. Accuracy of the algorithm was assessed in terms of a mean 3D-TRE for biplane X-ray view configurations and in terms of a reprojection distance (RPD) for monoplane configurations, measured over each chamber of the heart and over the whole heart (WH). Robustness of the algorithm was measured in terms of a capture range test using input and output accuracies quantified over the WH.

### 7.3.1. Looped-Catheter-Based 2D-3D Registration of Plastic Phantom Data

Nine lead fiducials placed around the hearted provided $\mathcal{M}_{\text{gold}}$. Data for each catheter configuration were acquired independently. The fiducial registration error (FRE) of the first dataset with images of the first catheter configuration was 1.29 mm, and the FRE for the second dataset with the second catheter configuration was 0.52 mm. An initial alignment of the images using the isocentre- supine constraint provides $\mathcal{M}_{\text{iso-sup}}$.

#### 7.3.1.1. Accuracy of Biplane Registration of Plastic Phantom Data

For biplane registration, accuracy of $\mathcal{M}_{\text{iso-sup}}$ compared to $\mathcal{M}_{\text{gold}}$ was 17.25 mm mean 3D-TRE (WH). Using this as an initial position, the two variations of the algorithm were applied to both catheter configurations using constraints from two X-ray views. The 1×BNHC variation, on average, yielded an accuracy error of 3.02 mm over the whole heart, while the 2×BNHC approach yielded a better accuracy of 2.81 mm. In addition to a higher accuracy, the 2×BNHC approach converged faster, taking 81 s on average, than the 1×BNHC approach, which took 117 s on average. Individual accuracies for each catheter loop configuration and for each chamber of the heart are provided in Table 7.3. Biplane registrations with both BNHC approaches are shown in Figure 7.10 using the first loop configuration and Figure 7.11 using the second.

| Config. | registration | *t* (s) | # | mean 3D-TRE (mm) | | | | | T |
|---|---|---|---|---|---|---|---|---|---|
| | | | | LA | LV | RA | RV | WH | |
| IVC-LA-LUPV | isocentre-supine | | | 15.91 | 14.92 | 13.60 | 12.98 | 14.35 | × |
| | 1× hill climbing | 49.3 | 219 | 4.36 | 2.53 | 5.82 | 4.00 | 4.18 | ✓ |
| | 2× hill climbing | 32.8 | 149 | 3.92 | 2.47 | 5.09 | 3.72 | 3.80 | ✓ |
| IVC-LA-RLPV | isocentre-supine | | | 21.88 | 20.55 | 19.60 | 18.57 | 20.15 | × |
| | 1× hill climbing | 185.6 | 870 | 1.42 | 1.24 | 2.54 | 2.20 | 1.85 | ✓ |
| | 2× hill climbing | 127.2 | 703 | 1.34 | 1.25 | 2.43 | 2.22 | 1.81 | ✓ |
| average | isocentre-supine | | | 18.90 | 17.74 | 16.60 | 15.78 | 17.25 | × |
| | 1× hill climbing | 117.5 | 545 | 2.89 | 1.89 | 4.18 | 3.10 | 3.02 | ✓ |
| | 2× hill climbing | 80.7 | 426 | 2.63 | 1.86 | 3.76 | 2.97 | 2.81 | ✓ |

Table 7.3 – Biplane looped-catheter-based image registration algorithm applied to data taken from CT and X-ray images of the plastic heart model. Two variations of the algorithm were applied based on two catheter loop configurations with the isocentre-supine constraint as the initial starting point of registration. Time taken (*t*) and number of iterations (#) were recorded for each registration, along with the accuracy in terms of a mean 3D-TRE over the four chambers of the heart (LA, LV, RA, RV) and over the whole heart (WH). A check (✓) is given to the registration if the accuracy was below the desired clinical tolerance of 5 mm, and a cross (×) if it was not, under the test column T.

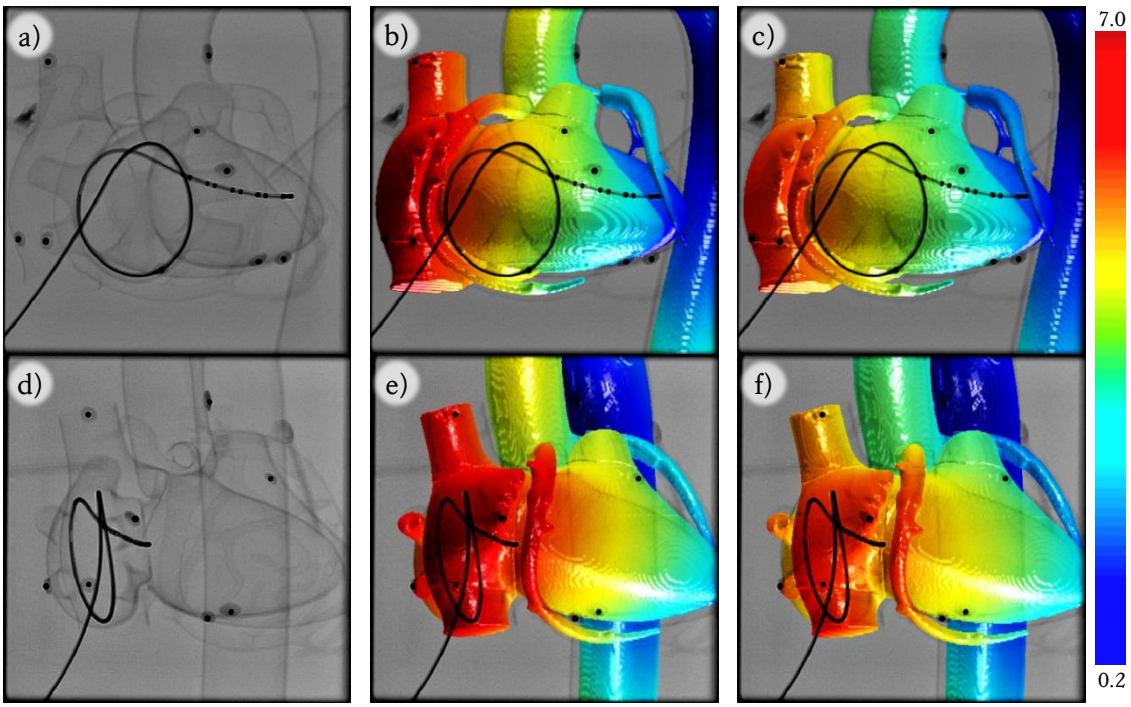


Figure 7.10) Visual representation of registration results using the b, e) biplane 1×BNHC strategy and c, f) the biplane 2×BNHC strategy applied to the first looped catheter configuration. Colour mapping of the CT data surface rending shows the spatial distribution of 3D-TRE. The data is overlaid onto X-ray in a, b, c) PA and d, e, f) RAO 45° views.

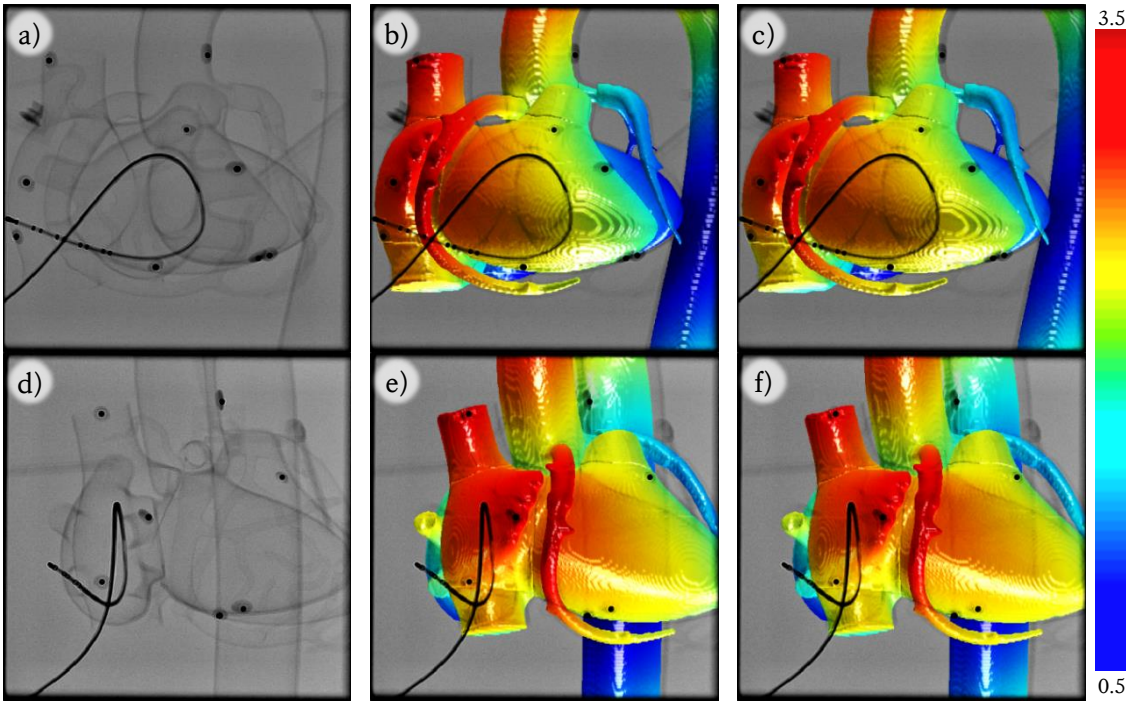


Figure 7.11) Same as Figure 7.10 using the second looped catheter configuration.

#### 7.3.1.2. Robustness of Biplane Registration of Plastic Phantom Data

Robustness analysis was performed on the plastic heart phantom for both catheter configurations, and for both the 1× and 2×BNHC strategies. Registration with the 1×BNHC approach had an average 5-mm capture range of 9.65 mm (Figure 7.12), and the 2×BNHC

approach had an average range of 7.79 mm (Figure 7.13). Individual capture ranges are shown in Table 7.4.

| configuration | registration | *X*-mm capture range (mm) | | | | | |
|---|---|---|---|---|---|---|---|
| | | 5 | 6 | 7 | 8 | 9 | 10 |
| IVC-LA-LUPV | 1× hill climbing | 13.83 | 20.34 | 24.39 | 24.99 | > 25 | > 25 |
| | 2× hill climbing | 9.45 | 24.89 | > 25 | > 25 | > 25 | > 25 |
| IVC-LA-RLPV | 1× hill climbing | 5.48 | 8.20 | 16.75 | > 25 | > 25 | > 25 |
| | 2× hill climbing | 6.13 | 11.32 | 16.02 | 19.97 | > 25 | > 25 |
| average | 1× hill climbing | 9.65 | 14.27 | 20.57 | > 25 | > 25 | > 25 |
| | 2× hill climbing | 7.79 | 18.11 | 21.01 | 22.98 | > 25 | > 25 |

Table 7.4 – 5- to 10-mm capture ranges measured for the four biplane registrations.

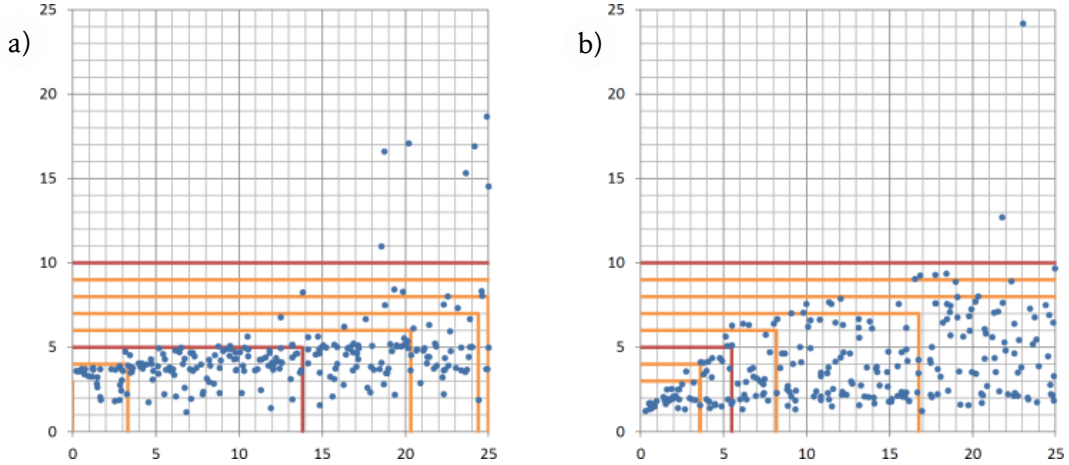


Figure 7.12) Plots of output vs. input mean 3D-TRE (WH) in mm for 1×BNHC approaches applied to a) the first catheter loop configuration IVC-LA-LUPV, and to b) the second configuration IVC-LA-RLPV. Red lines indicate where 95% of the registrations before the vertical line successfully registered with accuracy within 5-mm and 10-mm mean 3D-TRE (WH), while orange lines indicate the same but at 3-, 4-, 6-, 7-, 8- and 9-mm TREs.

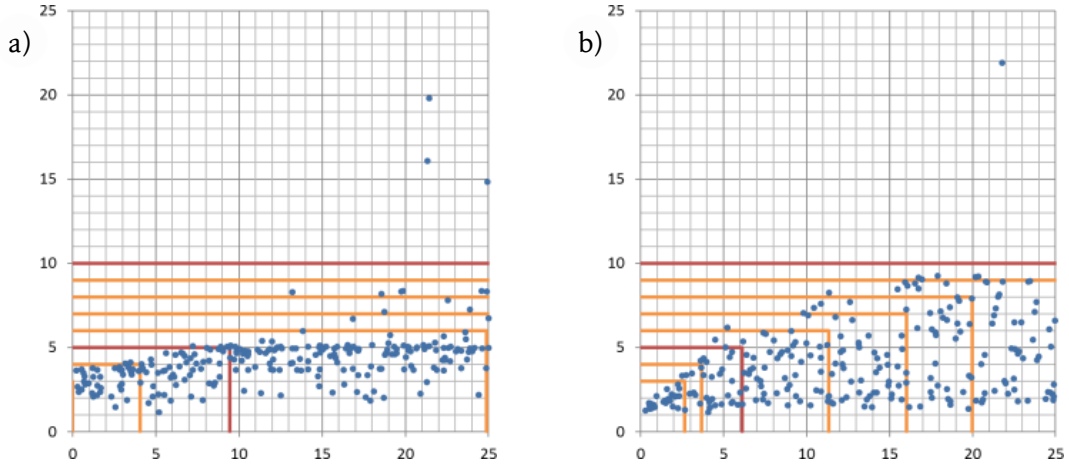


Figure 7.13) Same as Figure 7.12 but with the 2×BNHC approach.

#### 7.3.1.3. Accuracy of Monoplane Registration of Plastic Phantom Data

For monoplane registration, the accuracy of $\mathcal{M}_{\text{iso-sup}}$ was 9.67 mm mean RPD over the whole heart, averaged over the four views of the two looped-catheter configurations. Using this as an initial starting point, registration was performed for both catheter configurations, both monoplane views and both BNHC optimisation strategies, totalling eight registrations. Registration with the 1×BNHC approach had a mean RPD of 7.17 mm over the WH, and the 2×BNHC approach had a mean RPD of 4.47 mm. 2D-3D overlays are shown in Figure 7.14 and Figure 7.15 using the first and second catheter loop configurations as registration constraints respectively. Individual accuracies in terms of mean RPDs over the WH and over the individual chambers for the eight monoplane registrations are listed in Table 7.5.

| configuration | view | registration | t (s) | # | mean RPD (mm) | | | | | T |
|---|---|---|---|---|---|---|---|---|---|---|
| | | | | | LA | LV | RA | RV | WH | |
| IVC-LA-LUPV | L | isocentre-supine | | | 7.77 | 9.69 | 8.28 | 10.31 | 9.01 | × |
| | | 1× hill climbing | 18.6 | 161 | 3.06 | 1.72 | 3.73 | 3.26 | 2.94 | ✓ |
| | | 2× hill climbing | 20.8 | 283 | 1.78 | 1.30 | 2.51 | 1.52 | 1.78 | ✓ |
| | R | isocentre-supine | | | 8.79 | 9.08 | 7.47 | 8.05 | 8.35 | × |
| | | 1× hill climbing | 23.2 | 219 | 4.70 | 4.13 | 4.83 | 3.02 | 4.17 | ✓ |
| | | 2× hill climbing | 4.3 | 21 | 3.59 | 2.56 | 2.97 | 1.62 | 2.69 | ✓ |
| IVC-LA-RLPV | L | isocentre-supine | | | 8.16 | 10.47 | 8.58 | 11.01 | 9.55 | × |
| | | 1× hill climbing | 12.4 | 101 | 5.34 | 10.63 | 13.12 | 19.87 | 12.24 | × |
| | | 2× hill climbing | 24.9 | 286 | 6.37 | 3.16 | 3.32 | 6.32 | 4.79 | ✓ |
| | R | isocentre-supine | | | 12.86 | 12.51 | 10.89 | 10.80 | 11.77 | × |
| | | 1× hill climbing | 22.7 | 201 | 10.70 | 10.57 | 7.89 | 8.17 | 9.33 | × |
| | | 2× hill climbing | 8.8 | 66 | 9.80 | 9.46 | 7.66 | 7.61 | 8.63 | × |
| average | | isocentre-supine | | | 9.40 | 10.44 | 8.81 | 10.04 | 9.67 | × |
| | | 1× hill climbing | 19.5 | 171 | 5.95 | 6.76 | 7.39 | 8.58 | 7.17 | × |
| | | 2× hill climbing | 15.0 | 164 | 5.39 | 4.12 | 4.12 | 4.27 | 4.47 | ✓ |

Table 7.5 – Two variations of the monoplane registration algorithm applied to data from images of the plastic heart model on two catheter loop configurations with the isocentre-supine constraint as the initial starting point of registration. Time taken ($t$) and number of iterations (#) were recorded for each registration, along with the accuracy in terms of a mean 3D-TRE over the four chambers of the heart (LA, LV, RA, RV) and over the whole heart (WH). A ✓ denotes accuracy within 5 mm.

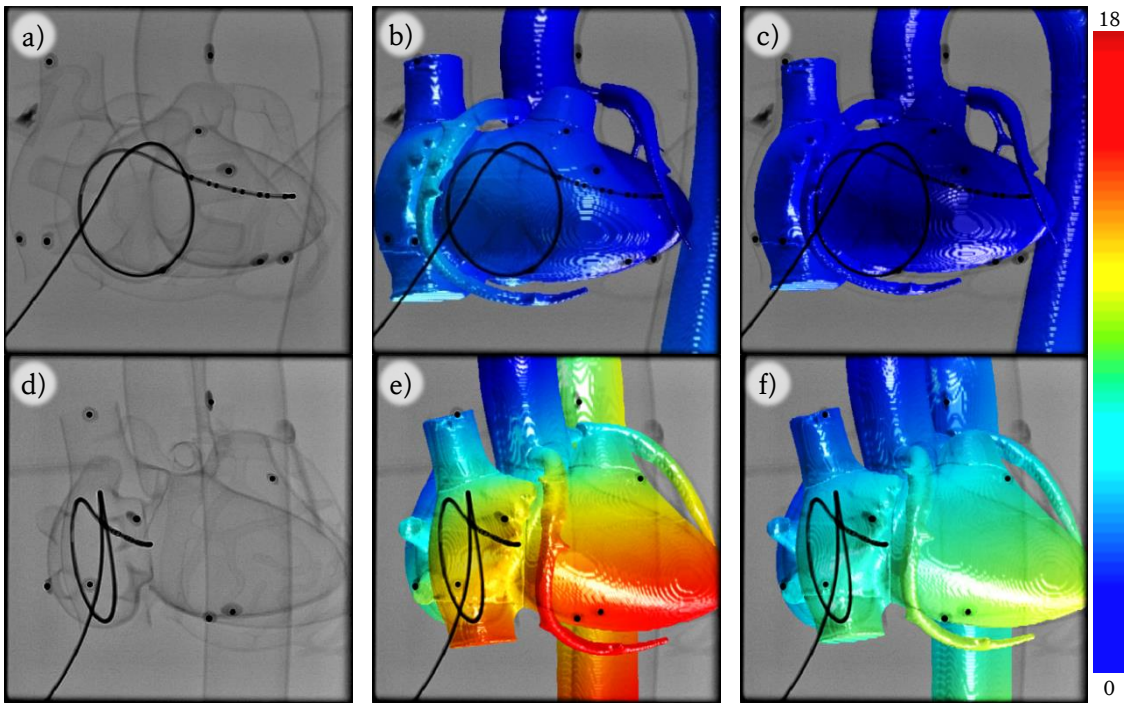


Figure 7.14) Visual representation of registration results using the b, e) monoplane 1×BNHC strategy and c, f) monoplane 2×BNHC strategy applied to the first looped catheter configuration. Colour mapping of the CT data surface rending shows the spatial distribution of RPD. The data is overlaid onto X-ray in a, b, c) PA and d, e, f) RAO 45° views.

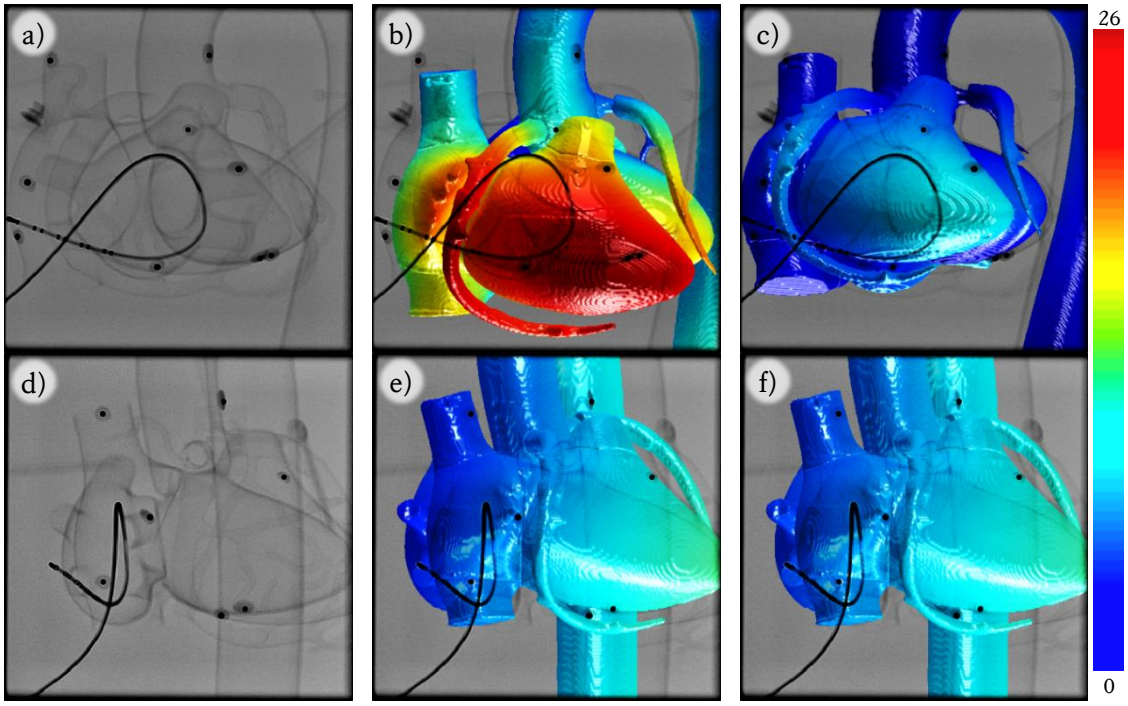


Figure 7.15) Same as Figure 7.14 but using the second looped catheter configuration.

#### 7.3.1.4. Robustness of Monoplane Registration of Plastic Phantom Data

Robustness of monoplane registration was assessed for all eight combinations of X-ray view, looped catheter-configuration and optimisation-strategy. Registration with the 1×BnHC approach had a 5-mm capture range of 7.67 mm, averaged over the PA (Figure 7.16) and RAO 45° (Figure 7.17) views and over the two looped-catheter configurations, while registration with the 2×BNHC approach had a 6.05-mm average capture range (Figure 7.18, Figure 7.19). Individual capture ranges are listed in Table 7.6.

| configuration | view | registration | *X*-mm capture range (mm) | | | | | | T |
|---|---|---|---|---|---|---|---|---|---|
| | | | 5 | 6 | 7 | 8 | 9 | 10 | |
| IVC-LA-LUPV | L | 1× hill climbing | 12.06 | 12.29 | 12.92 | 16.04 | 20.67 | 22.54 | ✗ |
| | L | 2× hill climbing | 8.68 | 8.68 | 13.03 | 13.41 | 17.93 | 24.48 | ✗ |
| | R | 1× hill climbing | 6.19 | 18.34 | 21.38 | 24.31 | > 25 | > 25 | ✗ |
| | R | 2× hill climbing | 2.77 | 19.26 | 24.32 | > 25 | > 25 | > 25 | ✓ |
| IVC-LA-RLPV | L | 1× hill climbing | 8.46 | 10.34 | 12.49 | 12.49 | 12.54 | 20.57 | ✗ |
| | L | 2× hill climbing | 8.26 | 10.34 | 11.05 | 11.41 | 11.41 | 12.81 | ✗ |
| | R | 1× hill climbing | 3.96 | 7.98 | 9.50 | 11.55 | 15.17 | 18.61 | ✓ |
| | R | 2× hill climbing | 4.48 | 6.13 | 9.50 | 10.70 | 18.23 | 23.23 | ✓ |
| average | | 1× hill climbing | 7.67 | 10.41 | 12.37 | 13.34 | 15.64 | 20.10 | ✗ |
| | | 2× hill climbing | 6.05 | 11.10 | 14.48 | 11.84 | 15.86 | 20.17 | ✗ |

Table 7.6 – Capture range (CR) measured for the eight monoplane registrations. A check (✓) under the test (T) column represents the 5-mm capture range being over 5 mm, and a cross (✗) indicates that it is not. Capture ranges greater than 25 mm are counted as 25 mm for averaging purposes.

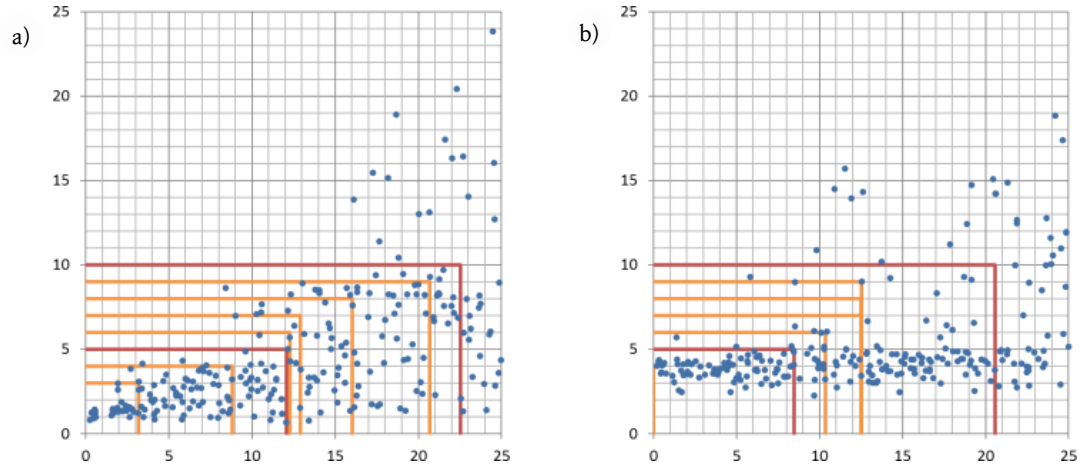


Figure 7.16) Plots showing output vs. input accuracy (mm), with orange and red boxes indicating the capture range of the 1×BNHC variation of the algorithm applied using the a) first and b) second looped catheter constraint in PA X-ray view.

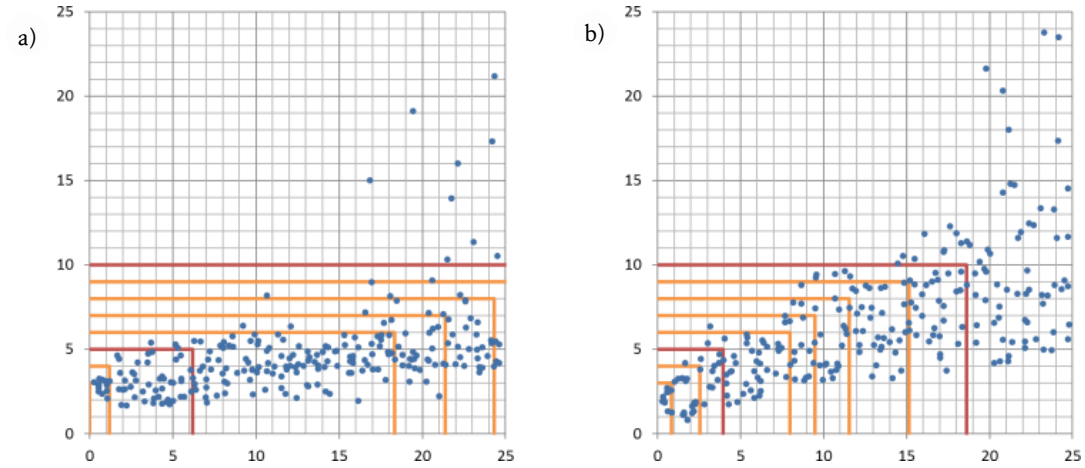

Figure 7.17) Same as Figure 7.15 but in RAO 45˚ view.

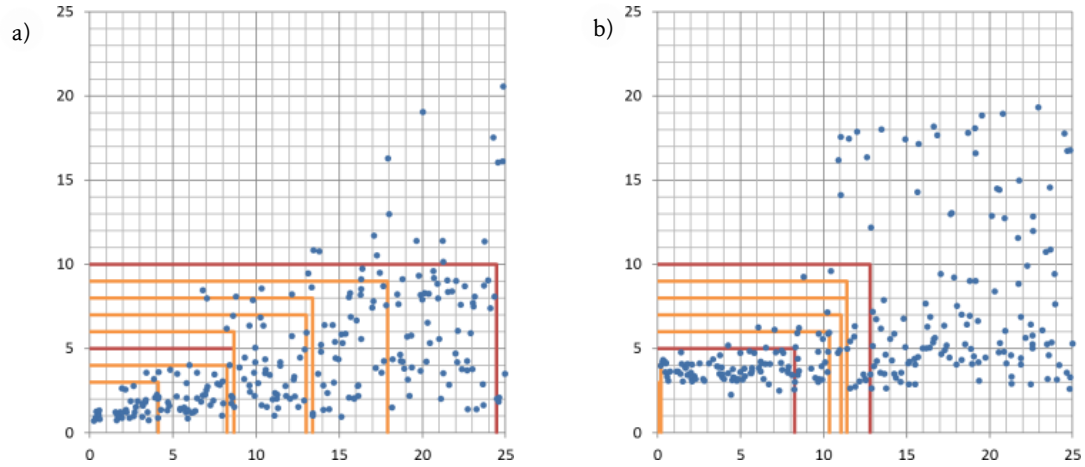

Figure 7.18) Same as Figure 7.16 but with the 2×BNHC optimisation strategy.

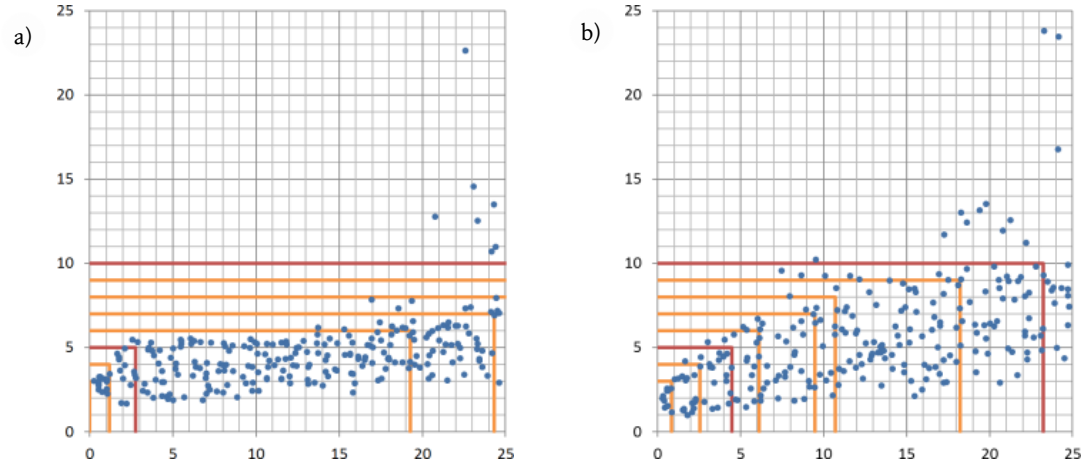

Figure 7.19) Same as Figure 7.21 but in RAO 45˚ view.

### 7.3.2. Looped-Catheter-Based 2D-3D Registration of *Ex Vivo* Porcine Heart Data

The registration algorithm was used to register both MR and 3DRx tomographic scans of the porcine heart onto PA and RAO 45˚ X-ray views in both biplane and monoplane modes. Six

fiducial markers placed on the bucket containing the heart provided a gold standard X-ray-MR and X-ray-3DRx registrations with FREs of 1.47 mm and 1.65 mm respectively.

#### 7.3.2.1. Accuracy of Biplane Registration of Ex Vivo Porcine Heart Data

The isocentre-supine constraint provided an initial starting point for the algorithm with 13.02-mm mean 3D-TRE (WH) with respect to the gold standard. Registrations using the first catheter-loop configuration DAo-LV are shown as overlays in Figure 7.20, and using the second configuration SVC-RA in Figure 7.21. The overlays in Figure 7.20 and Figure 7.21 show a spatial distribution of 3D-TRE over the heart and use the same colour scale for visual comparison across all 16 overlays. Poor registration can be quickly spotted as having a dominantly red colour. On average, the 1×BNHC yielded an average accuracy of 6.53-mm TRE while the 2×BNHC yielded an average accuracy of 4.63 mm. Individual accuracies are listed in Table 7.7.

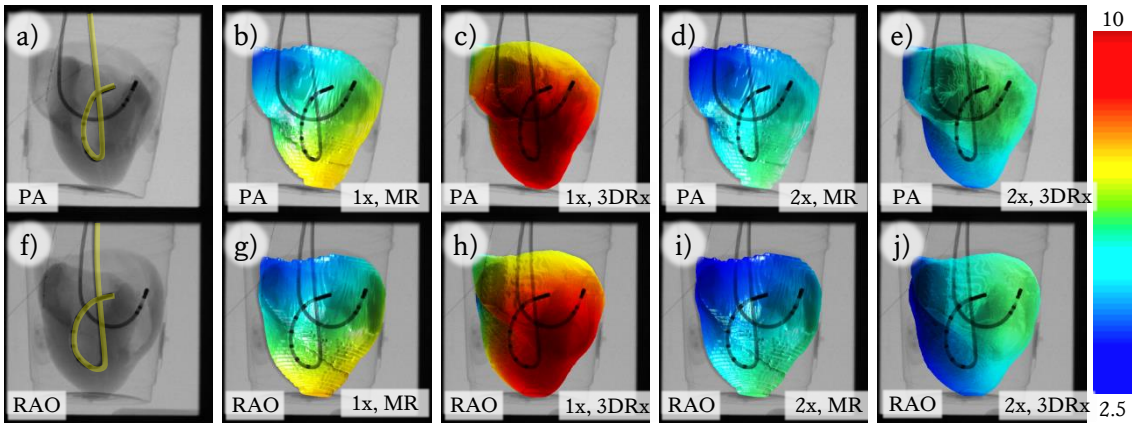


Figure 7.20) Visual representation of registration results using the b, c, g, h) biplane 1×BNHC strategy and d, e, i, j) biplane 2×BNHC strategy applied to the first looped catheter configuration. Colour mapping of the CT data surface rending shows the spatial distribution of RPD. The data is overlaid onto X-ray in a, b, c, d, e) PA and f, g, h, i, j) RAO 45˚ views.

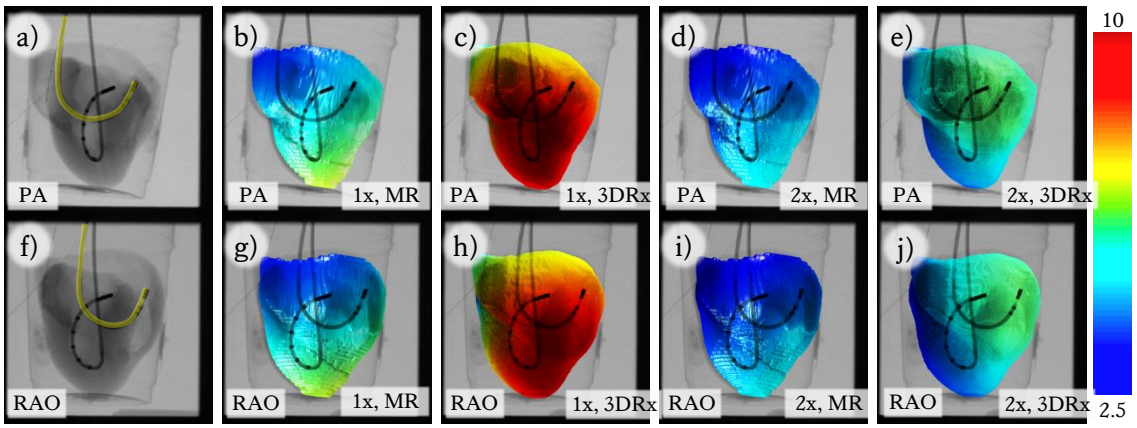


Figure 7.21) Same as Figure 7.20 but using the catheter inside the RV.

| configuration | registration | $t$ (s) | # | mean 3D-TRE (mm) | | | | | T |
|---|---|---|---|---|---|---|---|---|---|
| | | | | LA | LV | RA | RV | WH | |
| MR DAo-LV | isocentre-supine | | | 10.03 | 9.91 | 9.79 | 9.71 | 9.86 | × |
| | 1× hill climbing | 22.4 | 200 | 6.10 | 6.42 | 5.83 | 6.12 | 6.12 | × |
| | 2× hill climbing | 45.4 | 416 | 4.46 | 4.82 | 4.71 | 4.96 | 4.74 | ✓ |
| MR SVC-RV | isocentre-supine | | | 10.03 | 9.91 | 9.79 | 9.71 | 9.86 | × |
| | 1× hill climbing | 27.6 | 232 | 5.28 | 5.58 | 5.01 | 5.28 | 5.29 | × |
| | 2× hill climbing | 33.8 | 294 | 3.78 | 4.11 | 4.03 | 4.26 | 4.05 | ✓ |
| 3DRx DAo-LV | isocentre-supine | | | 15.68 | 15.80 | 16.56 | 16.69 | 16.18 | × |
| | 1× hill climbing | 50.3 | 138 | 6.21 | 7.02 | 7.85 | 8.33 | 7.35 | × |
| | 2× hill climbing | 32.4 | 87 | 4.19 | 4.38 | 5.38 | 5.53 | 4.87 | ✓ |
| 3DRx SVC-RV | isocentre-supine | | | 15.68 | 15.80 | 16.56 | 16.69 | 16.18 | × |
| | 1× hill climbing | 54.6 | 138 | 6.21 | 7.02 | 7.85 | 8.33 | 7.35 | × |
| | 2× hill climbing | 35.1 | 87 | 4.19 | 4.38 | 5.38 | 5.53 | 4.87 | ✓ |
| average | isocentre-supine | | | 12.86 | 12.86 | 13.18 | 13.20 | 13.02 | × |
| | 1× hill climbing | 38.73 | 177 | 5.95 | 6.51 | 6.64 | 7.02 | 6.53 | × |
| | 2× hill climbing | 36.68 | 221 | 4.16 | 4.42 | 4.88 | 5.07 | 4.63 | ✓ |

Table 7.7 – Biplane looped-catheter-based registration applied to MR, 3DRx and X-ray data of the porcine heart. Two variations of the algorithm were applied on two catheter loop configurations using isocentre-supine initialisation. Time taken ($t$) and number of iterations (#) were recorded for each registration, along with the accuracy in terms of a mean 3D-TRE over the four chambers of the heart (LA, LV, RA, RV) and over the whole heart (WH). A ✓ is given to the registration if the accuracy was below the desired clinical tolerance of 5 mm, and a × if it was not, under the test column T.

#### 7.3.2.2. Accuracy of Monoplane Registration of Ex Vivo Porcine Heart Data

For monoplane registration, the isocentre-supine constraint started the registration with a 10.57-mm TRE, on average. The first looped-catheter-configuration overlays are shown in Figure 7.22, and Figure 7.23 shows the second.

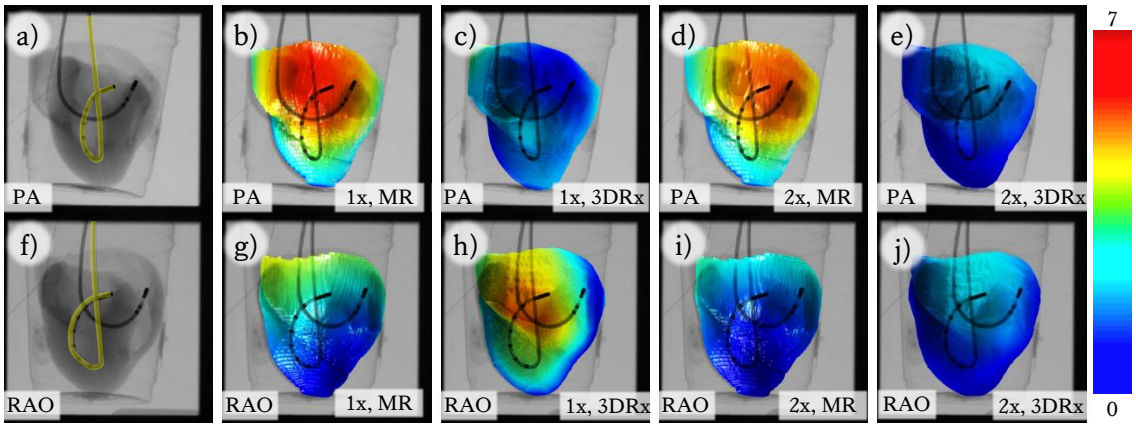


Figure 7.22) Visual representation of registration results using the b, c, g, h) monoplane 1×BNHC strategy and d, e, i, j) monoplane 2×BNHC strategy applied to the first looped catheter configuration. Colour mapping of the CT data surface rending shows the spatial distribution of RPD. The data is overlaid onto X-ray in a, b, c, d, e) PA and f, g, h, i, j) RAO 45° views.

The overlays in these two figures show a spatial distribution of RPD over the heart and use the same colour scale for visual comparison across all 16 overlays. Poor registration can be quickly spotted as having a dominantly red colour. The 1×BNHC yielded an average accuracy of 2.64-mm RPD while the 2×BNHC yielded an average accuracy of 1.85 mm. Individual accuracies are listed in Table 7.8.

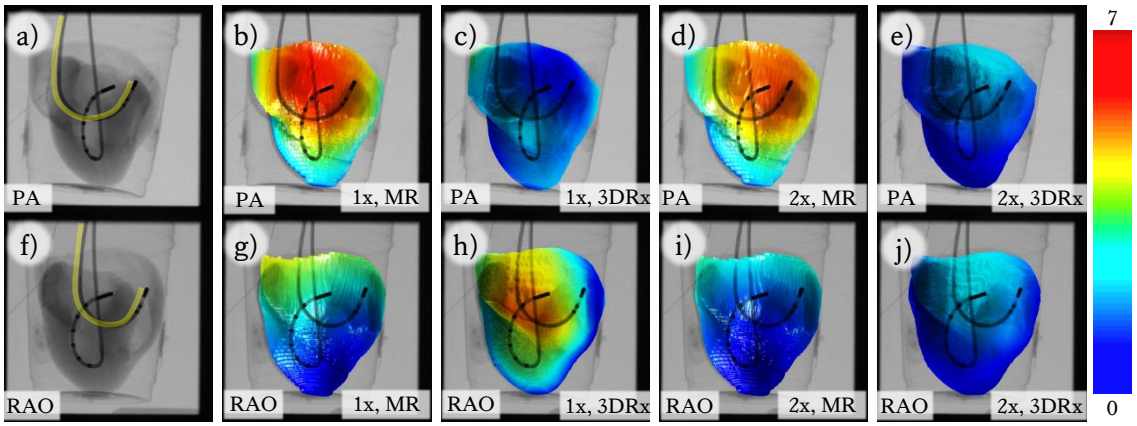

Figure 7.23) Same as Figure 7.22 but using the second catheter loop configuration.

| configuration | view | registration | t (s) | # | mean RPD (mm) LA | RV | RA | RV | WH | T |
|---|---|---|---|---|---|---|---|---|---|---|
| MR DAo-LV | L | isocentre-supine | | | 5.58 | 5.68 | 5.96 | 6.00 | 5.80 | × |
| | | 1× hill climbing | 21.1 | 387 | 1.65 | 1.96 | 3.86 | 3.78 | 2.81 | ✓ |
| | | 2× hill climbing | 43.1 | 940 | 2.36 | 2.42 | 3.68 | 3.58 | 3.01 | ✓ |
| | R | isocentre-supine | | | 8.39 | 8.48 | 8.54 | 8.60 | 8.50 | × |
| | | 1× hill climbing | 8.6 | 147 | 2.32 | 2.11 | 2.68 | 2.41 | 2.38 | ✓ |
| | | 2× hill climbing | 20.3 | 473 | 2.05 | 1.82 | 2.04 | 1.79 | 1.93 | ✓ |
| MR SVC-RV | L | isocentre-supine | | | 5.58 | 5.68 | 5.96 | 6.00 | 5.80 | × |
| | | 1× hill climbing | 5.2 | 76 | 2.20 | 2.31 | 3.70 | 3.60 | 2.95 | ✓ |
| | | 2× hill climbing | 7.7 | 119 | 2.20 | 2.25 | 3.41 | 3.29 | 2.79 | ✓ |
| | R | isocentre-supine | | | 8.39 | 8.48 | 8.54 | 8.60 | 8.50 | × |
| | | 1× hill climbing | 7.5 | 115 | 2.43 | 2.22 | 2.71 | 2.46 | 2.45 | ✓ |
| | | 2× hill climbing | 18.5 | 314 | 2.85 | 2.59 | 2.18 | 1.99 | 2.40 | ✓ |
| RX DAo-LV | L | isocentre-supine | | | 13.52 | 13.61 | 14.38 | 14.48 | 13.99 | × |
| | | 1× hill climbing | 15.1 | 76 | 2.91 | 2.73 | 1.84 | 1.98 | 2.37 | ✓ |
| | | 2× hill climbing | 21.5 | 128 | 0.73 | 0.89 | 1.35 | 1.49 | 1.12 | ✓ |
| | R | isocentre-supine | | | 13.54 | 13.65 | 14.32 | 14.44 | 13.99 | × |
| | | 1× hill climbing | 16.2 | 82 | 2.93 | 2.99 | 2.64 | 3.08 | 2.91 | ✓ |
| | | 2× hill climbing | 22.3 | 124 | 0.83 | 1.01 | 1.43 | 1.61 | 1.22 | ✓ |
| RX SVC-RV | L | isocentre-supine | | | 13.52 | 13.61 | 14.38 | 14.48 | 13.99 | × |
| | | 1× hill climbing | 16.5 | 76 | 2.91 | 2.73 | 1.84 | 1.98 | 2.37 | ✓ |
| | | 2× hill climbing | 23.2 | 128 | 0.73 | 0.89 | 1.35 | 1.49 | 1.12 | ✓ |
| | R | isocentre-supine | | | 13.54 | 13.65 | 14.32 | 14.44 | 13.99 | × |
| | | 1× hill climbing | 17.8 | 82 | 2.93 | 2.99 | 2.64 | 3.08 | 2.91 | ✓ |
| | | 2× hill climbing | 24.4 | 124 | 0.83 | 1.01 | 1.43 | 1.61 | 1.22 | ✓ |
| average | | isocentre-supine | | | 10.26 | 10.36 | 10.80 | 10.88 | 10.57 | × |
| | | 1× hill climbing | 13.5 | 130 | 2.54 | 2.51 | 2.74 | 2.80 | 2.64 | ✓ |
| | | 2× hill climbing | 22.6 | 294 | 1.57 | 1.61 | 2.11 | 2.11 | 1.85 | ✓ |

Table 7.8 – Same as Table 7.7 but with monoplane registration.

## 7.4. Clinical Catheterisation Example

Based on the non-clinical experiments, the algorithm was demonstrated on a clinical dataset (Figure 7.24) taken from a cardiac catheterisation of a patient who underwent pulmonary vein isolation for LAF.

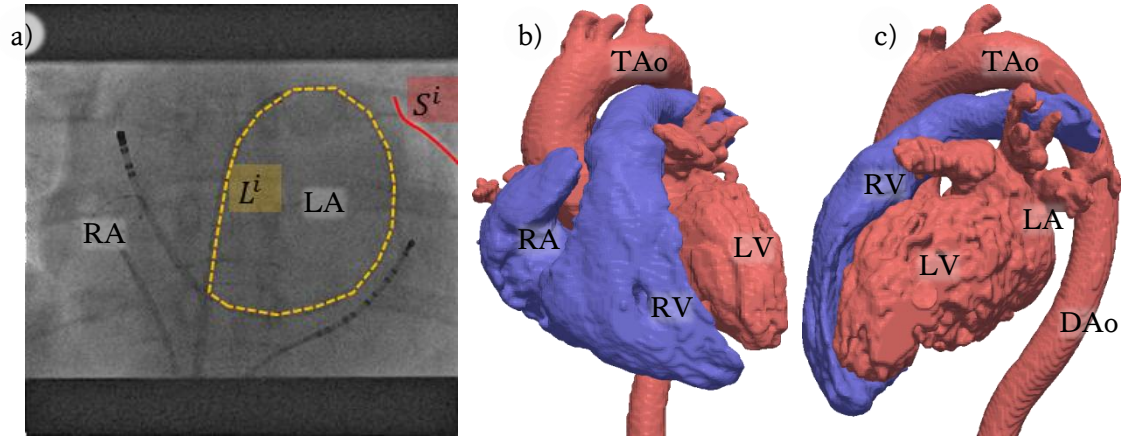


Figure 7.24 a) PA X-ray view of the patient's heart with a catheter inserted via the IVC and looped inside the LA. Both loop $L^i$ and upper cardiac border $S^i$ are manually segmented. Surface rendering of the heart obtained from MR image segmentation and triangulation is shown in b) AP and c) left lateral views. Different parts of the left (*light red*) and right (*light blue*) heart are labelled, including the transverse aorta (TAo).

### 7.4.1. Preoperative Imaging and Information Extraction

Prior to catheterisation, the patient underwent a tomographic Gadolinium-enhanced cardiac MR scan ($384^2 \times 120$ voxels, $0.8854^2 \times 1.2$ mm$^3$ resolution; Achieva, Philips Medical Systems) using a parallel imaging technique (SENSE, NEX = 1, TE = 1.158 ms, TR = 3.726 ms, θ = 40°). The chambers and great vessels of the heart were segmented and triangulated using ITK-SNAP [112]. Vertices of the LV and RV were used as $\{\vec{U}_j^{3D}\}$ and $\{\vec{W}_j^{3D}\}$ respectively in (7.7) and (7.8). Since the LA was the target vessel, vertices of its triangulation from the preoperative step were used as $\{\vec{C}_j^{3D}\}$ in (7.2).

### 7.4.2. Intraoperative Imaging and Information Extraction

During intervention, a catheter was inserted into the LA, via the IVC, where it formed a loop around its interior wall and eventually exited into the SVC. An fluoroscopy video ($512^2$ pixels, $(0.342 \text{ mm})^2$ resolution; SOD = 765 mm, SID = 988 mm) of the heart, lasting approximately four seconds, was acquired with a tracked and precalibrated fluoroscope (Allura Xper, Philips Medical Systems) in PA view with the catheter loop readily visible. The X-ray frame that corresponded to when the cardiorespiratory cycle was simultaneously at end-diastole and end-expiration was the frame used to manually extract the loop and upper cardiac border using the software titled Sara (§4.2.2) for use as $L^i$ and $S^i$ in (7.4) and (7.15) respectively.

### 7.4.3. Looped-Catheter-Based Image Registration

Since only one X-ray view was available, only monoplane registration could be performed. The isocentre-supine constraints provided the initial starting point for two looped-catheter-based registrations, one using the 1×BNHC optimisation strategy and the other using the 2×BNHC strategy.

As no gold standard registration was available, accuracy of registration was manually and independently estimated by a clinical expert. The expert was provided with eight X-ray images of the heart with the loop inserted into the target chamber in PA view. Six of the images were each overlaid with one of the LA, LV, RA, RV, Ao or pulmonary trunk surface renderings segmented from MR, while one of the images had all of the six segmentations overlaid. The last of the eight images had no overlay. The expert was asked to assess the accuracy of each chamber of the whole heart in terms of a maximum and mean 2D-TRE using scales drawn on each image (§6.4.2).

### 7.4.4. Clinical Catheterisation Results

The looped-catheter-based registration was applied to the clinical dataset to provide overlays on the X-ray images (Figure 7.25). The images and overlays were formatted as described in the previous chapter and presented to a clinical expert for accuracy estimations, listed in Table 7.9.

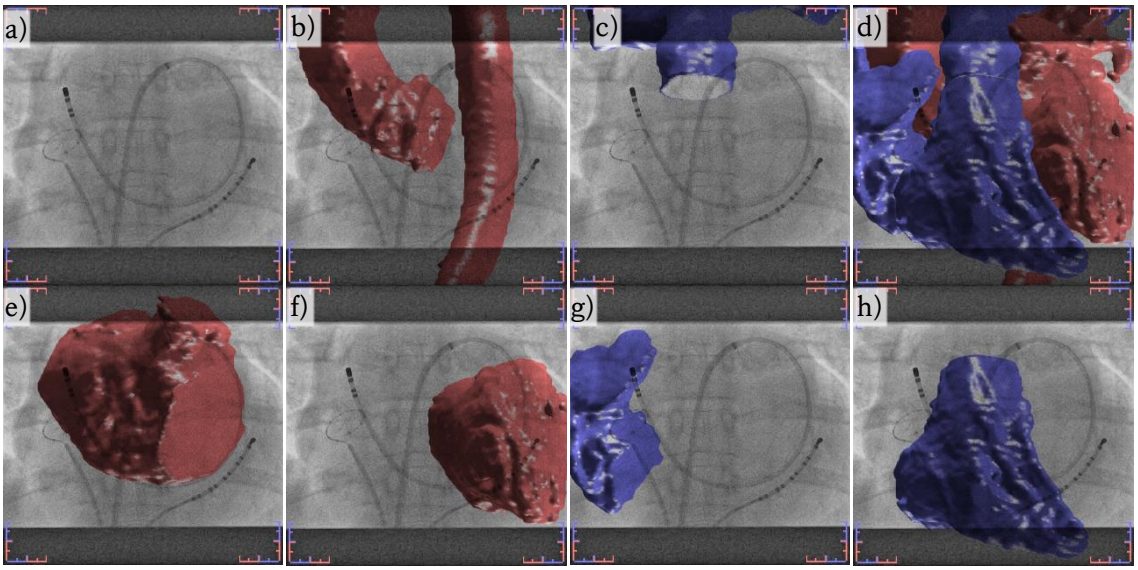


Figure 7.25 a) PA X-ray view of the patient's heart with catheter loop inserted into the LA. Surface renderings of the heart segmented from the preoperative MR scan are overlaid onto the X-ray based on the looped-catheter-based 2×BNHC registration method. Parts of the heart overlaid are b) Ao (*red*), c) pulmonary artery (*blue*), d) WH (*red and blue*), e) LA (*red*), f) LV (*red*), g) RA (*blue*), h) RV (*blue*). Scales drawn at the corners of each image, representing 1-cm between each major tick, allow estimation of the overlay accuracy in terms of a mean and maximum 2D-TRE.

| Reg. | 2D-TRE (mm) | | | | | | | | | |
|---|---|---|---|---|---|---|---|---|---|---|
| | LA | | LV | | RA | | RV | | WH | |
| | mean | max. | mean | max. | mean | max. | mean | max. | mean | max. |
| Isocentre-supine | 20.0 | 27.0 | 22.0 | 29.0 | 21.0 | 28.0 | 20.0 | 27.0 | 21.0 | 28.0 |
| 1×BNHC | 5.0 | 10.0 | 7.5 | 15.0 | 17.5 | 25.0 | 7.5 | 15.0 | 9.4 | 25.0 |
| 2×BNHC | 7.5 | 12.5 | 7.5 | 15.0 | 17.5 | 27.5 | 7.5 | 15.0 | 10.0 | 27.5 |

Table 7.9 – Estimation of registration accuracy of the four chambers of the heart for the isocentre-supine constraint and for the two variations of the looped-catheter-based registration algorithm by a clinical expert by visually inspecting X-ray-MR overlays. The WH mean is determined by an arithmetic average of the four chambers, and the maximum (max.) is taken as the maximum of the four chambers.

## 7.5. Discussion

In this chapter, a 2D-3D image registration algorithm was developed to overlay 3D CT, MR and 3DRx data onto X-ray images of the heart to act as a roadmap for catheter navigation in cardiac catheterisation procedures. The data alignment was achieved by using a catheter looped inside a target chamber and the upper cardiac border as registration constraints. The algorithm registers the data by projecting the segmented chambers onto the X-ray views available, and maximises the area of intersection between the projected target chamber and catheter loop, while minimizing the gap formed between the upper border of the cardiac shadow and the projected ventricles. Using isocentre and supine constraints, an initial estimate RBT is established to align the 3D preoperative data to the X-rays, and subsequently uses two variations of the best neighbour ascent hill climbing search strategy.

To test this algorithm, two non-clinical experiments were carried out on phantom and porcine heart experiments which were designed to emulate the clinical workflow in order to assess the accuracy and robustness of the registration algorithm.

The looped catheter was chosen as a constraint to take advantage of a common technique in cardiac catheterisation procedures which involves the looping of a catheter inside the target chamber of interest where it remains for duration of the procedure. Since the catheter has clearly visible in fluoroscopy images, this acts as a quick visual reference for the interventionalist when navigating other catheters into the heart. The catheter loop has also been demonstrated to provide a good reference for manual 2D-3D registration [23].

### 7.5.1. One-stage vs. Two-stage Hill Climbing: Accuracy

With the one-stage hill climbing approach, registration of the phantom data between CT and biplane X-ray yielded an accuracy of 3.02 mm mean 3D-TRE over the whole heart (WH), averaged over both catheter configurations. Registration with the porcine heart data yielded an accuracy of 6.53 mm, averaged over all configurations, which was outside the 5-mm clinical tolerance. When registering with the two-stage approach, accuracy was greater, with an average

TRE of 2.81 mm for the plastic heart and 4.63 mm for the porcine heart, with all six configurations achieving accuracy within the 5-mm clinical tolerance.

For monoplane registration, the one-stage strategy resulted in an average RPD of 7.17 mm for the plastic heart, and 2.64 mm for the porcine heart. Ten out of twelve of these registrations had accuracy within the 5-mm clinical tolerance. With the two-stage strategy, the average RPD was 4.47 mm for the plastic heart and 1.85 mm for the porcine heart, with eleven out of twelve registrations having accuracy within the 5-mm threshold.

For both mono- and biplane registrations, the two-stage strategy consistently performed better than the one-stage strategy. One possible reason is that the initial registration error due to the isocentre-supine constraint may contain a larger translational component than angular components. This may lead to large adjustments in rotations which may be an erroneous assumption by the optimising strategy. This issue can be avoided by first optimising for only the translational component, before optimising for both translational and rotational components, as in the two-stage approach. Another reason is that in the two-stage approach, when switching between the two stages, the increments are reset to the initial value of (2 mm, 2 mm, 2 mm, 3.5˚, 3.5˚, 3.5˚), commonly known as a *reset*. Resetting the optimisation strategy has the benefit of escaping potential local maxima if it was trapped in one.

### 7.5.2. One-stage vs. Two-stage Hill Climbing: Robustness

In terms of robustness, the biplane one-stage hill climbing approach had an average capture range of 9.65 mm where 95% of registrations were within the 5-mm clinical tolerance for ablations, while the biplane two-stage approach had an average capture range of 7.8 mm. For monoplane registrations, the one-stage approach had average 5-mm capture ranges of 7.7 mm for the one-stage approach and 6.0 mm for the two stage approach. Registration with accuracies within the 10-mm clinical tolerance, while not particularly suitable for ablation procedures, may still be deemed useful in catheterisation procedures to provide visual insight into the procedure. The 10-mm capture range for the biplane registrations, in both hill climbing variations, was larger than 25 mm, which was the testing limit of this analysis, while for monoplane registrations, the 10-mm capture ranges were 20 mm for both one- and two-stage strategies.

### 7.5.3. Initialisation Dependence

Since a local iterative approach was taken for this algorithm, an initial guess registration is required. When the algorithm is used to provide an initial registration, the initial guess is provided by the isocentre-supine constraint starting point accuracies. Starting accuracies of this constraint were a 3D-TRE of 14.43 mm and RPD of 10.27 mm. These TRE and RPD figures are larger than the 5-mm-capture range, but below the 10-mm-capture range. This means that

the algorithm is likely to produce registrations with accuracies between 5-mm and 10-mm, unless there is a good isocentre-supine constraint, in which case, the algorithm is likely to register to within an accuracy of 5-mm.

### 7.5.4. Catheter Configuration Dependence

In the plastic heart experiment, results show that the LUPV configuration yielded lower TREs than the RLPV configuration for all regions of interest for monoplane registrations. A possibility is that while the target chamber was the same size in both configurations, the catheter loop formed in PA in the RLPV configuration was only 1459 $mm^2$ while the in the LUPV configuration the loop was 1900 $mm^2$, suggesting that the larger the catheter loop, the better constraint the loop and chamber can provide, resulting in a more accurate registration. There is stronger evidence in the plastic heart experiment when comparing monoplane accuracy and robustness, as registering with the PA performs better than registering with the RAO 45˚ views, but only for the two-stage. In the PA view, the catheter loops encompass an area of 1900 $mm^2$ and 1459 $mm^2$ for the first and second configurations respectively, while in RAO 45˚ views, the encompassing areas are only 585 and 154 $mm^2$ respectively.

### 7.5.5. Biplane vs. Monoplane Registration

Registration with the catheter loop can be performed in two view-modes, either in biplane mode, requiring a sequential biplane X-ray acquisition, or in monoplane mode in which registration is performed in a single view. Single view registration is ideal when biplane acquisitions are not desired by the interventionalist, since this would require that the radiography rotate and then readjust the C-arm and possibly the patient table, causing an interruption to the clinical flow.

Furthermore, the reduced imaging requirement of single-view registration compared to registrations biplane is ideal for a faster registration. This is particularly well suited for correcting a prior registration after it has been spoiled by bulk patient motion. Bulk patient motion is a known problem in 2D-3D image registration of cardiac images [30], and according to clinical experts, occurs frequently when the patient is under a sedative as opposed to general aesthetics [141]. In these cases, the initial guess registration to start the local search is the position of the prior registration instead of the supine-isocentre constraints.

Single-view registration could also be used to detect if a prior registration has been spoiled. In this case, the correction can be performed immediately, or it can be flagged to the clinical team for them to decide how reregistration should occur.

### 7.5.6. Single-View Registration on a Clinical Dataset

To show clinical feasibility, registration was applied to a single cardiac catheterisation case where a patient underwent pulmonary vein isolation by radiofrequency ablation. Registration was based on a single view X-ray with a preoperative MR scan, and accuracy was assessed by a clinical expert by estimating mean 2D-TREs over the chambers of the heart from MR-X-ray overlays. The expert estimated that mean accuracy was 9.4 mm 2D-TRE (WH), with a maximum of 25 mm using the one-stage approach, and a 10 mm 2D-TRE (WH) with a maximum of 27.5 mm using the two-stage approach.

### 7.5.7. Limitations

While the experiment shows that registration with a plastic phantom can yield TREs within the 5-mm clinical tolerance, the phantom is rigid and stationary and therefore no errors are introduced in the reported TREs due to cardiac and respiratory motions. Although the main cause of error in rigid registration methods are not simulated, the experiments carried out in this chapter are still valid and applicable to cardiac catheterisation procedures by adding the requirement that the intraoperative X-ray images are phase-matched to the preoperative CT image with respect to the cardiorespiratory cycle, typically at end-diastole and end-systole.

Another limitation in the registrations of the phantom experiments is the absence of the pericardial sac that would contribute to the upper cardiac shadow when imaging a live heart. To account for this when working with patient data the pericardial sac should be included in the ventricle segmentation, as was done in the single clinical case in this chapter.

### 7.5.8. Future Improvements

While the single and two-view approaches can potentially provide accurate results, there is still potential for improvement in order for the algorithm to be deployable in a clinical setting. In the phantom experiments, the IVC-LA-LUPV configuration consistently performed better than the IVC-LA-RLPV configuration, which may be the result of having a larger loop size. The IVC-LA-RLPV configuration represents the scenario where the loop does not accurately follow the chamber wall (Figure 7.3b), and therefore encloses a smaller area than that of the projected chamber. One possible extension to this algorithm would be include the ostia of the vessels from where the catheter enters and exits as additional constraints for registration. This would add two positions along the catheter that are guaranteed to be touching the wall and therefore help limit the range of movement the catheter can make in relation to the chamber.

For both the phantom and porcine heart experiments, the two-stage hill climbing strategy generally performed better than the one-stage strategy. A likely reason is that the search space contains a large number of local minimum in which the algorithm can fall into and get trapped.

The two-stage strategy applies a single reset, which allows it to move out of the local minimum. Therefore, another potential improvement would be to change the search strategy to ones which include stochastic elements that enable the algorithm to escape local minima, such as a simulated annealing [145] or a genetic-based algorithm [146].

### 7.5.9. Registration Speed

The automatic registration algorithm can usually be performed within a minute and a half, which is a reasonable execution time under clinical settings. However, this does not include time required to extract the catheter used for registration, which requires an additional minute and a half, approximately. To avoid this, an automatic catheter extraction method could be used [137]. The speed of the algorithm can potentially be improved by using the optimised iterative search strategies found in [89], and by using a multi-resolution approach to reduce the number of points used in the CT segmentation during the initial alignment when the increments are relatively large, and then restore the number of points when the increments are small and finer resolution is needed.

### 7.5.10. Conclusion

Evaluation of the algorithm in the phantom setting yields mean 3D-TREs below the 5-mm clinical tolerance while [14] demonstrating feasibility for clinical interventional guidance and meriting thorough validation using further phantom and clinical images. In an exemplar clinical case, looped-catheter-based registration with a single view could achieve an estimated accuracy of 10 mm mean 2D-TRE, an improvement the isocentre-supine constraint which started with an estimated mean 2D-TRE of at 21 mm. The addition of the ostium constraints, combined with a local-minima avoiding search strategy, could potentially aid the algorithm in terms of accuracy and robustness.

# Chapter 8

## 8. Conclusions and Future Work

The work in this thesis aims to overlay 3D data from preoperative CT or MR scans of the heart onto intraoperative live X-ray fluoroscopy images, obtained during cardiac catheterisation procedures. A second aim is to further integrate electro-anatomical mapping (EAM) data with the preoperative 3D data using X-ray as an intermediate modality. The development and validation of translational algorithms to appropriately perform these 2D-3D image registrations in the clinical environment defines the objectives of this thesis. An algorithm is suitable for clinical deployment if it satisfies the three criteria of having a high degree of accuracy, robustness, and being minimally disruptive to the clinical workflow.

This chapter first summarises the 2D-3D image registration algorithms developed and validated in this thesis in terms of how well they fulfil the three criteria, while emphasising novel contributions to the field of imaging sciences and biomedical engineering. The next part of the chapter proposes future work that may help fulfil or extend beyond the thesis objectives. The chapter ends with concluding remarks.

### 8.1. Catheter-Based 2D-3D Image Registration of Cardiac Images

In Chapter 2, the clinical justification for performing 2D-3D image registration of cardiac images in image-guided catheterisation procedures is described. Based on the technical literature review in Chapter 3, the development of feature-based approaches using intracardiac catheters was chosen as the main strategy for performing the registration. For cardiac catheterisation procedures, a feature-based approach is appealing since the 2D-3D problem is *multi-modal* because of the difficulty in multimodal 2D-3D intensity-based approaches [90], and because feature-based approaches are generally faster than intensity-based approaches [103]. The use of catheter features to provide the constraints is attractive since they are clearly visible throughout the procedure and are usually within the target organ, i.e. the heart. They are also the main instruments of the operation and therefore no additional devices or images are required for registration, minimising the disruption to the clinical workflow and satisfying one of the objectives.

### 8.1.1. Catheter-Vessel-Based 2D-3D Image Registration on Phantom Data

The first novel catheter-based algorithm presented in this thesis (Chapter 5) performs registration by constraining multiple catheters extracted from X-ray to their corresponding vessels extracted from the preoperative 3D modality. While previous catheter-based 2D-3D registrations exist (§3.2.12 [71], §3.2.13 [17]), these methods register in 2D. The catheter-based approach presented in this thesis uses a biplane catheter reconstruction step to bring the catheter data into 3D and into spatial correspondence with their segmented corresponding vessels. There is evidence to suggest that a reconstruction-based approach can register more accurately than a biplane projection-based in two views [91] [99]. Registration is then performed in 3D and therefore large out-of-plane translational errors can be avoided. This provides a more accuracy registration, making it suitable for 3D biophysical modelling, and second, overlays can be generated in any X-ray view without the need to re-perform registration.

A catheter-reconstruction approach has been previous proposed (§3.2.14 [99]), however registration is performed using only a single catheter. The experiments conducted in Chapter 5 show that a single catheter alone is not enough to achieve the clinical accuracy objective. Introducing a second catheter, and weighting the registration based on the cross-sectional area of the vessels, improved results and was demonstrated to provide accuracies that meet the clinical objective. Furthermore, the approach in [99] uses the iterative closest point method to find registration, a local iterative strategy.

A novelty of the catheter-vessel-algorithm proposed in Chapter 5 is the global-fit approach to finding point correspondences between the catheter and vessel-centreline points. An advantage of global strategies is that the entire search space is explored, as opposed to local strategies which explore a subset of the space. Assuming that an accurate solution exists within the search space, the global strategy is almost guaranteed to find it all the time. This gives global search strategies a high degree of robustness, one of the thesis criteria, as long as the problem is not dominated by other errors, for example during information extraction. Global searches are also independent of an initial starting estimate.

Using two catheters, the experiments show that registration accuracy largely depends on which catheter pairs were used and answers the question, *which catheter configuration produces the best accuracy?* The best performing configurations involved using the CS (Table 5.12) in conjunction with the descending aorta (DAo) (0.55 mm 3D-TRE), with the ascending aorta (AAo) (3.6 mm 3D-TRE) and using the right coronary artery in conjunction with the DAo (3.5 mm 3D-TRE, Table 5.13), all of which satisfy the 5-mm objective. Accuracy could be achieved within 10 mm using configurations involving the CS in conjunction with the IVC, SVC, LUPV and AAo; and within 15 mm using configurations involving the LUPV in conjunction with the DAo and AAo.

The 5 mm, 10 mm and 15 mm accuracy requirements are general guidelines for various interventional procedures [14]. Another question the experiments help to answer is: *among the accurate catheter configurations, which ones are clinically applicable*? Interventional procedures, such as PCI, CRT and RFA, have different catheter configurations (Table 3.3) and accuracy requirements (§1.5).

For PCI, the target for registration is the LV, and ideal accuracy is 2.5 mm 3D-TRE, which could be achieved using when registering with the CS and DAo. Other useful catheter configurations include which are used during a PCI include:

- CS/AAo and RCA/DAo for accuracy within 5 mm over the whole heart (WH),
- CS/IVC, CS/SVC, DAo/AAo and LAD/DAo for accuracy within 10 mm (WH)

The ideal accuracy requirement for CRT is between 5 and 6 mm at the LV to navigate a pacing lead into the CS ostium. However, in these procedures, the only suitable two-catheter configuration is the CS with CVS combination. There therefore, this algorithm is not suitable to assist in navigation of these procedures and the interventionist would need to rely on other techniques and other sources of information for navigation into the CS ostium. However, once the lead is placed inside the CS, the algorithm can perform registration with an accuracy within 4.9 mm over the LV, which would be sufficient accuracy to help navigate the lead into the branches of the CS such as the great, posterior and middle cardiac veins. Registration would also be useful in these procedures for both post-procedural validation and offline biophysical modelling.

During RF ablations, an EP catheter is usually placed in CS to collect essential ECG information throughout the procedure. Treating the right side of the heart (RH) would involve inserting an ablation catheter via the IVC or SVC into the RA, or RV via the RA. For RH ablations, registrations with mean accuracy within 10 mm over the WH could be achieved using the CS in conjunction with the IVC or SVC.

Access into the left side is slightly more complication, requiring a septal puncture from the RA into the LA, or inserting a catheter into the Ao and into the LV. For left heart ablations, accuracy within the ideal 4 mm can be achieved using the CS in conjunction with the DAo or AAo. Otherwise, using the CS with the IVC, SVC or LUPV, or using the AAo with the DAo could provide registration with a mean accuracy within 10 mm over the WH.

Not only did the analysis show which configurations work best, it also showed that some configurations performed badly and resulted in large errors. Presenting a clinician with poorly registered images may lead to fatal mistakes made during the procedure. Configurations leading to poor registrations, i.e. larger than 15-mm, include the DAo/IVC, DAo/SVC, AAo/IVC, AAo/SVC, IVC/SVC, IVC/LUPV and SVC/LUPV (Table 5.12) and therefore should be avoided.

### 8.1.2. Catheter-Vessel-Based 2D-3D Image Registration on Clinical Data

When moving from the overly simplistic phantom coronary vasculature to clinical data with real vasculature necessitates a second novelty of the catheter-based registration algorithm, which is the two-fold global-fit strategy. The first global-fit nature of the algorithm allows catheters and vessel centrelines of any length or direction to be picked, and determines the best possible fit, in terms of minimising the vessel-radius-weighted RMS distance error between the catheter and vessel centreline, as above. The second global-fit approach accounts for the large number of branching coronary vessels where catheters are usually inserted and well constrained, a necessary adaption to work with clinical data demonstrated in Chapter 6. The immediate benefit of this is avoiding the need for a clinical expert to inject nephrotoxic contrast agent into the vasculature to determine which branch the catheter is inserted into, thereby preventing disruption to the clinical workflow. Manually verifying the registrations in Chapter 6, the algorithm was always able to match the catheter to the correct branch of the vessel, and in the correct direction. Another benefit of a global-fit approach is that there is no longer a need for a good initial starting location. Finding an initial estimate is often a problem in local search strategies. This limits the robustness of the algorithm, and often requiring knowledgeable manual interaction, reducing the clinical applicability of the algorithm [105].

Chapter 6 showed clinical applicability of the catheter-vessel-based approach, confirming its validity as a translational algorithm on three example cardiac catheterisations. Expert clinicians estimate an average 2D-TRE of 5.9 mm (Table 6.5) for the global-fit approach. While this does not meet the clinical objective of a 5-mm 2D-TRE, it was demonstrated to perform better than a current standard manual registration method using EP Navigator, which had an average accuracy of 6.5 mm (Table 6.6). The catheter-vessel-based approach was also able to perform registration much faster, with an average speed of under two minutes (Table 6.5) per registration. This is a suitable time for registration compared to the standard set by EP Navigator, which took an average of about 7½ minutes (Table 6.6).

### 8.1.3. Looped-Catheter-Based 2D-3D Image Registration

The looped-catheter-based approach extends on the novelty of exploring different catheter configurations typical in cardiac catheterisation procedures. This approach makes use of

catheters inserted within a target chamber of the heart and looped along the inner wall of the chamber. Catheter-looping is a common technique use by interventionalists to create a quick visual reference of the chamber they are working on in X-ray without the need for contrast agent injections. This technique is often used as a constraint for manual registration using EP Navigator [23]. The work in this thesis is the first to automate this approach, and improves upon it by also using the upper cardiac border as an additional constraint since this is a common feature visible when imaging the heart without the need for contrast agents.

This algorithm was designed to be applicable during complementary scenarios of the catheterisation compared to the catheter-vessel approach. The algorithm is complementary in terms of the catheter configuration, and also the number of X-ray views used. Registration can be performed using any number of views, including just a single view.

In order to register, this algorithm relies on a good initial estimate of the registration by using the isocentre-supine constraint. This provides an initial accuracy of around 15 mm 3D-TRE or 10 mm RPD. Afterwards, the algorithm refines the registration using a one- or two-staged iterative search strategy. The two-stage strategy was more accurate than the one-stage strategy, using a single view. The two-stage algorithm performed registration with an accuracy of 2.7 mm RPD, averaged over 12 experiments (Table 7.5, Table 7.8) with 83% of these registrations were within the clinical tolerance, and the average capture range was 6.05 mm RPD (Table 7.6).

Registration using two views had a comparable accuracy of 4.0 mm 3D-TRE, equivalent to approximately 3.2 mm RPD, averaged over 6 experiments (Table 7.3, Table 7.7) with 100% of these within the clinical tolerance, and a slightly larger capture range of 7.79 mm 3D-TRE (Table 7.4).

The capture range does not encompass the initial accuracy of 15-mm provided by the isocentre-supine constraint, and therefore, the robustness objective has not been met. However, for some catheterisation procedures, where a 6-mm 3D-TRE or RPD accuracy is a sufficient target, the capture ranges are significantly larger at 11.10 mm RPD for monoplane registrations and 18.11 mm 3D-TRE for biplane registrations which do encompass the isocentre-supine constraint accuracies and meets the robustness objective where 6-mm accuracy is the requirement.

### 8.1.4. Combined Use of Complementary Catheter-Based Registration

The two algorithms are intended to work under complementary catheter configuration scenarios. Based on the non-clinical experiment, the catheter-vessel approach using at least one narrow vessel can perform registration more accurately than the biplane looped-catheter approach.

If the catheter-vessel approach is unavailable due to non-catheterisation of vessels, a recommended use of the looped-catheter approach would be to first register with two views using the isocentre-supine constraint initialisation, since it has a wider capture range and can register within the clinical tolerance, or at least within 6-mm 3D-TRE. Then the single view method could be used to detect and potentially correct for registration errors due to bulk patient motion. According to clinical experts, bulk patient motion occurs frequently enough in a catheterisation lab for single-view registration to be desirable, although there is no definitive statement on this matter in the literature. Registration from a single-view is demonstrated at the end of Chapter 7. This started with the isocentre-supine constraint and gave an estimated accuracy of 10 mm, as assessed by a clinical expert.

### 8.1.5. Electroanatomical Mapping

An advantage of biplane registration is that the results are valid in 3D, since large out-of-plane translational and rotational errors from a single view can be eliminated using the second view. This is useful for applications such as biophysical modelling [18] [19] [55] and further co-registration of electroanatomical mapping (EAM) data onto the preoperatively acquired 3D data to improve catheterisations [125] [127].

In Chapter 6, co-registration between EAM data, collected using EnSite, and preoperative MR data was demonstrated on a clinical case using the catheter-vessel approach to perform the X-ray-MR co-registration. EAM-MR co-registration for the clinical case was calculated to have an accuracy of 3.7 mm 3D-TRE by comparing the region of scars segmented from a preoperative late gadolinium enhanced scan and from low bipolar voltages of the EAM data. The accuracy is comparable to two commercially available registration platforms, Cartomerge™ and NavX™ Fusion™, which are capable of achieving accuracies of 2.7 mm and 3.3 mm respectively [127]. However, the main benefit of the approach in Chapter 6 is that most of the registration is performed from the chamber geometry with only a few additional landmark locations needed to calculate the rotation, four in the case presented. Registration is therefore fast and can be performed in less than one minute. For the commercial platforms, between 15 and 30 corresponding landmarks positions need to be taken for NavX Fusion, or a venogram needs to be acquired in the case of the Cartomerge to verify five landmark locations, adding 15 and 11 minutes to the clinical workflow respectively [127].

## 8.2. Future Work

The suggested future work is divided into two parts. The first part discusses the limitations and suggests ways to improve the registration so that the clinical objectives are met or exceeded. The second part is concerned with clinical validation. This section discusses the catheter-based

algorithms together. Their individual limitations and future work are discussed in their respective discussion sections (§5.4, §6.6, §7.5).

### 8.2.1. Improvement of the 2D-3D Image Registration Algorithms

In the catheter-based approaches, the segmentation of the chambers and vessels from the preoperative images, and the extraction of catheters and upper cardiac border from the X-ray, are stages that require manual interaction, thereby causing disruptions to the clinical workflow. Automated approaches are potentially faster, are more reproducible, require less training than manual approaches.

Chamber segmentation can be performed automatically using [147] for cardiac MR data and [148] for CT. Vessel segmentation can be bypassed using algorithms that automatically extract the centrelines and radius-function [140] [149]. Since segmentation of the heart on preoperative data can be done before the intervention starts, it does not necessary disrupt the clinical workflow. However, obtaining and segmenting 3D anatomy from intraoperative 3DRx could cause disruptions and therefore would benefit from automation. Catheters can also be extracted automatically since many of them, especially those used to collect essential electrophysiology data, have radio-opaque leads that are readily visible in X-ray. They can therefore be automatically detected using blob-tracking techniques [137] or using principal component analysis when screening with a low dose [150].

Both catheter-based registration algorithms require retrospective cardiorespiratory gating of the fluoroscopy images. This means that for every single-view registration, approximately four seconds of fluoroscopy is acquired to capture at least one cardiac and one respiratory cycle. The problem doubles for two-view registration in terms of fluoroscopy acquisitions and therefore X-ray exposure to patient and staff. Most of this can be avoided by ECG triggered gating, available in most X-ray systems, and respiratory triggered gating using devices such as the one proposed in [151]. The X-ray can also be prospectively gated using catheter-based predictive models [152]. Automatic gating has the added benefit of reducing the time needed to perform the manual gating for each view.

In terms of accuracy and robustness, adjustments to the individual catheter-based approaches are described in their respective discussion sections. While the two catheter-based approaches were designed to perform under complementary scenarios, it is possible for a cardiologist to both insert one or more catheters inside vessels while also looping a catheter inside a chamber. In these scenarios, ideally, a combined algorithm could simultaneously use the constraints of the catheter within the vessel, the catheter looped inside the chamber, and the upper cardiac border (Figure 8.1). However, the two catheter-based approaches achieve registration in very different

ways; the catheter-vessel based approach uses a global search strategy and therefore is not dependent on the initial estimate of the registration; while the loop-based approach employs an iterative search strategy using the isocentre-supine constraint to provide an initial estimate of the registration. Therefore, a new method of consolidating both types of constraints simultaneously would be a novel contribution to knowledge yet to be explored.

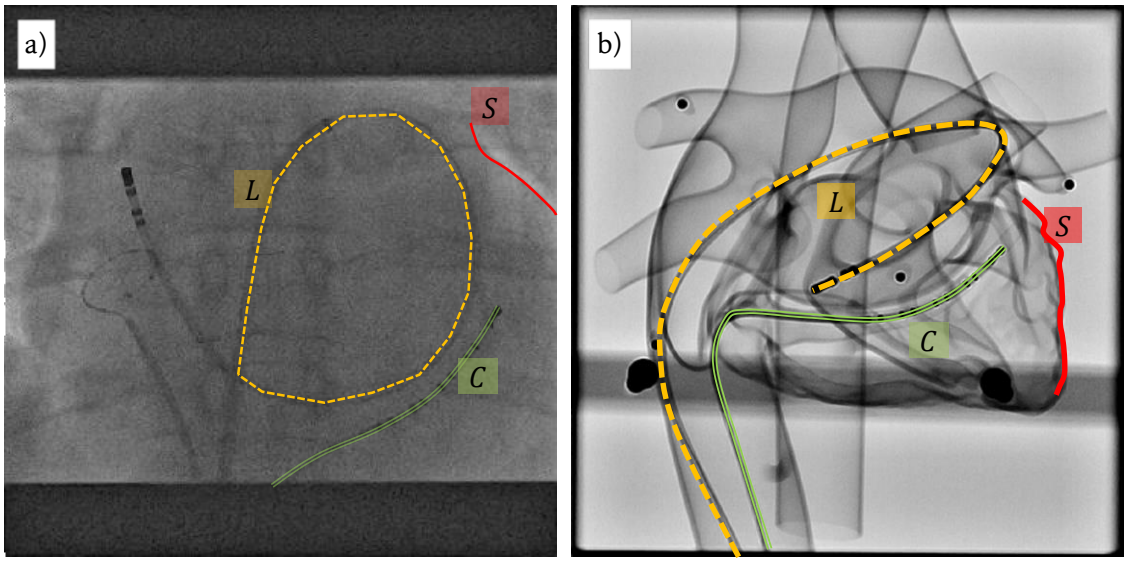


Figure 8.1 a) PA X-ray view of a patient, with a catheter (*C, green double arc*) inserted into the coronary sinus and a catheter looped inside the left atrium (*L, yellow dashed loop*). Upper cardiac border is highlighted (*S, red solid arc*). b) Same view of an anatomically correct glass phantom model of the heart with same catheter configurations.

### 8.2.2. Simulation of Catheters in Vessels and Chambers

The work in [118] indicates that the path of a guidewire inserted into a vessel is relatively reproducible in shape and position. Therefore, registration accuracy can potentially be improved by simulating the catheter path within the vessel using techniques in [119] [120] and assuming that the catheter lies close to this path instead of the vessel's medial line. However, these methods have only been shown to apply where the catheter is well constrained in thin and tortuous vessels, which would not be the case for large vessels that are long and straight, such as the DAo, inferior vena cava (IVC) and SVC. A method that models the catheter within the vessel or chamber and then tries to match a reconstructed catheter to its simulated position could potentially improve registration accuracy and would be a novel algorithm worth investigation.

### 8.2.3. Clinical Validation

The bulk of the work in this thesis was the deployment and analysis of the catheter-based registration approaches applied to phantom and porcine hearts. Chapters 6 and 7 demonstrated the feasibility of performing 2D-3D registration on clinical datasets: three using the catheter-vessel approach, one using the looped-catheter approach and one demonstrating co-registration of EAM data onto the preoperative scans. As a translational research work, the algorithms are

intended to be clinically applicable. Therefore, thorough validation on a cohort study of patients is required.

However, there are a number of difficulties involved in clinical validation. The first is that it is difficult to assess for certain what makes a good registration. Linte *et al.* [14] report that 5 mm 3D-TRE is a good target value for catheter ablation procedures. This choice of tolerance is justified based on the average radius of target lesions and is used as an objective in this thesis. On the other hand, EP navigator registration, a current clinical standard, was shown to register with accuracy around 10-mm by clinical experts given a 10 min time limit (Table 6.6). According to independent expert opinion, 67% of these registrations would be valid for guiding cardiac catheterisation procedures. The main reason is that there are a number of patient specific factors that determine whether a registration is valid or not and this may not necessarily correlate with the accuracy. For example, the location of the lesion with respect to the chambers is important, since accuracy of either manual or automatic algorithms vary from chamber to chamber.

To truly correlate the usefulness of a registration to its accuracy, a much larger study across multiple centres needs to be conducted in order to remove interventionalist bias and variability. Such a study could, for example, try to correlate measurable targets such as reduction in procedure and X-ray exposure times, fewer contrast agent injections and increased success rates, to the accuracy and robustness measures of the algorithm. 2D-3D registration algorithms such as the ones presented in this thesis could contribute to such a study.

## 8.3. Concluding Remarks

The objective in this thesis was to develop and validate 2D-3D image registration algorithms applicable to the clinical setting for cardiac catheterisation procedures. Two novel algorithms were developed which satisfied the criteria to a reasonable degree. The three main contributions to knowledge in this thesis are:

1) The development of a novel reconstruction-based catheter-vessel 2D-3D registration algorithm
2) Registration with a global-fit approach, thereby providing a robust catheter-vessel algorithm
3) The exploration of different catheter configurations and determining which configurations are best, and which would result in large errors and providing clinically dangerous registration
4) The development of a looped-catheter-based 2D-3D registration algorithm exploiting the current clinical protocol of using looped catheters for registration

The use of 2D-3D image registration of cardiac images is becoming more popular in catheterisation procedures, in order to provide overlays and for EAM fusion. It is the goal of the author to architect the development of a software platform that will eventually be deployed routinely in the clinical environment to provide these registrations using the catheter-based approaches presented in this thesis. The intelligent system would be able to track catheters entering into the heart and automatically initiate registration by deducing which chamber or vessel the catheter has been inserted into and applying the appropriate constraints. Registration will be fully automated, accurate, and robust and use only data from the clinical protocol, thereby providing the cardiologists with improved visual information to help guide the safe and accurate placement of catheters, while introducing minimal disruption to the clinical workflow.

# References


[1] European Heart Network and European Society of Cardiology, "European Cardiovascular Disease Statistics," European Heart Network AISBL, Brussels, Belgium, 2012.

[2] BMJ Group, "Guideline for the Management of Patients with Acute Coronary Syndromes without Persistent ECG ST Segment Elevation," *Heart,* vol. 85, pp. 133-142, 2001.

[3] S. Yusuf, M. Flather, J. Pogue, D. Hunt, J. Varigos, L. Piegas, A. Avezum, J. Anderson, M. Keltai, A. Budaj, K. Fox and L. Ceremuzynski, "Variations between Countries in Invasive Cardiac Procedures and Outcomes in Patients with Suspected Unstable Angina or Myocardial Infarction without Initial ST Elevation," *The Lancet,* vol. 352, no. 9127, pp. 504-517, 1998.

[4] D. R. Holmes and D. O. Williams, "Catheter-Based Treatment of Coronary Artery Disease," *Contemporary Reviews in Interventional Cardiology,* vol. 1, pp. 60-73, 2008.

[5] J. Fajadet and A. Chieffo, "Current Management of Left Main Coronary Artery Disease," *European Heart Journal,* vol. 33, no. 1, pp. 36-50, 2012.

[6] M. S. Lee, G. W. Stone, S. J. Park, P. Teirstein, J. Moses, A. Colombo and D. E. Kandzari, "Percutaneous Coronary Intervention of Unprotected Left Main Coronary Artery Disease: Procedural Strategies and Technical Considerations," *Catheter Cardiovascular Interventions,* vol. 79, no. 5, pp. 812-822, 2012.

[7] Ö. Birim, A. J. Bogers and A. P. Kappetein, "Comparing Cost Aspects of Coronary Artery Bypass Graft Surgery with Coronary Artery Stenting," *Journal of Cardiovascular Surgery,* vol. 53, no. 5, pp. 641-650, 2012.

[8] G. Lee, P. Sanders and J. M. Kalman, "Catheter Ablation of Atrial Arrythmias: State of the Art," *Lancet,* vol. 380, no. 9852, pp. 1509-1519, 2012.

[9] A. Verma and A. Natale, "Why Atrial Fibrillation Ablation Should be Considered First-Line Therapy for Some Patients," *Circulation,* vol. 112, pp. 1214-1230, 2005.

[10] A. Hoye, "Management of Chronic Total Occlusion by Percutaneous Coronary Intervention," *Heart,* vol. 98, pp. 822-828, 2012.

[11] J. B. Shea and M. O. Sweeney, "Cardiac Resynchronization Therapy: A Patient's Guide," *Circulation,* vol. 108, pp. e64-e66, 2003.

[12] A. Ames and W. G. Stevenson, "Catheter Ablation of Atrial Fibrillation," *Circulation,* vol. 113, pp. e666-e668, 2006.

[13] L. Lickfett, M. Mahesh, C. Vasamreddy, D. Bradley, V. Jayam, Z. Eldadah, T. Dickfeld, D. Kearney, D. Dalal, B. Lüderitz, R. Berger and H. Calkins, "Radiation Exposure During Catheter Ablation of Atrial Fibrillation," *Circulation,* vol. 110, pp. 3003-3010, 2004.

[14] C. A. Linte, P. Lang, M. E. Rettmann, D. S. Cho, D. R. Holmes III, R. A. Robb and T. M. Peters, "Accuracy Considerations in Image-Guided Cardiac Interventions: Experience and Lessons Learned," *International Journal of Computer Assisted Radiology and Surgery,* vol. 7, pp. 13-25, 2011.

[15] K. Rhode, Y. Ma, J. Housden, R. Karim, C. A. Rinaldi, M. Cooklin, J. Gill, M. O'Neill, T. Schaeffter, J. Relan, M. Sermesant, H. Dilingette, N. Ayache, M. Krüger, W. Schulze, G. Seemann, O. Dössel and R. Razavi, "Clinical Applications of Image Fusion for Electrophysiology Procedures," in *9th IEEE ISBI*, Barcelona, Catalonia, Spain, 2012.

[16] L. F. Gutiérrez, R. de Silva, C. Ozturk, M. Sonmez, A. M. Stine, A. N. Raval, V. K. Raman, V. Sachdev, R. J. Aviles, M. A. Waclawiw, E. R. McVeigh and R. J. Lederman, "Technology Preview: X-ray Fused with Magnetic Resonance during Invasive Cardiovascular Procedures," *Catheterization and Cardiovascular Interventions,* vol. 70, pp. 773-882, 2007.

[17] J. Sra, D. Krum, B. Belanger and R. Vaillant, "Registration of three-dimensional left atrial computed tomographic images with fluoroscopy," *Heart Rhythm,* vol. 2, no. 9, p. 1020, 2005.

[18] K. Rhode and M. Sermesant, "Modeling and Registration for Electrophysiology Procedures Based on Three-Dimensional Imaging," *Current Cardiovascular Imaging Reports,* vol. 4, no. 2, pp. 116-126, 2012.

[19] M. Sermesant, R. Chabiniok, P. Chinchapatnam, T. Mansi, F. Billet, P. Moireau, J.-P. Peyrat, K. C. L. Wong, R. Rhode, M. Ginks, P. Lambiase, H. Delingette, M. Sorine, C. A. Rinaldi, D. Chapelle, R. Razavi and N. Ayache, "Patient-Specific Electromechanical Models of the Heart for the Prediction of Pacing Acute Effects in CRT: A Preliminary Clinical Validation," *Medical Image Analysis,* vol. 16, no. 1, pp. 201-215, 2013.

[20] L. G. Brown, "A Survey of Image Registration Techniques," *ACM Computing Surveys,* vol. 24, no. 4, pp. 325-375, December 1992.

[21] P. Markelj, D. Tomaževič, B. Likar and F. Pernuš, "A Review of 3D/2D Registration Methods for Image-Guided Interventions," *Medical Image Analysis,* vol. 16, no. 3, pp. 642-661, 2012.

[22] G. P. Penney, Registration of Tomographic Images to X-ray Projections for Use in Image Guided Interventions, PhD Thesis, London, England, UK: King's College London, University of London, 2001.

[23] Y. Ma, S. Duckett, Chinchapatnam, G. Gao, A. Sheety, C. A. Rinaldi, T. Schaeffter and K. S. Rhode, "MRI to X-ray Fluroscopy Overlay for Guidance of Cardiac Resynchronization Therapy Procedures," in *Computing in Cardiology*, Belftast, Northern Ireland, UK, 2010.

[24] J. M. Fitzpatrick, J. B. West and C. R. J. Maurer, "Predicting Error in Rigid-Body, Point-Based Registration," *IEEE Transactions on Medical Imaging,* vol. 17, pp. 694-702, 1998.

[25] J. M. Fitzpatrick, "Fiducial Registration Error and Target Registration Error Are Uncorrelated," *In proceedings of SPIE,* vol. 7261, no. 02-1, p. 12 pages, 2009.

[26] K. Ilg, T. S. Baman, S. K. Gupta, S. Swanson, E. Good, A. Cugh, K. Jongnarangsin, F. Pelosi, T. Crawford, H. Oral, F. Morady and F. Bogun, "Assessment of Radiofrequency Ablation Lesions by CMR Imaging After Ablation of Idiopathic Ventricular Arrythmias," *JACC: Cardiovascular Imaging,* vol. 3, no. 2, pp. 286-288, 2010.

[27] J. T. J. Dodge, B. G. Brown, E. L. Bolson and H. T. Dodge, "Lumen diameter of normal human coronary arteries. Influence of age, sex, anatomic variation, and left ventricular hypertrophy or dilation.," *Circulation,* vol. 86, pp. 232-246, 1992.

[28] J. C. Doig, J. Saito, L. Harris and E. Downar, "Coronary Sinus Morphology in Patients With Atrioventricular Junctional Reentry Tachycardia and Other Supraventricular Tachyarrhythmias," *Circulation,* vol. 92, pp. 436-441, 1995.

[29] Y. Ma, A. P. King, N. Gogin, G. Gijsbers, C. A. Rinaldi, J. Gill, R. Razavi and K. S. Rhode, "Clinical Evaluation of Respiratory Motion Compensation for Anatomical Roadmap Guided Cardiac Electrophysiology Procedures," *IEEE Transactions on Biomedical Engineering,* vol. 59, no. 1, pp. 122-131, 2012.

[30] K. S. Rhode, M. Sermesant, D. Brogan, S. Hegde, J. Hipwell, P. Lambiase, E. Rosenthal, C. Bucknall, S. A. Qureshi, J. S. Gill, R. Rezavi and D. L. G. Hill, "A System for Real-time XMR Guided Caridovascular Intervention," *IEEE Trans. Med. Imag.,* vol. 24, no. 11, pp. 1428-1440, 2005.

[31] E. B. van de Kraats, G. P. Penney, D. Tomaževič, T. van Walsum and W. J. Niessen, "Standardized Evaluation Methodology for 2-D–3-D Registration," *IEEE Trans Med Imaging,* vol. 24, no. 9, pp. 1177-1189, 2005.

[32] S.-I. Seldinger, "Catheter Replacement of the Needle in Percutaneous Arteriography; a New Technique," *Acta Radiologica,* vol. 39, no. 5, pp. 368-376, 1953.

[33] G. Penney, A. Varnvas, N. Dastur and T. Carrell, "An Image-Guided Surgery System to Aid Endovascular Treatment of Complex Aortic Aneurysms: Description and Initial Clinical Experience," *IPCAI, LNCS,* vol. 6689, pp. 13-24, 2011.

[34] K. Park, A. Montillo, D. Metaxas and L. Axel, "Volumetric Heart Modelling and Analysis," *Communications of the ACM,* vol. 48, no. 2, pp. 43-48, 2005.

[35] M. Pop, M. Sermesant, D. Lepiller, M. V. Truong, E. R. McVeigh, E. Crystal, A. Dick, H. Delingette, N. Ayache and G. A. Wright, "Fusion of optical imaging and MRI for the evaluation and adjustment of macroscopic models of cardiac electrophysiology: A feasibility study," *Medical Image Analysis,* vol. 13, no. 2, pp. 370-380, 2008.

[36] P. Kumar and M. Clark, "Cardiovascular Disease," in *Clinical Medicine, Eighth Edition*, International, Elsevier Ltd, 2012, pp. 669-790.

[37] S. K. S. Huang and M. A. Wood, Catheter Ablation of Cardiac Arrhythmias, Philadelphia, PA, USA: Elsevier, 2006.

[38] D. Patterson and T. Treasure, "Resuscitation," in *Disorders of the Cardiovascular System*, London, UK, Edward Arnold, 1993, pp. 312-331.

[39] G. J. Tortora and B. Derrickson, "The Cardiovascular System: Heart," in *Introduction to the Human Body: The Essentials of Anatomy and Physiology, 9th Edition*, Hoboken, NJ, USA, John Wiley & Sons, Inc., 2012, pp. 397-419.

[40] A. M. Pertsov, J. M. Davidenko, R. Salomonsz, W. T. Baxter and J. Jalife, "Spiral Waves of Excitation Underlie Reentrant Activity in Isolated Cardiac Muscle," *Circulation Research,* vol. 72, no. 3, pp. 631-650, 1993.

[41] W. C. Röntgen, "On A New Kind Of Rays," *Nature,* vol. 53, pp. 274-276, 1896.

[42] NHS choices, "Recoverying from Heart Bypass Surgery," National Health Service, 22 04 2012. [Online]. Available: http://www.nhs.uk/Conditions/Coronary-artery-bypass/Pages/Recovery.aspx. [Accessed 07 04 2013].

[43] S. Pursnani, F. Korley, R. Gopaul, P. Kanade, N. Chandra, R. Shaw and S. Bangalore, "Percutaneous Coronary Intervention Versus Optimal Medical Therapy in Stable Coronary Artery Disease: a Systematic Review and Meta-Analysis of Randomized Clinical Trials," *Circulation: Cardiovascular Interventions,* vol. 5, no. 4, pp. 476-490, 2012.

[44] A. D. Scott, J. Keegan and D. N. Firmin, "Motion in Cardiovascular MR Imaging," *Radiology,* vol. 250, no. 2, pp. 331-342, 2009.

[45] P. P. Dendy and B. Heaton, Physics for Diagnostic Radiology, 2nd Edition, Bristol, England, UK: IOP Publishing Ltd, 1999.

[46] W. D. Coolidge, "A Powerful Röntgen Ray Tube with a Pure Electron Discharge," *Phys Rev 2,* vol. 2, no. 6, pp. 409-430, 1913.

[47] M. Yorimitsu, K. Yokoyama, T. Nitatori, H. Yoshino, S. Isono and S. Kuhara, "Whole-Heart 3D Late Gadolinium-Enhanced MR Imaging: Investigation of Optimal Scan Parameters and Clinical Usefulness," *Magn Reson Med Sci,* vol. 11, no. 1, pp. 9-16, 2012.

[48] L. Axel, A. Montillo and D. Kim, "Tagged Magnetic Resonance Imaging of the Heart: a Survey," *Medical Image Analysis,* vol. 9, pp. 376-393, 2005.

[49] Y. Rudy and R. Plonsey, "A Comparison of Volume and Source Geometry Effects on Body Surface and Epicardial Potentials," *Circulation Research,* vol. 46, pp. 283-291, 1980.

[50] A. Intina, R. N. Goldstein, P. Jia, C. Ramanathan, K. Ryu, B. Giannattasio, R. Gilkeson, B. S. Stambler, P. Brugada, W. Stevenson, Y. Rudy and A. Waldo, "Electrocardiographic Imaging (ECGI), a Novel Diagnostic Modality Used for Mapping of Focal Left Ventricular Tachycardia in a Young Athlete," *Heart Rhythm,* vol. 2, no. 11, pp. 1250-1252, 2005.

[51] P. Verfürth, Reconstruction of the Epicardial Potential from Body Surface Potential Maps, Diplomarbeit, Münster, Germany: Westfälische Wilhelms-Universität Münster, 2011.

[52] Y. Wang, P. S. Cuculich, J. Zhang, K. A. Desouza, R. Vijayakumar, J. Chen, M. N. Faddis, B. D. Lindsay, T. W. Smith and Y. Rudy, "Noninvasive Electroanatomical Mapping of Human Ventricular Arrhythmias with Electrocardiographic Imaging," *Sci Transl Med,* vol. 3, no. 98, p. 98ra84, 2011.

[53] D. Bhakta and J. M. Miller, "Principles of Electroanatomical Mapping," *Indian Pacing and Electrophysiology Journal,* vol. 8, no. 1, pp. 32-50, 2008.

[54] M. Pop, M. Sermesant, D. Lepiller, M. Truong, E. McVeigh, E. Crystal, A. Dick, H. Delingette, N. Ayache and G. Wright, "Fusion of Optical and MR Imaging for Evaluation of Macroscopic Cardiac Computer Models: a Feasibility Study," *Medical Image Analysis,* vol. 13, no. 2, pp. 370-380, 2009.

[55] M. Pop, M. Sermesant, G. Liu, J. Relan, T. Mansi, A. Soong, J.-M. Peyrat, M. V. Truong, P. Fefer, E. McVeigh, H. Delingette, A. J. Dick, N. Ayache and G. A. Wright, "Construction of 3D MR Image-Based Computer Models of Pathologic Hearts, Augmented with Histology and Optical Imaging to Characterize the Action Potential Propagation," *Medical Image Analysis,* vol. 16, no. 2, pp. 505-523, 2012.

[56] R. M. Bell, M. M. Mocanu and D. M. Yellon, "Retrograde Heart Perfusion: The Langendorff Technique of Isolated Heart Perfusion," *Journal of Molecular and Cellular Cardiology,* vol. 50, no. 6, pp. 940-950, 2011.

[57] H. W. Heiss, "Werner Forssmann: A German Problem with the Nobel Prize," *Clinical Cardiology,* vol. 15, no. 7, pp. 547-549, 1992.

[58] R. A. Lange and L. D. Hillis, "Diagnostic Cardiac Catheterisation," *Criculation,* vol. 107, pp. e111-e113, 2003.

[59] G. K. R. Sirineni and A. E. Stillman, "Understanding the Heart: CT and MRI for Coronary Heart Disease," *Journal of Thoracic Imaging,* vol. 22, no. 1, pp. 107-113, 2007.

[60] U. Hoffmann, M. Ferencik, R. C. Cury and A. J. Pena, "Coronary CT Angiography," *Journal of Nuclear Medicine,* vol. 47, no. 5, pp. 797-806, 2006.

[61] H. Sakuma, "Coronary CT Versus MR Angiography: The Role of MR Angiography," *Radiology,* vol. 258, pp. 340-349, 2011.

[62] A. J. Nordmann, P. Hengstler, T. Harr, J. Young and H. C. Bucher, "Clinical Outcomes of Primary Stenting Versus Balloon Angioplasty in Patients with Myocardial Infarction: a Meta-Analysis of Randomized Controlled Trials," *American Journal of Medicine,* vol. 116, no. 4, pp. 253-262, 2004.

[63] K. Rioual, E. Unanua, S. G. M. Laguitton, D. Boulmier, P. Haigron, C. Leclerq and J.-L. Coatrieux, "MSCT labelling for pre-operative planning in cardiac rescynchronization therapy," *Comput Med Imaging Graph,* vol. 29, no. 6, pp. 431-439, 2007.

[64] H. Niinuma, R. T. George, A. Arbab-Zadeh, J. A. C. Lima and C. A. Henrikson, "Imaging of pulmonary veins during catheter ablation for atrial fibrillation: the role of multi-slice computed tomography," *Europace,* vol. 10, pp. iii14-iii21, 2008.

[65] K. Rhode, Y. Ma, A. Chandrasena, A. King, G. Gao, P. Chinchapatnam, M. Sermesant, D. Hawkes, T. Shaeffter, J. Gill and R. Razavi, "Evaluation of the use of multimodality skin markers for the registration of pre-procedure cardiac MR images and intra-procedure x-ray fluoroscopy images for image guided cardiac electrophysiology procedures," in *SPIE*, 2008.

[66] J. Ector, S. De Buck, W. Huybrechts, D. Nuyens, S. Dymarkowski, J. Bogaert, F. Maes and H. Heidbuchel, "Biplane three-dimentional augmented fluoroscopy as single navigation tool for ablation of atrial fibrillation: accuracy and clinical value," *Heart Rhythm. Epub,* vol. 5, no. 7, pp. 957-64, 2008.

[67] C. Daul, J. Lopen-Hernandez, D. Wolf, G. Karcher and G. Ethévenot, "3-D Multimodal Cardiac Data Superimposition using 2-D Image Registration and 3-D Reconstruction from Multiple Views," *Image and Vision Computing,* vol. 27, pp. 790-802, 2009.

[68] J. Ector, S. De Buck, J. Adams, S. Dymarkowski, J. Bogaert, F. Maes and H. Heidbüchel, "Cardiac Three-Dimensional Magnetic Resonance Imaging and Fluorscopy Merging: a New Approach for Electroanatomic Mapping to Assist Catheter Ablation," *Circulation,* vol. 112, no. 24, pp. 3779-3776, 2005.

[69] J. Ector, S. De Buck, J. Adams, S. Dymarkowski, J. Bogaert, F. Maes and H. Heidbüchel, "Biplane three-dimensional augmented fluoroscopy as single navigation tool for ablation for atrial fibrillation: accuracy and clinical value," *Heart Rhythm,* vol. 5, no. 7, pp. 957-964, 2008.

[70] J. Sra and S. Ratnakumar, "Cardiac image registration of the left atrium and pulmonary veins," *Heart Rhythm,* vol. 5, no. 4, pp. 609-617, 2008.

[71] L. Duong, R. Liao, B. Tailhades, A. Meyer and C. Xu, "Curve-based 2D-3D Registration of Coronary Vessels for Image Guided Procedure," in *SPIE*, Orlando, FL, USA, 2009.

[72] B. Zitová and J. Flusser, "Image Registration Methods: a Survey," *Image and Vision Computing,* vol. 21, pp. 977-1000, 2003.

[73] C. R. Maurier and J. M. Fitzpatrick, "A Review of Medical Image Registration," *Interactive Image-Guided Neurosurgery,* pp. 17-44, 1993.

[74] P. A. van den Elsen, E.-J. D. Pol and Viergever, "Medical Image Matching - A Review with Classification," *IEEE Eng. Med. Biol.,* vol. 12, no. 2, pp. 16-39, 1993.

[75] J. B. A. Maintz and M. A. Viergever, "A Survey of Medical Image Registration," *Medical Image Analysis,* vol. 2, no. 1, pp. 1-36, 1998.

[76] A. W. Habboosh, "A Review of MRI and PET Correlation," *Proceedings of IEEE Conference on Bioengineering,* pp. 16-17, 1992.

[77] M. C. Gilardi, G. Rizzo, A. Savi and F. Fazio, "Registration of Multi-Modal Biomedical Images of the Heart," *Quarterly Journal of Nuclear Medicine,* vol. 40, no. 1, pp. 142-150, 1996.

[78] T. Mäkelä, P. Clarysse, O. Sipilä, N. Pauna, Q. C. Pham, T. Katila and I. E. Magnin, "A Review of Cardiac Image Registration Methods," *IEEE Transactions on Medical Imaging,* vol. 21, no. 9, pp. 1011-1021, 2002.

[79] G. P. Penney, J. Weese, J. A. Little, P. Desmedt, D. L. G. Hill and D. J. Hawkes, "A Comparison of Similarity Measures for Use in 2-D-3-D Medical Image Registration," *IEEE Transactions on Medical Imaging,* vol. 17, no. 4, pp. 586-595, 1998.

[80] S. I. Grossman, Elementary Linear Algebra, California, US: Cengage Learning, Inc, 1994.

[81] S. Abraham, I. Kiss, S. Sanyal and M. Sanglikar, "Steepest Ascent Hill Climbing for a Mathematical Problem," in *Advanced Engineering and Applied Management*, Hunedoara, Romania, 2010.

[82] J. A. Nedler and R. Mead, "A Simplex Method for Function Minimization," *The Computer Journal,* vol. 7, no. 4, pp. 308-313, 1965.

[83] M. J. D. Powell, "An Efficient Method for Finding the Minimum of a Function of Several Variables without Calculating Derivatives," *Computer Journal,* vol. 7, no. 2, pp. 155-162, 1964.

[84] P. J. Besl and N. D. McKay, "A Method for Registration of 3-D Shapes," *IEEE Trans on Pattern Analysis and Machine Intelligence,* vol. 14, no. 2, pp. 239-256, 1992.

[85] P. H. Schönemann, "A Generalised Solution of the Orthogonal Procrustes Problem," *Psychometrika,* vol. 31, no. 1, pp. 1-10, 1966.

[86] B. Horn, "Closed-Form Solution of Absolute Orientation Using Unit Quaternions," *J Opt Soc Am A,* vol. 41, no. 4, pp. 629-642, 1987.

[87] L. Lemieux, R. Jagoe, D. R. Fish, N. D. Kitchen and D. G. T. Thomas, "A Patient-to-Computed-Tomography Image Registration Method Based on Digitally Reconstructed Radiographs," *Medical Physics,* vol. 21, no. 11, pp. 1749-1960, 1994.

[88] D. Tomaževič, B. Likar, T. Slivnik and F. Pernuš, "3-D/2-D Registration of CT and MR to X-ray Images," *IEEE Transactions on Medical Imaging,* vol. 22, no. 11, pp. 1407-1416, 2003.

[89] W. H. Press, B. P. Flannery, S. A. Teukolosky and W. T. Vetterling, Numerical Recipes in C, 2nd Edition, Cambridge, UK: Cambridge University Press, 1992.

[90] E. B. van de Kraats, G. P. Penney, T. van Walsum and W. J. Niessen, "Multispectral MR to X-Ray Registration of Vertebral Bodies by Generating CT-Like Data," in *MICCAI*, Palm Springs, 2005.

[91] P. Markelj, D. Tomaževič, F. Pernuš and B. Likar, "Robust Gradient-Based 3-D/2-D Registration of CT and MR to X-ray Images," *IEEE Transactions on Medical Imaging,* vol. 27, no. 12, pp. 1704-1714, 2008.

[92] M. A. Fischler and R. Bolles, "Random Sample Consensus - A Paradigm for Model-Fitting with Applications to Image-Analysis and Automated Cartography," *Communications of the ACM,* vol. 24, no. 6, pp. 381-395, 1981.

[93] F. Maes, A. Collignon, D. Vandermeulen, G. Marchal and P. Suetens, "Multimodality Image Registration by Maximization of Mutual Information," *IEEE Transactions on Medical Imaging,* vol. 16, no. 2, pp. 187-198, 1997.

[94] M. Kass, A. Witkin and D. Terzopoulos, "Snakes: Active Contour Models," *International Journal of Computer Vision,* vol. 1, no. 4, pp. 321-331, 1988.

[95] Y. Kita, D. L. Wilson and J. A. Noble, "Real-time Registration of 3D Cerebral Vessels to X-ray Angiograms," *MICCAI Lecture Notes in Computer Science,* vol. 1496, pp. 1125-1133, 1998.

[96] A. Franze, "Voronoi Diagrams - A Survey of a Fundamental Geomettric Data Structure," *ACM Computing Surveys,* vol. 23, no. 3, pp. 345-405, 1991.

[97] G.-A. Turgeon, G. Lehmann, M. Drangova, D. Holdsworth and T. Peters, "2D-3D Registration of Coronary Angiograms for Cardiac Procedure Planning and Guidance," *Medical Physics,* vol. 32, no. 12, pp. 3737-3749, 2005.

[98] A. Frangi, W. Niessen, K. Vincken and M. Viergever, "Multiscale Vessel Enhancement Filtering," *In Proceedings of MICCAI,* vol. 1496, pp. 130-137, 1998.

[99] R. Liao, N. Xu and Y. Sun, "Location Constraint Based 2D-3D Registration of Fluroscopic Images and CT Volumes for Image-Guided EP Procedures," in *SPIE*, San Diego, CA, US, 2008.

[100] S. Sauer, An Optimized Algorithm for Coronary Sinus Segmentation in MSCT Datasets, Diploma Thesis, Germany: University of Karlsruhe, 2005.

[101] M. Dewey, "Coronary CT Versus MR Angiography: Pro CT - The Role of CT Angiography," *Radiology,* vol. 258, pp. 329-339, 2011.

[102] A. M. Neubauer, J. A. Garcia, J. C. Messenger, E. Hansis, M. S. Kim, A. J. P. Klein, G. A. F. Schoonenberg, M. Grass and J. D. Carroll, "Clinical Feasibility of a Fully Automated 3D Reconstruction of Rotational Coronary X-Ray Angiograms," *Circulation: Cardiovascular Interventions,* vol. 3, pp. 71-79, 2010.

[103] R. A. Mclaughlin, J. Hipwell, G. P. Penney, K. Rhode, A. C. S. Chung, J. A. Noble and D. J. Hawkes, "Intensity-Based Registration versus Feature-Based Registration for Neurointerventions," in *Medical Image Understanding and Analysis*, Birmingham, England, UK, 2001.

[104] M. Vaseghi, D. A. Cesario, A. Mahajan, I. Wiener, N. G. Boyle, M. C. Fishbein, B. N. Horowitz and K. Shivkumar, "Catheter Ablation of Right Ventricular Outflow Tract Tachycardia: Value of Defining Coronary Anatomy," *J Cardiovasc Electrophysiol,* vol. 17, no. 6, pp. 632-637, 2006.

[105] G. Chintalapani and P. Chinnadurai, "Role of 3D/3D and 2D/3D Registration in Computer-Assisted Stenting in Aneurysms," in *MICCAI-STENT*, Nice, France, 2012.

[106] X. Zhao, "Heart Model for Valentine's Day," 15 February 2008. [Online]. Available: http://www.mathworks.com/matlabcentral/fileexchange/18754. [Accessed 2 September 2012].

[107] J. Bloomenthal and J. Rokne, "Homogenous Coordinates," *The Visual Computer,* vol. 11, no. 1, pp. 15-26, 1994.

[108] R. Penrose, "A Generalized Inverse for Matrices," *Proceedings of the Cambridge Philosophical Society,* vol. 51, pp. 406-413, 1955.

[109] J. V. Hajnal, D. L. G. Hill and D. J. Hawkes, Medical Image Registration, Boca Raton, Florida, USA: CRC Press LLC, 2001.

[110] National Electrical Manufacturers Association, "Digital Imaging and Communications in Medicine (DICOM)," National Electrical Manufacturers Association, Rosslyn, Virginia, USA, 2011.

[111] Y. Masutani, T. Dohi, F. Yamane, H. Iseki and K. Takakura, "Interactive Virtualized Display System for Intravascular Neurosurgery," in *CVRMed-MRCAS'97*, Grenoble, France, 1997.

[112] H. Zhang, C. Goodlett, T. Burke and N. Tustison, "ITK-SNAP," ITK-SNAP Team, 17 02 2011. [Online]. Available: http://www.itksnap.org. [Accessed 10 12 2012].

[113] P. A. Yushkevich, J. Piven, H. C. Hazlett, R. G. Smith, S. Ho, J. C. Gee and G. Gerig, "User-Guided 3D Active Contour Segmentation of Anatomical Structures: Significantly Improved Efficiency and Reliability," *Neuroimage,* vol. 31, no. 3, pp. 1116-1128, 2006.

[114] W. E. Lorensen and H. E. Cline, "Marching Cubes: A High Resolution 3D Surface Reconstruction Algorithm," *Computer Graphics,* vol. 21, no. 4, pp. 163-169, 1987.

[115] M. A. G. Merkx, J. O. Bescós, L. Geerts, E. M. H. Bosboom, F. N. van de Vosse and M. Breeuwer, "Accuracy and Precision of Vessel Area Assessment: Manual Versus Automatic Lumen Delineation Based on Full-Width at Half-Maximum," *J Magn Reson Imaging,* vol. 36, pp. 1186-1193, 2012.

[116] J. Peters, O. Ecabert, C. Meyer, R. Kneser and J. Weese, "Optimizing boundary detection via Simulated Search with applications to multi-modal heart segmentation," *Medical Image Analysis,* vol. 14, pp. 70-84, 2010.

[117] Y. Ma, G. Gao, G. Gijsber, C. A. Rinaldi, J. Gill, R. Razavi and K. S. Rhode, "Image-Based Automatic Ablation Point Tagging System with Motion Correction for Cardiac Ablation Procedures," *Information Processing in Computer-Assisted Interventions, Lecture Notes in Computer Science,* vol. 6689, pp. 145-155, 2011.

[118] S. Shafer, K. R. Hoffman, P. B. Noël, C. N. Ionita and J. Dmochowski, "Evaluation of Guidewire Path Reproducibility," *Medical Physics,* vol. 35, no. 5, pp. 1884-1892, 2008.

[119] V. Luboz, R. Blazewski, D. Gould and F. Bello, "Real-time Guide Wire Simulation in Complex Vascular Models," *The Visual Computer,* vol. 25, no. 9, pp. 827-834, 2009.

[120] F. Wang, L. Durratti, E. Samur, U. Spaelter and H. Bleuler, "A Computer Based Real-Time Simulation of Interventional Radiology," in *IEEE-EMBS*, 2007.

[121] M. V. N. Truong, A. Aslam, M. Ginks, R. Rinaldi, G. P. Penney and K. Rhode, "2D-3D Registration of Cardiac Images Using Catheter Constraints," in *Computing in Cardiology*, Park City, Utah, US, 2009.

[122] H. Wang, J. Kearney and K. Atkinson, "Arc-Length Parameterized Spline Curves for Real-Time Simulation," in *Curve and Surface Design*, Saint-Malo, 2002.

[123] R. Lissitz, P. Schönemann and J. Lingoes, "A Solution to the Weighted Procrustes Problem in Which the Transformation is in Agreement with the Loss Function," *Psychometrika,* vol. 41, no. 4, pp. 547-550, 1976.

[124] S. Li, J. Qin, J. Guo, Y.-P. Chui and P.-A. Heng, "A Novel FEM-Based Numerical Solver for Interactive Catheter Simulation in Virtual Catheterization," *International Journal of Biomedical Imaging,* no. 815246, pp. 1-8, 2011.

[125] J. Dong, D. Dalal, D. Scherr, A. Cheema, S. Nazarian, K. Bilchick, I. Almasry, A. Cheng, C. A. Henrikson, D. Spragg, J. E. Marine, R. D. Berger and H. Calkins, "Impact of Hearth Rhythm Status on Registration Accuracy of the Left Atrium for Catheter Ablation of Atrial Fibrillation," *Journal of Cardiovascular Electrophysiology,* vol. 18, pp. 1269-1276, 2007.

[126] H. Zhong, J. M. Lacomis and D. Schwartzman, "On the Accuracy of CartoMerge for Guiding Posterior Left Atrial Ablation in Man," *Heart Rhythm,* vol. 4, no. 5, pp. 596-602, 2007.

[127] M. C. Finlay, R. J. Hunder, V. Baker, L. Richmond, F. Goromonzi, G. Thomas, K. Rajappan, E. Duncan, M. Tayebjee, M. Dhinoja, S. Sporton, M. J. Earley and R. J. Schilling, "A Randomised Comparison of Cartomerge vs. NavX Fusion in the Catheter Ablation of Atrial Fibrillation," *Journal of Interventional Cardiac Electrophysiology,* vol. 33, pp. 161-169, 2012.

[128] C. Lohou and G. Bertrand, "A 3D 6-Subiteration Curve Thinning Algorithm Based on P-simple Points," *Discrete Applied Mathematics,* vol. 151, no. 1-3, pp. 198-228, 2005.

[129] R. C. Gonzalez and R. E. Woods, Digital Image Processing, 2nd Ed., Upper Saddle River, New Jersey: Prentice-Hall, 2002.

[130] S. Gray, "The Graph Abstract Data Type," in *Data Structures in Java: From Abstract Data Types to the Java Collections Framework*, Boston, MA, USA, Addison-Wesley, 2006, pp. 649-691.

[131] S. A. M. Baert, E. B. van de Kraats, T. van Walsum, M. A. Viergever and W. J. Niessen, "Three-Dimensional Guide-Wire Reconstruction from Biplane Image Sequences for Integrated Display in 3-D Vasculature," *IEEE Trans Med Imag,* vol. 22, no. 10, pp. 1252-1258, 2004.

[132] B. R. Knowles, M. Ginks, D. Caulfield, M. Cooklin, R. Razavi, N. Gall, T. Schaefter and K. Rhode, "Fusion of MR-Derived Anatomical and Late Enhancement Image Data with Ablation Mapping for Vertification of Lesion Delivery for Cardiac Radio-Frequency Ablation," in *SCMR*, Los Angeles, CA, USA, 2008.

[133] P. E. Radau, S. Pintilie, R. Flor, L. Biswas, S. O. Oduneye, V. Ramanan, K. A. Anderson and G. A. Wright, "VURTIGO: Visualisation Platform for Real-time, MRI-Guided Cardiac Electroanatomical Mapping," in *STACOM, MICCAI*, Toronto, ON, Canada, 2011.

[134] D. A. Spears, A. M. Suszko, R. Dalvi, A. M. Crean, J. Ivanov, K. Nanthakumar, E. Downar and V. S. Chauhan, "Relationship of Bipolar and Unipolar Electrogram Voltage to Scar Transmurality and Composition Derived by Magnetic Resonance Imaging in Patients with Nonischemic Cardiomyopathy Undergoing VT Ablation," *Heart Rhythm,* vol. 9, no. 11, pp. 1837-1846, 2012.

[135] J. E. Jackson, A User's Guide to Principal Components, Hoboken, NJ, USA: John Wiley and Sons, 1991.

[136] M. Truong, T. Gordon, R. Razavi, G. Penney and K. S. Rhode, "Analysis of Catheter-Based Registration with Vessel-Radius Weighting of 3D CT Data to 2D X-ray for Cardiac Catheterisation Procedures in a Phantom Study," in *STACOM, MICCAI*, Toronto, ON, Canada, 2011.

[137] Y. L. Ma, A. P. King, N. Gogin, C. A. Rinaldi, J. Gill, R. Razavi and K. S. Rhode, "Real-Time Respiratory Motion Correction for Cardiac Electrophysiology Procedures using Image-Base Coronary Sinus Catheter Tracking," in *MICCAI*, Beijing, China, 2010.

[138] D. G. Altman and J. M. Bland, "Diagnostics Tests 2: Predictive Values," *British Medical Journal,* vol. 309, p. 102, 1994.

[139] C. Pathak, M. Van Horn, S. Weeks and E. Bullitt, "Comparison of Simultaneous and Sequential Two-View Registration for 3D/2D Registration of Vascular Images," in *MICCAI*, Palm Springs, CA, USA, 2005.

[140] J. Velut, C. Toumoulin and J.-L. Coatrieux, "3D Coronary Structure Tracking Algorithm with Regularization and Multiple Hypotheses in MRI," in *IEEE International Conference on Biomedical Imaging: From Nano to Macro*, Piscataway, NJ, USA, 2010.

[141] E. M. C. Ashley, "Anaesthesia for Electrophysiology Procedures in the Cardiac Catheter Laboratory," *Continuing Education in Anaesthesia, Critical Care & Pain,* vol. 12, no. 5, pp. 230-236, 2012.

[142] D. Sinclair, "S-hull; a fast sweep hull routine for Delauney triangulation," *http://www.s-hull.org,* 2010.

[143] A. Johnson, "Clipper - an Open Source Freeware Polygon Clipping Library," 23 May 2013. [Online]. Available: http://www.angusj.com/delphi/clipper.php. [Accessed 06 June 2013].

[144] B. R. Vattie, "A Generic Solution to Polygon Clipping," *Communications of the ACM,* vol. 35, no. 7, pp. 56-63, 1992.

[145] D. Henderson, S. H. Jacobson and A. W. Johnson, "The Theory and Practice of Simulated Annealing," in *Handbook of Metaheuristics*, Dordrecht, South Holland, Netherlands, Kluwer Academic Publishers, 2003, pp. 287-319.

[146] D. Whitley and M. P. Fitzhorn, "Delta Coding: An Iterative Search Strategy for Genetic Algorithms," in *Fourth International Conference on Genetic Algorithms*, San Diego, CA, USA, 1991.

[147] J. Peters, O. Ecabert, C. Meyer, H. Schramm, R. Kneser, A. Groth and J. Weese, "Automatic Whole Heart Segmentation in Static Magnetic Resonance Image Volumes," in *MICCAI*, Brisbane, Australia, 2007.

[148] O. Ecabert, J. Peters, H. Schramm, C. Lorenz, J. von Berg, M. J. Walker, M. Vembar, M. E. Olszewski, K. Subramanyan, G. Lavi and J. Weese, "Automatic Model-Based Segmentation of the Heart in CT Images," *IEEE Transactions in Medical Imaging,* vol. 27, no. 9, pp. 1189-1201, 2008.

[149] M. Vandana, G. Sundaramoorthi and A. Tannenbaum, "Tubular Surface Segmentation for Extracting Anatomical Structures from Medical Imagery," *IEEE Transactions on Medical Imaging,* vol. 29, no. 12, pp. 1945-1958, 2010.

[150] M. Panayiotou, K. A. P, K. K. Kanwal, R. J. Housden, M. Y, C. A. Rinaldi, G. J, C. M, M. O'Neill and K. S. Rhode, "Extraction of Cardiac and Respiratory Motion Information from Cardiac X-ray Fluoroscopy Images using Hierarchical Manifold Learning," in *STACOM Workshop, MICCAI*, Nagoya, Japan, [in press].

[151] Kearns and K. L, "Respiratory Monitor and X-ray Triggering Apparatus". United States of America Patent US4387722 A, 14 June 1983.

[152] M. Panayiotou, K. A. P, Y. Ma, R. J. Housden, C. A. Rinaldi, J. Gill, M. Cooklin, M. O'Neill and K. S. Rhode, "A Statistical Model of Catheter Motion from Interventional X-ray Images: Application to Retrospective and Prospective Image-Based Gating," *Physics in Medicine and Biology,* [under review].

# Selected Publications

## Reviewed Conference Paper Publications

1. M. V. N. Truong, G. P. Penny and K. S. Rhode, "Feasibility Study of Looped-Catheter-Based 2D-3D Image Registration of CT and X-Rays for Cardiac Catheterization Procedures in a Phantom Experiment," *In proceedings of STACOM, MICCAI, LNCS (7746)*: 317-325. 2013.

2. M. Truong, T. Gordon, R. Razavi, G. Penney and K. S. Rhode. "Analysis of Catheter-Based Registration with Vessel-Radius Weighting of 3D CT Data to 2D X-ray for Cardiac Catheterisation Procedures in a Phantom Study," *In proceedings of STACOM, MICCAI, LNCS (7085)*: 139-148. 2012.
   *(Recipient of the Best Paper Award)*

3. M. V. N. Truong, A. Aslam, M. Ginks, C. A. Rinaldi, R. Razavi, G. P. Penney and K. S. Rhode, "2D-3D Registration of Cardiac Images Using Catheter Constraints," *In proceedings of Computers in Cardiology (36)*: 605-608. 2009.

4. M. V. N. Truong, A. Aslam, M. Ginks, C. A. Rinaldi, R. Razavi, G. P. Penney and K. S. Rhode, "Preliminary Investigation: 2D-3D Registration of MR and X-ray Cardiac Images Using Catheter Constraints," *In proceedings of CI2BM, MICCAI*: 9 pages. 2009.
   http://hal.inria.fr/inria-00418352

## Reviewed Abstract Publications

1. M. V. N. Truong, G. P. Penney and K. S. Rhode, "Looped-Catheter-Based 2D-3D Image Registration of CT and X-rays for Cardiac Catheterisation Procedures," *In proceedings of CTCIBM*: 49. 2012.
   https://imagingresearch.centraldesktop.com/cardiacworkshop/